NASA Contractor Report 182193

P-291

Improved Silicon Nitride for Advanced Heat Engines

H.C. Yeh and H.T. Fang
Allied–Signal Aerospace Company
Torrence, California

April 1991

Date for general release April 1993 .

Prepared for
Lewis Research Center
Under Contract NAS3-24385

ABSTRACT

This report summarizes the results of a four-year program to improve the strength and reliability of injection-molded silicon nitride. Statistically designed processing experiments were performed to identify and optimize critical processing parameters and compositions. Process improvements were monitored by strength testing at room and elevated temperatures, and microstructural characterization by optical, scanning electron microscope, and scanning transmission electron microscope. Processing modifications resulted in a 20-percent strength and 72-percent Weibull slope improvement of the baseline material. Additional sintering aids screening and optimization experiments succeeded in developing a new composition (GN-10) capable of 581.2 MPa (84.3 ksi) at 1399°C (2550°F). A SiC whisker-toughened composite using this material as a matrix achieved a room-temperature toughness of 6.9 $MPa.m^{1/2}$ by the Chevron notched bar technique. Exploratory experiments were conducted on injection molding of turbocharger rotors.

FOREWORD

Fabrication and processing of the ceramic specimens was conducted by the Garrett Ceramic Component (GCC) of Allied-Signal Aerospace Company, Torrance, California. The Garrett Auxiliary Power Division (GAPD) of Allied-Signal Aerospace Company, Phoenix, Arizona, was responsible for statistical design of experiments, modulus of rupture (MOR) and fracture toughness (K_{IC}) determination, and fractography and statistical analysis under subcontract. Grain boundary characterization was performed by Allied-Signal Research and Technology, Desplains (ASRT).

The co-principal investigators were Dr. Harry C. Yeh of GCC and Mr. Ho T. Fang of GAPD. Dr. Harry C. Yeh also served as overall Program Manager and Dr. Jay R. Smyth served as Program Manager at GAPD. Mr. Marc R. Freedman of NASA Lewis Research Center was Project Manager. The significant contributions of Lonnie Anderson, Dr. Bernard Busovne, Terry Hill, Ethel Solidum, and Kwei Teng of GCC, Dave Carruthers, Henry Hwang, Annie Lu, Jim Schienle, and Dr. Jim Wimmer of GAPD, and Dr. Steve Bradley and Dr. Keith Karasek of ASRT, are gratefully acknowledged.

The contributions of the following former employees of Allied-Signal Aerospace Company are also acknowledged: Dave Richerson, Mike Rorabaugh, Herb Gersch, and Karsten Styhr.

TABLE OF CONTENTS

TABLE OF CONTENTS (Continued)

NOTE: Section 2.1 performed under Task I of the contract.
Sections 2.2, 2.5, and 2.6 performed under Task II of the contract.
Sections 2.3 and 2.4 performed under revised Task II of the contract.

LIST OF ILLUSTRATIONS

LIST OF ILLUSTRATIONS (Continued)

LIST OF ILLUSTRATIONS (Continued)

LIST OF ILLUSTRATIONS (Continued)

LIST OF ILLUSTRATIONS (Continued)

LIST OF ILLUSTRATIONS (Continued)

LIST OF TABLES

LIST OF TABLES (Continued)

LIST OF TABLES (Continued)

GLOSSARY

ACC	AiResearch Casting Company
A/C	Air classified
AR	As-received
ASRT	Allied-Signal Research and Technology
BET	Brunauer-Emmett-Teller Surface Area Measurement Method
BSE	Back scatter electron imaging in SEM
CIP	Cold isostatic pressing
EDX	Energy dispersive X-ray
GAPD	Garrett Auxiliary Power Division, Allied-Signal Aerospace Company
GCC	Garrett Ceramic Components, Allied-Signal Aerospace Company
GTE	General Telephone and Electronics, Inc.
HIP	Hot isostatic pressing
IRT	IRT Corporation, San Diego, CA
ksi	Thousand pounds per square inch
L/N	Leeds and Northrup
MOR	Modulus of rupture
MPa	MegaPascals
NASA	National Aeronautics and Space Administration
NDE	Nondestructive evaluation
PSD	Particle size distribution
RBSN	Reaction-bonded silicon nitride
RPM	Revolutions per minute
SEM	Scanning electron microscope

STEM	Scanning transmission electron microscope
TGA	Thermogravimetric analysis
TMA	Thermomechanical analysis
USP	Ultrasonic probe dispersion time
XRD	X-ray diffraction analysis

EXECUTIVE SUMMARY

This document, submitted by Garrett Ceramic Components (GCC), Allied-Signal Aerospace Company (formerly AiResearch Casting Company (ACC)), is the final report for the Improved Silicon Nitride for Advanced Heat Engines program. The program was conducted for the National Aeronautics and Space Administration (NASA) under Contract NAS3-24385. Garrett Auxiliary Power Division (GAPD), Allied-Signal Aerospace Company, was the major subcontractor to this program. This report covers the period September 1984 through August 1988.

The objective of the program was to establish the technology base required to fabricate silicon nitride components by injection molding with the strength, reliability, and reproducibility necessary for heat engine applications.

Significant advances in processing of Si_3N_4 materials were made during the course of this program. The as-processed baseline material flexural strength was increased 20 percent at both room temperature and 1232°C (2250°F) to 668.8 MPa (97 ksi) and 403.4 MPa (58.5 ksi), respectively. The Weibull slope was increased by 72 percent to 13.6. Both strength and Weibull slope improvements were attained by optimizing raw materials and processing through statistically designed matrix experiments. This was achieved without changing sintering aid chemistry. In addition, a material was developed with MOR values of 889.5 MPa (129 ksi) at room temperature, 706.7 MPa (102.5 ksi) at 1232°C (2250°F), and 581.3 MPa (84.3 ksi) at 1232°C (2550°F) through sintering aid chemistry changes. A patent (U.S. patent No. 4,870,036) concerning the composition, processing, and properties of this material was issued on September 26, 1989. This material has been selected for component fabrication and heat engine testing under the DOE/NASA/ATTAP program. Reproducibility of this new material system was demonstrated and areas for further property improvement were identified. The work described above was accomplished by dividing the program into six major technical efforts supported by a series of small exploratory experiments. The highlights of each effort are summarized as follows:

- Baseline Material Characterization

  The objective of this effort was the complete characterization of GCCD baseline injection-molded and sintered silicon nitride (92% GTE SN-502 Si_3N_4 + 6% Y_2O_3 + 2% Al_2O_3). This characterization provided a foundation for the subsequent material/process improvement efforts. As-sintered test bars were evaluated for phase content, room and elevated temperature MOR strength, Weibull slope, stress rupture life, strength after oxidation, fracture origin locations, microstructure, and density.

  A total of 208 test bars were strength tested at room temperature, 1066°, 1232°, and 1399°C (1950°, 2250°, and 2550°F). The mean strength at room temperature was 540 MPa (79.3 ksi), with a Weibull slope of 7.9. The mean strengths at 1066°, 1232°, and 1399°C were 420, 320, and 140 MPa (61.1, 47.1, and 21.7 ksi), respectively. Static oxidation test data showed that test bars exposed for 200 hours

to air in the temperature range of 388° to 1296°C (730° to 2365°F) exhibited a maximum degradation of 13 percent in room temperature strength.

- Improvement of Baseline Material

  Statistically designed experiments were performed to establish the optimum materials and processing parameters aimed at a 20-percent improvement in room temperature MOR and 100-percent improvement in Weibull slope over the baseline material. Two statistically designed half-replicate of 2^5 factorial experiments were performed. Five processing variables--sintering aids, mixing, binder, sintering powder bed, and sintering cycle--were evaluated at two levels.

  The experiments identified a material and process which produced test bars with an average room temperature MOR of 670.9 MPa (97.3 ksi) and a Weibull slope of 13.6. The material met the initial program goal of 20-percent increase in strength, and approached the Weibull slope goal (72 percent improvement vs the goal of 100 percent). The improved material/process was used for a subsequent net shape fabrication effort.

  A statistically designed experiment was performed to demonstrate the reproducibility of the improved material/process. Reproducibility was achievable when the same lot of material, same injection molder, and same sinter/HIP furnace and cycle were used.

- Development of High Temperature Material

  The objective of this effort was to develop a new Si_3N_4 composition and process with a minimum flexure strength of 586.1 MPa (85 ksi) at 1232°C (2550°F). Two approaches were taken to achieve the goal: (1) reduce the amount of sintering aids in the baseline Y_2O_3 + Al_2O_3 system and (2) screen for alternate sintering aids.

  The Y_2O_3 + Al_2O_3 system was selected because of GCC's experience with the Code 1 (8 wt% Y_2O_3 + 4 wt% Al_2O_3) and Code 2 (6 wt% Y_2O_3 + 2 wt% Al_2O_3) materials and the trend of improved high-temperature properties with decreasing sintering aid content. A statistically designed experiment was used to evaluate the composition/strength relationship in this system at room temperature, 1232°C (2250°F), and 1399°C (2550°F). A mathematical model was generated to produce a contour plot that describes and predicts the flexure strength as a function of composition in the range evaluated. The optimum high temperature composition identified in the Y_2O_3 + Al_2O_3 system did not meet the high-temperature strength goal.

  However, the alternate approach of screening various sintering aid systems for improved high temperature strength was successful. The investigation developed a new HIP'ed, high-temperature material,

GN-10, with excellent strengths of 889.5 MPa (129.1 ksi) at room temperature, 706.7 MPa (102.5 ksi) at 1232°C (2250°F), and 581.3 MPa (84.3 ksi) at 1399°C (2550°F). A follow-up optimization experiment using the modeling technique developed for the Y_2O_3 + Al_2O_3 system produced a new material with even higher strength (620.6 MPa (90 ksi)) at 1399°C (2550°F).

- Process Development for the New High-Temperature Material

  Since the excellent flexure strength of the new high temperature material (GN-10) was achieved with test bars machined from HIP'ed billets, the objective of this effort was to fabricate the new material by sinter/HIP of injection-molded test bars. This effort was not successful because HIP furnace problems prevented obtaining straight, fully dense test bars.

- Development of SiC Whisker/Si_3N_4

  Exploratory experiments were conducted to fabricate dense SiCw/Si_3N_4 composites and to characterize their properties. Both the improved baseline Si_3N_4 and the GN-10 formulations were used as the matrix material. The goal was to develop a composite with high-temperature strength and high toughness. Tokawhisker SiC whisker from Tokai Carbon Company, and SC-9 SiC whisker from Advanced Composite Materials Company (ACMC, formerly ARCO) were investigated.

  A uniform dispersion of whiskers in Si_3N_4 was achieved with both dry and wet blending techniques. Green samples were successfully fabricated by both cold isostatic processing and injection molding. Whisker loadings investigated ranged from 10- to 30-weight percent. A series of sinter/HIP experiments were conducted to determine the feasibility of densifying SiCw/Si_3N_4 composites without encapsulation. The best density achieved was 2.60 g/cc (80 percent theoretical). The conclusion was that encapsulated HIP was necessary to achieve full-density, net-shape parts. One such experiment was conducted using the ASEA glass encapsulation technique. Full density was achieved for both 20-percent Tokai SiC whisker/GN-10 matrix and 20-percent ACMC SiC whisker/GN-10 matrix samples. Relative to monolithic GN-10, the dense composites exhibited up to 14 percent improvement in toughness; however, the flexural strength of the composites was lower. A comparison between the two whiskers evaluated showed that the ACMC whisker was superior in achieving toughening improvements.

- Net-Shape Component Fabrication

  One of the goals of this program was to apply the fabrication technology learned through injection-molded test bars to net-shape fabrication. A decision was made to evaluate how much of the material/process data base learned from the improved baseline material/process could be transferred to the fabrication of net-shape components.

Available in-house molds for two different size turbocharger rotors, T-2 (47 mm dia) and T-25 (53 mm dia) were used. T-25, the larger of the two, was selected for the initial evaluation. The results of the improved baseline study were found applicable only in establishing compositions and parameters through blending and pelletizing and in serving as a starting point for injection molding and dewaxing. Injection molding parameter adjustments were necessary to make the transition from test bars to large, complex components.

Improvements in molding parameters were guided by correlating defects and molding parameters of T-25 rotors. Defect types, location, and causes were identified and characterized. It was concluded that total elimination of defects in T-25 rotors would require molding tool design changes. The tooling used to produce T-25 wax patterns for metal castings could not be directly applied to molding ceramics. Thicker blades and smooth transition from shaft to hub are examples of some of the modifications needed.

The T-2 tool, which had previously been modified to provide a smoother hub-to-shaft transition (tapered shaft) and slightly thicker blades, was used to produce molding with significantly fewer defects.

This illustrates the need for an interdisciplinary approach at the onset between engine designer, tool engineer, ceramic process engineer, and mold manufacturer.

In conclusion, a better understanding of processing of silicon nitride has been established. Key processing parameters were identified and resulted in the development of improved materials.

1. INTRODUCTION

Significant improvements in turbine engine operating efficiencies can be obtained through the use of uncooled ceramic components at material temperatures above those attainable with high-temperature metal alloys. Both Department of Energy (DOE) and Department of Defense (DOD) advanced turbine-engine programs provide evidence that improved engine performance can be realized However, current state-of-the-art ceramic materials lack the strength, reliability and toughness required for extensive engine use. In addition, the ultimate application of ceramics in heat engines requires a reproducible net-shape fabrication process.

The objective of this program was to develop the technology base required to fabricate silicon nitride components that have the strength, reliability, and reproducibility necessary for actual heat engine applications. It consisted of six major technical efforts, five of which addressed material improvements in injection-molded test bars and isopressed billets, and one which addressed incorporating the advanced materials into injection-molded parts. The objectives of these efforts follows:

(1) Baseline Material Characterization--To characterize the baseline-sintered silicon nitride.

(2) Improvement of Baseline Material--To improve the strength by 20 percent and Weibull slope by 100 percent, and to demonstrate material/process reproducibility.

(3) Development of High-Temperature Material--To develop a new Si_3N_4 with an average flexural strength of at least 586.1 MPa (85 ksi) at 1399°C (2550°F).

(4) Process Improvement for the New High-Temperature Material--To increase the as-processed strength and reliability of the new high-temperature material.

(5) Development of SiC Whisker/Si3N4 Matrix Composite--To develop a composite with high-temperature strength and improved toughness.

(6) Net Shape Component Fabrication--To apply the fabrication technology learned through injection molding of test bars to net-shape fabrication.

To support the above efforts, a series of exploratory experiments was conducted to evaluate new material and process concepts. In addition to the state-of-the-art ceramic processing and characterization methods, statistical experimental design, analysis, and modeling were used throughout the program. Experiments were performed in a series of processing iterations, and critical variables were identified for optimization.

2. TECHNICAL PROGRESS

2.1 BASELINE MATERIAL CHARACTERIZATION*

2.1.1 Summary/Introduction

The GCCD baseline fabrication process selected for study in this program was direct injection molding of test bars to net shape. The baseline material selected was a silicon nitride composition consisting of 92 percent GTE SN-502 Si_3N_4, 6 percent Y_2O_3, and 2 percent Al_2O_3.

Figure 1 is a logic chart showing the major steps in the baseline process and the characterization conducted at or after each step. Detailed characterization was necessary in order to establish a baseline fabrication process and demonstrate future improvements.

Statistical analysis of the baseline as-sintered test bars showed that the baseline material had an average room temperature flexural strength of 546.8 MPa (79.3 ksi) and Weibull slope of 7.9. High-temperature flexural strength, stress rupture, and oxidation properties of the baseline material were also established.

2.1.2 Characterization of Starting Powders

The starting powders, as listed in Table 1, are characterized as follows:

(1) Particle Size Distribution.--Particle size distribution (PSD) of the starting powders was measured by a Leeds & Northrup Microtrac. The sample preparation method employed for particle size distribution measurements combined a chemical dispersant with a high-energy, ultrasonic agitation. A sonication time of 2.5 minutes was sufficient for complete deagglomeration of powders.

To verify uniformity throughout the large drum of as-received (AR) SN-502 silicon nitride, samples were taken from the top, middle, and bottom of the drum. Figure 2 shows that the PSD curves of the three samples were coincident with each other as measured by the L/N Microtrac particle size analyzer.

The lot sizes of as-received Y_2O_3 and Al_2O_3 powders were relatively small and thus only one sample was taken from each material. Figures 3 and 4 are the respective PSD's. Also shown in the figures are effects of ultrasonic agitation time in minutes (USA) as indicated by the two dotted curves in each figure.

(2) Surface Area.--The surface area of the as-received baseline powders was measured by a Micromeritics Model FlowSorb II 2300 surface area analyzer. A 1-cc powder sample was loaded into the sample tube for measurement. The surface area of each powder is shown in table 1.

(3) Morphology.--The as-received GTE SN-502 powder was evaluated optically and found to be coarse and nonhomogenous. The bulk of the powder was beige in color, but typically contained numerous white particles and

*Performed under Task I of the contract.

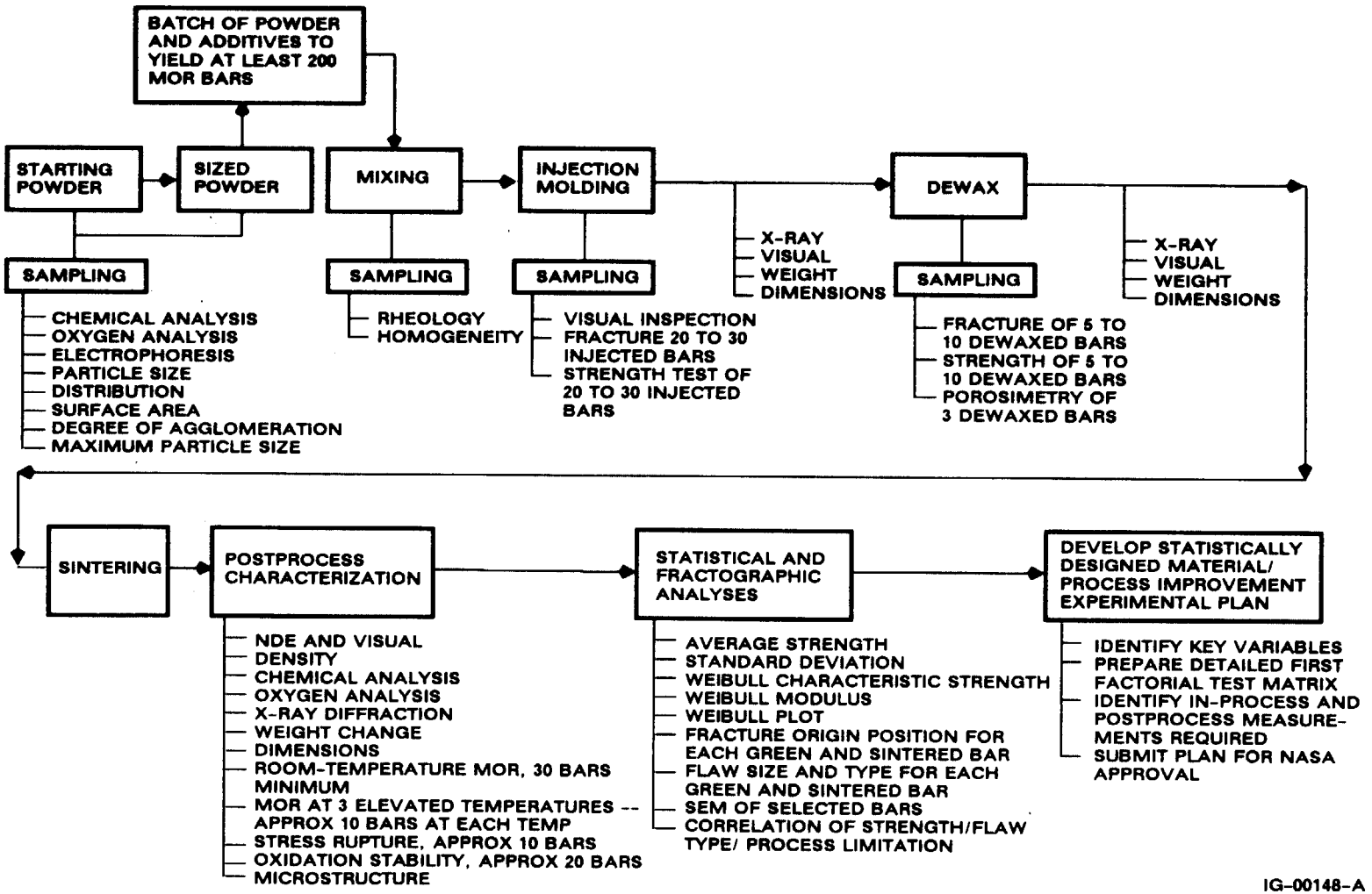

Figure 1.--Process Flow Chart.

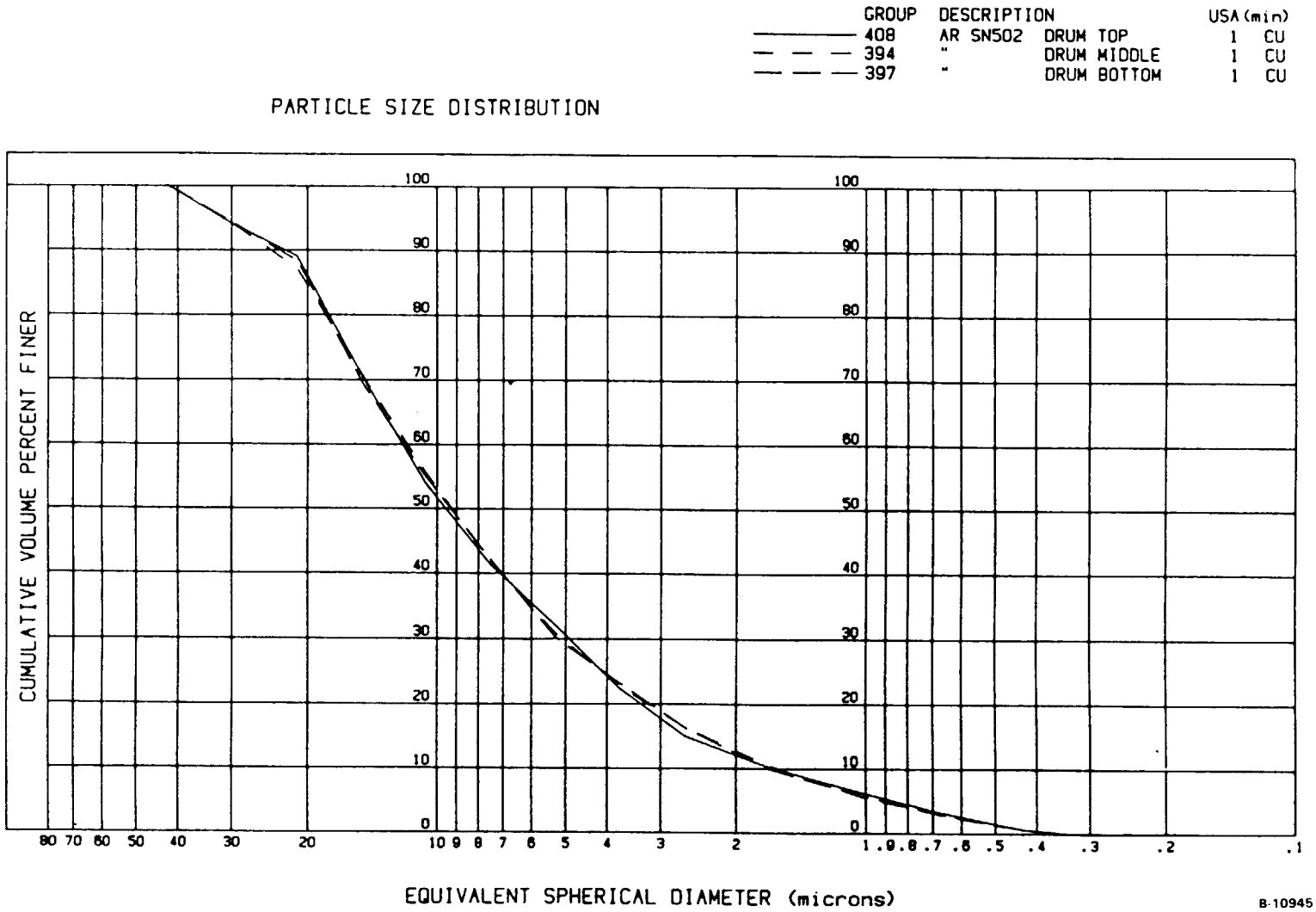

Figure 2.--Particle Size Distributions of Powders Sampled from the Top, Middle, and Bottom of a GTE SN-502 Si_3N_4 Drum (Lot SN 107).

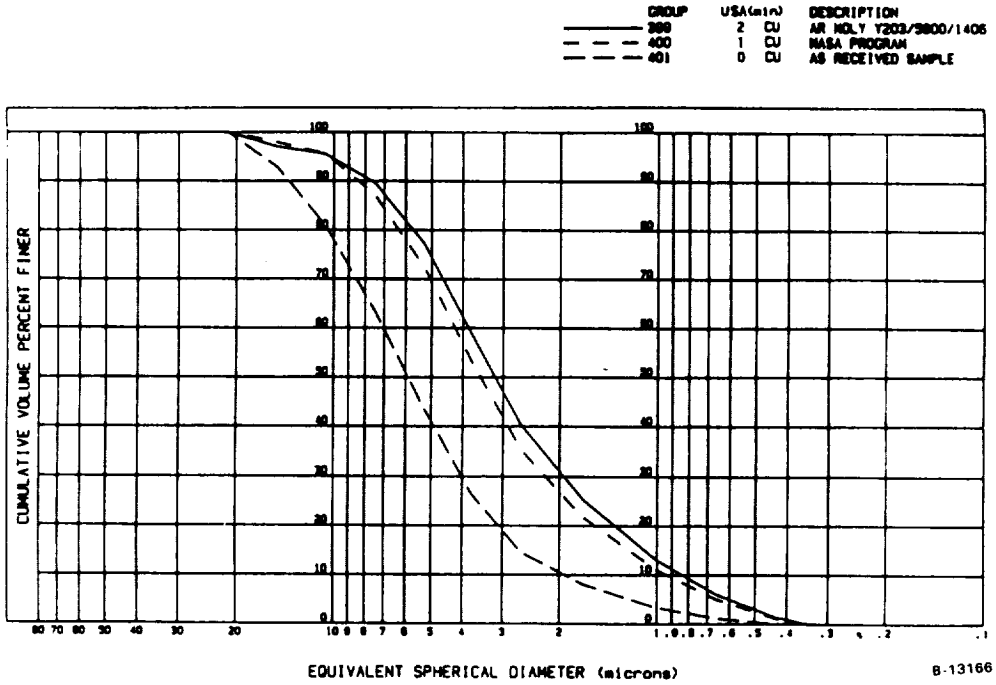

Figure 3.--Particle Size Distribution of As-Received Molycorp Y_2O_3 L&N Microtrac.

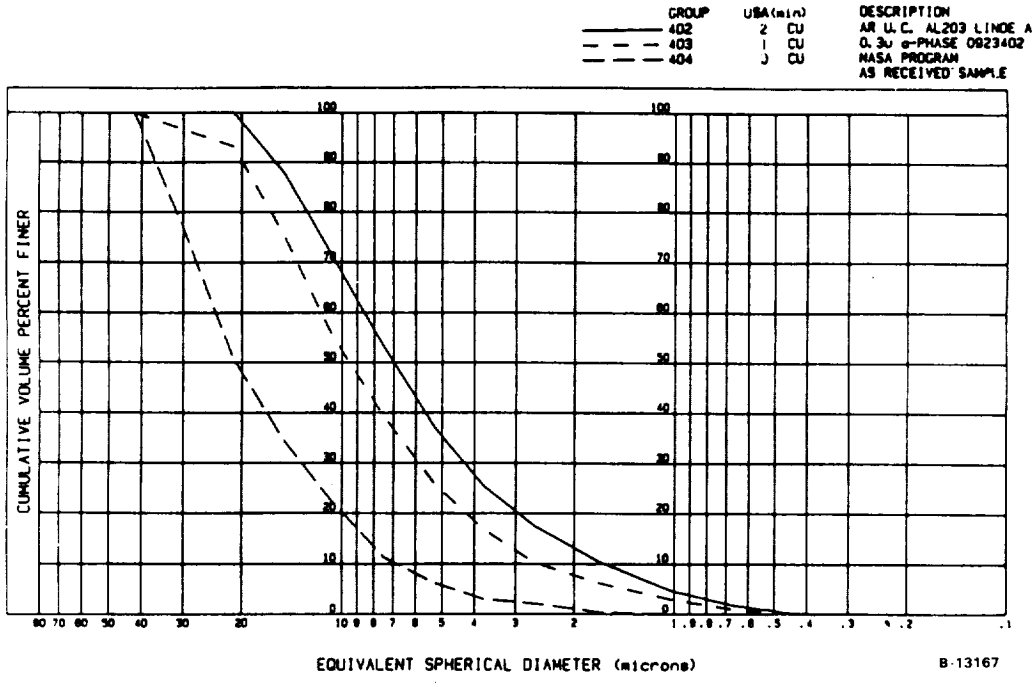

Figure 4.--Particle Size Distribution of As-Received Linde Al_2O_3 L&N Microtrac.

TABLE 1.--TASK 1 BET SURFACE AREA OF AS-RECEIVED POWDERS FOR BASELINE BARS

GTE SN-502, lot SN-107	Si_3N_4	5.26 sqm/g
Molycorp	Y_2O_3	6.51 sqm/g
Linde A	Al_2O_3	13.13 sqm/g

black particles. White particles and black particles were hand-separated and inspected by energy dispersive X-ray analysis (EDX). Chemically, the white particles were indistinguishable from the bulk of the powder (beige particles). The black particles contained Cr, Fe, Ni, and Cu impurities as shown in the EDX spectral plots illustrated in figure 5.

The coarse particles ranged in size up to 750 μm in diameter and appeared to be agglomerates of many very fine particles. Some of the agglomerates were relatively soft, but most were quite hard. Individual agglomerates were hand-sorted and examined by SEM. Others were washed and concentrated in a sequence of elutriations in deionized water. Samples of both the concentrated coarse fraction and the fine fraction from the supernatant liquid were applied to slides, gold coated, and examined by SEM.

Coarse particles or agglomerates which settled after two elutriations in deionized water are shown in figure 6. As shown in figure 6a, these range in size to over 500 μm. All were soft and could be deformed, although the ease of deformation varied substantially between "particles." Examination at high magnification (figure 6b) showed that these "particles" were actually agglomerates of much finer particles, some of which had a high aspect ratio (which will subsequently be referred to as whiskers). The whiskers appeared to be less than 1 μm in diameter and up to about 40 μm long. The particles appeared to be equiaxed and under 1 μm, but had a tendency to agglomerate into short chain-like structures (figure 6c).

A sequence of elutriations was conducted on as-received GTE SN-502 Si_3N_4 powder using ultrasonic agitation prior to settling. Figure 7a and 7b illustrate agglomerates retained in the deionized water after brief settling. Individual agglomerates varied substantially. The one shown in figure 7c consisted largely of needle-like material, whereas particles predominated in the type of agglomerate shown in figure 7d. Note that many of the needles interpenetrate. This reticulation contributes to the strong tendency of the as-received GTE SN-502 powder to form large agglomerates.

The as-received Y_2O_3 powder was visually more homogenous than the GTE Si_3N_4 powder and appeared to be free of large agglomerates. No significant coarse fraction was isolated by elutriation. A typical SEM view of the powder is shown in figure 8. Particle sizes ranged up to

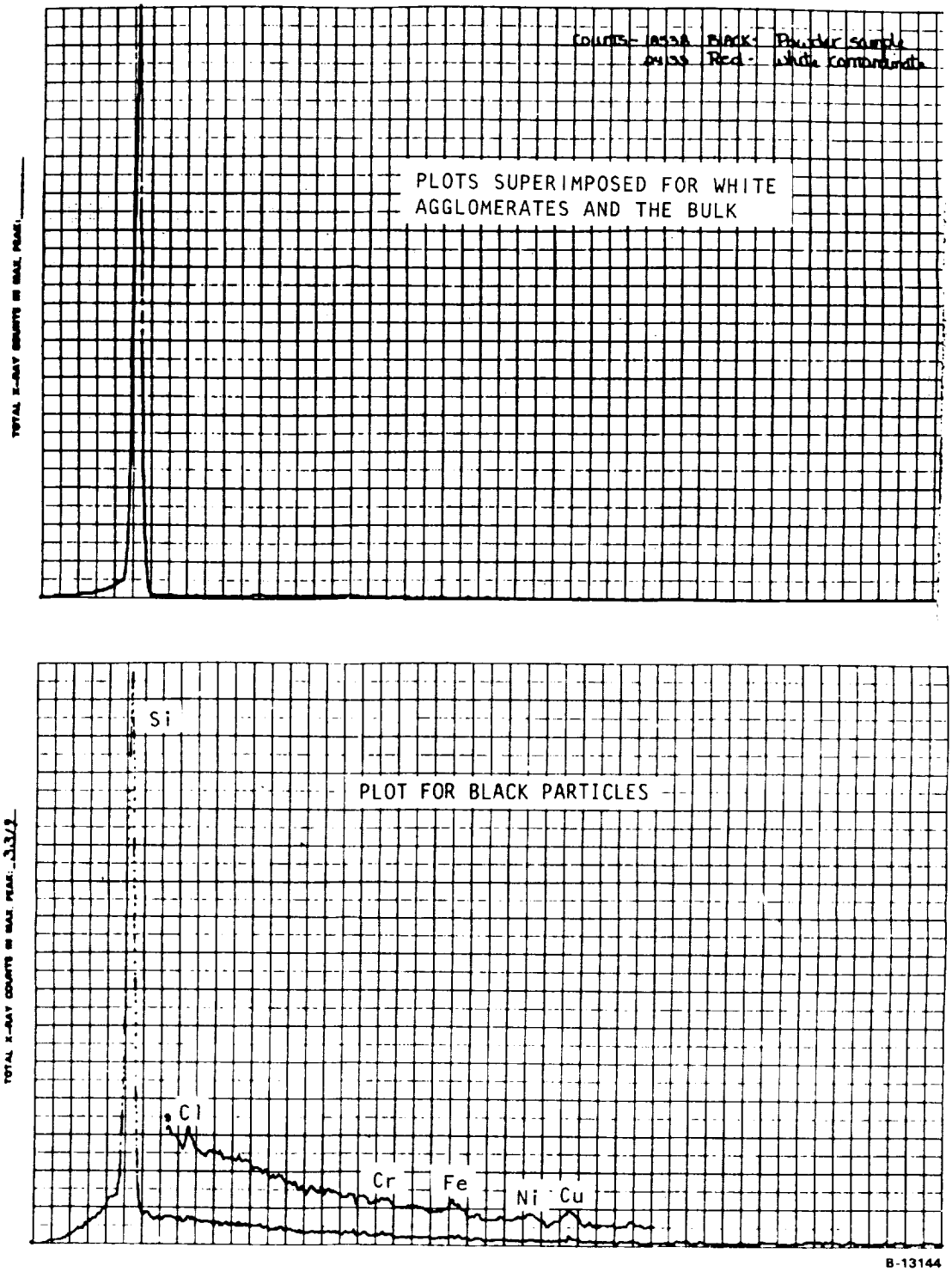

Figure 5.--EDX Results of Coarse Particles Separated from GTE SN-502 As-Received Powder.

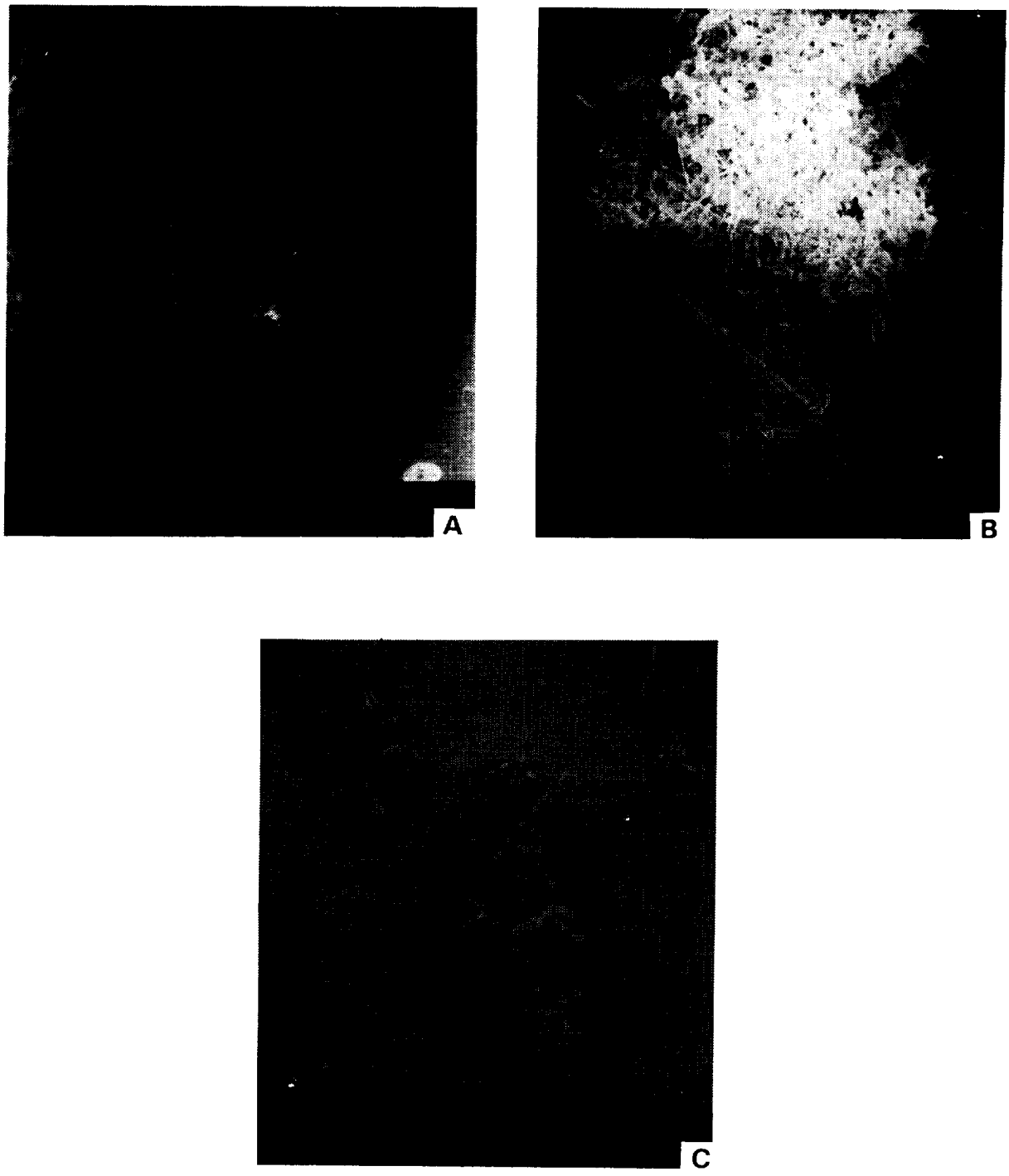

F-48909

Figure 6.--SEM Photomicrographs of Coarse Particles/Agglomerates Separated from As-Received GTE SN-502 Si_3N_4 Powder by Elutriation.

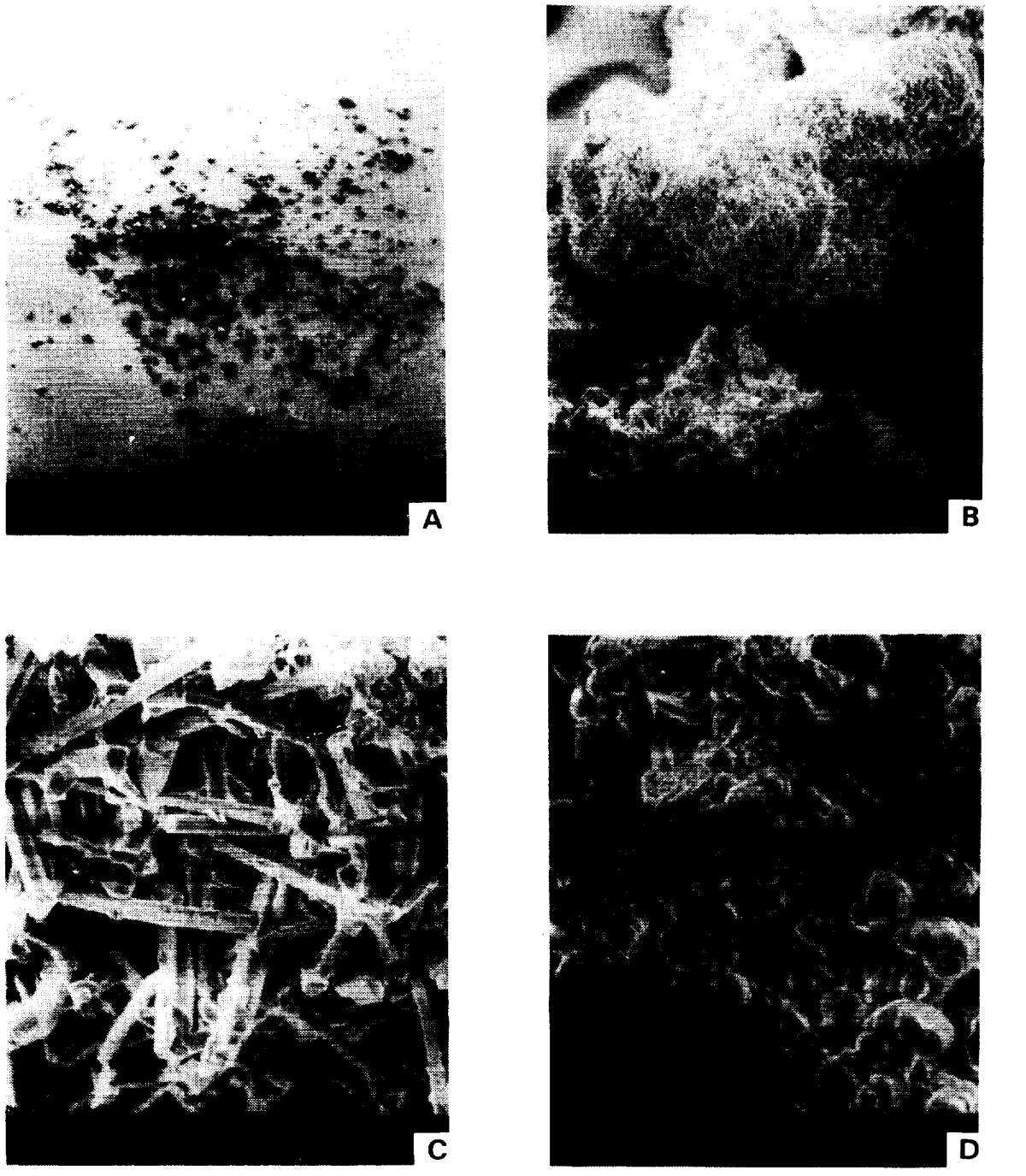

F-48901

Figure 7.--SEM Photomicrographs of Fraction of GTE SN-502 Powder from the Liquid after Ultrasonic Agitation and Elutriation.

F-48907

Figure 8.--SEM Photomicrograph of the As-Received Y_2O_3 Powder.

12 μm but were typically 1 to 5 μm. Particles are angular with a fractured appearance and contrast sharply with the rounded particles and elongated whiskers of the GTE SN-502 Si_3N_4. Some Y_2O_3 particles contained cracks and laminar porosity.

The as-received Al_2O_3 powder was also visually more homogenous than the GTE Si_3N_4 powder, but unlike the Y_2O_3 it formed agglomerates during elutriation. As shown in figure 9, the agglomerates were much smaller than typical of SN-502 Si_3N_4 and contained no whiskers. The Al_2O_3 particles appeared to be equiaxed and about 0.2 μm across. However, they are agglomerated into highly porous networks with a low coordination number for individual particles.

The examinations of the as-received powders verified the need to process the powders before fabrication into test bars.

(4) Chemical Analysis.--The chemical analysis of the as-received GTE SN-502, lot 107, the Y_2O_3, and Al_2O_3 is listed in table 2. Table 3 lists the neutron activation oxygen analysis results of the as-received powders. The measured oxygen contents of Y_2O_3 and Al_2O_3 were below theoretical values.

2.1.3 Binder System Characterization

The baseline binder used was LN 205-208 supplied by J. F. McCaughin, Rosemead, California. The rheology of the binder was characterized by a Haake Buchler rheometer. Figure 10 shows a torque-vs-temperature curve over the injection molding temperature range. The weight loss characteristic is shown in a thermogravimetric analysis (TGA) curve in figure 11.

2.1.4 Baseline Process

The major processing steps used in fabricating the baseline test bars as well as the characterization performed are outlined in figure 1. The following describes the experimental procedures for each processing step and the characterization/inspection conducted at or after each processing step.

(1) Powder Preparation.--The as-received GTE SN-502 Si_3N_4 powders were air-classified to remove the major portion of large, dense particles and agglomerates. Figure 12 shows the particle size distribution results of air-classified (A/C) GTE SN-502, lot 107 powder. Although there was a systematic shift in PSD from coarse to fine, it was evident that the PSD's of the three fractions of the air-classified powder overlapped extensively. This overlap is attributed to the needle-like nature of the as-received SN-502 powders. The weight percent of the coarse, fine, and finest fractions of the powder after air-classification were 17.7, 69.4, and 12.9 percent, respectively. The coarse fraction was discarded and the fine and finest fractions were recombined, in the appropriate ratio (69.4 to 12.9), to form the batch material.

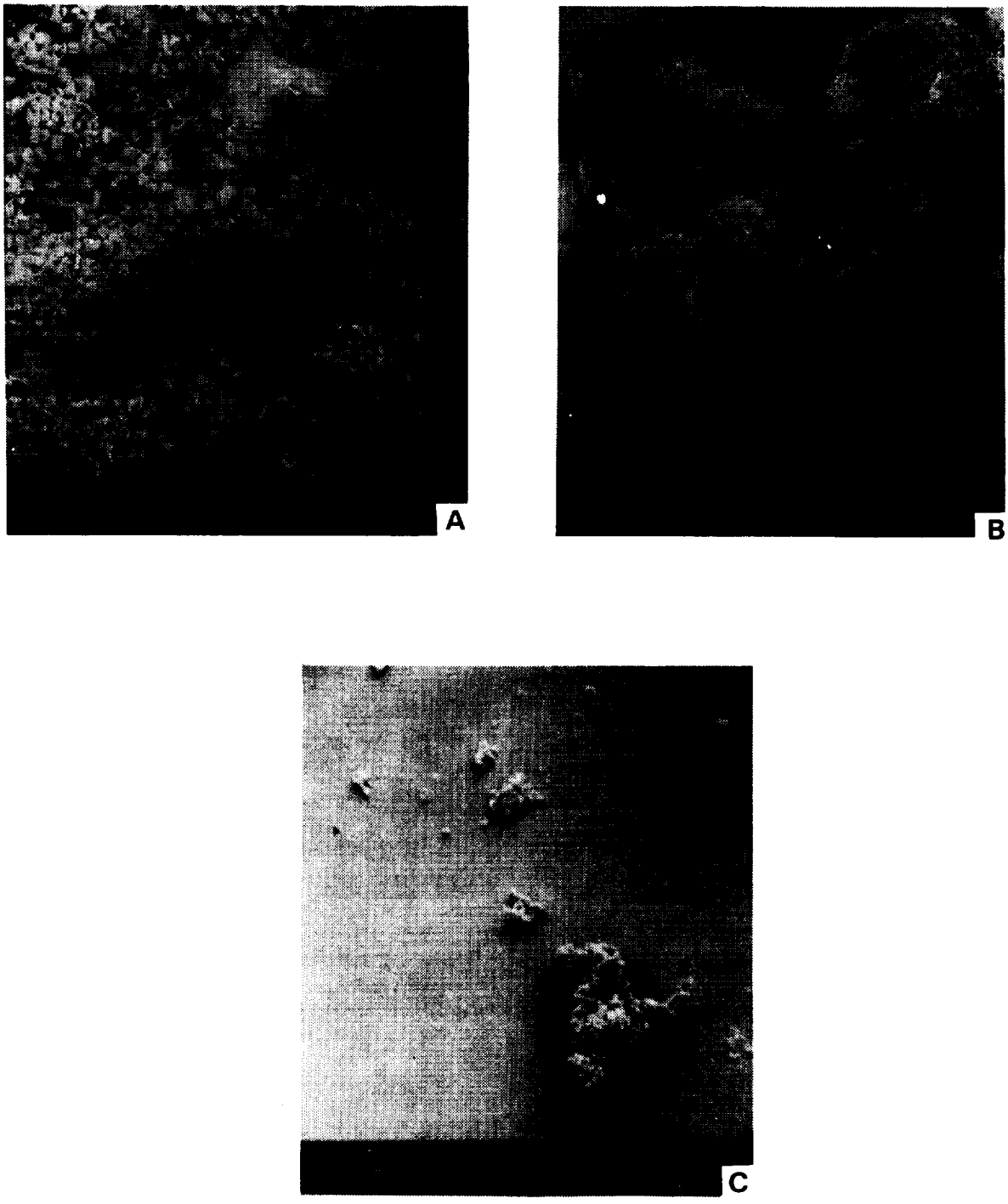

F-48902

Figure 9.--SEM Photomicrographs Illustrating the Characteristics of the As-Received Al_2O_3 Powder.

TABLE 2.--CHEMICAL ANALYSIS OF AS-RECEIVED MATERIALS BY SEMIQUANTITATIVE EMISSION SPECTROGRAPHY

Impurity	Si_3N_4	Y_2O_3	Al_2O_3
Al	0.004[1]	0.001	H[2]
Ca	ND[3]	ND	ND
Fe	0.004	ND	0.001
Ga	ND	ND	0.001
K	<0.001	<0.001	0.005
Li	<0.001	<0.001	<0.001
Mo	0.02	ND	ND
Na	<0.001	<0.001	0.003
Si	H	0.001	0.008
Y	ND	H	ND

[1]Percentage

[2]L = low, M = medium, H = high

[3]ND = not detected

TABLE 3.--OXYGEN CONCENTRATION OF AS-RECEIVED POWDER

	Weight, %		Deviation
	Measured	Theoretical	(± %)
SN-502	2.18	---	0.046
Y_2O_3	20.30	21.30	0.250
Al_2O_3	45.30	47.10	0.560

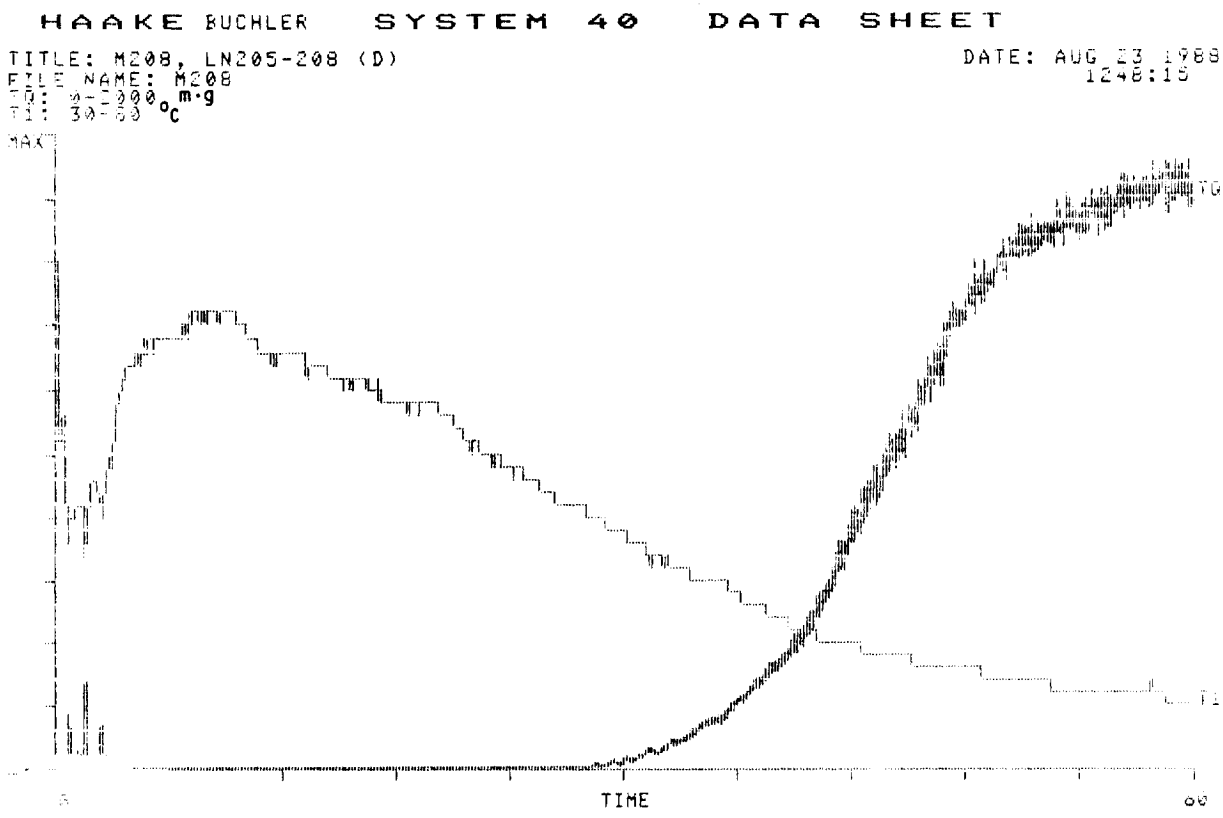

Figure 10.--Rheology of Baseline Binder.

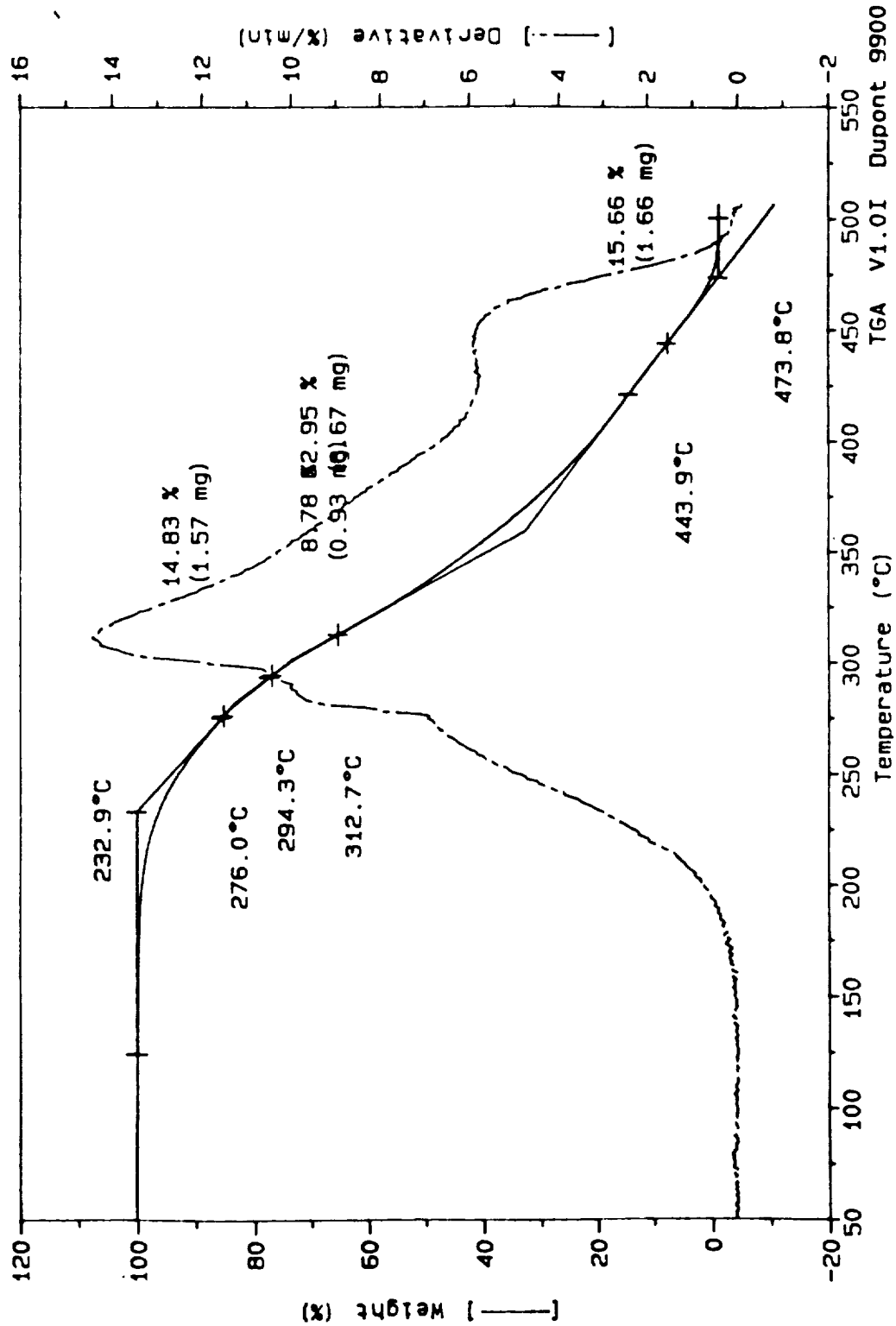

Figure 11.--TGA Curve for Baseline Binder Run in Nitrogen at 20°C/Minute.
(Sample size was 10.60 mg)

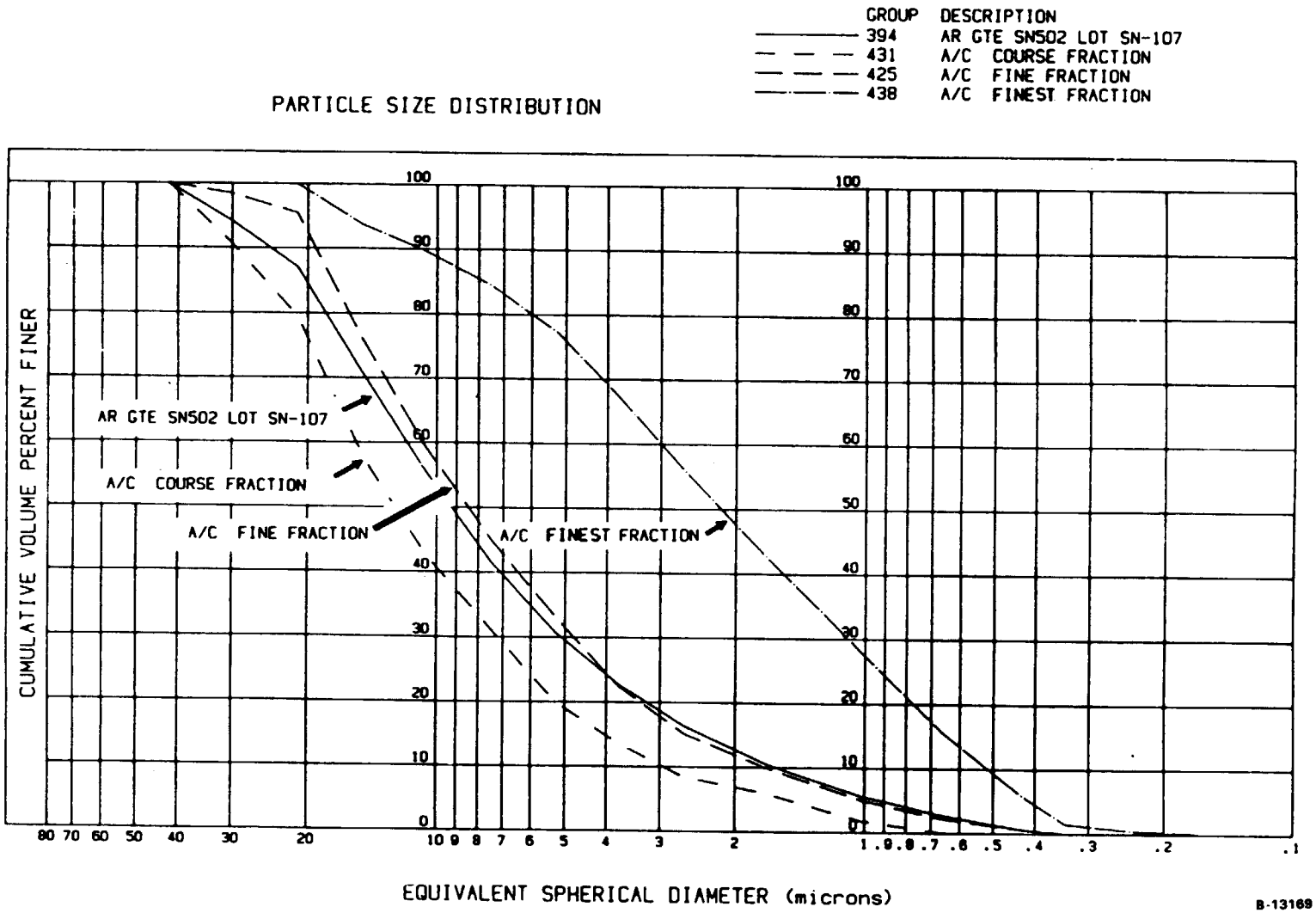

Figure 12.--Particle Size Distributions of Air-Classified GTE SN-502 Si_3N_4 Powder.

The GCCD baseline powder dry milling procedure employed the following elements:

(a) Rubber-lined, 2-gallon capacity steel jar (Norton No. 2)

(b) 5930 g of Si_3N_4 milling media, 15.9 mm (5/8 inch) dia

(c) 800 g of 92% Si_3N_4 + 6% Y_2O_3 + 2% Al_2O_3

(d) 24-hour milling at 52 rpm jar speed

Two powder samples were taken from each of three locations in each mill jar--the lid edge, bottom end corner, and the center of jar--to ensure particle size distribution consistency throughout the mill jar. Figures 13 and 14 show the comparison between particle size distribution as measured by L&N Microtrac and X-ray sedigraph. The results showed that there was no detectable difference in PSD between powders sampled from different locations in the mill jar.

Typical morphology of the baseline milled powder is shown in figure 15. Most of the particles were less than 1 μm diameter but some were observed up to 5 μm. The particles were generally equiaxed and angular. Many, however, retained some of the needle-like shape of the as-received powder, but with reduced aspect ratios (maximum after milling is about 6 to 10 μm).

No settling of coarse particles was observed after elutriation. SEM and elutriation indicated that the large agglomerates identified in the as-received powder were effectively reduced by air-classifying and ball milling. The milled powders were analyzed chemically by emission spectroscopy for cation concentration and by nuclear activation for oxygen concentration. The results are listed in table 4.

(2) Preparation of Injection Molding Mix.--The ball-milled powder was blended with 15.5 wt% of baseline binder in a heated Sigma mixer. After being cooled to room temperature, the mix was pelletized in a pelletizer (Polymer Machine Co.). The pelletized mix (injection molding mix) was characterized on the Haake Rheometer as shown in figure 16.

TABLE 4.--CHEMICAL ANALYSIS OF BALL-MILLED POWDER BY EMISSION SPECTROGRAPHY

Element:	Al	Ca	Fe	Ga	K	Li	Mo	NA	Si	Y	O*
Wt%:	L-M	.001	.005	ND	<.001	<.001	0.02	<.001	H	M-H	4.66

NOTE: L: Low ND: Not detected
M: Medium *: Nutron Activation Analysis
H: High

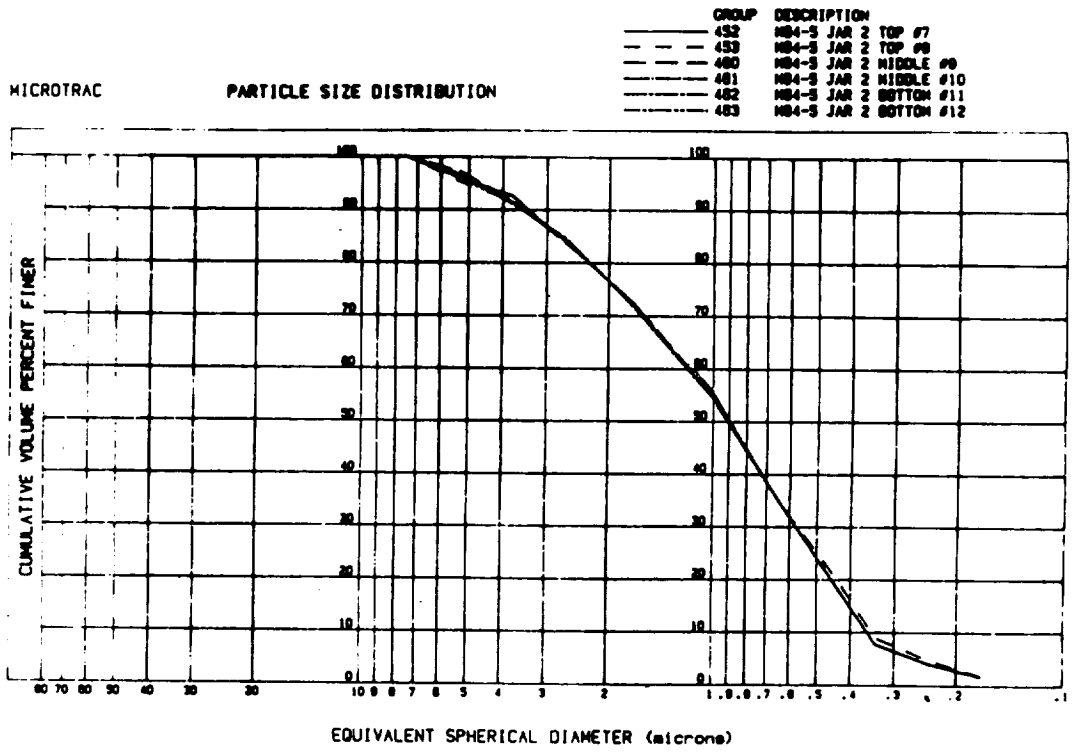

Figure 13.--Milled Baseline Powder PSD Measured by L&N Microtrac.

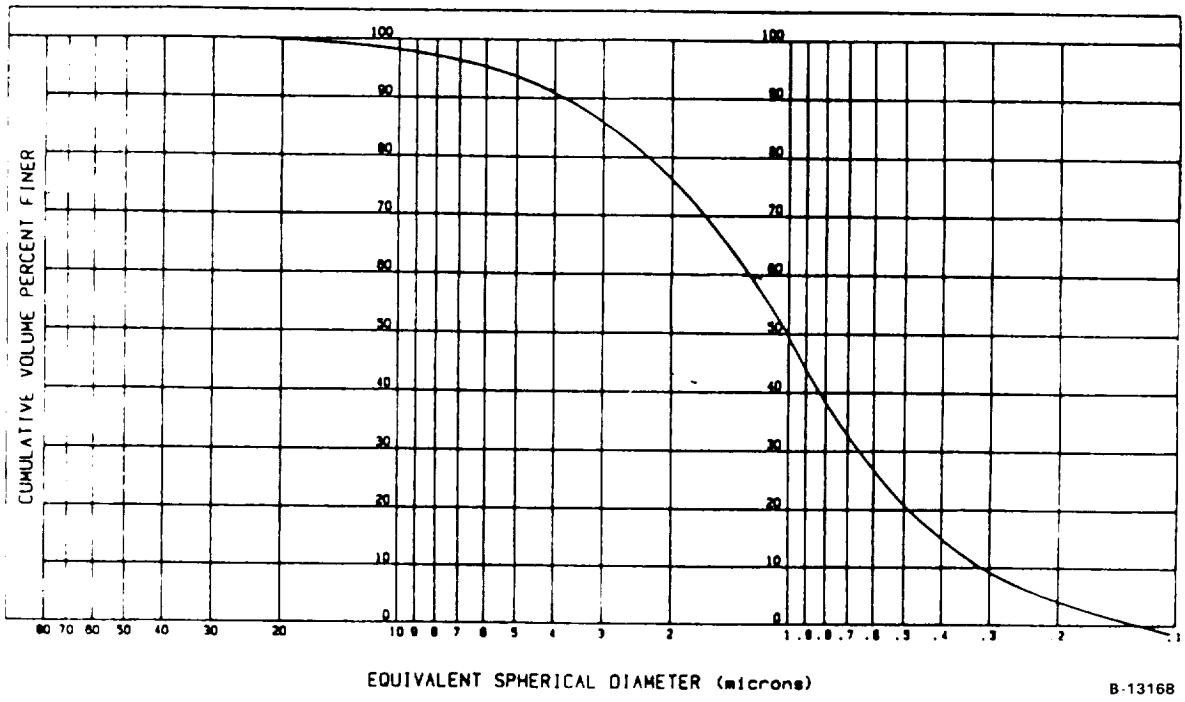

Figure 14.--Milled Baseline Powder PSD Measured by X-ray Sedigraph.

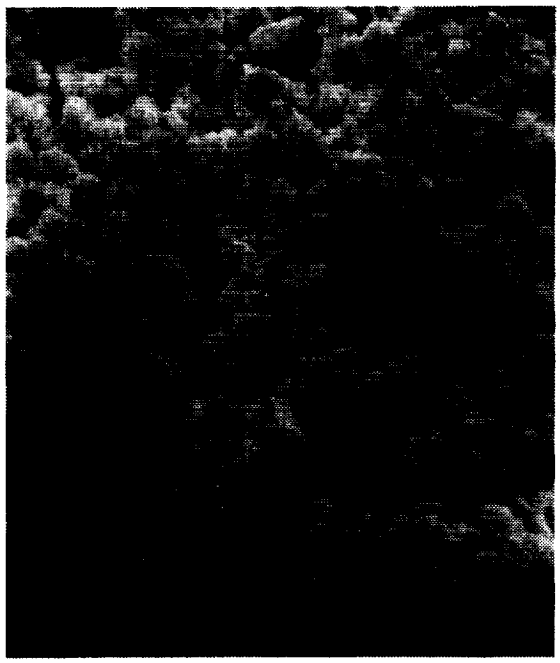

F-48908

Figure 15.--SEM Photomicrograph Showing the Particle Size and Shape Distribution of Milled Baseline Powder.

(3) Injection Molding of Test Bars.--An Arburg 2.2 screw-meter-feed, plunger injection molding machine was used to injection mold the test bars. The following baseline parameters were used.

Temperature of mold	32°C (90°F)
Temperature of nozzle	77°C (170°F)
Temperature of nozzle zone	77°C (170°F)
Temperature of feed zone	66°C (150°F)
Injection speed	4 (on dial scaled from 0 to 5)
Clamp time	110 seconds
Injection time	61 seconds

A total of 452 baseline test bars were molded using a four-cavity die. Each cavity in the die was numbered for traceability. All bars were then numbered sequentially. All of the as-molded bars were visually inspected and then X-rayed for internal flaws such as pores or laminations. Table 5 presents the visual inspection results with respect to the type and degree of defect observed.

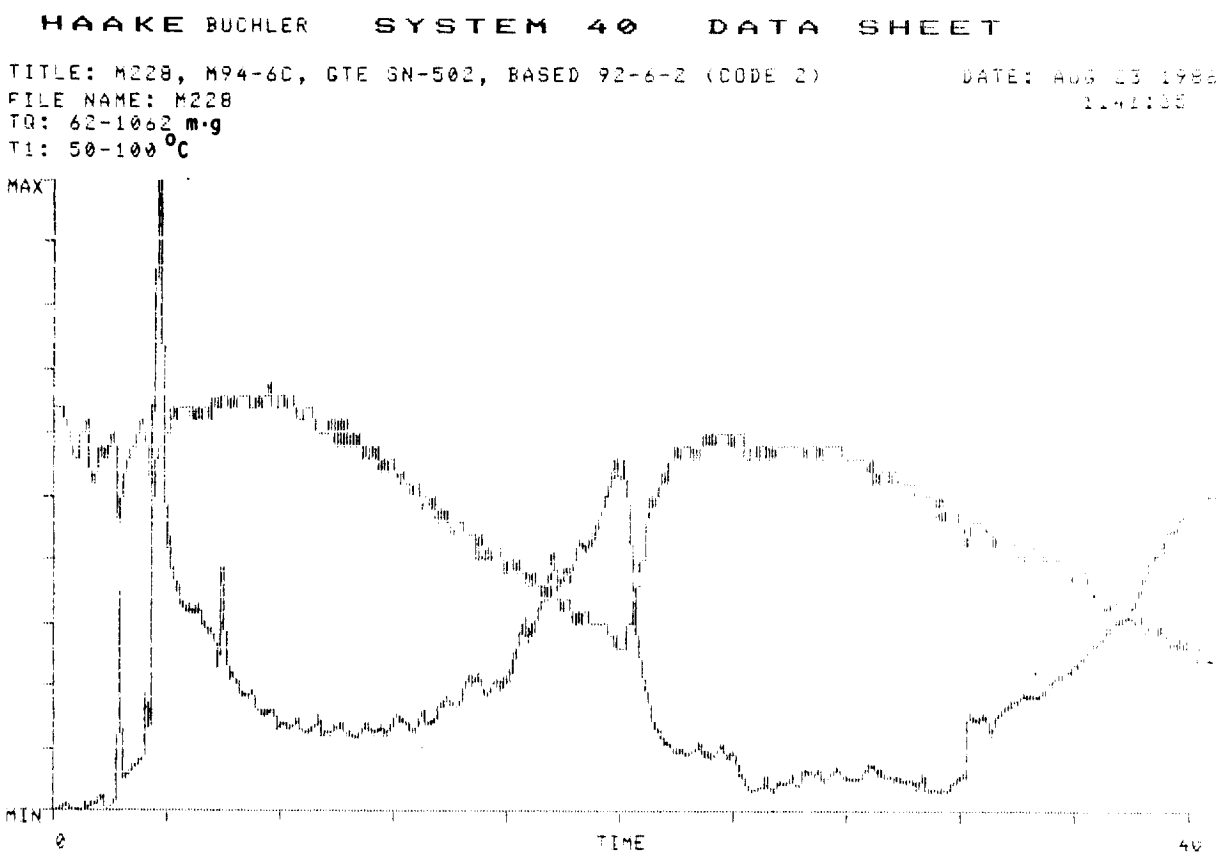

ORIGINAL PAGE IS
OF POOR QUALITY

Figure 16.--Rheology of Baseline Injection Molding Mix.

TABLE 5.--VISUAL EVALUATION OF AS-INJECTION-MOLDED BASELINE TEST BARS

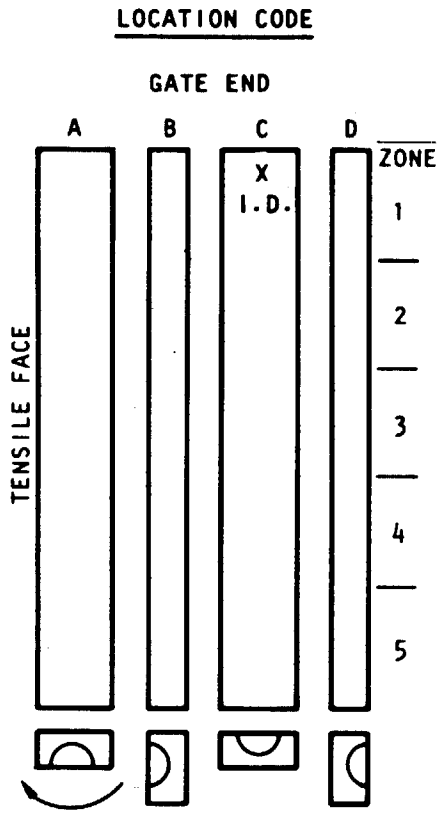

FLAW DESCRIPTION *	DESCRIPTION CODE		
	FLAW TYPE	LEVEL	LOCATION
LIGHT FLOWLINES ON TENSILE FACE NEAR INGATE	FL	0	A1
SLIGHT SURFACE POROSITY OVER MOST OF BAR	SPL SPR	0 1	A1, A5
SCRATCHES FROM HANDLING	SC	0	------
OCCURRING FROM TOOL DAMAGE	--	-	------

CODE

FLAW TYPE	LEVEL
FL - FLOW LINE	0 - NOTICEABLE AT 30X MAG.
SPL - SURFACE POROSITY LINEAR	1 - MORE THAN DESIREABLE
SPR - SURFACE POROSITY DUE TO EXCESS MOLD RELEASE	2 - POSSIBLE EFFECT ON PROPERTIES
SPC - SURFACE POROSITY CIRCULAR	3 - DEFINITE EFFECT ON PROPERTIES
SC - SCRATCHES	
P - PIT	

*UNLESS OTHERWISE STATED, ALL BARS EVALUATED CONTAIN THESE FLAWS. ONLY FEATURES OTHER THAN THESE WILL BE RECORDED.

A-71384

Optical and SEM examinations indicated that the baseline as-molded test bars were uniform and did not have major visible defects. Test bars were evaluated by optical microscopy at up to 1000X. Particle packing appeared uniform except for occasional shiny inclusions and black regions, less than 10 μm, shown in figure 17. These features were present on the as-molded surface and were revealed in the interior by etching the surface with a solvent. The black regions were identified as porosity by dark field illumination. Figure 17 also shows some elongated particles similar to SEM photomicrographs of the as-received Si_3N_3 powder. Chemical analysis of the inclusions by energy dispersive X-ray using the SEM was unsuccessful.

Flexure strength testing was conducted on selected as-molded bars. Strength and visual fractography results are presented in table 6. A typical load-deflection curve is shown in figure 18.

The point of fracture initiation was easily visible and occurred at the tensile surface for each specimen. Four features noted on the fracture surfaces were:

(a) All specimens contained a dispersion of very small black particles that were visible at 40X magnification.

(b) Many of the specimens had a distinct comma-shaped feature extending from the fracture origin into the material.

(c) Some specimens had roughly spherical raised "nodules" on one fracture surface with a matching depression in the other fracture surface.

(d) Each specimen showed a slight perturbation in the fracture path symmetrically around the core of the test bars. This suggested the presence of a residual stress in the test bar, probably due to temperature gradients during cooling.

Figure 19 shows SEM photomicrographs that are typical of most of the specimens tested. Figure 19a shows the complete fracture surface. All of the faint surface lines emanate from the small sunburst pattern near the lower left corner of the specimen, which was in tension during the fracture test. The "sunburst" is the likely fracture origin. Figure 19b illustrates this region at higher magnification. The apex of the sunburst is shown at still higher magnification in figure 19c and is compared with a typical microstructure (figure 19d) from the interior of the specimen. Other than some possible porosity, no clearly defined discontinuity is evident to distinguish the fracture origin from the general microstructure.

Figure 20 illustrates the fracture surface features for specimen 118. This specimen contained a distinct "comma" feature at the origin and several "nodules" on the fracture surface, well away from the origin. No discontinuity is apparent at (or adjacent to) either the comma or nodule features.

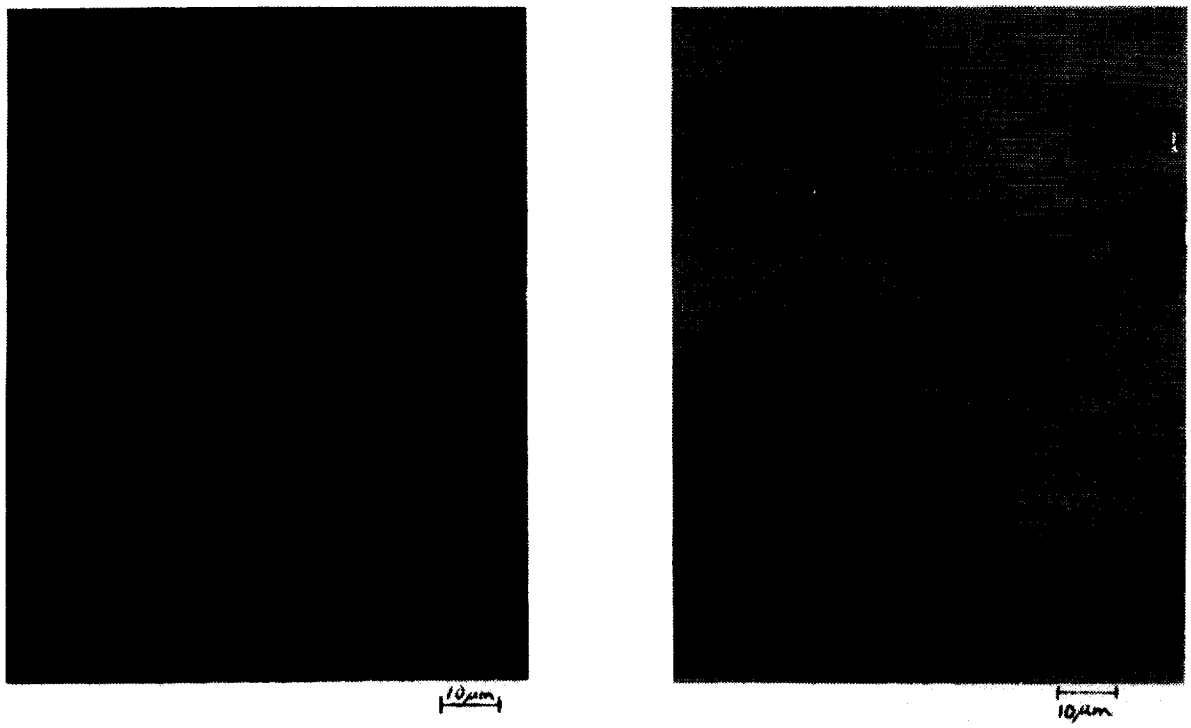

F-48910

Figure 17.--Optical Micrographs of As-Injected Test Bar 119.

TABLE 6.--FOUR-POINT FLEXURE STRENGTH RESULTS FOR AS-INJECTED BASELINE TEST BARS

Sample Number	MOR, ksi	Failure Origin	Observations
37	1.09	TF*	Black inclusion; nodules
38	1.05	TF	- - - - -
39	1.16	TF	Nodules; comma
40	1.16	TF	- - - - -
77	1.19	TF	- - - - -
78	1.16	TF	- - - - -
79	1.19	TF	Comma
80	1.19	TF	Large void or pullout at origin
117	1.12	TF	Large non-spherical node
118	1.09	TF	Nodules; exaggerated hackle
119	1.16	TF	- - - - -
120	1.16	TF	- - - - -
197	1.16	TF	Nodules
198	1.12	TF	- - - - -
199	1.16	TF	- - - - -
200	1.09	TF	- - - - -
277	1.16	TF	Exaggerated hackle; no core
278	1.19	TF	- - - - -
279	1.16	TF	Large comma
280	1.12	TF	Nodule
357	0.99	TF(corner)	Possible flaw at origin
358	1.05	TF(corner)	- - - - -
359	1.09	TF	Large comma
360	1.12	TF	- - - - -
397	1.12	TF	Possible crack
398	1.12	TF	Void or pullout away from origin
399	----		Specimen dropped
400	0.99	TF	- - - - -
437	1.05	TF	- - - - -
438	1.12	TF	- - - - -
439	1.02	TF	- - - - -
440	1.02	TF	Large nodule

Mean MOR:	1.11 ksi	Inner span:	0.75 inch
Standard deviation:	0.06 ksi	Outer span:	1.50 inch
Weibull characteristic:	1.14 ksi	Specimen width:	0.315 inch
Weibull slope:	2.17	Specimen thickness:	0.145 inch

Load rate 0.02 inch per minute
*TF = Tensile Face

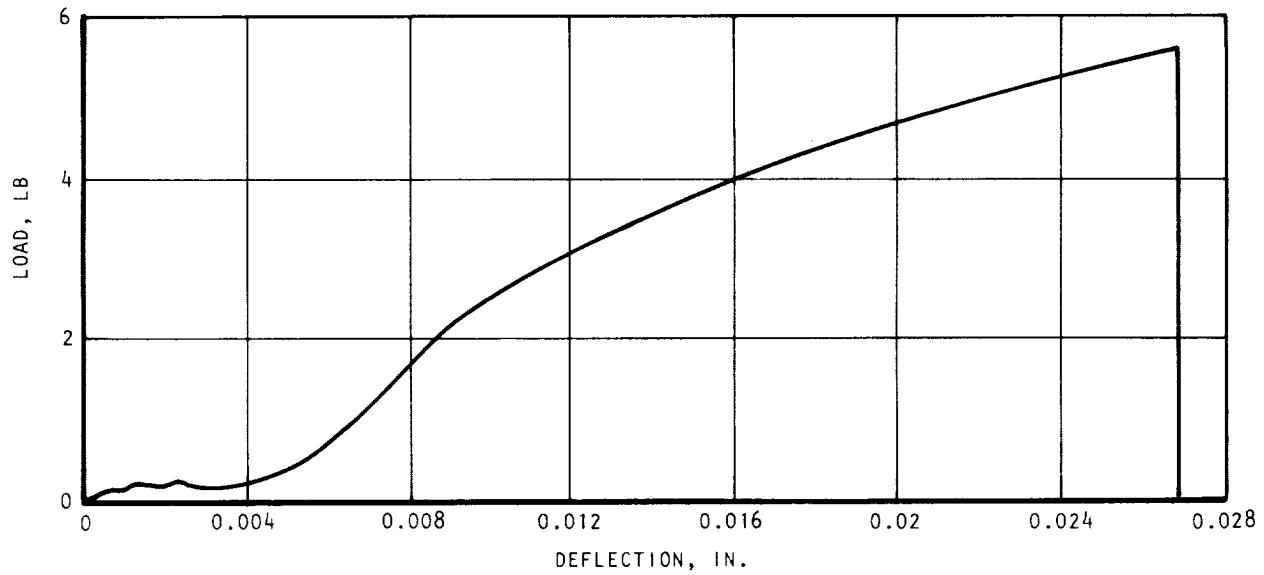

Figure 18.--Typical Load-Deflection Curve for an As-Injected Specimen Strength Tested in Four-Point Flexure.

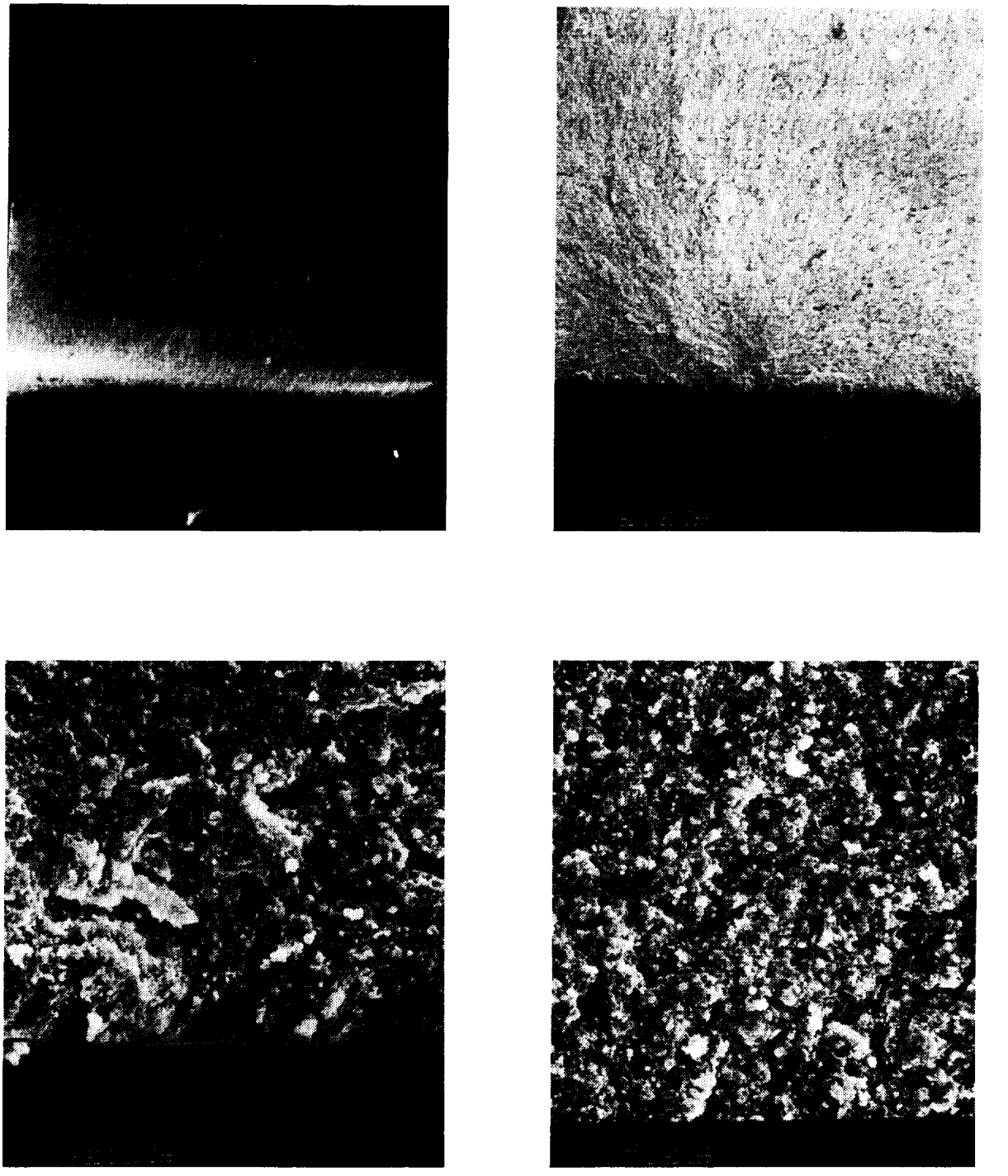

F-48906

Figure 19.--Scanning Electron Photomicrographs Illustrating the Fracture Surface and Origin for a Typical As-Injection-Molded Specimen.

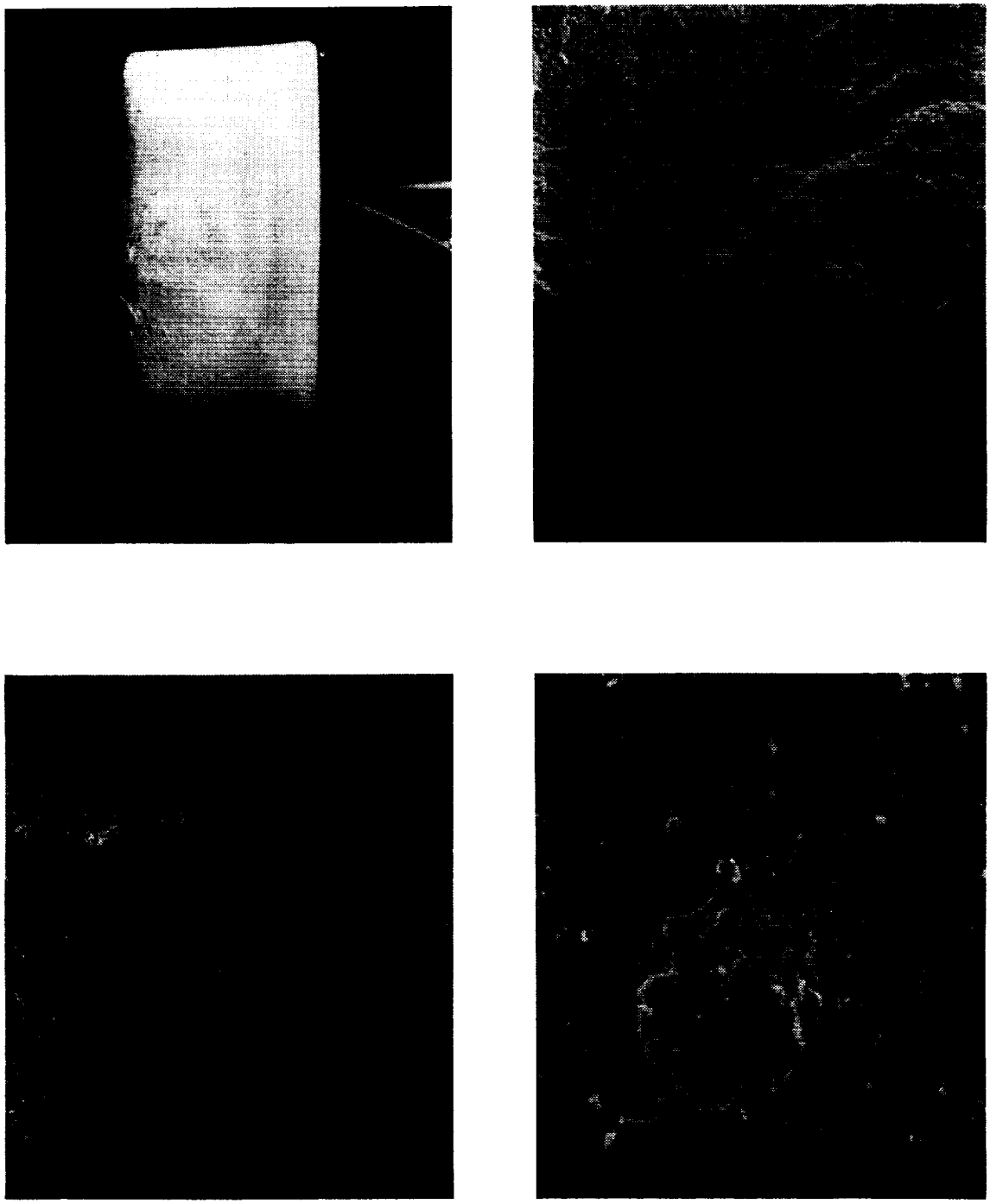

F-48904

Figure 20.--Scanning Electron Photomicrographs Illustrating the Fracture Surface Features for As-Injection-Molded Specimen 118.

Figure 21 shows a large flake-like feature at the fracture origin of specimen 80. Figure 21a illustrates the overall fracture surface with the flake-like feature at the origin on the tensile face. The higher magnification view in figure 21b reveals possible linear discontinuities at the origin.

(4) Dewax.--All of the 452 injection-molded test bars, except those selected for destructive evaluation, were dewaxed and sintered. Dewax was performed in GCCD dewax chamber BE-I, a front-load, atmosphere, vacuum, or pressure furnace with programmable control.

The test bar grouping for dewax and sintering runs is shown in the block diagram, figure 22. A computer-generated random number sequence was used to locate each numbered test bar in dewax runs and each of the four sintering runs in a manner conducive to statistical analysis. Variables considered in the arrangement are position within the furnace, mold cavity (in the multicavity molding die), and test bar serial number.

A total of 328 bars were dewaxed in four dewax runs. The first run included the first 88 bars injected in the four-cavity die. The specimens were distributed in a 30.5 by 30.5 cm (12 by 12 inches) dewax tray. In order to obtain additional information on the effect of the molding sequence, the remaining as-molded bars were randomized over three subsequent dewax runs (80 bars per run). Figure 23 shows a typical test bar arrangement and identification in these three dewax runs.

The percent weight loss after dewax was recorded for each bar. The data for each individual run were statistically analyzed to detect whether the molding cavity, dewax location, and injection sequence had any effect on weight loss. To detect differences in two groups of data, a student t-test was performed. Three comparisons were computed: (1) t-test with separate variances, (2) t-test with pooled variances, and (3) F-test for variances. The results indicated that:

(a) The test bars injected into cavity 3 had lower dewax weight loss than those injected into the other cavities.

(b) The dewax locations had no significant effect on dewax weight loss. A typical dewaxed bar was analyzed by SEM and EDX. Figure 24a is an X-ray image for yttrium throughout the matrix with some very localized high concentrations. A back-scatter electron image, figure 24b, shows that these high concentrations may be large individual particles of Y_2O_3.

(5) Sintering.--Densification of the dewaxed test bars was accomplished by sintering in an induction furnace capable of 0.68 MPa (100 psi) N_2 overpressure at 2000°C (3632°F). The test bar groupings in relation to dewax runs were previously shown in figure 22.

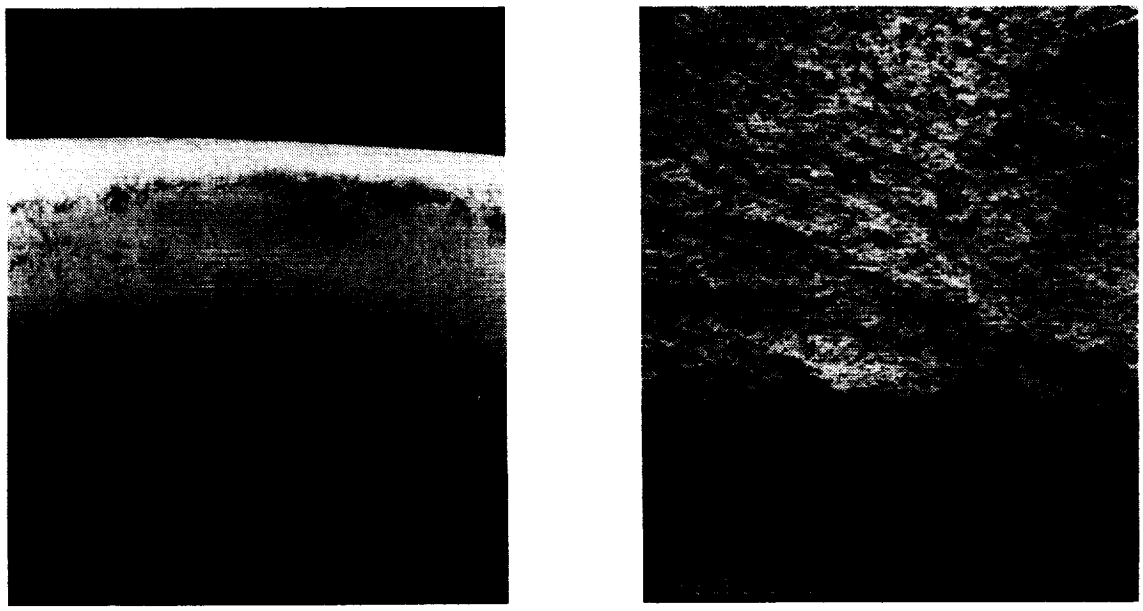

F-48903

Figure 21.--Scanning Electron Photomicrographs of the Fracture Surface of As-Injected Si_3N_4 Specimen 80.

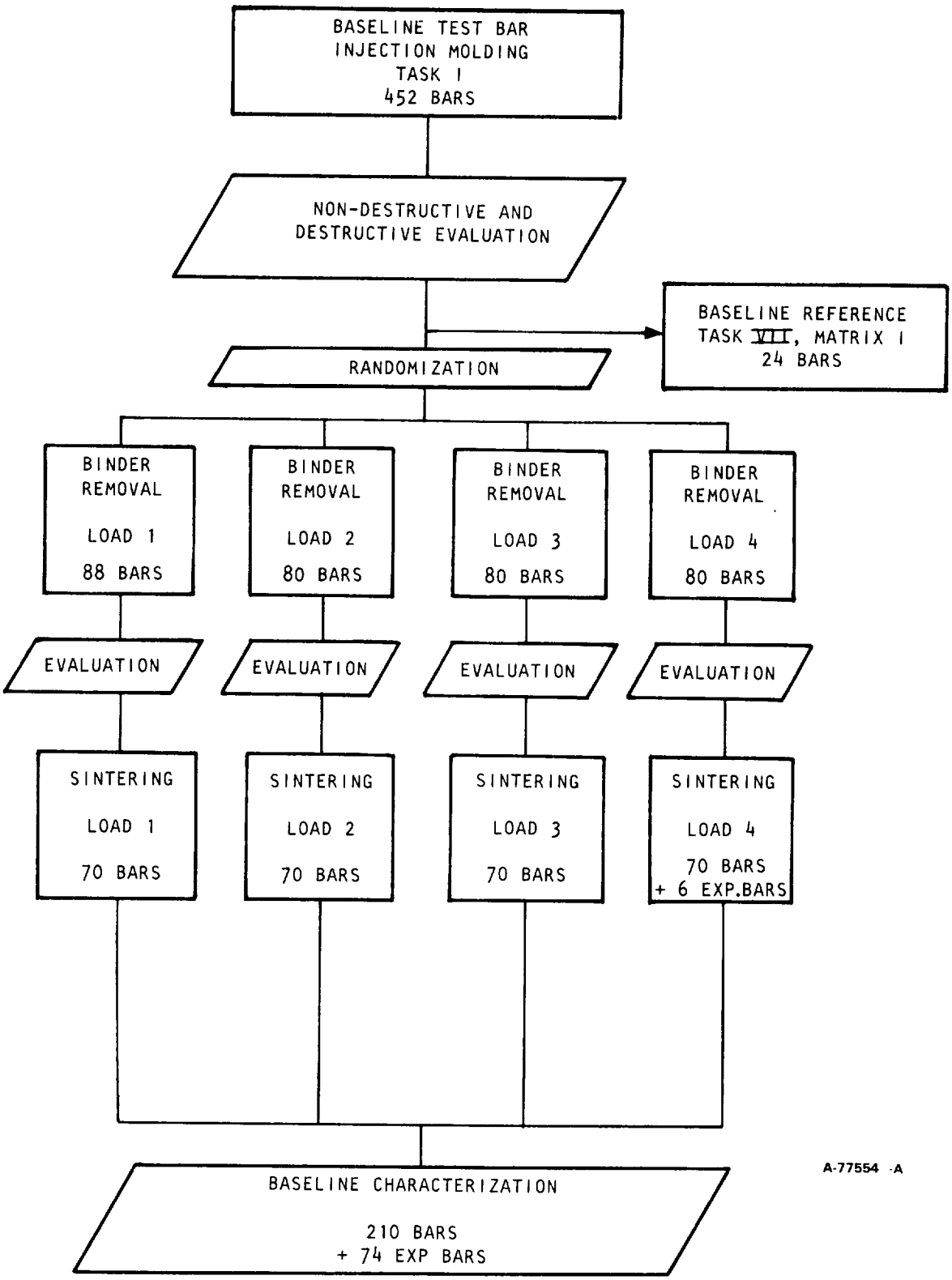

Figure 22.--Processing and Evaluation History of Baseline Test Bars.

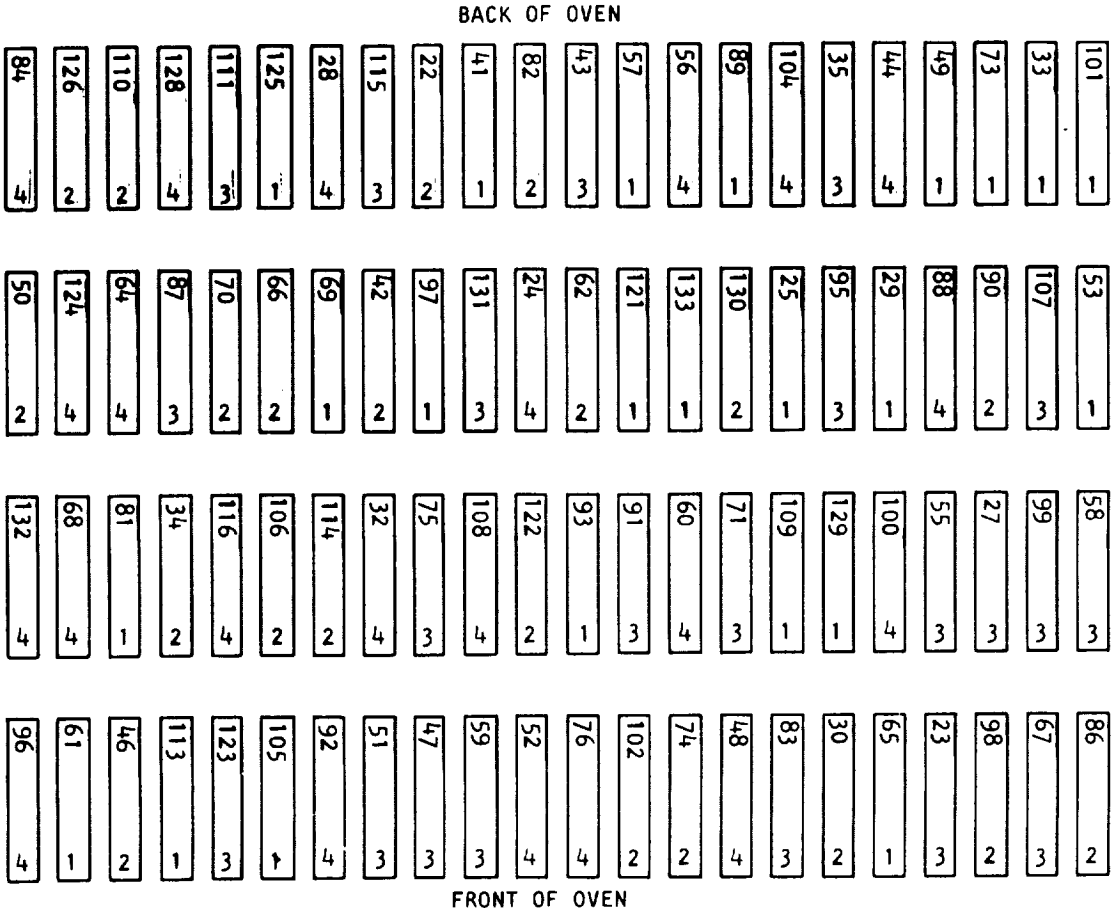

Figure 23.--Detail of Test Bar Arrangement in Binder Removal Oven. (Numbers on the top of the bars indicate part sequence number. Numbers on the bottom of the bars indicate cavity location in mold tool.)

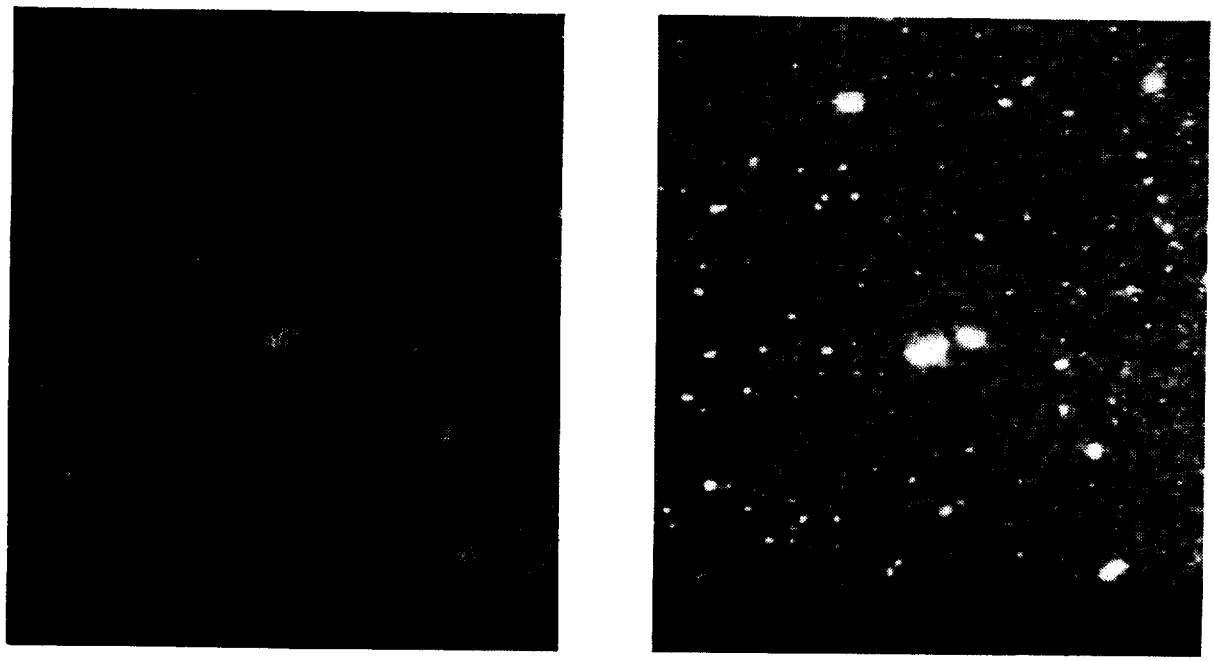

F-48905

Figure 24.--SEM Examination of the Surface of a Test Bar after Dewax:
(a) X-ray Image for Yttrium (b) Back-scatter Electron Image.

Variables considered in the arrangement were position within the furnace, mold cavity (in the multicavity molding die), and injection sequence.

The sintering plan included the following features.

- Four identical sintering runs with 70 bars in each run
- Bars sintered in each run would represent one binder removal cycle
- Several bars with known defects were included to observe possible flaw healing during sintering

The positioning of bars allowed statistical analysis of mold cavity, location in binder removal, sintering layer, and location on the supporting plate in sintering. Specially designed reaction-bonded Si_3N_4 kiln furniture, figure 25, was used for all sintering runs. This kiln furniture consisted of five trays, of which the middle three, labeled 1, 2 and 3, supported the test bars during sintering.

Sintering data of all four sintering runs were analyzed. The data included percent weight loss, sintered test bar density, sintering tray layer, and test bar location on each sintering tray. The tray location of the test bars, indicated by location zones A, B, C, and D are shown in figure 26. The purpose of using the specially designed kiln furniture and documenting the test bar locations was to determine whether the sintering tray layer level and the test bar location within each tray had any effect on test bar weight loss and sintered density.

The results were analyzed statistically, for mean value of weight loss (percent) and density (g/cc) for each location on different layers, and for the probability (P) that the mean of any two groups X and Y would be equal. An example of the results for sintering run load is shown in table 7. The value of P is a function of the means, standard deviations, and sample sizes of two groups. A comparison from the data from load to load is shown in table 8.

The following conclusions were drawn from the test results.

(a) On the same layer, location A produced the lowest weight loss. The bars in location A exhibited an average 0.315 percent less weight loss than the bars in other locations.

(b) The statistically significant difference test indicated, with a 99-percent confidence, that the difference between location A and other locations was significant.

(c) Except for location A (P-value <0.150), there was no difference in weight loss between locations.

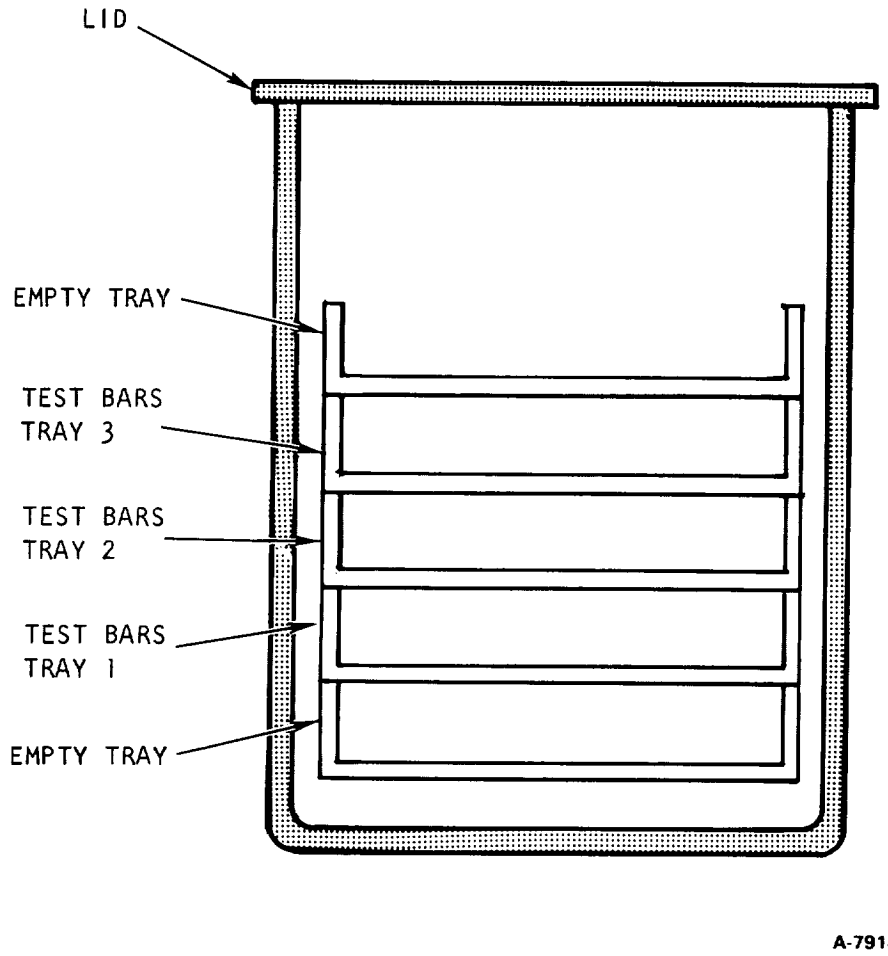

Figure 25.--Schematic Showing the Cross Section of the Reaction-Bonded Silicon Nitride Kiln Furniture.

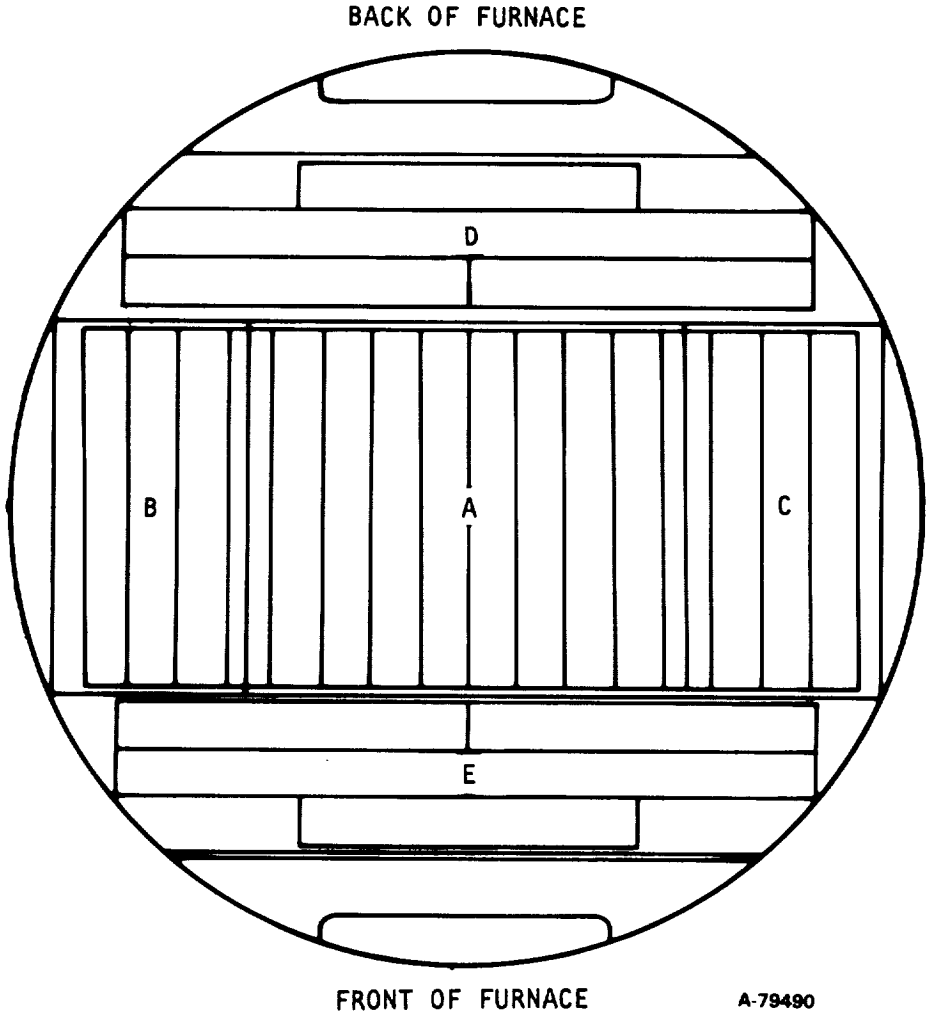

Figure 26.--Test Bar Location Codes on Sintering Tray.

TABLE 7.--SINTERING DATA: BASELINE MATERIAL TASK I, LOAD I

All Layers			Separate Layer					
Location	$\bar{X}$ % Weight Loss	$\bar{X}$ g/cc Density	Location	$\bar{X}$ % Weight Loss	$\bar{X}$ g/cc Density	Significant Diff. Test	P-Value Weight Loss	P-Value Density
A	1.291	3.226	A1*	1.025	3.220	A1 - A2	0.957	0.337
B	1.867	3.233	A2	1.028	3.216	A1 - A3	0.000	0.004
C	1.678	3.229	A3	1.857	3.243	A2 - A3	0.000	0.0004
D	1.787	3.225	B1	1.567	3.230	B1 - B2	0.834	0.491
E	1.540	3.225	B2	1.633	3.223	B1 - B3	0.0379	0.0668
			B3	2.40	3.247	B2 - B3	0.0735	0.0352
Center*	1.291	3.226	C1	1.30	3.227	C1 - C2	0.643	0.374
Circumf.*	1.740	3.227	C2	1.43	3.220	C1 - C3	0.0194	0.116
			C3	2.30	3.24	C2 - C3	0.0383	0.075
Significant Difference Test of the Mean Groups	P-Value Weight Loss	P-Value Density	D1	1.780	3.224	D1 - D2	0.410	0.724
			D2	1.380	3.222	D1 - D3	0.387	0.346
			D3	2.20	3.230	D2 - D3	0.000	0.650
A - B	0.0003	0.242	E1	1.280	3.214	E1 - E2	0.259	0.108
A - C	0.040	0.647	E2	1.380	3.228	E1 - E3	0.107	0.034
A - D	0.0075	0.848	E3	1.960	3.232	E2 - E3	0.161	0.373
A - E	0.124	0.756						
B - C	0.462	0.461	Circumf. 1	1.493	3.223	Circumf. 1 - Circumf. 2	0.730	0.785
B - D	0.757	0.0813						
B - E	0.162	0.121	Circumf. 2	1.437	3.224	Circumf. 1 - Circumf. 3	0.000	0.0026
C - D	0.680	0.393						
C - E	0.559	0.419	Circumf. 3	2.306	3.235	Circumf. 2 - Circumf. 3	0.000	0.0004
D - E	0.162	0.121						
Center - Circumf.	0.001	0.553						

*Center location is the location A. Circumferential location is B + C + D + E

*Number 1, 2, 3, is layer 1, 2, 3

*P Value is the probability the two groups to be equal

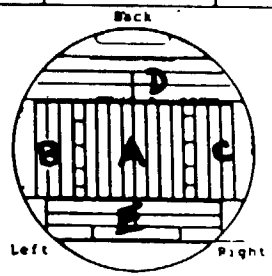

TABLE 8.--COMPARISON OF DATA BETWEEN DEWAX RUNS

Dewax Run	$\bar{X}$ Weight loss	$\bar{X}$ Density	Significant Difference Test of the Mean Groups	P-value, Weight Loss	P-Value, Density
1 (Rerun)	1.63	3.227	1-2	0.000	0.000
2	0.48	3.197	1-3	0.000	0.060
3	0.70	3.221	1-4	0.002	0.856
4	1.00	3.228	2-3	0.007	0.000
			2-4	0.001	0.000
			3-4	0.035	0.046

(d) In the same location, layer level had an effect on weight loss. Layer 3 (top) produced the highest weight loss and layer 1 (bottom) the least.

(e) The statistically significant difference test indicated, with 90-percent confidence, that the difference in weight loss between layers 1 and 2 was not significant, but the differences between layers 1 and 3 and layers 2 and 3 were significant.

(f) There was no difference in sintered test bar density between locations on the same or different layers.

(g) Statistical difference tests indicated that differences did exist in weight loss and density, with more than 95-percent confidence in most cases. The average difference from run to run is more than 0.15 percent for weight loss but less than 0.03 percent for density.

2.1.5 Postprocess Characterization and Fractographic and Statistical Analyses

Extensive characterization was performed on the sintered test bars, which included flexural strength (MOR) at room temperature and selected elevated temperatures and after-exposure to oxidation. Stress rupture data, probability of failure data, and determination and analysis of origin of failure during testing were also included in the postprocess characterization.

Prior to MOR testing, all specimens were visually inspected at 40X magnification and then examined using X-ray and Zyglo dye penetrant. Each test bar was assigned a grade of 0 to 5, based on visual inspection in accordance with the definitions of these grades in table 9. The higher the grade number, the lower the surface quality. The results of this inspection on sintering runs 2, 3, and 4 are summarized in figure 27.

TABLE 9.--VISUAL GRADE DEFINITIONS

Grade	Description
0	Best
1	Minor flaw(s) outside test zone
2	Major flaw(s) outside test zone
3	Minor flaw(s) in test zone, probably not strength limiting*
4	Moderate flaw(s) in test zone, probably strength limiting
5	Serious flaw(s) in test zone, significantly strength limiting

*Does not exclude the possibility of major flaws outside the test zone.

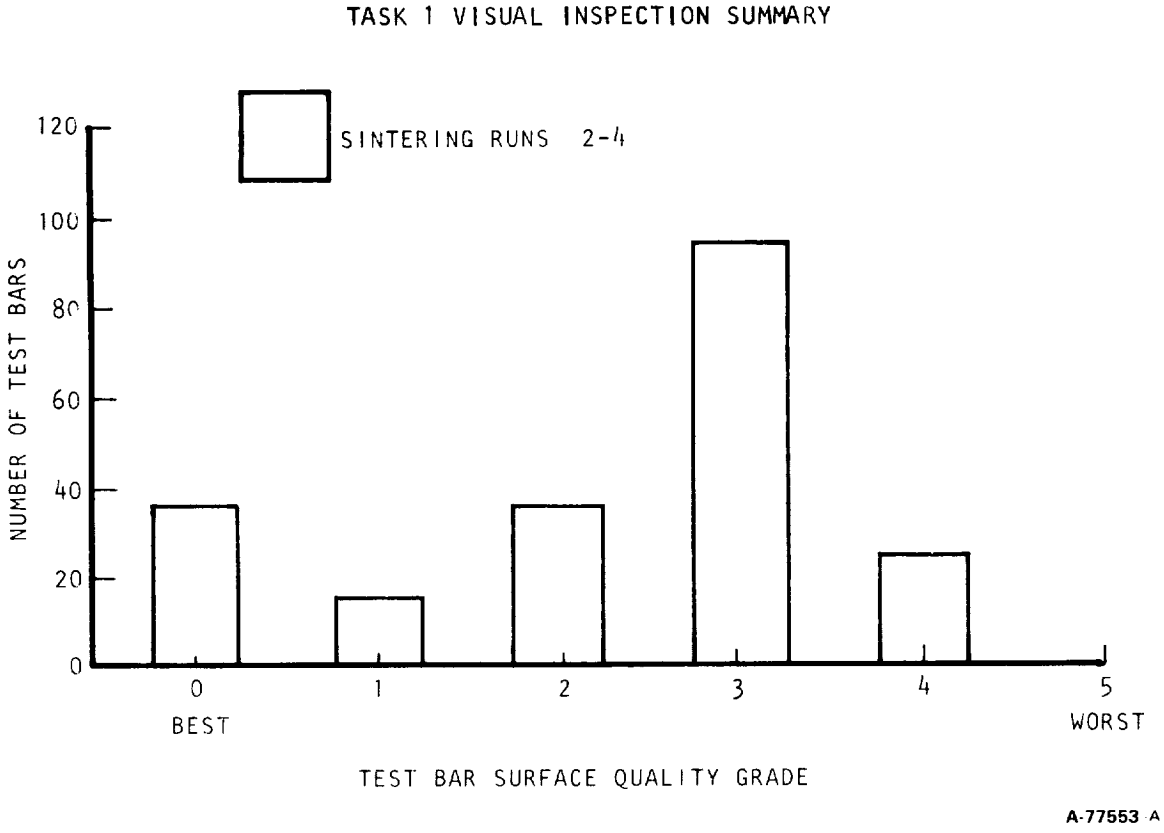

Figure 27.--Distribution of Sintered Test Bars as a Function of Surface Quality.

Strength data were generated on an Instron Model 1125 at a cross-head speed of 0.020 inch per minute . X-ray radiography was conducted using microfocus X-ray techniques. Zyglo dye penetrant inspection was done using ultraviolet light at magnifications up to 40X. Fractography was conducted using light microscopy and an Autoscan SEM.

Sixty-six bars were tested to measure flexural strength (MOR) and Weibull slope at room temperature. Figure 28 is a two-parameter Weibull plot of 66 MOR values with bar number and visual quality grade marked at each datum point. The average MOR, 540 MPa (79.3 ksi), and Weibull slope of 7.9 are consistent with the properties typical of the baseline material at the time the proposal was prepared.

To establish the dependency of strength as a function of temperature, flexural strengths were measured at three elevated temperatures, 1066°C (1950°F), 1232°C (2250°F), and 1399°C (2550°F). The results are listed in table 10, and plotted in figure 29.

A dropoff in strength is seen at 1066°C (1950°F). Because 1066°C was the lowest elevated test temperature, the threshold temperature for strength degradation is not evident. At 1399°C (2550°F), the highest elevated test temperature, the sintered specimens exhibited slow crack growth during fast fracture tests.

All fracture surfaces of the tested specimens were examined using a 40X magnification binocular microscope. Some of the failures originated from inclusions, which were either metallic or rust-colored in appearance. SEM and EDX analyses were performed on selected specimens flexure tested at room and elevated temperature to determine the nature of these inclusions. Inclusions were seen on the fracture surfaces of several specimens. An example is shown in figure 30. The EDX analysis of this inclusion, shown in figure 31, revealed iron as the major constituent. Traces of chromium and nickel were present along with the iron, suggesting a stainless steel as the contaminant source. Some specimens exhibited spherical inclusions as shown in figures 32 and 33, which contained, in addition to iron, a significant amount of molybdenum (typically found in this batch of GTE SN-502 power). Molybdenum was detected only in these spherical inclusions. Many of the fracture surfaces of the 1399°C (2550°F) test specimens exhibited bright areas near the tensile face. An example is shown in figure 34. An EDX spectrum of this area (figure 35) showed that the bright area consisted of titanium and chromium with several other minor elements. Most of the 1399°C specimens exhibited rust colored inclusions on the fracture surfaces as well as on the test bar surfaces. Also, some large green areas were visible on the fracture surfaces of some specimens.

Large flaws (of about 2 mm) were detected in specimens by X-ray radiography. Figures 36 and 37 show internal and subsurface flaws. Laminar flaws, revealed by SEM on a fractured surface as shown in figure 36, are generally clear in X-radiography. The effect these flaws have on the strength is entirely dependent on their location. They may not influence the reported strength of a specific bar.

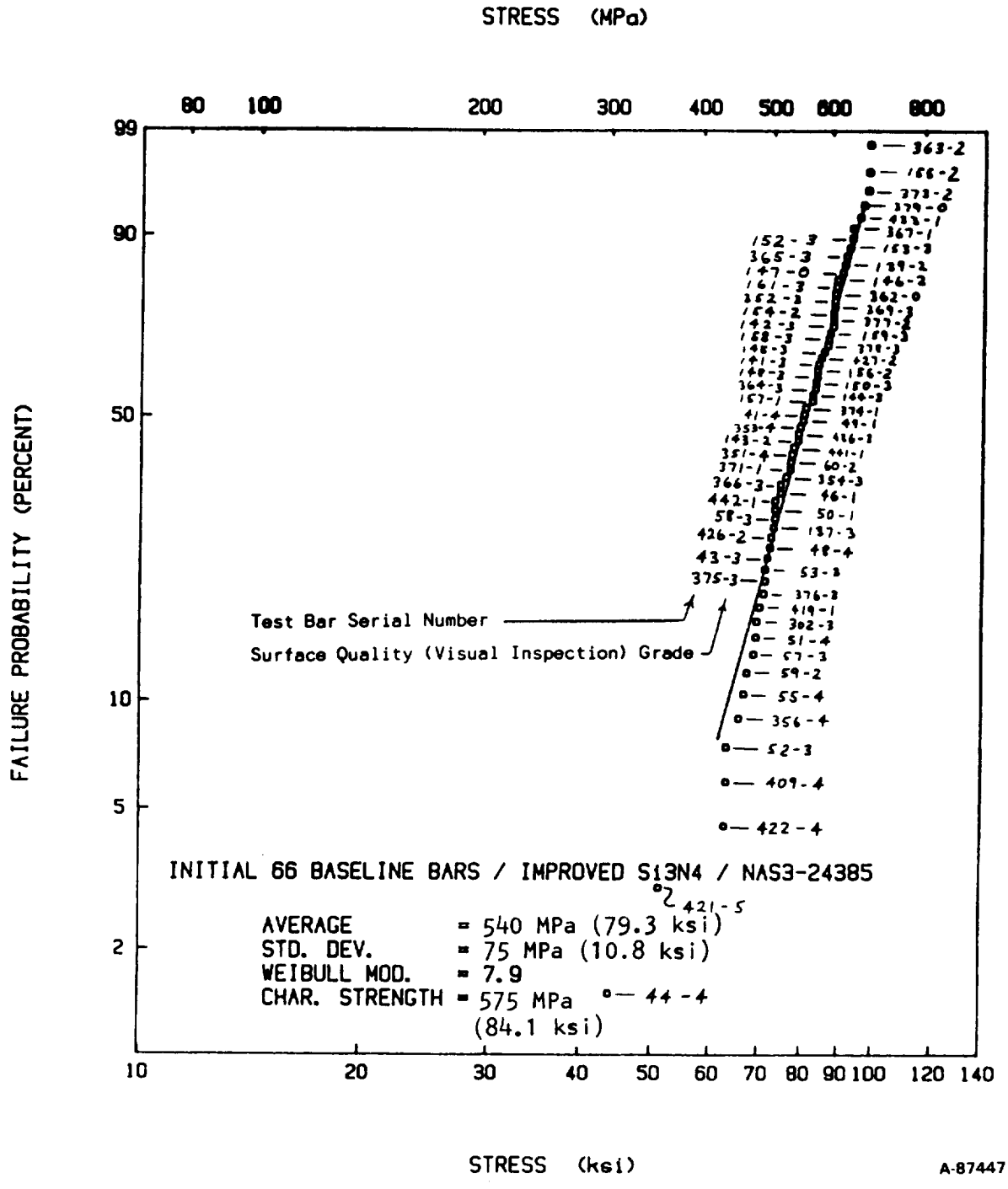

Figure 28.--Weibull Plot of Baseline Bars.

TABLE 10.--FLEXURE STRENGTH OF THE SINTERED TEST BARS AT ELEVATED TEMPERATURES

Temperature, °C (°F)	Flexure Strength, Sintered, MPa (ksi)	Number of Samples
Room temp.	560 ±53 (81.8 ±7.9)	90
1066 (1950)	420 ±48 (61.1 ±7.2)	10
1232 (2250)	320 ±38 (47.1 ±5.7)	10
1399 (2550)	140 ±43 (21.7 ±6.3)	10

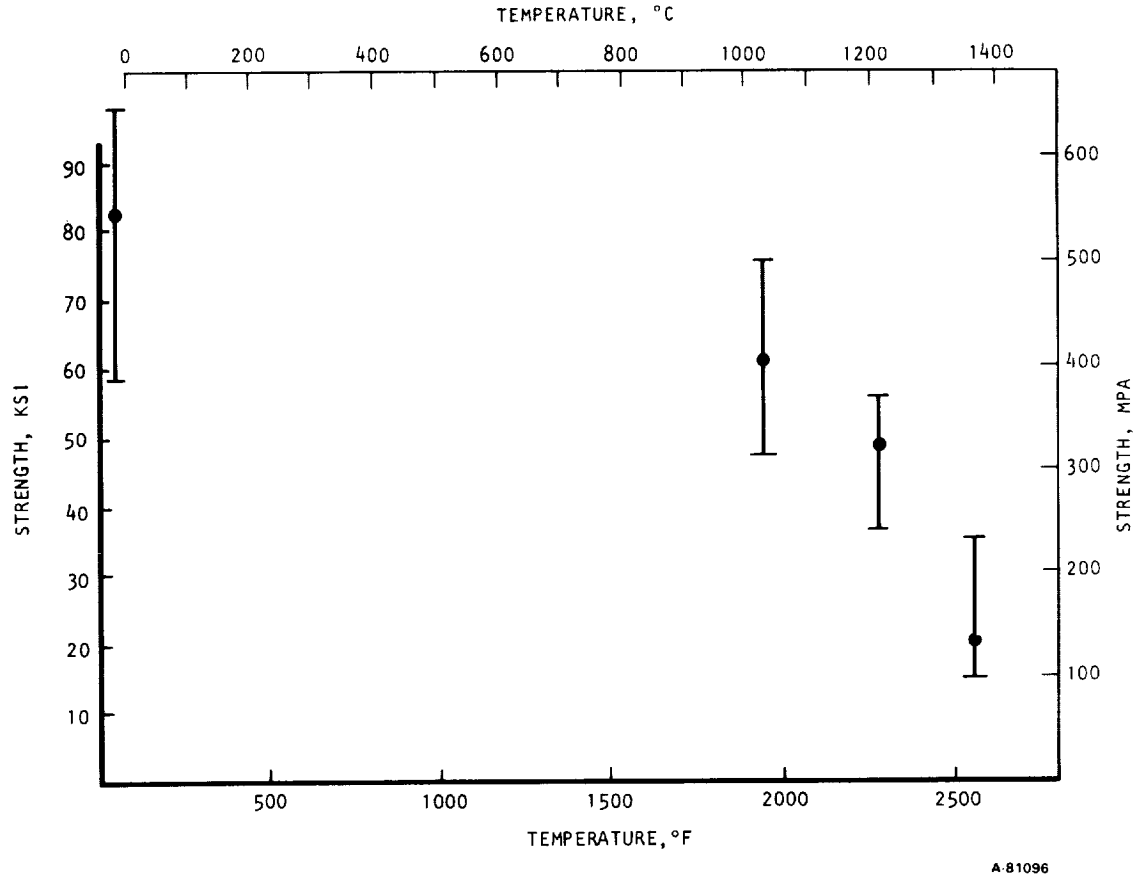

Figure 29.--Task I Sintered Test Bars--Strength vs Temperature.

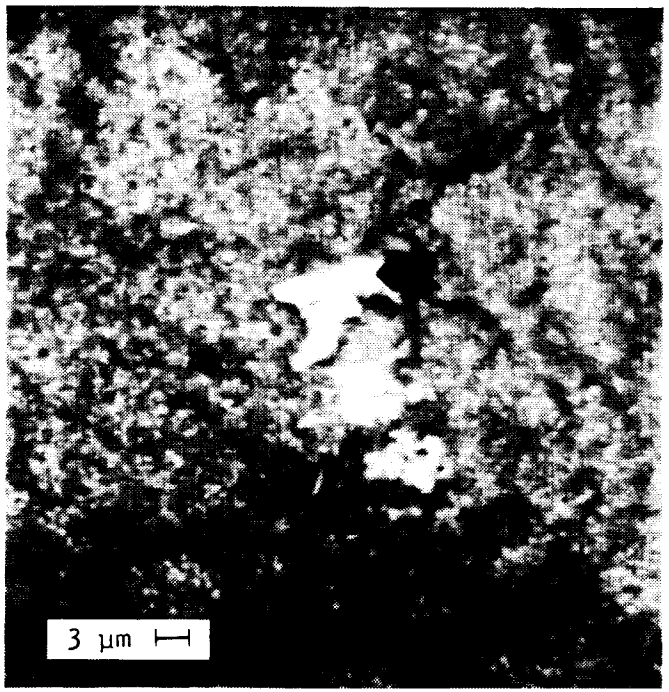

BSE Image

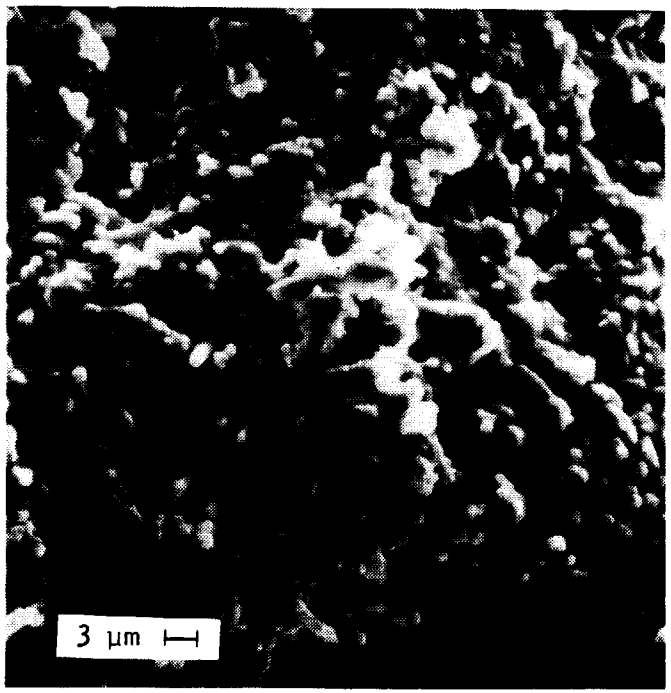

Secondary Emission Image

91689-4

F-47919

Figure 30.--SEM Micrographs of Fractured Surface (Test Bar 202, Fractured at Room Temperature) Showing a Metallic, Irregularly Shaped Inclusion.

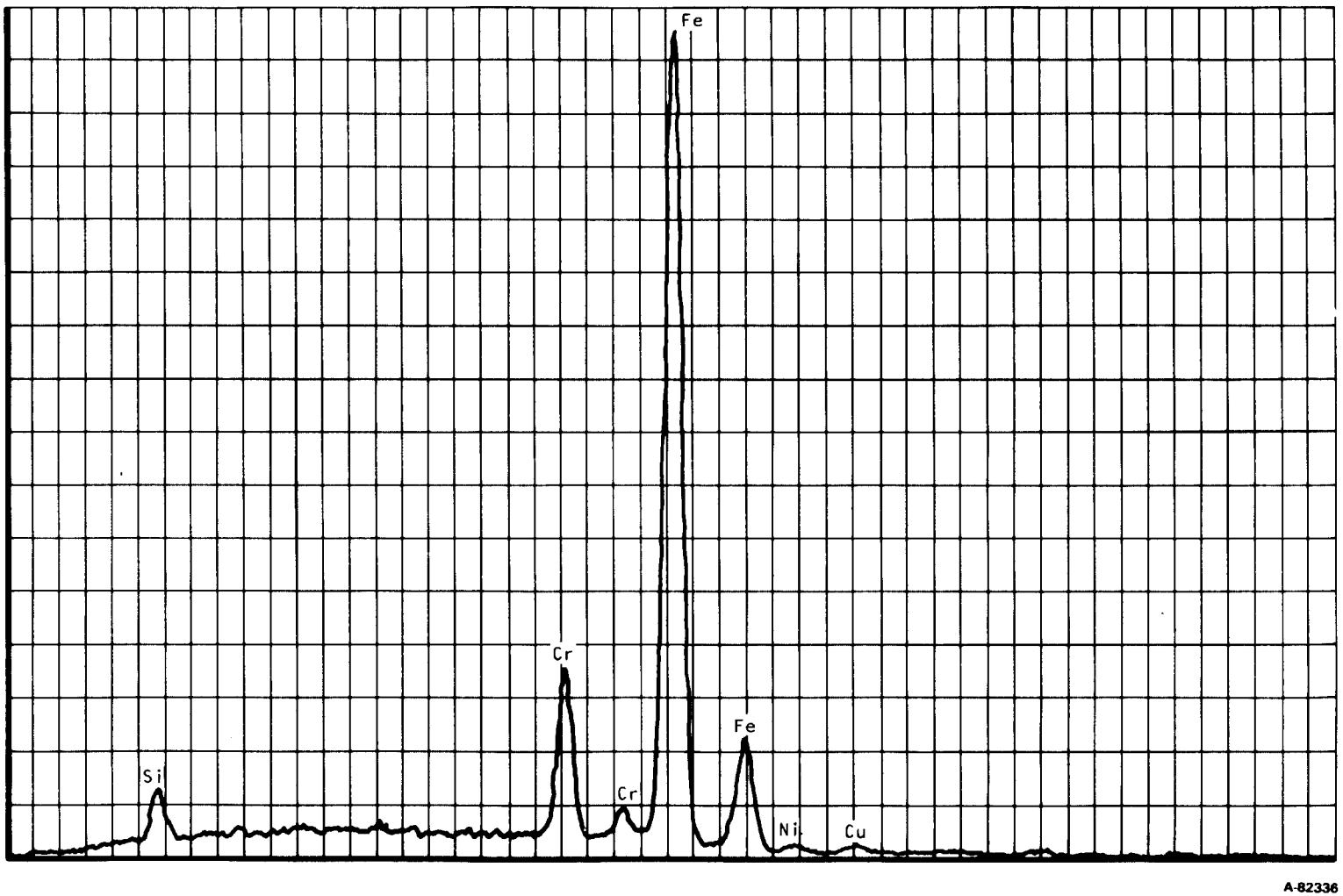

Figure 31.--EDX Spectrum of Bright Area in BSE Image of Test Bar 202, Showing Inclusion to Consist of Iron, Chromium, and Nickel.

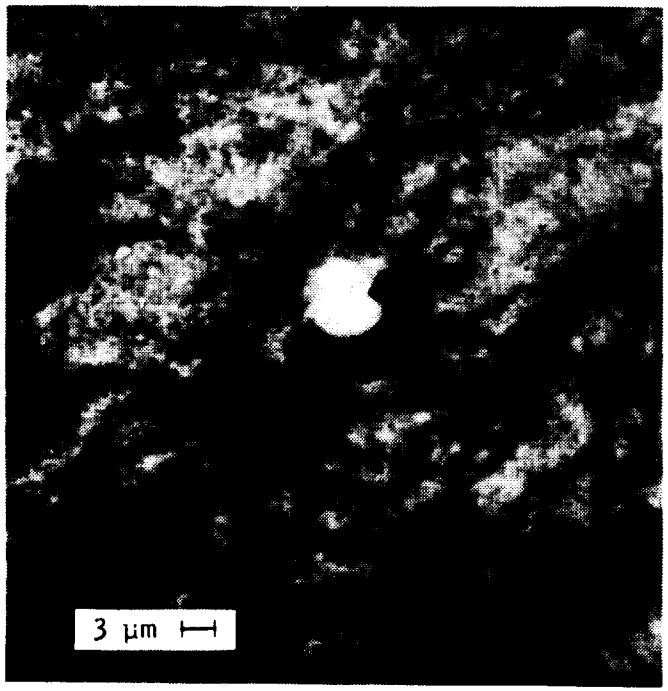

BSE Image

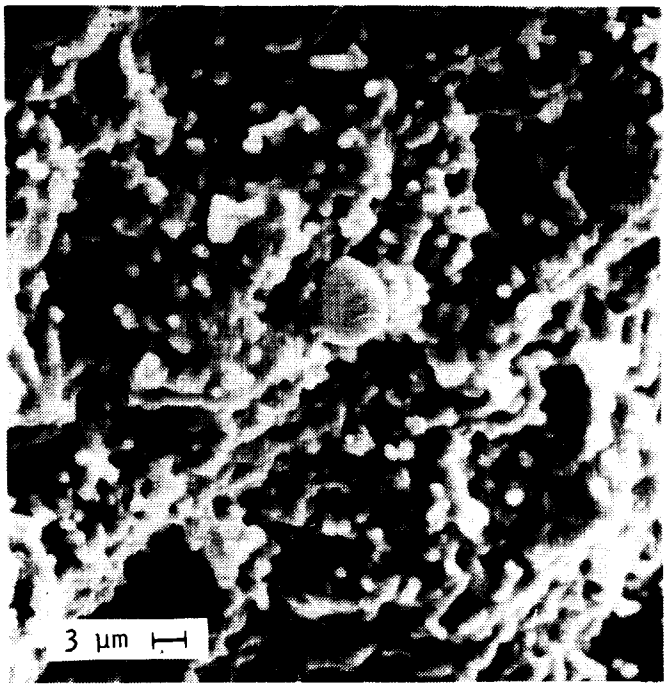

Secondary Emission Image

91689-5

F-47920

ORIGINAL PAGE
BLACK AND WHITE PHOTOGRAPH

Figure 32.--SEM Micrographs of Fractured Surface of Test Bar 202, Showing a Spherical Metallic Inclusion.

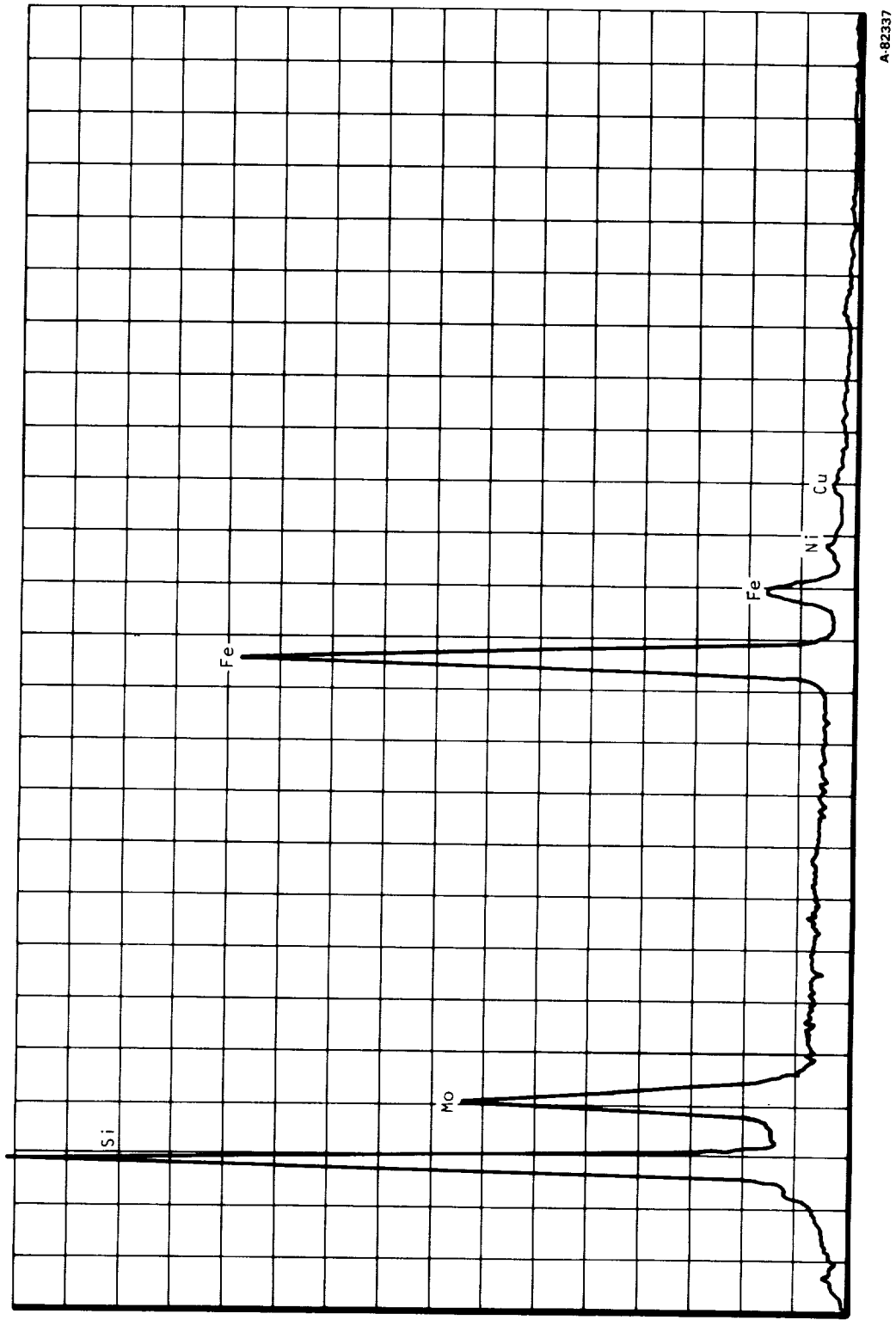

Figure 33.--EDX Spectrum of the Spherical Inclusion in Figure 32, Showing Inclusion to Consist of Iron, Molybdenum, Nickel, and Copper.

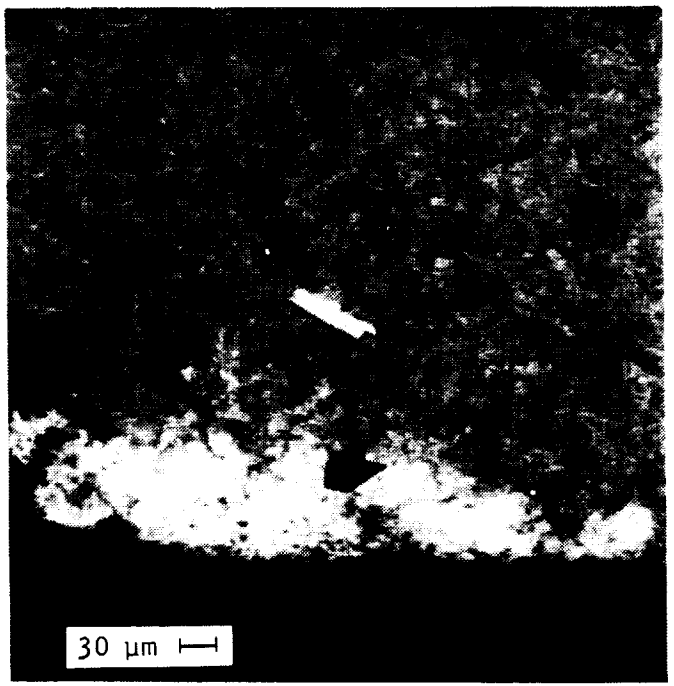

BSE Image

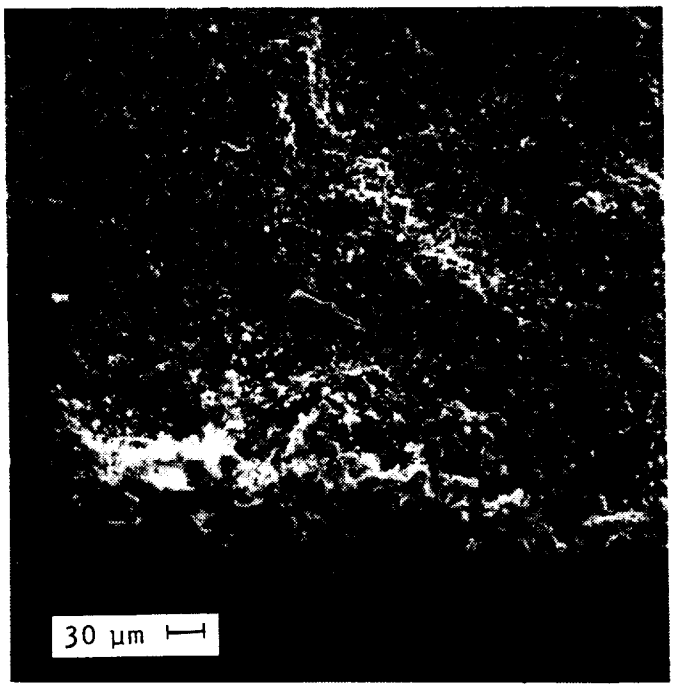

Secondary Emission Image

91689-6

F-47921

Figure 34.--SEM Micrographs of the Fracture Surface of Test Bar 255 (Flexure Tested at 1399°C (2550°F)).

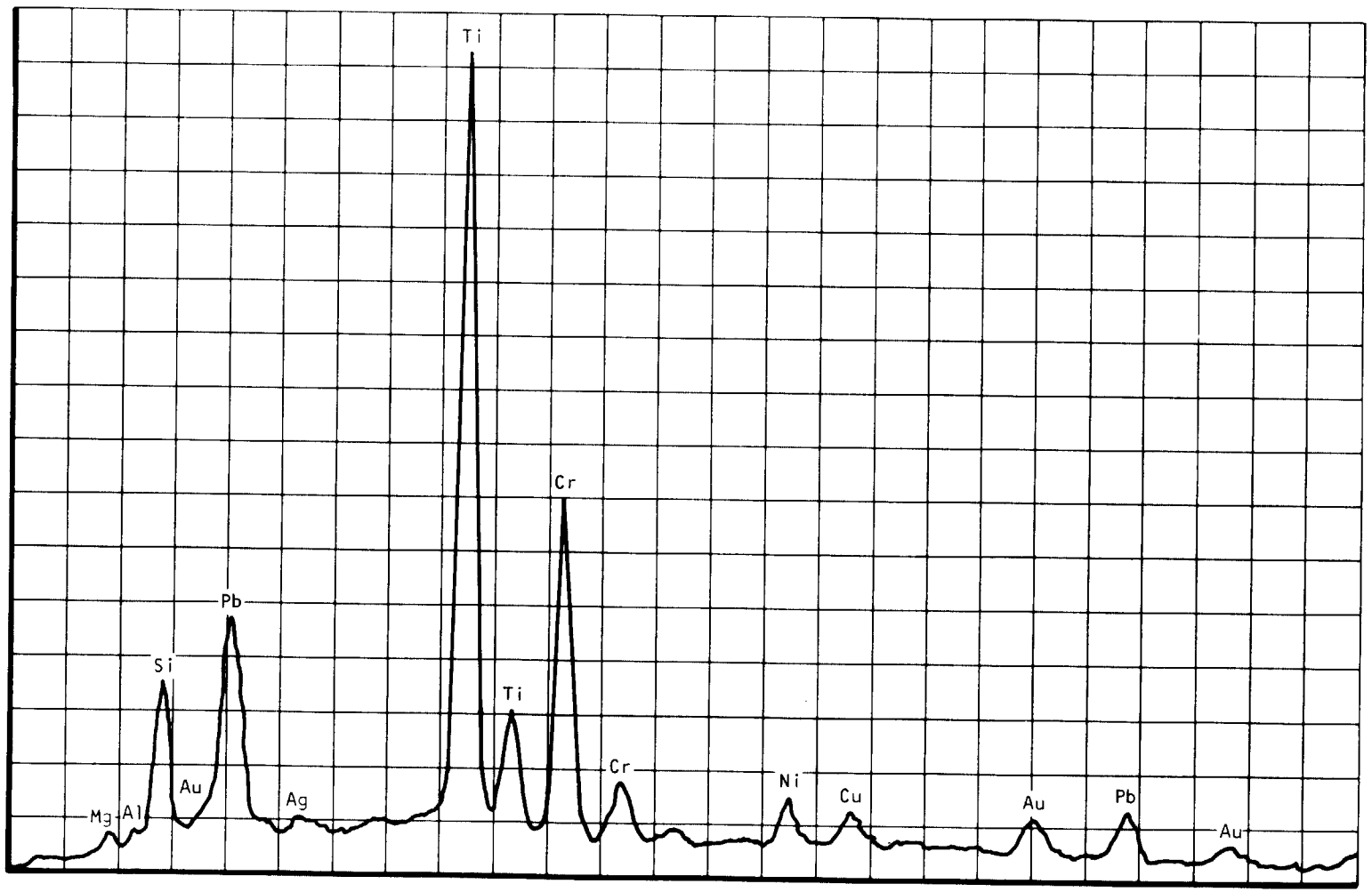

Figure 35.--EDX Spectrum of the Bright Area Near Tensile Face of Test Bar 255 (Fig. 34), Showing Mostly Titanium and Chromium with Other Minor Constituents.

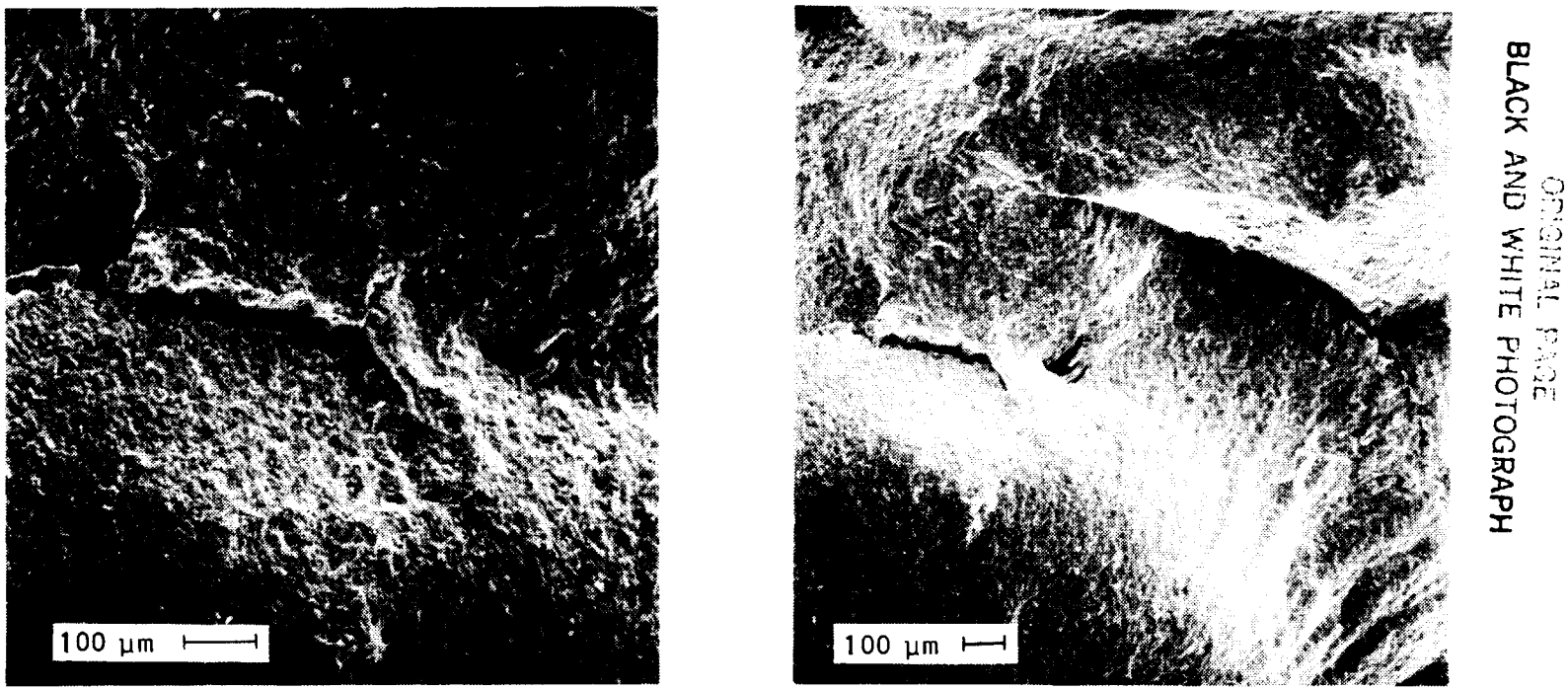

Figure 36.--SEM Micrographs Showing Internal Laminar Flaw Observed on Fractured Surface (Test Bar 321).

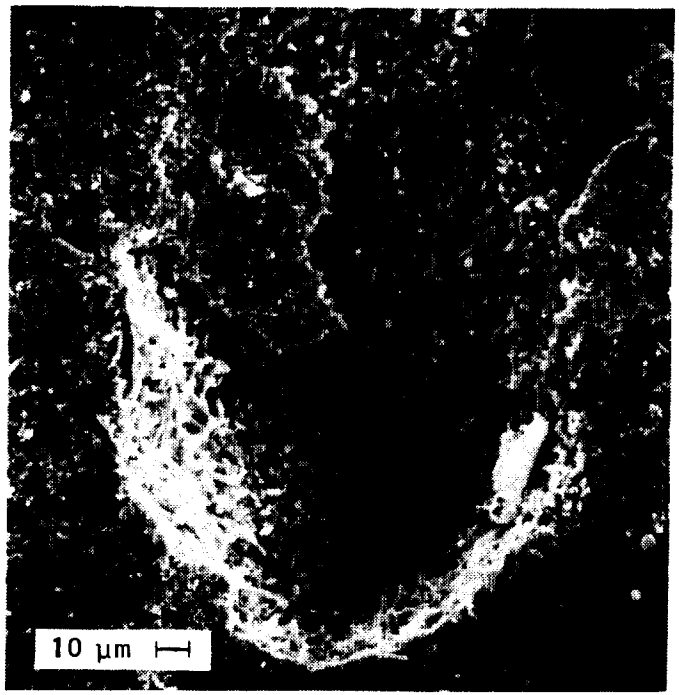

TEST BAR NO. 302

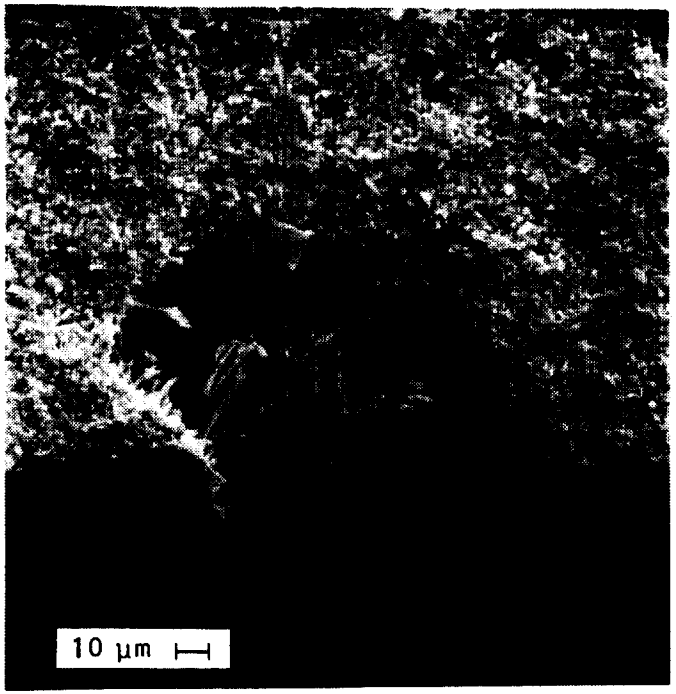

TEST BAR NO. 356

91644-11

F-47924

Figure 37.--SEM Micrographs Showing Internal and Subsurface Flaws on Fractured Surfaces (Test Bars 302 and 356).

Oxidation resistance tests were also conducted. Twenty bars were exposed to air for 200 hours in a temperature gradient furnace over a temperature range of 388° to 1296°C (730° to 2365°F). The bars were visually inspected after the exposure. The only specimens that changed significantly during treatment were those exposed to temperatures above 1260°C (2300°F). These specimens changed from light gray (as-processed) to pale yellow speckled with brown. Figure 38 shows the room-temperature MOR as measured on individual specimens after exposure. Fractography on the specimens was compared to previous nondestructive evaluations (NDE) and showed that the two lowest strength values resulted from flaws existing before treatment. All other data are within the normal distribution for the baseline material room temperature strength. It appears that a slight strength decrease occurs as a result of increasing exposure temperatures.

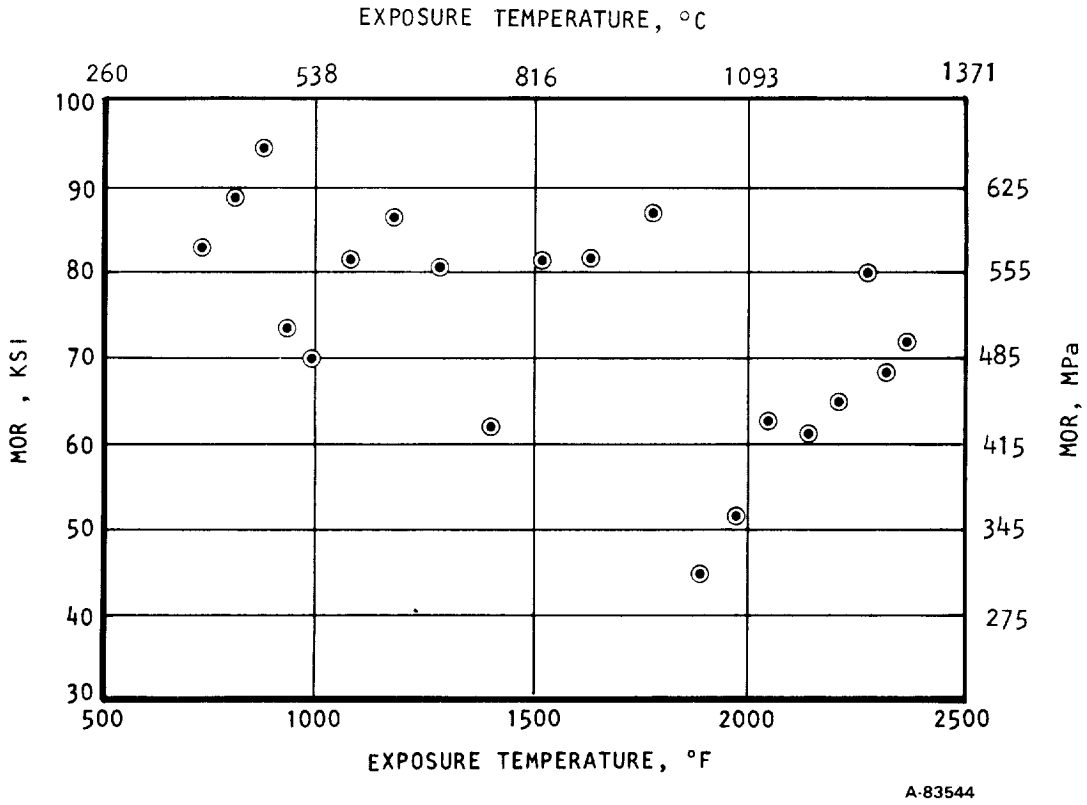

Figure 38.--Room Temperature Strength after 200 Hours at Temperature in Air.

Ten baseline specimens were stress rupture tested. Initially, a stepped stress rupture test was conducted at each test temperature (982°, 1204°, and 1371°C) (1800°, 2200°, and 2500°F). The tests were started at 65 MPa (448.2 ksi) and increased by 65 MPa every 24 hours until the specimen failed. The results are listed in table 11.

TABLE 11.--ONE-STEP STRESS RUPTURE TEST

982°C	1204°C	1371°C
65 MPa - 24 hr	65 MPa - 24 hr	65 MPa - 9 hr, 42 min
130 MPa - 24 hr	130 MPa - 24 hr	
195 MPa - 24 hr	195 MPa - 24 hr	
260 MPa - 1 min	260 MPa - 24 hr	
	235 MPa - 0	

These results furnished information for choosing test conditions for additional stress rupture tests. The conditions and results of these tests on seven specimens are listed in table 12.

TABLE 12.--CONTROLLED STRESS RUPTURE TEST

982°C	1204°C
260 MPa - 7 hr, 22 min	260 MPa - 0
260 MPa - 17 hr, 19 min	195 MPa - 1 min
	195 MPa - 4 hr, 55 min
195 MPa - 100 hr (survived)	195 MPa - 3 hr, 38 min

A computerized data base for the test bars was established. Table 3 presents the information included in the data base. Relationships between variables in this data base were analyzed for the sintered material.

Two-variable relationships of the sintered material and process were analyzed using the computerized data base. Figures 39 and 40 show some of the results of these relationships. From these results, it can be concluded that:

(1) There is no relationship between dewax weight loss and sintered weight loss (figure 39b) or between dewax weight loss and sintered density (figure 39c). The relationship between sintering weight loss and density, however, cannot be conclusively determined from the results (figure 39a).

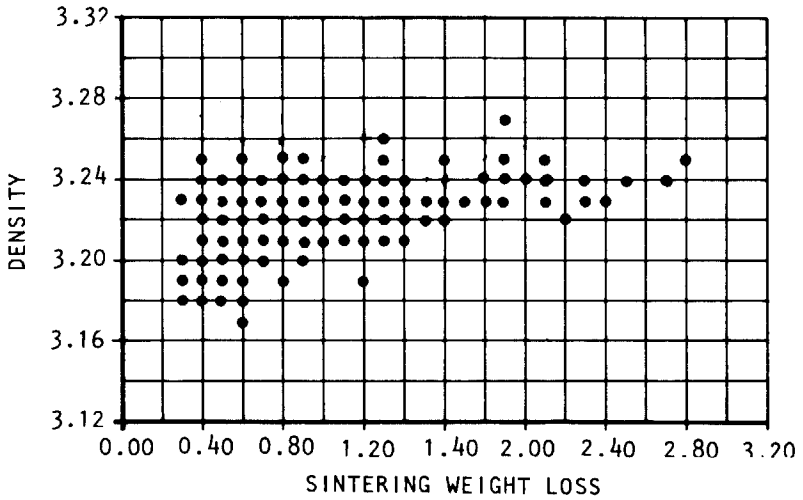

a. SINTERING WEIGHT LOSS VS DENSITY

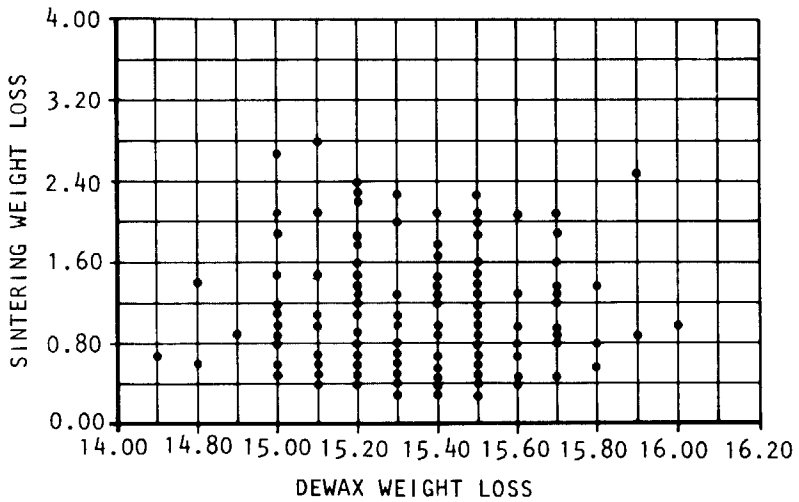

b. DEWAX WEIGHT LOSS VS SINTERING WEIGHT LOSS

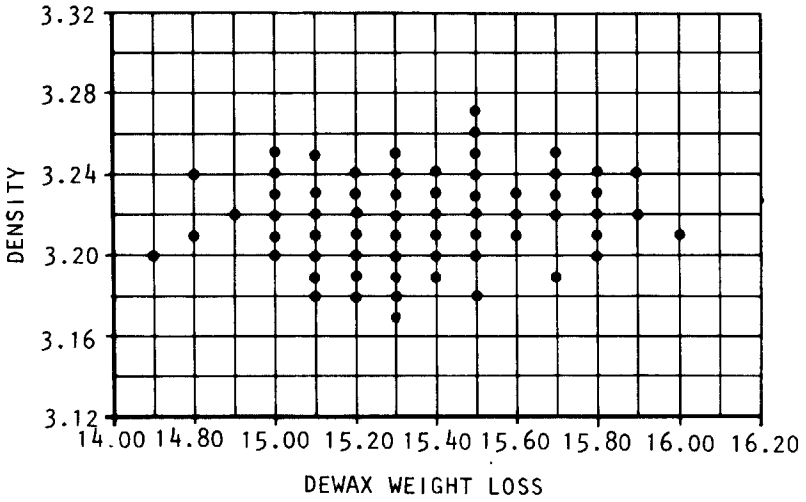

c. DEWAX WEIGHT LOSS VS DENSITY

A-81094

Figure 39.--Room Temperature Data, Relationship of the Variables--Set I.

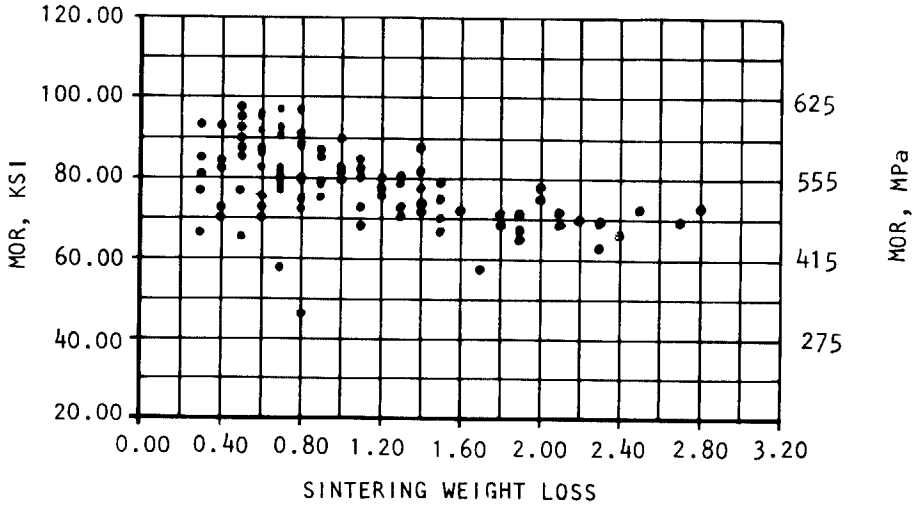

a. **SINTERING WEIGHT LOSS VS MOR**

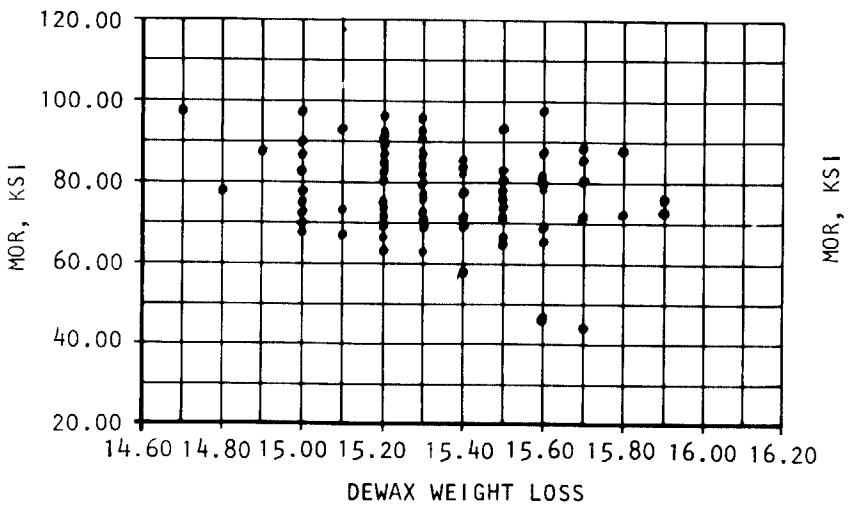

b. **DEWAX WEIGHT LOSS VS MOR**

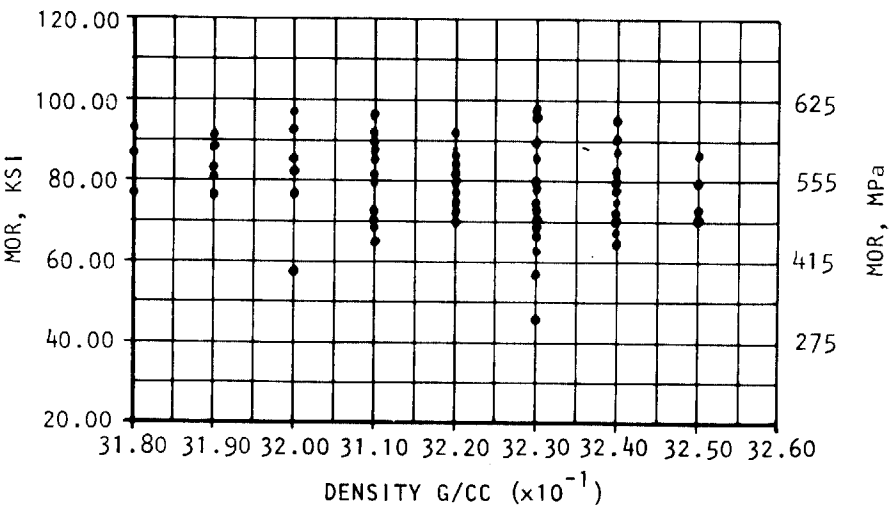

c. **DENSITY VS MOR**

A-81093

Figure 40.--Room Temperature Data, Relationship of the Variables--Set II.

(2) The relationship of MOR to sintered density or dewax weight loss is insignificant (random) at room temperature (figures 40b and 40c) and at high temperature (not shown) for this batch of material. However, the relationship of MOR to sintering weight loss appears significant both at room temperature (figure 40a) and high temperature (not shown). With these samples, there is a tendency toward low strengths associated with high weight loss. Therefore, the variables which related to sintering weight loss should be investigated more carefully.

(3) Table 13 indicates that there is no relationship between molding cavity and surface visual inspection grade.

TABLE 13.--MOLDING CAVITY LOCATION AND VISUAL INSPECTION GRADE RELATIONSHIP

	Number of bars				
	Visual inspection grade				
Molding cavity	0	1	2	3	4
1	9	7	14	30	14
2	9	7	10	34	10
3	14	10	14	22	10
4	4	10	14	28	15

Molding cavity location: $i = 1, 2, 3, 4$

Visual inspection grade: $j = 0, 1, 2, 3, 4$

2.2 DEVELOPMENT OF IMPROVED BASELINE MATERIAL*

2.2.1 Summary/Introduction

The objective of this task was to improve the baseline material mechanical properties through process optimization. The goal was to increase the average as-processed test bar flexural strength 20 percent to 661.9 MPa (96 ksi), and the Weibull slope by 100 percent to 16, without altering the basic composition chemistry.

Due to the large number of variables involved, statistically designed experiments were conducted to facilitate the optimization. The variables selected for evaluation were: starting Si_3N_4 powder material, binder content, blending method, sintering aid level, densification environment, and densification cycle. A five-parameter two-level fractional factorial matrix was designed and applied to two Si_3N_4 powders, Starck H-1 and Denka 9FW. It was anticipated that several iterations would be required to achieve the goal. However, in the first iteration, a material, designated "ab," with 670.9 MPa (97.3 ksi) strength and 13.6 Weibull slope was achieved. This material, utilizing Denka 9FW Si_3N_4 with 6 percent Y_2O_3 and 2 percent Al_2O_3, met the mechanical strength goal but was slightly lower than the Weibull slope goal. A detailed statistical analysis was performed to identify the most important variables and interactions between parameters.

A separate experimental matrix was designed to evaluate process reproducibility when different Si_3N_4 lots, molders, and densification runs of the same cycle were used. The results from the reproducibility experiment demonstrated that material properties can be reproduced only if the raw material was from the same lot and the test bars were injection molded using the same molder. The original "ab" properties were not reproduced due to the lot-to-lot Si_3N_4 PSD and sinter/HIP cycle variations.

2.2.2 Selection of Processing Parameters

Based on prior experience along with the results of baseline material characterization and some of the exploratory experiments (Appendix A), the following six variables were considered most important and thus were selected for evaluation.

(1) Raw Materials.--It was found in the exploratory experiments (Appendix A, Matrixes 1 and 6) that the starting raw material has a strong influence on the processing behavior. The results showed that process parameters may be optimum for one material but unsatisfactory for another.

Baseline powder GTE SN-502 was not included in the experimental matrix evaluation due to its large lot-to-lot variations. In addition, the version of GTE SN-502 Si_3N_4 used in Task I was no longer commercially available.

*Performed under Task II of the contract.

Two commercial Si_3N_4 materials, Starck H-1 and Denka 9FW, were found to be more consistent in properties and were selected for evaluation in parallel as Matrix II-1 and Matrix II-2, respectively.

(2) Consolidation Method.--A new sinter/HIP cycle had been developed at GCCD which produced higher density parts than the baseline 0.69 MPa (100 psi) N_2 sintering. Two levels of sinter/HIP cycles were included in the test matrix.

(3) Consolidation Environment.--Covering Si_3N_4 samples in a high-temperature powder such as Si_3N_4 or BN during sintering usually improves the density and surface quality of the sintered parts, based on GCCD's prior experience in the AGT program. Sinter/HIP with and without a selected powder bed was chosen for comparison.

(4) Mixing (Blending).--Some of the internal flaws in the baseline test bars resulted from nonuniform mixing of the injection mix. The baseline sigma mixing was selected for comparison with sigma mixing plus extrusion. Extrusion is an efficient high-shear mixing action.

(5) Sintering Aid.--Part of the program goal is to improve the high-temperature strength of the test bars by 20 percent; one approach is to reduce the sintering aid level. A 6% Y_2O_3 + 1% Al_2O_3 additive level was selected for comparison with the baseline 6% Y_2O_3 + 2% Al_2O_3 level.

(6) Binder Concentration.--Results from the exploratory experiments (Appendix A, Matrixes 2 and 3) suggested that a lower binder content may minimize dewax defects and increase green densities. Concentrations of 15.5 percent (baseline) and 14.5 percent were selected for evaluation.

2.2.3 Statistical Experimental Design

Two five-factor matrixes were designed to include all six variables of interest. One matrix applied to Starck H-1 and the other to Denka 9FW Si_3N_4. These first two matrixes differed only in the raw materials selected.

The matrix design was half replicate of a 2^5 fractional factorial design as shown in figure 41. A brief discussion of this design follows.

For an experiment of five factors, each in two levels, the full-factorial design consists of 32 treatment* combinations (2^5). The full matrix is then divided into two blocks of confounding ABCDE interaction. Each block includes 16 treatment. The following block of treatment combinations was chosen for this experiment:

1, ab, ac, bc, ad, bd, cd, abcd, ae, be, ce, abce, de, abde, aede, bcde

*Treatment is a statistical term referring to a unique combination of experimental parameters.

1/2 REPLICATE OF A 2^5 FRACTIONAL FACTORIAL DESIGN

		C+				C-			
		D+		D-		D+		D-	
		E+	E-	E+	E-	E+	E-	E+	E-
A+	B+		abcd	abce		abde			ab
	B-	acde			ac		ad	ae	
A-	B+	bcde			bc		bd	be	
	B-		cd	ce		de			1

A SINTER/HIP TIME 2 HR (A-) VS 4 HR (A+)

B SINTER/HIP ENVIRONMENT - WITHOUT POWDER BED (B-) VS WITH POWDER BED (B+)

C MIXING — SIGMA MIXER (C-) VS SIGMA MIXER PLUS EXTRUDER (C+)

D SINTERING AIDS — (6% Y_2O_3 + 2% Al_2O_3) (D-) VS (6% Y_2O_3 + 1% Al_2O_3) (D+)

E BINDER CONTENT — 15.5% (E-) VS 14.5% (E+)

A 82151 A

Figure 41.--Experimental Design.

The "1" denotes the treatment combination in which every factor is at its lower level; treatment "ab" represents the higher levels ("+") of factors A and B and the lower levels ("-") of all other factors; treatment "abed" is the higher levels of four factors except factor "C," and so on. These treatment combinations are indicated in the shaded areas to figure 41.

By conducting only a half replicate of a factorial design, each effect could be indistinguishable with another effect, that is, the effects which occur in pairs (termed "aliases"). It is imperative to determine the aliases for any fractional design in order to avoid confusion of important effects. The alias structure of the fractional factorial experiment in figure 41 is shown in table 14. The symbol "=" in Table 14 implies "alias with." Table 14 shows that all the main effects and two factor interactions can be evaluated if three or more factor interactions are negligible. Thirty bars were tested in each treatment. It is realized that this is only one sample. Replication of the experiment is prohibited by time and budget. However, in the case of ceramic materials, the within-sample variation is so large compared with the variation of between-sample that the repeat sampling is statistically less important, but the ability for detecting differences in the analysis of variables will be reduced.

TABLE 14.--ALIAS STRUCTURE OF THE HALF REPLICATE OF A 2^5 FRACTIONAL FACTORIAL DESIGN CONFOUNDING ABCDE

A = BCDE	AD = BCE
B = ACDE	BD = ACE
C = ABDE	CD = ABE
D = ABCE	AE = BDC
E = ABCD	BE = ACD
AB = CDE	CE = ABD
AC = BDE	DE = ABC
BD = ADE	

NOTE: The symbol "=" implies "alias with."

2.2.4 Experimental Procedure for Test Bar Fabrication

The experimental procedure is described as follows:

(1) Process Flow Chart.--Based on the experimental design and the parameters selected for evaluation, both of which were discussed in the last section, a process flow chart was constructed (figure 42). The flow chart was used to systematically control the overall processing procedure so that the designed experiments could be conducted with maximum efficiency and minimum error. The flow chart is applicable to both Matrix II-1 (Starck H-1 Si_3N_4) and Matrix II-2 (Denka 9FW Si_3N_4).

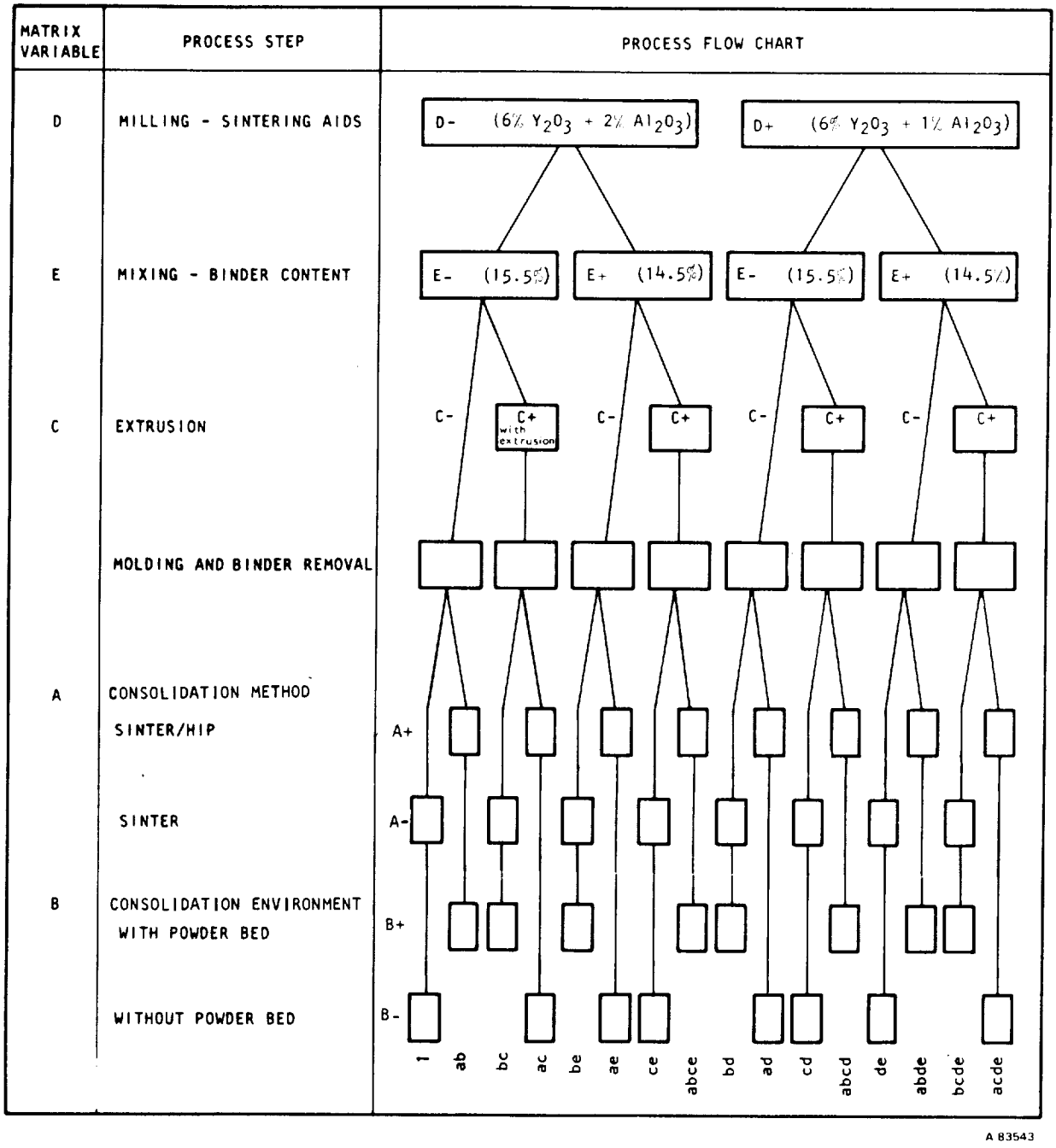

Figure 42.--Process Flowchart for Matrixes I and II.

The unspecified processing parameters (for example, molding temperature) were optimized according to Si_3N_4 type, sintering aid level, and binder content.

(2) Materials.--Starck H-1 and Denka 9FW Si_3N_4 were selected for evaluation. The two sintering aids, Moly Corp. Y_2O_3 and Linde A Al_2O_3, were from the same lots used in fabricating the baseline material. Description of the sintering aids was presented earlier. The characteristics of both Si_3N_4 powders are described below.

Table 15 lists the results of the chemical analysis of both as-received Si_3N_4 powders as well as the milled powders. Both Si_3N_4 powders contain higher levels of calcium, iron, and magnesium than the baseline powder (GTE SN-502); however, the powders are free of molybdenum, an SN-502 impurity. Oxygen analysis data are also included in Table 15. Both as-received Si_3N_4 powders have a lower oxygen content than the baseline powder: 1.52 percent for Starck H-1 and 0.98 percent for Denka 9FW, compared with 2.18 percent for the baseline. Good agreement was obtained in higher oxygen levels in milled powder corresponding to the addition of oxide sintering aids.

Particle size distributions for the as-received Si_3N_4 powders and the batched and milled powders are shown in figures 43 and 44. Milled Starck H-1 is comparable to the GTE SN-502 baseline. Milled Denka 9FW powder is much finer than either of the above materials. Figure 44 shows that the as-received Denka 9FW is slightly finer than the milled powder. This seemingly unreasonable shift in particle size distribution is evidently the result of the larger particle sizes of the sintering aids.

Surface area data are presented in table 16. In both material systems, only a slight change occurred in surface area during the milling process. All milled powders have surface areas greater than the baseline powder (7.2 m^2/g).

Scanning electron micrographs illustrate the general shape of the powders. Figure 45 shows the as-received Starck H-1, and figure 46 shows the as-received Denka 9FW; both samples were dispersed prior to SEM examination. The powders appeared to be similar in size and shape; both showed angular, equiaxed grains with an average grain size of about 0.5 micron and containing a few large grains about 5 microns in diameter. In the nondispersed form, the Denka 9FW powder appears as spherical agglomerates between 20 to 60 microns in diameter and the Starck H-1 powders were 20- to 200-micron irregular agglomerates.

(3) Preparation and Characterization of Injection Mixes.--Following the process flow chart (figure 42), injection molding mixes were prepared for each Si_3N_4 powder with two sintering aid levels, two binder content levels, and two mixing levels, resulting in eight different mixes per Si_3N_4 powder type. A torque rheometer was used to characterize the rheology of these mixes. A standard procedure with a specific combination of cooling rate and rheometer rpm was established

TABLE 15.--CHEMICAL, AND OXYGEN ANALYSIS[1] OF AS-RECEIVED AND MILLED POWDERS (WEIGHT PERCENT)

Element	Matrix II-1 (Starck H-1)			Matrix II-2 (Denka 9FW)		
	AR[2] Si_3N_4	Milled (6+1)[3]	Milled (6+2)[4]	AR[2] Si_3N_4	Milled (6+1)[3]	Milled (6+2)[4]
Aluminum	0.03	0.7	L-M[5]	0.07	0.8	L-M
Calcium	0.002	0.01	0.007	0.09	0.2	0.2
Chromium	--	--	--	0.01	0.01	0.01
Iron	0.02	0.01	0.01	0.02	0.02	0.01
Lithium	<0.001	<0.001	<0.001	<0.001	<0.001	<0.001
Magnesium	0.004	0.007	0.007	0.003	0.007	0.007
Manganese	--	--	--	0.002	0.001	0.001
Sodium	<0.001	<0.001	<0.001	<0.001	<0.001	<0.001
Silicon	H[5]	H	H	H	H	H
Titanium	0.002	0.002	0.002	0.006	0.002	0.007
Vanadium	--	--	--	0.001	--	--
Yttrium	--	M	M	--	M	M
Potassium	<0.001	<0.001	<0.001	<0.001	<0.001	<0.001
Oxygen	1.52	3.39	3.86	0.98	3.00	3.67

NOTES:

1. Spectrographic analysis, oxygen analysis by neutron activation
2. As-received powder
3. 93 percent Si_3N_4, 6 percent Y_2O_3, and 1 percent Al_2O_3
4. 92 percent Si_3N_4, 6 percent Y_2O_3, and 2 percent Al_2O_3
5. L, M, H, = low 0.1 to 1 percent, medium 1 to 10 percent, and high 10 to 100 percent, respectively

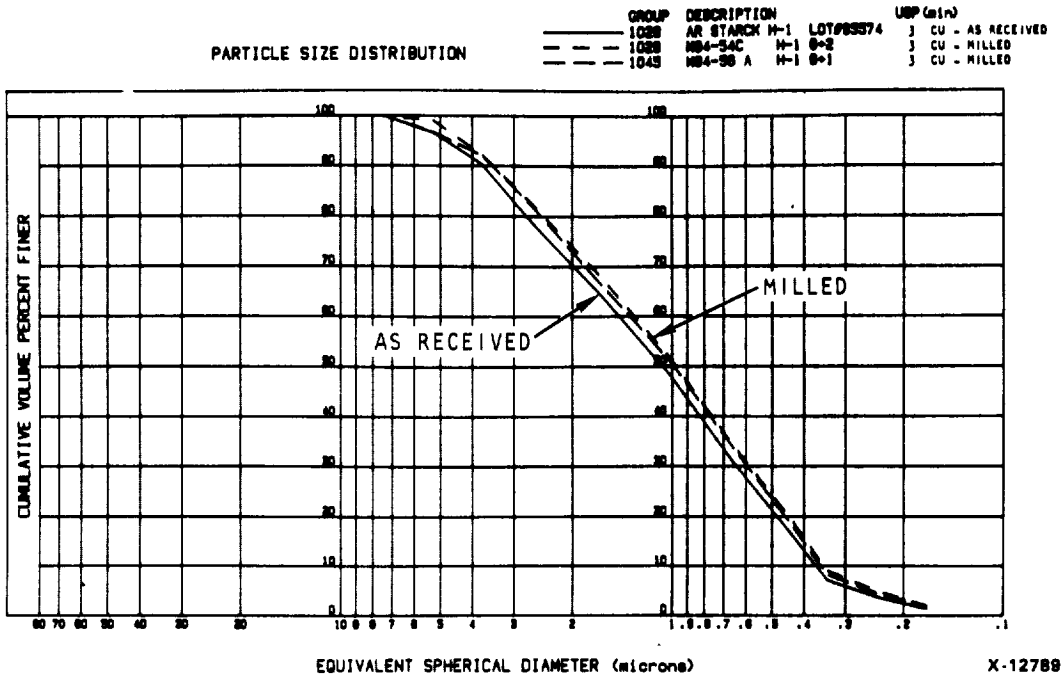

Figure 43.--Particle Size Distribution Data for As-Received and Milled Starck H-1 Powders (Matrix II-1).

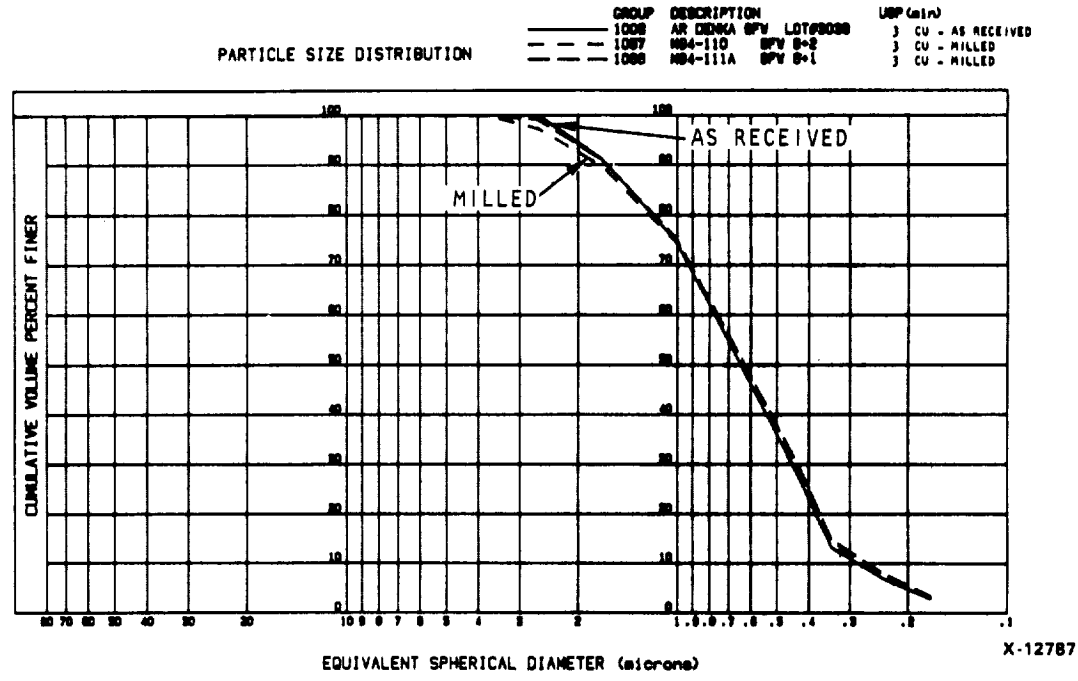

Figure 44.--Particle Size Distribution Data for As-Received and Milled Denka 9FW Powders (Matrix II-2).

TABLE 16.--SURFACE AREAS

Powder	Surface Area, m^2/g
AR Starck H-1	10.78
Milled H-1 6+2 (M94-54C)*	11.78
Milled H-1 6+1 (M94-56A)*	11.32
AR Denka 9FW	11.81
Milled 9FW 6+2 (M94-110)*	11.97
Milled 9FW 6+1 (M94-111A)*	12.15

*Mill bath number

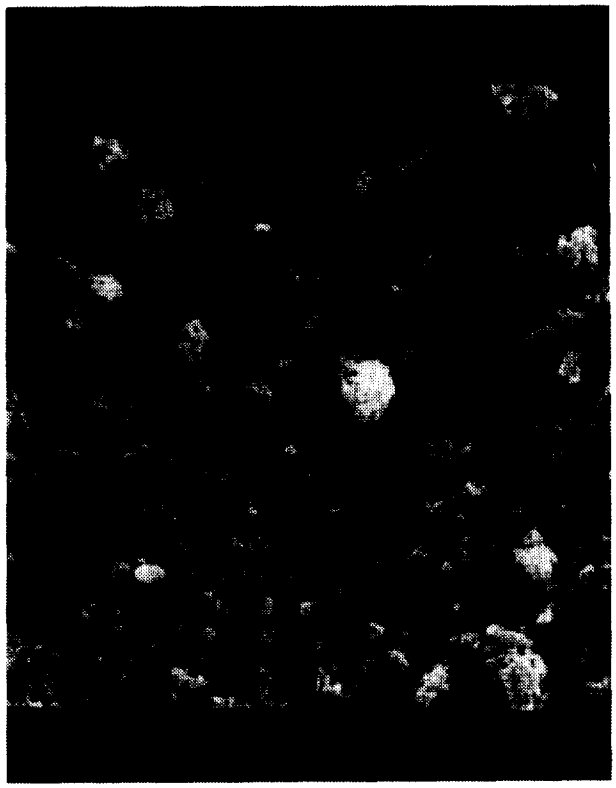

F-48892

Figure 45.--SEM Micrograph of As-Received Starck H-1 Powder.

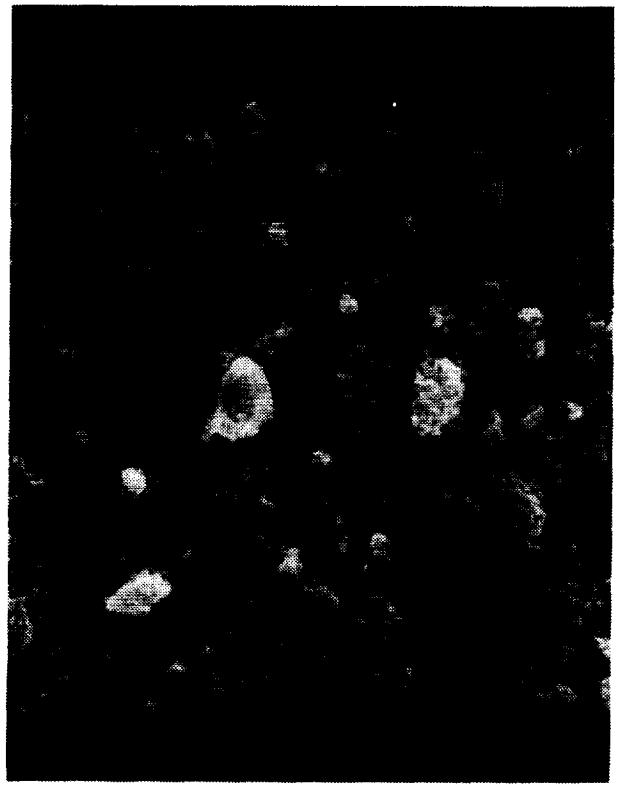

F-48892

Figure 46.--SEM Micrograph of As-Received Denka 9FW Powder.

to compare the mixes. For example, figure 47 shows the rheometer outputs for the four Starck H-1 Si_3N_4 mixes mixed with a regular Sigma mixer (no additional extrusion). For a more quantitative comparison, the torque at 65°C (150°F) (baseline injection molding temperature) was found to be sensitive enough to reveal the rheology differences between mixes and thus was used as a comparison. Table 17 lists the torque values at 65°C for all eight mixes made with Starck H-1 Si_3N_4.

The data in table 17 are consistent in showing that by reducing the binder content from 15.5 to 14.5 wt%, the torque is increased. The data also indicate that passing the mix through a high-shear, twin-screw extruder reduces the torque. The reason for the exceptionally low value at condition (C+D+E-) is not known.

The torque data for the eight mixes made with Denka 9FW Si_3N_4 are presented in table 18. Similar to Starck H-1 Si_3N_4, torque of the extruded mixes is consistently 36 to 50 percent lower than the as-mixed material, indicating better mixing. All torque-vs-temperature curves show a smooth transition from high temperature and low torque to low temperature and high torque. Finally, torque values are lower than those for Starck H-1 (see table 17). This suggests that Denka 9FW Si_3N_4 is easier to injection mold.

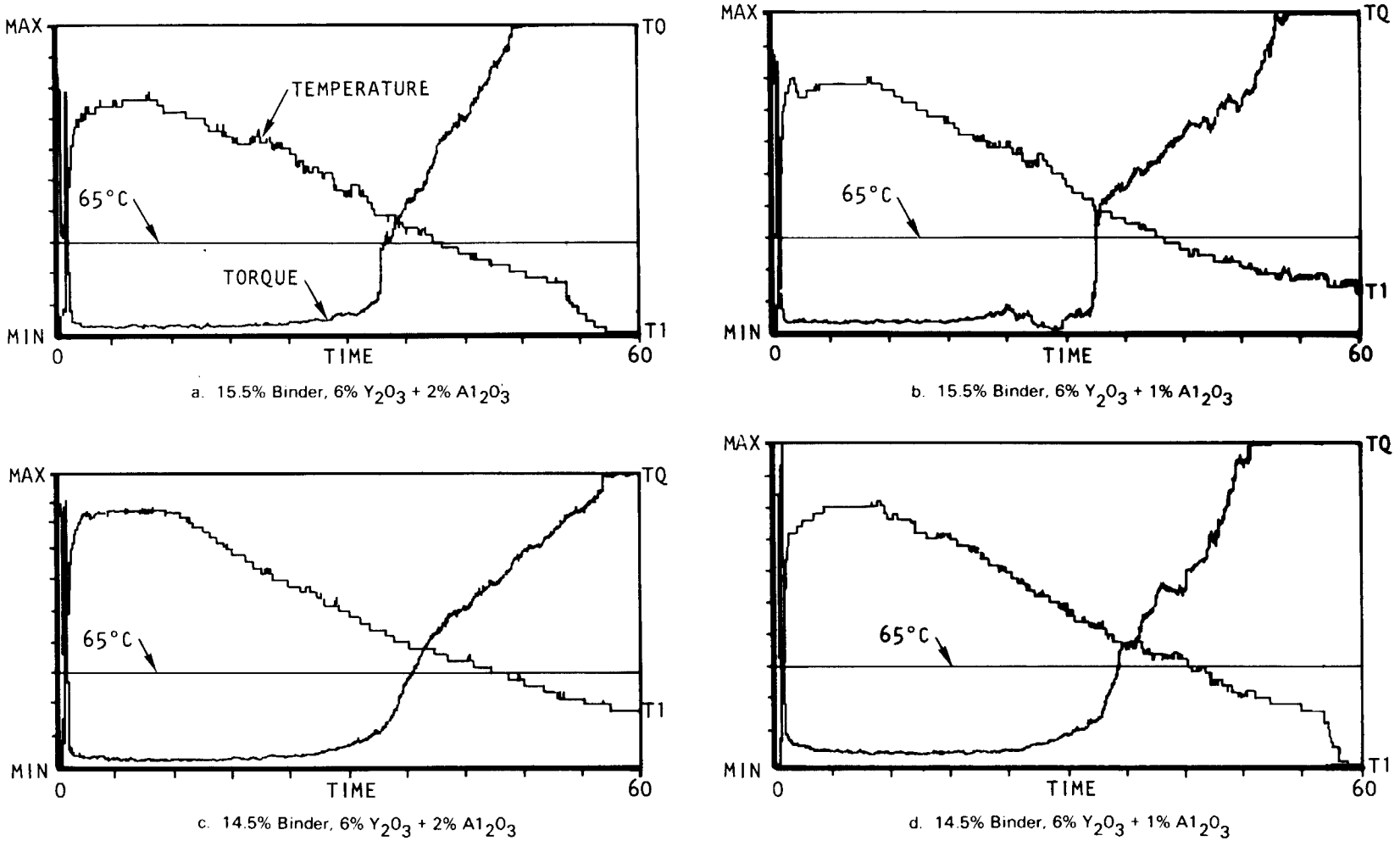

Figure 47.--Torque Characterization Curves, Matrix II-1, Not Extruded; Torque and Temperature Are Plotted as a Function of Time with Scale Minimum Values of 0 m·g and 50°C (122°F) and Maximum Values of 2500 m·g and 100°C (212°F).

TABLE 17.--TORQUE AT 65°C (150°F) FOR MATRIX II-1 INJECTION MOLDING BATCHES

	Torque, m·g			
	D- (6% Y_2O_3 + 2% Al_2O_3)		D+ (6% Y_2O_3 + 1% Al_2O_3)	
Mixing Procedure	E- 15.5% Binder	E+ 14.5% Binder	E- 15.5% Binder	E+ 14.5% Binder
C-	1450	1500	1386	1544
C+ (Extruded)	1100	1452	762	1290

NOTES:

1. Values are from single mixer runs.
2. Mixer cooling rate was 1°C (1.8°F) per minute.
3. m·g = meter·gram

TABLE 18.--TORQUE AT 65°C (150°F) FOR MATRIX II-2 INJECTION MOLDING BATCHES

	Torque, m·g			
	D- (6% Y_2O_3 + 2% Al_2O_3)		D+ (6% Y_2O_3 + 1% Al_2O_3)	
Mixing Procedure	E- 15.5% Binder	E+ 14.5% Binder	E- 15.5% Binder	E+ 14.5% Binder
C-	876	1304	948	1175
C+ (Extruded)	439	796	500	748

NOTES:

1. Values are from single mixer runs.
2. Mixer cooling rate was 1°C (1.8°F) per minute.
3. m·g = meter·gram

(4) Injection Molding.--Injection molding of test bars was accomplished using the Arburg molder in the standard four-cavity die used for the baseline material. Injection molding parameters were adjusted because of the rheology differences.

X-ray radiography on all as-molded test bars was evaluated. Bars with internal voids were identified, and the yield for each of eight groups per Si_3N_4 type is presented in table 19. These data indicate that for Stark H-1 Si_3N_4, additional mixing, using a twin-screw extruder, provided a better yield at the injection molding stage of processing. This is consistent with the earlier observation that the extruded materials exhibited lower torque on the rheometer output due to improved uniformity of the mix.

TABLE 19.--X-RAY RADIOGRAPHY YIELD OF AS-INJECTED BARS

	Yield in Percent			
	D- (6% Y_2O_3 + 2% Al_2O_3)		D+ (6% Y_2O_3 + 1% Al_2O_3)	
Mixing Procedure	E- 15.5% Binder	E+ 14.5% Binder	E- 15.5% Binder	E+ 14.5% Binder
	Matrix II-1, Starck H-1 Si_3N_4, 200 Bars Injected for Each Condition			
C-	77	77	69	76
C+ (Extruded)	87	92	68	92
	Matrix II-2, Denka 9FW Si_3N_4, 160 Bars Injected for Each Condition			
C-	95	95	95	95
C+ (Extruded)	96	96	98	96

The yield for Denka 9FW Si_3N_4 is significantly better than for Stark H-1 Si_3N_4. This is probably a result of the good flow behavior of the Denka 9FW material as seen in lower torque values as shown in table 18 as compared with those in table 17.

(5) Dewax and Sintering.--Bars that showed x-ray defects were deleted from dewaxing. A 3-day cycle was used instead of the baseline 7-day cycle, and the number of bars was increased to 213 in the dewax load. These changes were demonstrated satisfactorily in the exploratory experiments (Appendix A, Matrixes 3, 6, and 7) and represented an 80-percent reduction in time and energy for dewax when compared with the baseline process.

After binder removal, visual and radiographic inspection were performed on all bars. All test bars yielded satisfactory dewax results. Defects observed in the as-injected bars appeared unchanged and no new defects were observed.

Densification was achieved by sinter/HIP. Four runs were conducted, each containing up to 160 test bars. Runs 1 and 2 satisfied the parameter requirements of the A- sintering condition, and runs 3 and 4 satisfied the requirements of the A+ conditions. Each run contained both bars covered and bars not covered with a powder bed (B+ and B-) to ensure that effects of the powder bed covering could be distinguished from potential variations between runs.

(6) Characterization of Sintered Test Bars.--The sintered bars were inspected using standard visual and X-ray radiography, and their densities were measured by water immersion. Room temperature and elevated temperature (1232°C/2250°F) four-point flexural strength (MOR) was measured and the fracture surfaces were examined. Statistical analyses were performed on Matrix II-2 test bars (Denka 9FW) but not on Matrix II-1 (Starck H-1) bars because of their low density and MOR values. The characterization results for Matrix II-1 are presented first, followed by II-2 results.

(a) The density results showed that the Starck H-1 bars were not fully densified with the processing conditions used. Most of the specimens had low densities of less than 3.00 g/cc (92 percent theoretical). Only one treatment condition, abce, produced bars with an average density above 3.10 g/cc (95 percent theoretical). Table 20 lists the density results of a sinter/HIP run using (A+) sinter/HIP level, in which all bars were fabricated with (C+) (extruded) mixing level. The spread in the density data clearly demonstrates the effects of various processing effects on densification. The data show that bars with the (6+2) sintering aid (D-) composition densified better, powder bed (B+) enhanced densification, and lower binder content (E+) improved final densification due to increased green density. The above observed trends are consistent with the concepts used in selecting these parameters in the matrix experimental design.

The average room temperature was 416.5 MPa (60.4 ksi) and the highest value was only 583.3 MPa (84.6 ksi). Only a partial fractographic evaluation was carried out for these specimens. Among the 120 specimens examined, 75 percent failed from surface flaws and 25 percent from internal flaws. Some specimens were flexural tested at 1232°C (2250°F). Most of these specimens deformed severely during testing, with some bottoming out in the test fixture. Slow crack growth was observed in most fractured specimens.

Because of the low density and poor MOR results, no statistical analysis was conducted, and Starck H-1 Si_3N_4 was eliminated from further evaluation in this program.

TABLE 20.--MATRIX II-1 DENSITY* (g/cc)

	D- (6+2 Sintering Aid)						D+ (6+1 Sintering Aid)					
	E- (15.5% Binder)			E+ (14.5% Binder)			E- (15.5% Binder)			E+ (14.5% Binder)		
Powder Bed	Average	Max.	Min.	Average	Max.	Min.	Average	Max.	Min.	Average	Max.	Min.
No	2.96	2.99	2.90	3.00	3.04	2.93	2.66	2.73	2.62	2.69	2.71	2.65
Yes	3.07	3.12	3.01	3.15	3.18	3.13	2.83	2.85	2.80	2.86	2.89	2.83

*Test bar fabrication parameters included (A+) sinter/HIP level and (C+) mixing level

TABLE 21.--AVERAGE DENSITY OF MATRIX II-2 (DENKA 9FW Si_3N_4) SINTERED TEST BARS (g/cc)

		D-				D+			
		E-		E+		E-		E+	
		B-	B+	B-	B+	B-	B+	B-	B+
C-	A-	3.04	--	--	3.20	--	3.00	2.96	--
	A+	--	3.17	3.11	--	2.97	--	--	2.99
C+	A-	--	3.16	3.08	--	2.96	--	--	3.01
	A+	3.09	--	--	3.16	--	3.01	2.97	--

(b) Matrix II-2 (Denka 9FW Si_3N_4).--A summary of the densification results is given in table 21. The densities are higher than those fabricated under Matrix II-1. Similar process parameter effects are also apparent.

Four-hundred eighty Matrix II-2 test bars, 30 per treatment, were tested in four-point bending at room temperature. The overall room-temperature strength of the test bars was high; there were 65 bars with an MOR over 690.0 MPa (100 ksi). The average MOR was 596.4 MPa (86.5 ksi) with a standard deviation of 12.9, and the strength of the bars ranged from 288.9 to 792.9 MPa (41.9 to 115.0 ksi).

Sixteen different process treatment conditions were included in this matrix, and six of the eight conditions in the 6+2 composition produced test bars with a characteristic strength greater than 620.6 MPa (90 ksi), among which condition "ab" produced the highest average strength of 670.9 MPa (97.3 ksi) and Weibull slope of 13.6. Table 22 lists the strength and Weibull slope values for all sixteen process treatment conditions conducted under this matrix. A detailed discussion of these results will be presented in section 2.3.

Optical fractography results show that there were 115 test specimens (26 percent) with failure from internal flaws, and 333 (74 percent) with failure from surface defects. The average MOR of test specimens that failed from the surface was 606.8 MPa (88.0 ksi), and the average MOR of specimens that failed from internal flaws was 551.6 MPa (80.0 ksi). Fractography showed that 91 (79.9 percent) of the internal flaws were inclusions, while the rest consisted of cracks and pores.

Nearly all of the inclusions that caused failure were either dark-colored or surrounded by a dark patch. Selected specimens with these inclusions were

TABLE 22.--ROOM TEMPERATURE MOR AND WEIBULL SLOPE OF TREATMENT CONDITIONS

Processing Condition	Strength,* MPa (ksi)	Weibull Slope
1	571.6 (82.9)	7.0
ab	670.9 (97.3)	13.6
bc	634.3 (92.0)	7.7
ac	659.2 (95.6)	12.7
be	635.7 (92.2)	10.2
ae	631.6 (91.6)	10.1
bd	525.4 (76.2)	12.8
de	570.9 (82.8)	7.0
ce	590.9 (85.7)	7.9
abce	657.1 (95.3)	13.4
abcd	586.1 (85.0)	11.2
abde	584.7 (84.8)	19.9
bcde	535.7 (77.7)	9.7
acde	544.7 (79.0)	5.3
ad	615.7 (89.3)	12.2
cd	513.0 (74.4)	5.6

*30 samples tested for each condition

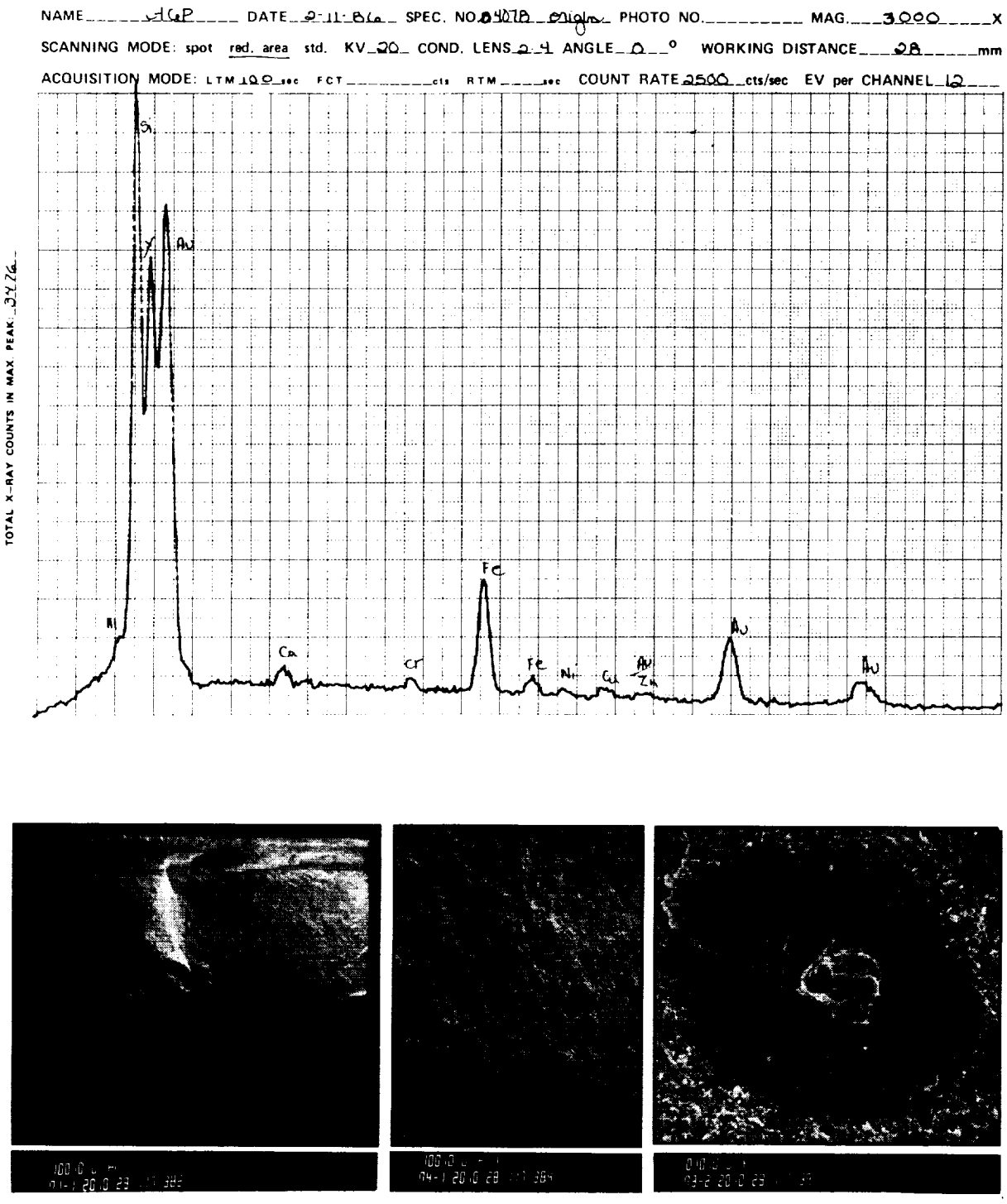

Figure 48.--EDX and SEM Photos of Fractured Bar 4078 Showing Stainless Steel Inclusion and Surrounding Dark Patch.

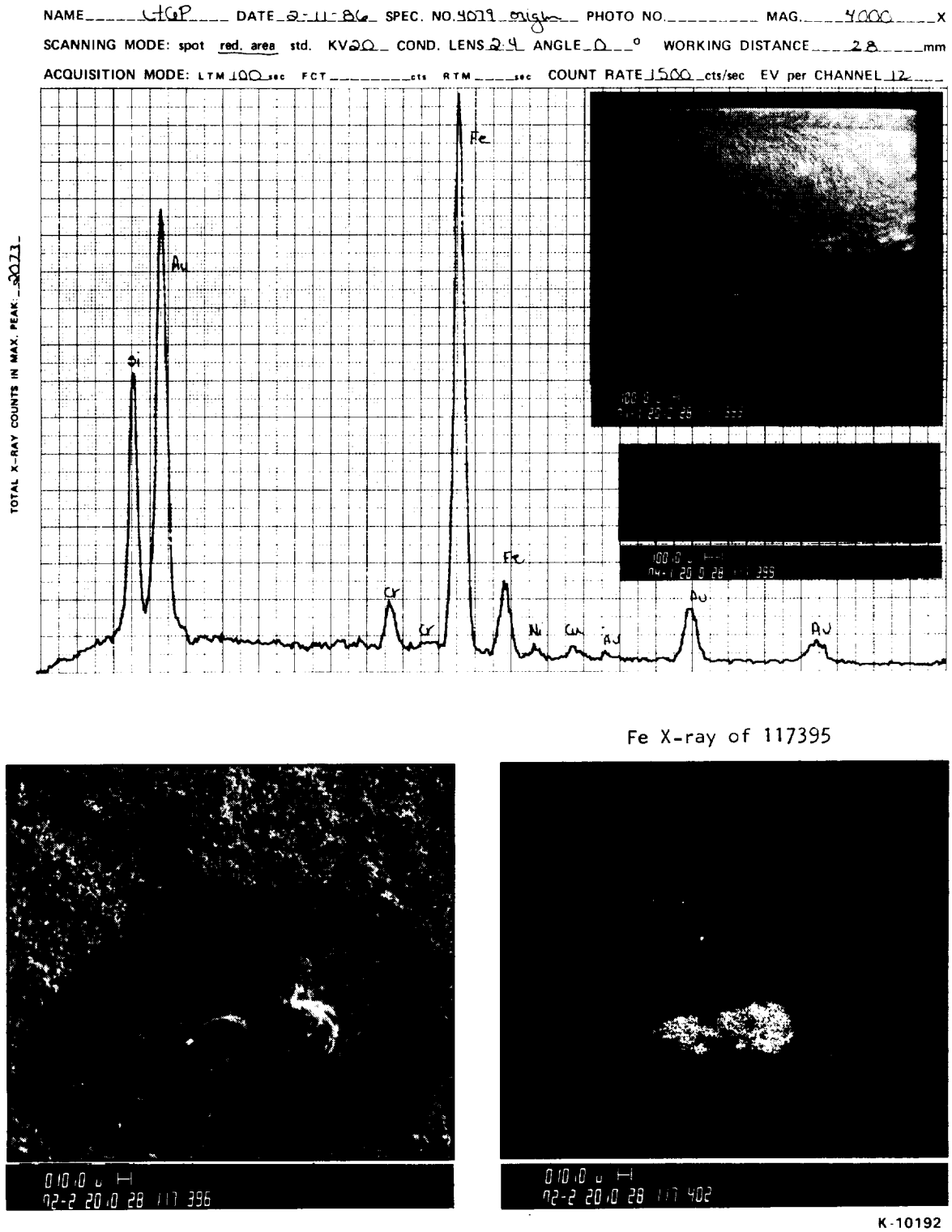

Figure 49.--EDX and SEM Photos of Fractured Bar 4079
Showing Dark Inclusion and Surrounding Dark Patch.

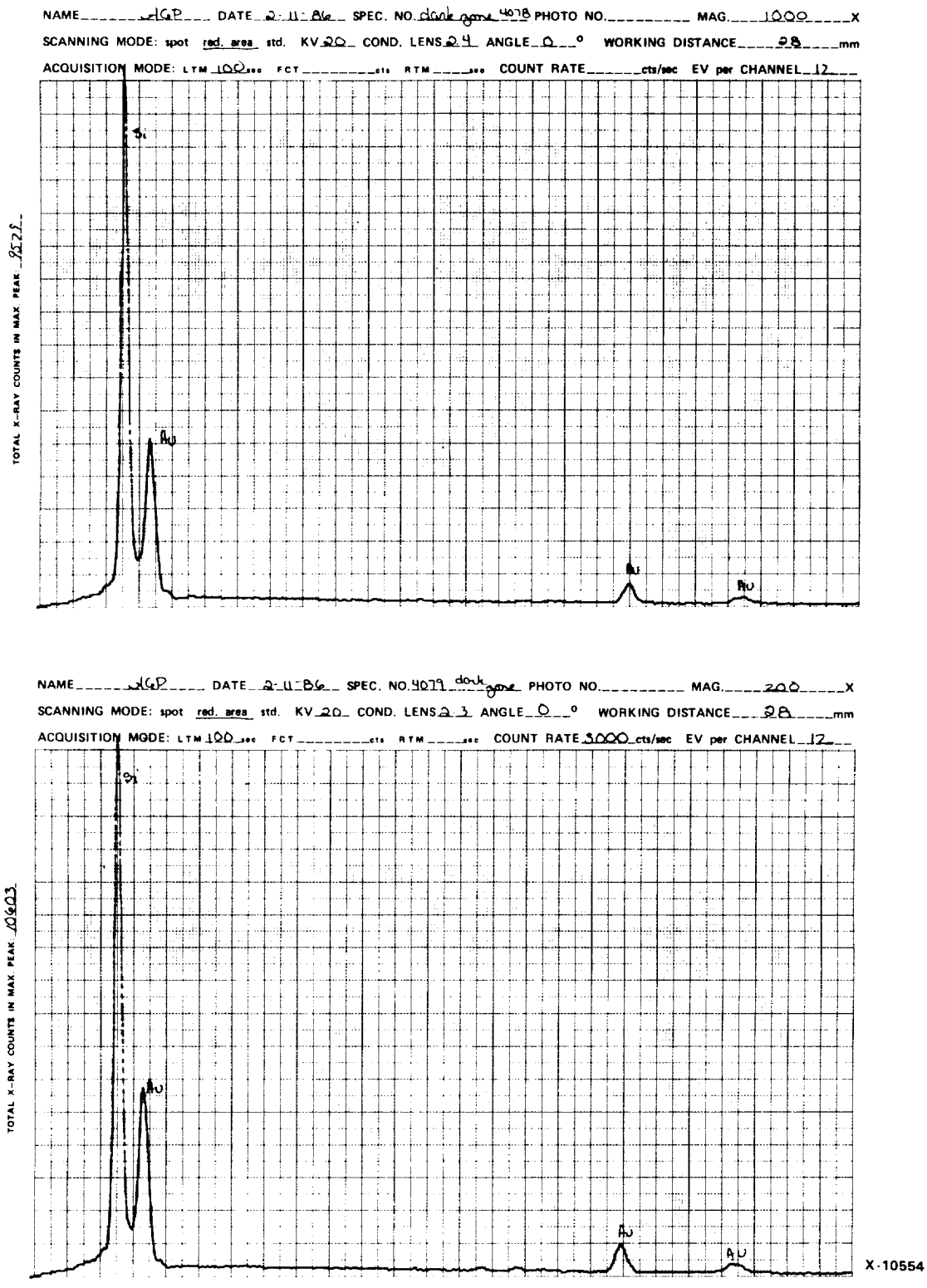

Figure 50.--EDX Plots of the Dark Areas of Bars 4078 and 4079 Showing Only Si (the Au Signal Was From the Sputtered Coating).

examined under SEM and analyzed by EDX. Micrographs and EDX plots of the specimens are presented in figures 48 through 50. EDX analysis showed that the inclusions contained mainly iron and small quantities of chromium and nickel. No other element except silicon was detected in the surrounding dark zone. SEM examination indicated that the fracture mode in the dark zone was predominantly transgranular and this patch of smooth flat surface probably emitted less electrons into the detector and appeared dark due to a surface morphology effect. The change in fracture mode for the dark zones may be due to the formation of a different grain boundary phase with higher iron concentration. The fact that the majority of test specimens with dark inclusions of dark patches were extruded (C+ condition) suggests that the extruder was introducing stainless steel particles into the mixture.

Internal and surface voids were also found at the fracture origins of some specimens. Figures 51 and 52 show an example of each type. The void shown in figure 52 probably existed before sintering, judging from the growth of needle-shaped Si_3N_4 grains inside the void (figure 52d).

The typical fracture surfaces of the 6+2 specimens in this matrix are shown in figures 53a, 53b, and 53c. The specimens were processed with treatment conditions "ab," "ae," and "be," respectively. The microstructure consisted of predominantly elongated hexagonal Si_3N_4 grains with a small proportion of fine equiaxed grains. The larger grains were about 5 to 30 microns (0.0002 by 0.0012 inch).

Five test bars from each treatment combination were flexural tested at 1232°C (2250°F). Table 23 lists the average strengths. Most specimens tested exhibited fast fracture features, but the influence of temperature could also be observed. Compared to specimens tested at room temperature, fewer failures due to inclusions were observed and the inclusions did not seriously affect the strength. Fractures at this temperature generally originated from the tensile surface. Internal and surface voids were also observed at some of the origins. Figures 54 and 55 show two examples of the voids.

2.2.5 Statistical Analysis of Matrix II-2 Results

A detailed statistical analysis was conducted on Matrix II-2 experiments based on room temperature MOR results. The average room temperature MOR and Weibull slope of the specimens from the 16 treatment conditions have already been listed in table 22. The treatment that yielded the highest MOR (670.9 MPa (97.3 ksi)) is condition "ab," which utilized 6% Y_2O_3 + 2% Al_2O_3 sintering aid (D-), 15.5 percent binder (E-), mixing without extrusion (C-), and longer sintering time (A+) in a powder bed (B+). The treatment that yielded the highest Weibull slope (19.1) is condition "abde," but the average MOR is only 585.4 MPa (84.9 ksi). The average MOR of the specimens is also plotted in figure 56, in descending order of MOR. The graph also shows the variations in MOR between sintering runs. Detail analysis, including the variations, will be discussed later.

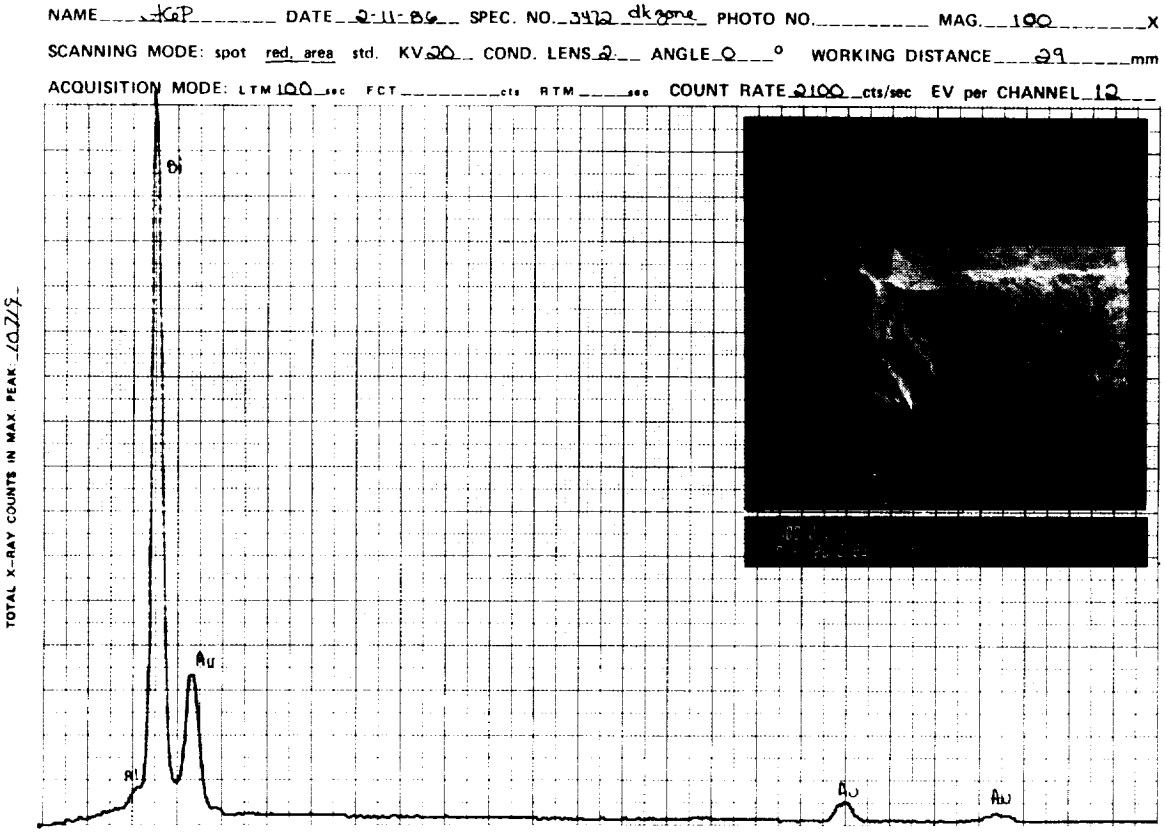

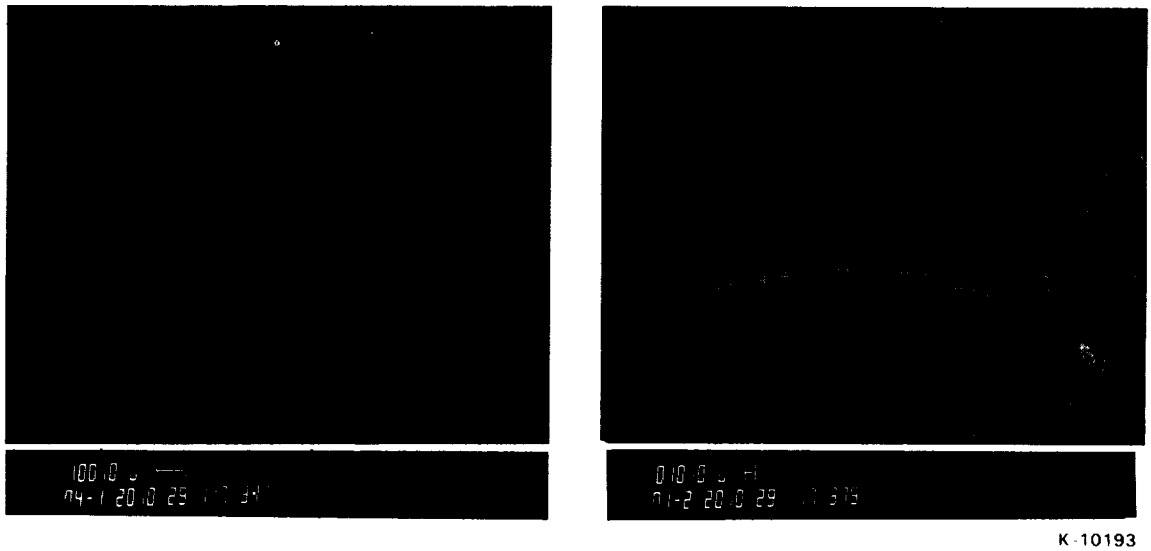

K-10193

Figure 51.--EDX and SEM Photos of Fractured Bar 3472 Showing an Internal Void Probably Formed During Injection Molding.

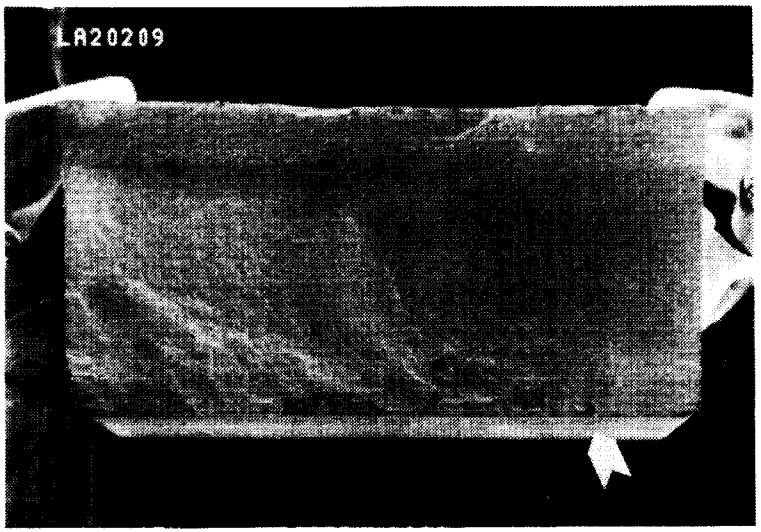

a. VIEW 1

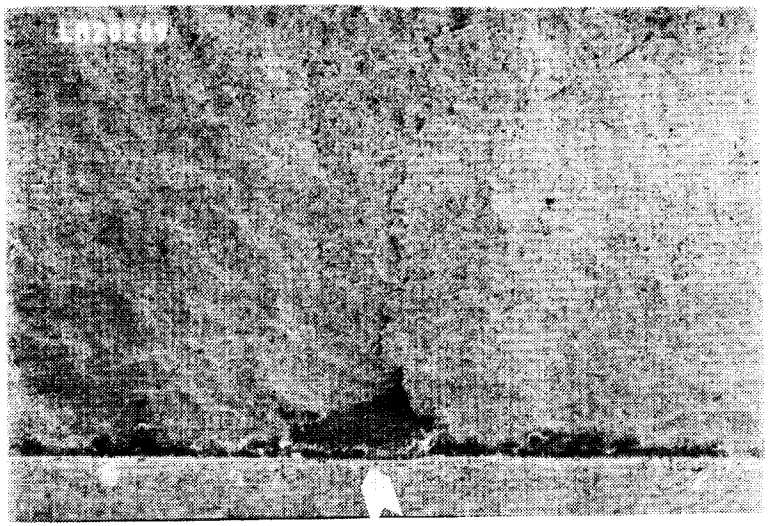

b. VIEW 2

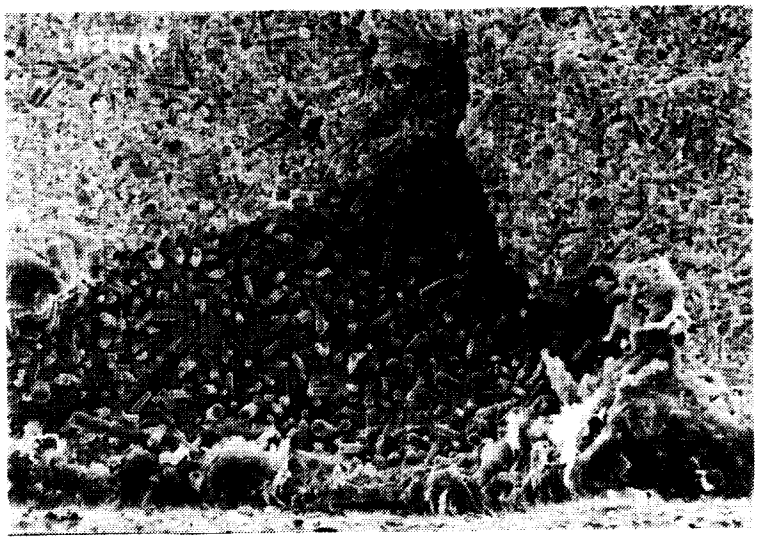

c. VIEW 3

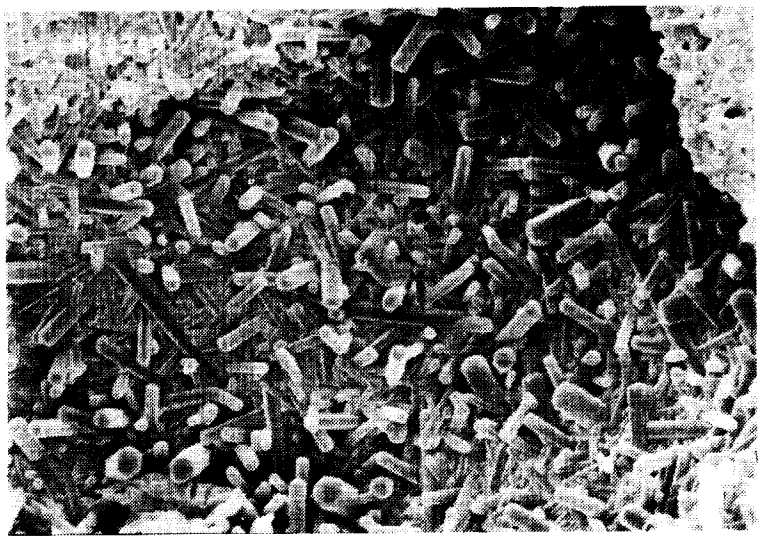

d. VIEW 4

K-10987

Figure 52.--Void in Specimen 3331, Condition "ab"--MOR = 502.3 MPa (72.9 ksi); ρ = 3.07 g/cc (Room Temperature).

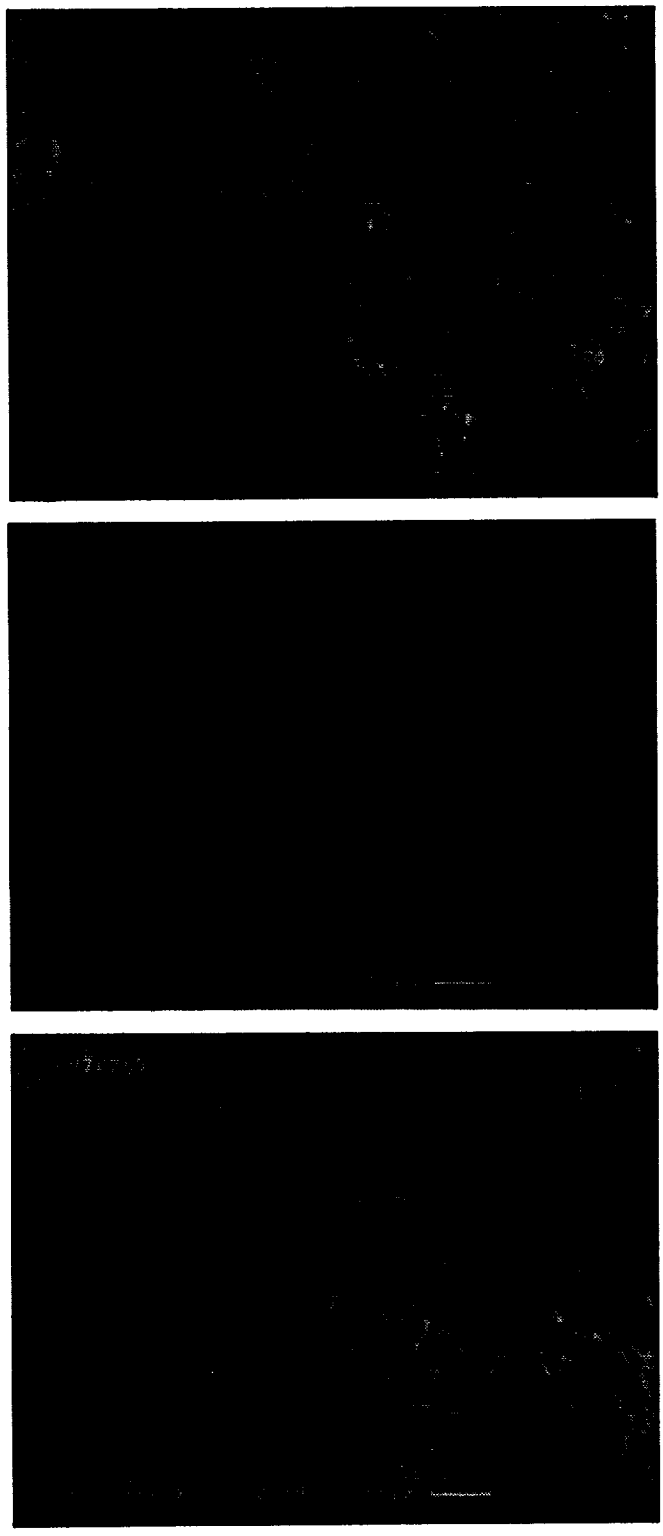

Figure 53.--Fracture Surfaces of Specimens from "ab," "ae," and "be" Conditions.

TABLE 23.--1232°C (2250°F) MOR OF MATRIX II-2 BARS

Process Treatment Condition	Average Flexural Strength, MPa (ksi)
1	--
ab	403.4 (58.5)
ac	379.9 (55.1)
abcc	393.0 (57.0)
be	379.2 (55.0)
bc	386.1 (56.0)
ae	413.7 (60.0)
ad	331.0 (48.0)
ce	380.6 (55.2)
abcd	379.2 (55.0)
abde	358.5 (52.0)
1	337.9 (49.0)
de	393.0 (57.0)
acde	355.1 (51.5)
bcde	358.5 (52.0)
bd	355.1 (51.5)
cd	348.2 (50.5)

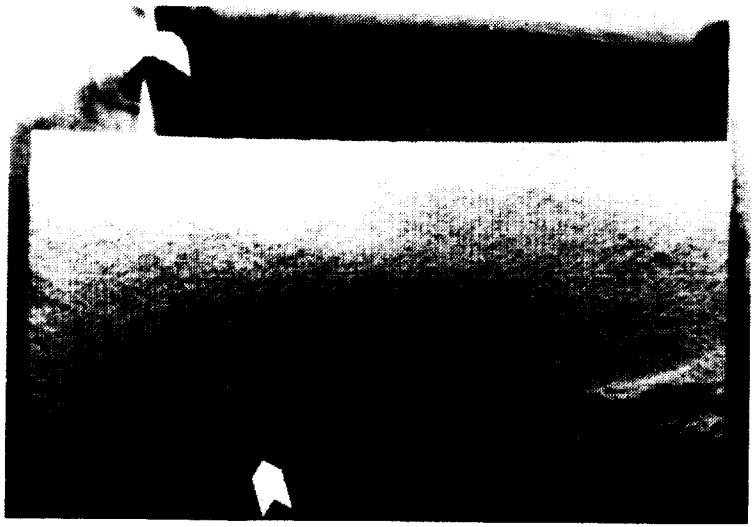

a. VIEW 1

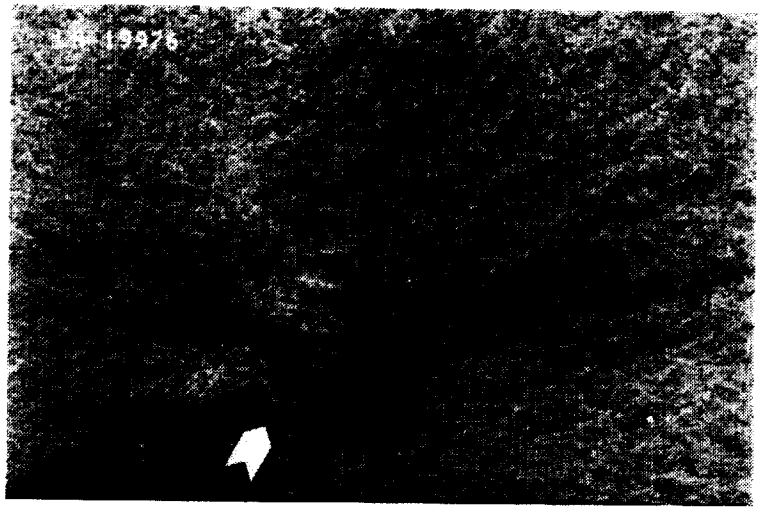

b. VIEW 2

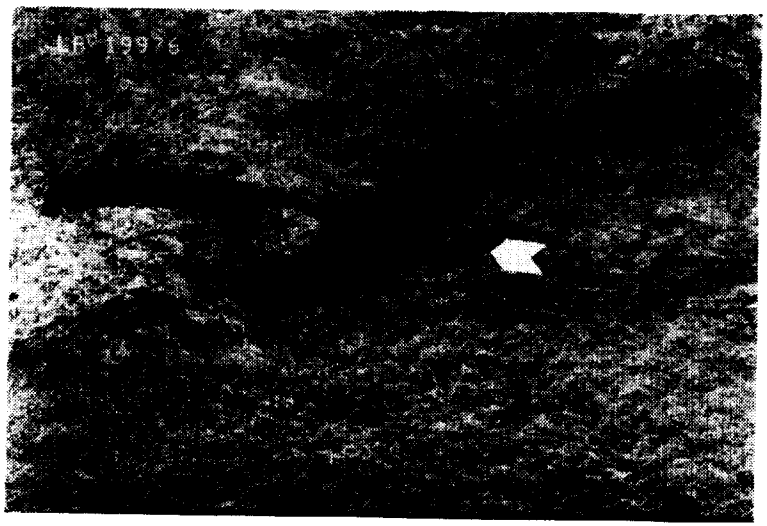

c. VIEW 3

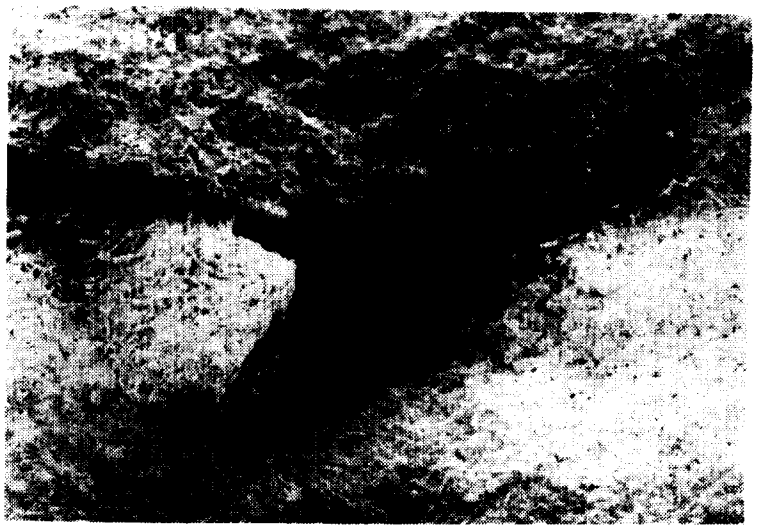

d. VIEW 4 K-10989

Figure 54.--Void in Specimen 3352, Condition "ab"--MOR = 423.7 MPa (61.5 ksi); Density Not Measured, Tested at 1232°C (2250°F).

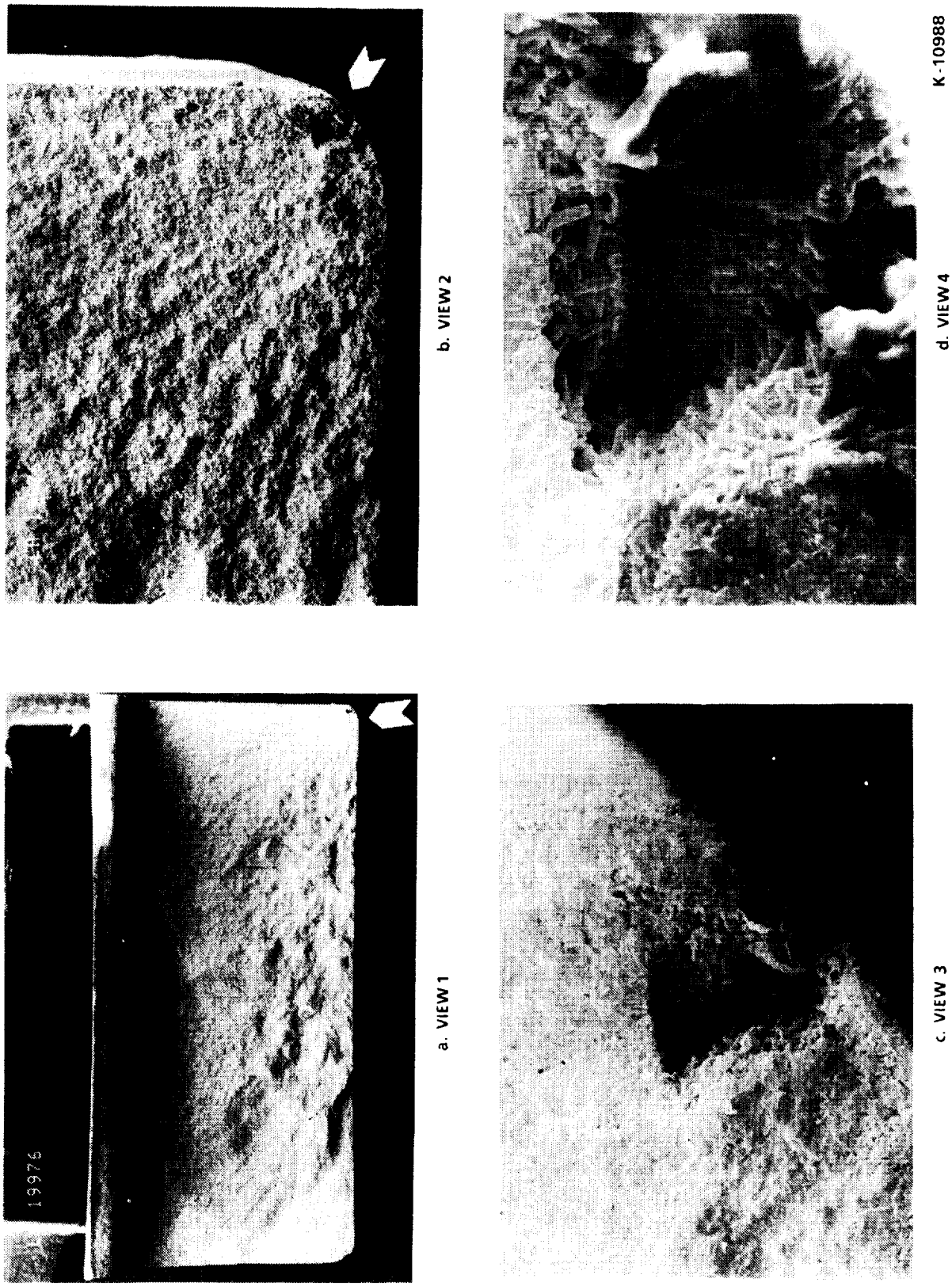

Figure 55.--Void at Chamfer Corner of Specimen 3604--MOR = 519.4 MPa (75.8 ksi); Density = 3.22 g/cc (Room Temperature).

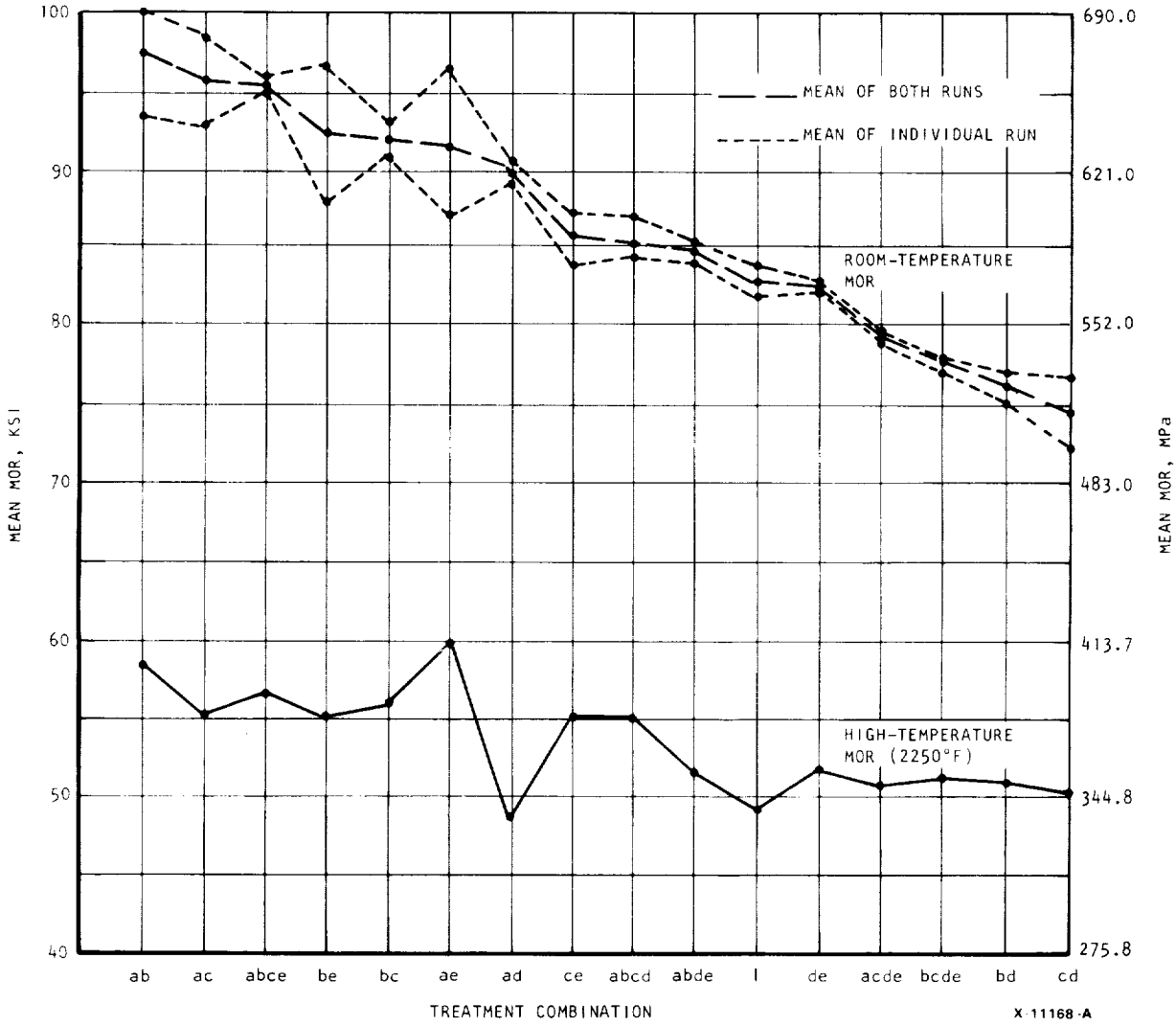

Figure 56.--Comparison of Mean MOR Between Runs.

The analysis of variance was used to determine the factors of multifactor interactions that affected the MOR values. The processing factors that have statistically significant effects (at 95 percent confidence level) were A (sinter/HIP cycle), B (powder bed), and D (sintering aid), and the two-factor interactions B*C, B*D, and C*D. The factor E, binder content, is the only insignificant factor in the determination of MOR. The significant factors and two-factor interactions and their corresponding probabilities are listed in table 24. The change in MOR between different levels of the processing factors and two-factor interactions are listed in tables 25 through 28.

In view of the fractographic analysis results concerning the dark inclusions that reduce the MOR, statistical analysis was repeated after eliminating test data of specimens that failed from these inclusions. Overall, the previous statistical analysis results remain the same. The change in average MOR and Weibull slope is negligible except for conditions "cd" and "acde." The MOR and Weibull slope is also presented in figure 57. For condition "cd," there was an increase of 64.1 MPa (9.3 ksi) in average MOR and 6.7 in Weibull slope after eliminating the specimens that failed from inclusions. For condition "acde," the increase was 10.7 ksi and 6.3 in Weibull slope. Both conditions include the 6+1 additive composition and extrusion.

The effect of sintering run variations is documented in table 29. Thirty-three specimens were tested in the A- and A+ conditions. However, the effect of sintering time is confounded by the effect of sinter/HIP runs. It is impossible to separate the effect of sintering time from the effect due to the differences between runs. At each treatment condition, the mean and standard deviations were calculated for each run. For every treatment combination, the mean MOR of each run and the mean of both runs are plotted in figure 58 to show the variation between runs. The difference between runs was then computed and a t-test was used for testing the significance of the difference at 0.05 level (see table 30). Test results showed that under two treatment conditions (ab and ae), the differences in MOR between runs was significant. The differences range from 48.3 to 65.2 MPa (7.00 to 9.45 ksi). No consistent pattern of the MOR difference can be found for run 25 and run 26. However, for run 30 and run 32, a pattern was found. In general, bars sintered in run 32 have higher MOR values than bars sintered in run 30.

Further analysis was undertaken to check the validity of the best processing condition, including both 6+2 and 6+1 compositions. Four data sets were formed by combining data from different runs. The first data set consisted of data of run 25 and run 30, the second data set of run 26 and run 32, the third set of run 26 and run 30, and the fourth data set of run 26 and run 32. For each data set, the significant factors on the determination of MOR were identified and the results are summarized in table 31, along with results from previous analyses in which data of all four runs were used. Common significant factors for all analyses are factor A, sinter/HIP cycles, and factor D, sintering aids.

Table 32 shows the mean MOR of each factor at both the "+" and "-" levels for each analysis from all four data sets. These mean values are also presented in figure 59 to show the importance of factors on MOR, based on the statistical

TABLE 24.--SIGNIFICANT FACTORS/INTERACTIONS AND CORRESPONDING PROBABILITY FOR ROOM TEMPERATURE MOR

Significant Factor/Interaction	Probability
A	0.0001*
B	0.0206
D	0.0001
B*C	0.0003
B*D	0.0044
C*D	0.0085

*Significant at 95 percent confidence level, if probability is less than 0.05.

TABLE 25.--SUMMARY OF ROOM TEMPERATURE MOR CHANGE AT DIFFERENT LEVELS

Condition	Level	MOR, MPa (ksi)
Sinter/HIP	A+	620.6 (90.0)
	A-	573.7 (83.2)
Powder bed	B+	604.7 (87.7)
	B-	588.1 (85.3)
Extrusion	C+	590.9 (85.7)
	C-	601.9 (87.3)
Sintering aid	D+	560.6 (81.3)
	D-	632.3 (91.7)
Binder content	E+	567.5 (82.3)
	E-	597.8 (86.7)

TABLE 26.--EFFECT OF B*C ON MOR, MPa (ksi)

	MOR, MPa (ksi)	
	(B+) PB2	(B-) No PB
(C+) Extruded	604.7 (87.7)	578.5 (83.9)
(C-) Not Extruded	604.0 (87.6)	598.5 (86.8)

TABLE 27.--EFFECT OF B*D ON MOR

	MOR, MPa (ksi)	
	(D+) 6% + 1%	(D-) 6% + 2%
(B+) PB2	558.5 (81.0)	650.2 (94.3)
(B-) No PB	562.6 (81.6)	614.3 (89.1)

TABLE 28.--EFFECT OF C*D ON MOR

	MOR, MPa (ksi)	
	(C+) Extruded	(C-) Not extruded
(D+) 6%, 1%	546.1 (79.2)	575.0 (83.4)
(D-) 6%, 2%	636.4 (92.3)	628.1 (91.1)

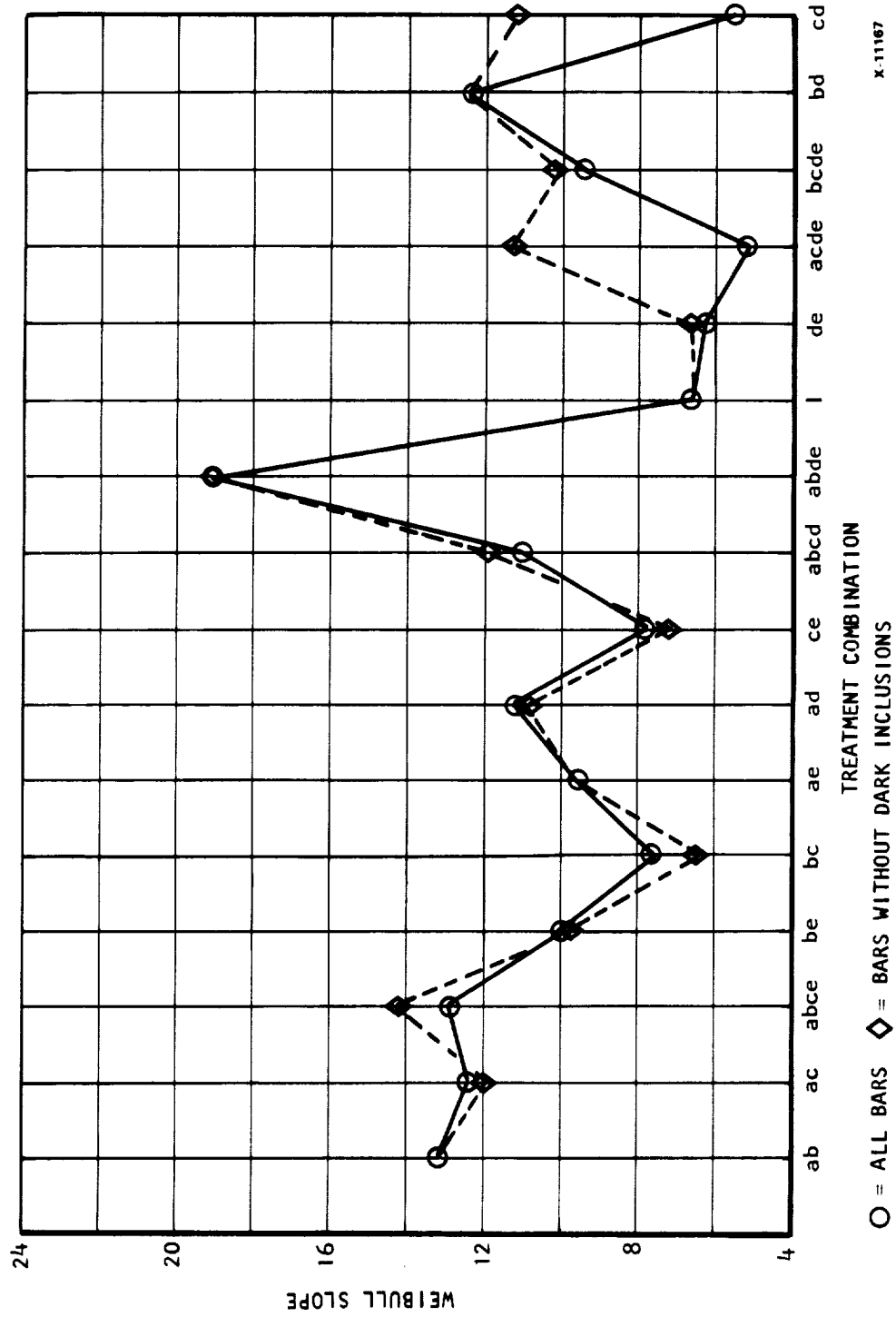

Figure 57.--Comparison of Weibull Slopes.

TABLE 29.--MATRIX II-2 SINTER/HIP RUN VARIATION VS PROCESS CONDITIONS (BY MOR VALUE)

Cycle			A-				A+			
Sinter/HIP Run No.			25		26		30		32	
Presinter T, °C			1750		1750		1750		1830	
Sinter T_{max}, °C			1950		1950		1950		1950	
Time at T_{max}			1.11x*		x		2.22x		2.44x	
Percent additional load mass in furnace			50%		--		--		60%	
Powder Bed			B-	B+	B-	B+	B-	B+	B-	B+
D-	6+2 Non-extruded MOR, ksi	C-	1 82	be 97	1 84	be 88	ae 87	ab 95	ae 96	ab 100
	6+2 Extruded MOR, ksi	C+	ce 84	bc 93	ce 87	bc 91	ac 93	abce 95	ac 98	abce 96
D+	6+2 Non-extruded MOR, ksi	C-	de 83	bd 77	de 83	bd 76	ad 88	abde 84	ad 90	abde 86
	6+2 Extruded MOR, ksi	C+	cd 73	bcde 78	cd 77	bcde 78	acde 79	abcd 86	acde 79	abcd 84

*x is time at T_{max} for run 2, two hours.

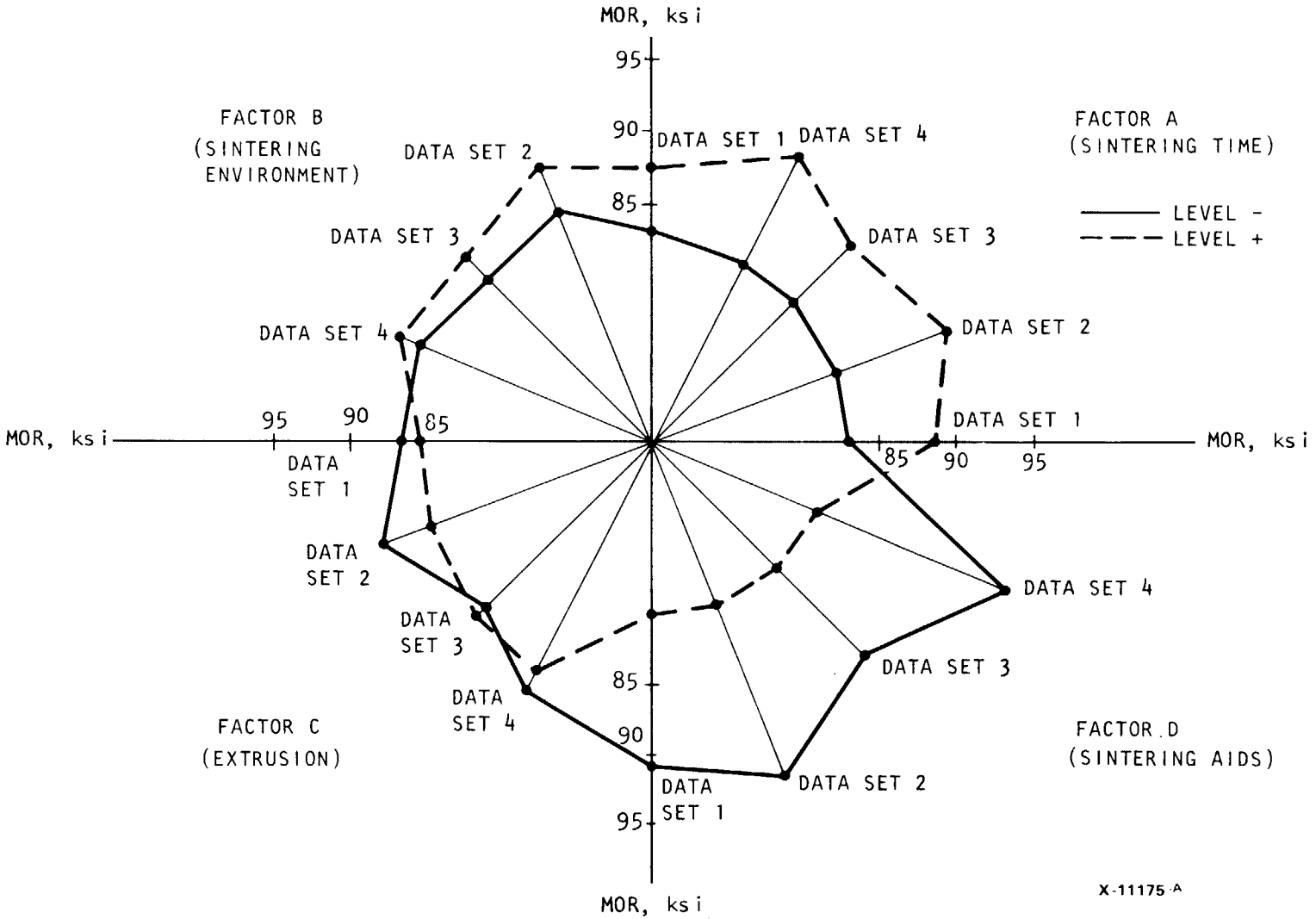

Figure 58.--Matrix II-2 Denka 9FW Comparison of Low-Level vs High-Level Treatment.

TABLE 30.--MATRIX II-2 DENKA 9FW STUDY OF THE SINTER/HIP RUN EFFECT ROOM-TEMPERATURE MOR DATA (RUN 30 VS RUN 32)

Treatment Combination	MOR, MPa (ksi)				
	Mean		Std. Dev.		
	Run 30	Run 32	Run 30	Run 32	D
ae	597.7 (87.0)	664.2 (96.4)	76.5 (11.1)	48.3 (7.0)	65.5 (9.5*)
ad	610.1 (88.8)	621.2 (90.1)	72.4 (10.5)	40.7 (5.9)	9.0 (1.3)
ac	639.6 (93.1)	677.8 (98.3)	54.5 (7.9)	63.4 (9.2)	35.2 (5.1)
acde	544.8 (79.3)	544.0 (78.9)	127.6 (18.5)	104.1 (15.1)	-0.69 (-0.1)
ab	645.1 (93.9)	695.7 (100.9)	63.4 (9.2)	42.1 (6.1)	48.3 (7.0*)
abde	579.8 (84.4)	589.5 (85.5)	39.3 (5.7)	31.0 (4.5)	7.6 (1.1)
abce	655.7 (95.1)	660.5 (95.8)	65.5 (9.5)	51.7 (7.5)	4.8 (0.7)
abcd	595.7 (86.4)	578.5 (83.9)	53.8 (7.8)	66.9 (9.7)	-17.2 (-2.5)

D = mean MOR (run 32) - mean MOR (run 30)

*An asterisk indicates the difference in mean MOR between runs is significant at $\alpha = 0.05$.

TABLE 31.--MATRIX II-2 DENKA 9FW--SUMMARY OF ANALYSIS OF VARIANCES AND SIGNIFICANT FACTORS FOUND IN EACH ANALYSIS

Data Source	Significant Factors						
Runs 25 and 30	A	B		D	A*E[1]	B*D	C*D
Runs 25 and 32	A	B	C	D	A*E	B*D	C*E
Runs 26 and 30	A			D	A*E		C*D
Runs 26 and 32	A			D	A*E		C*D
Runs 25, 26, 30, and 32	A	B		D	B*C	B*D	C*D
Common factors for all sets	A, D, A*E						

Note: 1. A*E = B*C*D

TABLE 32.--TASK II-2 DENKA 9FW--SUMMARY TABLE OF MEAN MOR FOR "+" AND "-" LEVEL OF EACH FACTOR

Factor	Mean MOR, MPa (ksi)			
	Data Set 1 Runs 25, 30	Data Set 2 Runs 25, 32	Data Set 3 Runs 26, 30	Data Set 4 Runs 26, 32
A-	574.4 (83.3)	574.4 (83.3)	572.3 (83.0)	572.3 (83.0)
A+	609.5 (88.4)	628.8 (91.2)	609.5 (88.4)	628.8 (91.2)
B-	577.8 (83.8)	590.9 (85.7)	585.4 (84.9)	599.2 (86.9)
B+	605.4 (87.8)	611.6 (88.7)	596.4 (86.5)	603.3 (87.5)
C-	596.4 (86.5)	613.7 (89.0)	588.8 (85.4)	606.8 (88.0)
C+	587.5 (85.2)	589.5 (85.5)	593.0 (86.0)	595.7 (86.4)
D-	624.7 (90.6)	644.0 (93.4)	619.9 (89.9)	639.2 (92.7)
D+	559.2 (81.1)	559.2 (81.1)	561.9 (81.5)	561.9 (81.5)
E-	591.6 (85.8)	601.2 (87.2)	593.7 (86.1)	604.0 (87.6)
E+	591.6 (85.8)	601.2 (87.2)	588.1 (85.3)	597.8 (86.7)

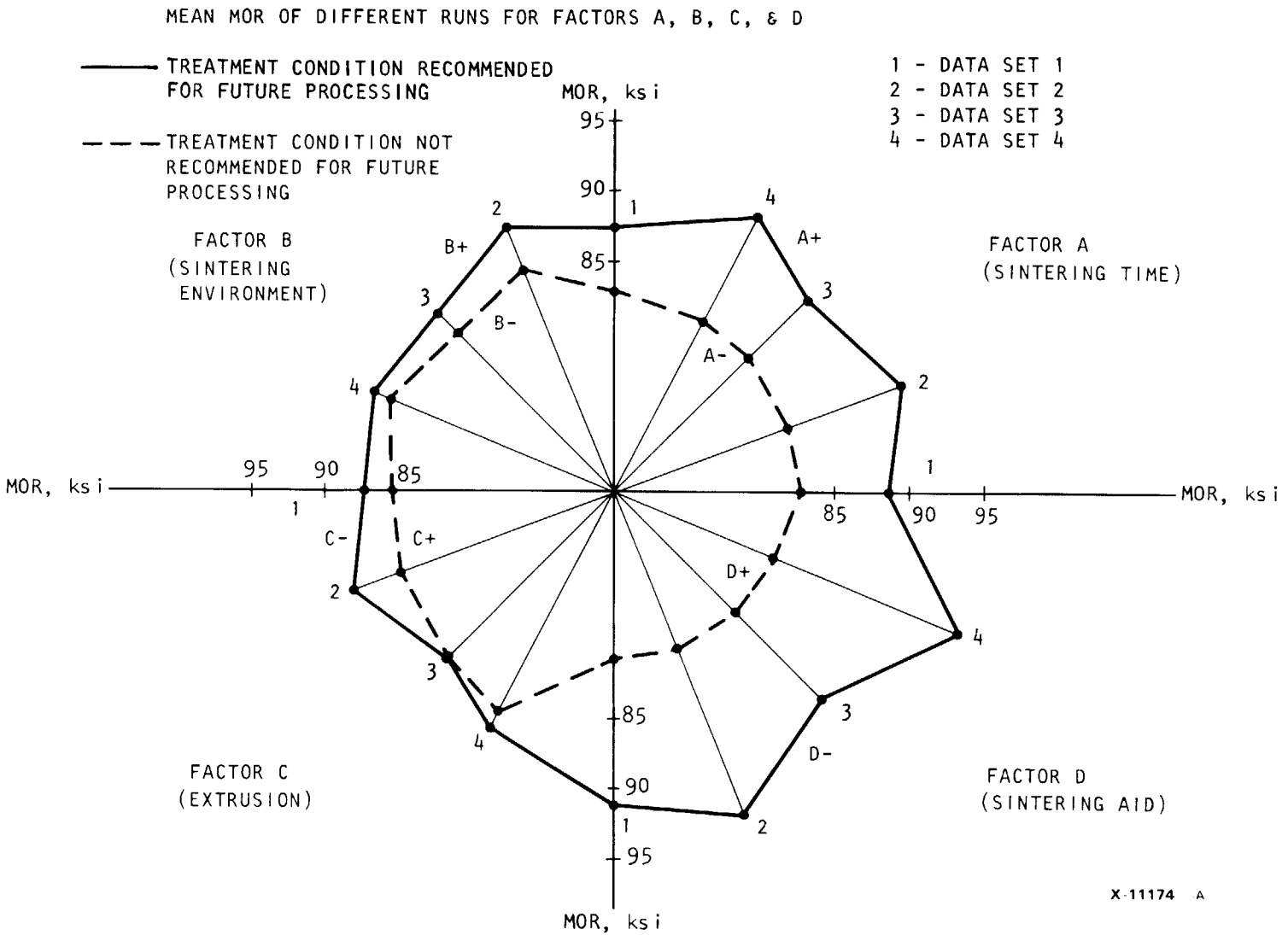

Figure 59.--Matrix II-2 Denka 9FW--Comparison of Recommended Processing Condition vs Not Recommended Ones; Mean MOR of Different Runs for Factors A, B, C, and D.

results. For each factor, four sets of points are plotted. Each pair of points represent the mean MOR obtained from a set of data; one point represents the "+" level, the other point represents the "-" level. The distance between the "+" level and the "-" level of every pair of points represents the effect of a factor when its level is changing from one to the other. The distances between the "+" and the "-" level for factors A and D are larger than for factors B and C, indicating that factors A and D are more important. A pattern is also noticed: the combination of A+, B+, C-, and D- (ab treatment) results in a higher MOR than the combination of A-, B-, C+, and D+ (figure 59).

2.2.6 Reproducibility of the Improved Baseline Material

In view of the near program goal combination of MOR and Weibull slope of the material fabricated by "ab", material/process combination (treatment), a decision was made to evaluate the reproducibility of the properties using the "same" raw materials and processing procedures. The raw Si_3N_4 powder was to be the same grade from the same manufacturer but a different lot than the one used to fabricate the original "ab" test bars. In addition, it was decided to also evaluate the effects of and the interactions between different processing day, separate sinter/HIP run, and injection molder type, when the raw material used was from the same lot. A factorial matrix experiment was designed for this evaluation. The results were to be considered as reproducible if the average room temperature MOR's are between 641.2 and 696.4 MPa (93 and 101 ksi) and the densities are between 3.10 and 3.26 g/cc.

(1) Statistical Experimental Design and Experimental Procedures.--A 2^3 full fractional experiment was designed to use processing identical to that of the "ab" treatment with variations such as separate powder processing days, Battenfeld versus Arburg injection molder, and identical but separate sinter/HIP cycles. Table 33 shows the factorial design used for this reproducibility study. It has a total of eight processing combinations denoted by ghi, gi, ..., etc. as shown in table 33.

TABLE 33--FACTORIAL DESIGN FOR REPRODUCIBILITY STUDY

Process Day	Sintering Run	Injection Molder	
		I+	I-
G+	H+	ghi	gh
	H-	gi	g
G-	H+	hi	h
	H-	i	1

G = Material processing day - First processing day (G+)
Second processing day (G-)

H = Sintering run - First run (H+)
Second run (H-)

I = Injection molder - Arburg (I+)
Battenfeld (I-)

The two processing days (G+ and G-) represent two separate batches of material. The material composition (92% Si_3N_4, Denka 9FW, 6% Y_2O_3 and 2% Al_2O_3) was the same as the "ab" composition except that the Si_3N_4 was from a different lot of Denka 9FW. The main difference between the lot of Si_3N_4 used for the original "ab" and the one used in this study is PSD. Figure 60 compares the PSD's of these two lots.

Milling, mixing, and pelletizing were performed identically to the "ab" material/process. Each batch of the pelletized mix (processed on G+ or G- day) were subsequently injection molded using two different molders, Arburg (I+) and Battenfeld (I-). The injection molding portion of the original "ab" material/process used the Arburg molder. However, transferring the same setting parameters to the Battenfeld was unsatisfactory due to major differences in molder design and capacity. A set of modified injection molding parameters was developed for the Battenfeld, which produced test bars comparable to those injected on the Arburg based on visual and X-ray inspections.

Subsequent to the completion of Matrix II-1 and Matrix II-2, the sinter/HIP furnace was determined to be incapable of prolonged use at temperatures higher than 1900°C (3452°F). In order to preserve the furnace life for the remainder of this program, it was decided to limit the peak temperature for any future sinter/HIP run to 1900°C (3452°F). Consequently, the sinter/HIP cycle peak temperature for this experiment was reduced to 1900°C, although 1950°C (3542°F) was the peak temperature used for "ab." To compensate for the lower temperature, a longer holding time (6 hours vs 4 hours) was used. Density results of several test runs showed that test bars sinter/HIP'ed by this modified cycle produced densities in the range of 3.10 to 3.26 g/cc, which was considered acceptable for the reproducibility experiment.

Other than the above-mentioned modifications, all other experimental procedures were identical to the original "ab" within experimental errors.

(2) Characterization Results and Discussion.--The test bar average density, MOR, and Weibull slope results are summarized in table 34. Consistent with the sinter/HIP test runs mentioned earlier, the average density of the eight groups ranged from 3.241 to 3.26 g/cc, exceeding the target of 3.18 g/cc. In fact, all of the specimens had densities higher than 3.20 g/cc, at between 3.23 and 3.28 g/cc. The

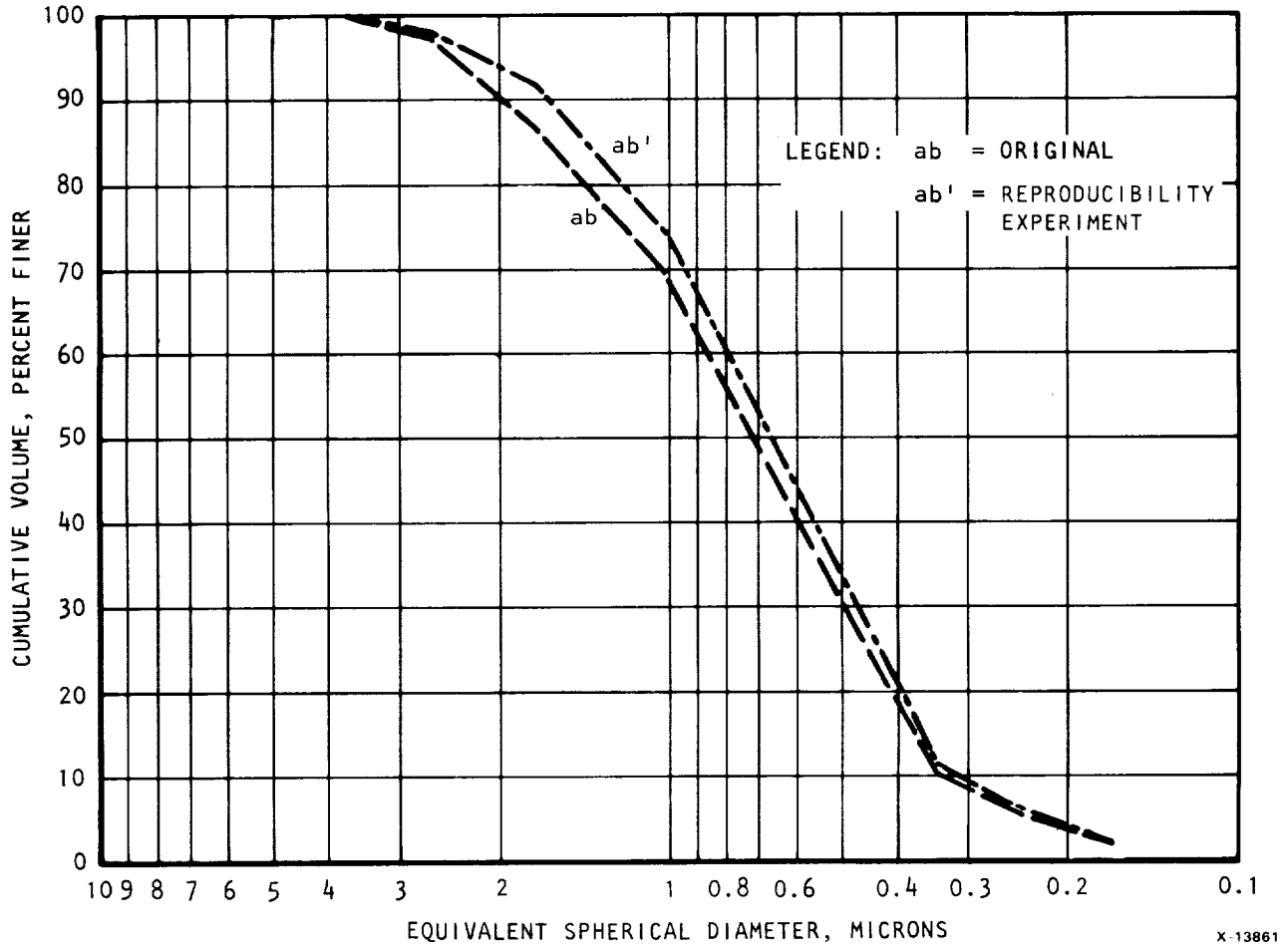

Figure 60.--Particle Size Distributions of Two Lots of As-Received Denka 9FW Si_3N_4.

TABLE 34--MOR AND WEIBULL SLOPE

Processing Day	Molder	Sinter/ HIP Run	Mean MOR, MPa (ksi)	Weibull Slope	Characteristic MOR, MPa (ksi)	Average Density, g/cc
1 (G+)	Arburg (I+)	(H-)	614.6 (89.2)	7.24	655.9 (95.2)	3.26
1 (G+)	Arburg (I+)	(H-)	605.6 (87.9)	10.24	635.9 (92.3)	3.26
2 (G-)	Arburg (I+)	(H+)	623.5 (90.5)	10.61	653.9 (94.9)	3.26
2 (G-)	Arburg (I+)	(H-)	634.6 (92.1)	10.57	665.6 (96.6)	3.26
1 (G+)	Battenfeld (H+)	(H+)	539.5 (78.3)	5.17	613.9 (89.1)	3.24
1 (G+)	Battenfeld (H-)	(H-)	611.1 (88.7)	5.44	662.1 (96.1)	3.26
2 (G-)	Battenfeld (I-)	(H+)	638.0 (92.6)	6.42	684.9 (99.4)	3.26
2 (G-)	Battenfeld (I-)	(H-)	622.2 (90.3)	5.86	671.8 (97.5)	3.26

higher density is a desirable property although it exceeded the value desired to establish reproducibility. The average strengths of the specimens were lower than the target range. Figure 61 compares the average MOR of each group with the MOR required to establish reproducibility. Only two processing groups produced specimens with average MOR close to the requirements.

The requirements for Weibull slope was not formally stated for this experiment, but a value close to or higher than the value of 13.6 obtained with the "ab" processing condition was desired. The Weibull results listed in table 34, which are also plotted in figure 62, show that specimens injection-molded in the Arburg molder generally have higher Weibull slopes, but the best Weibull slope obtained (10.6) is still 20 percent less than the slope of the original "ab" condition.

The optical fractography results of the specimens showed that, with both molders, lower strength (less than 90 ksi) specimens generally failed from voids and agglomerates. Distinct differences in fracture characteristics were also observed between specimens injection molded in the Arburg and the Battenfeld. The average MOR of the specimens that failed from different fracture types or locations are listed in table 35 and plotted in figure 63. Table 35 shows that the Battenfeld produced significantly more specimens with failures originated from the chamfer corner and from agglomerates than the Arburg.

STEM characterization was performed on test bars fabricated by different routes, including one of the original Matrix II-2 test bars.

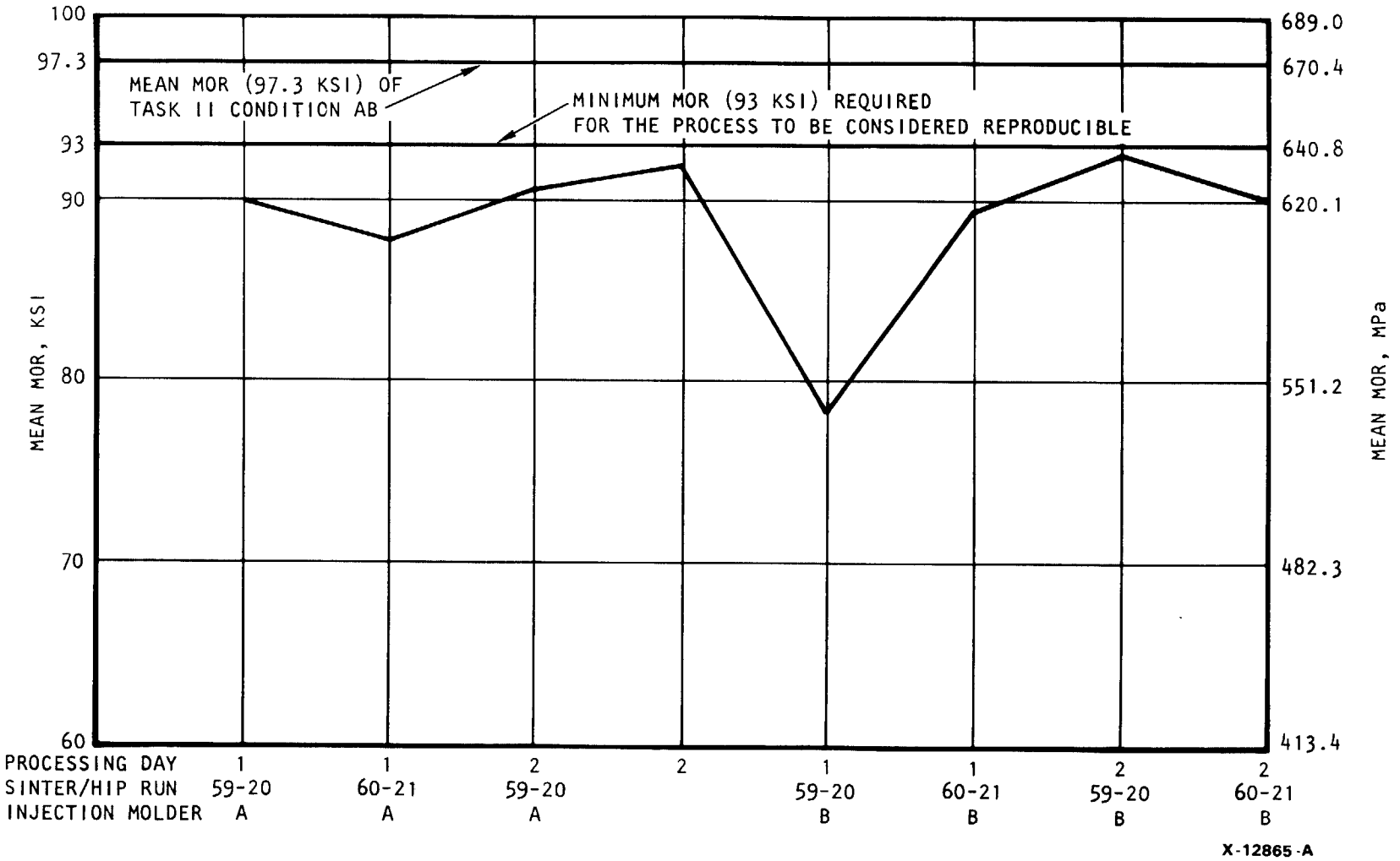

Figure 61.--Comparison of Mean MOR of "ab" Condition with Reproducibility Experiments.

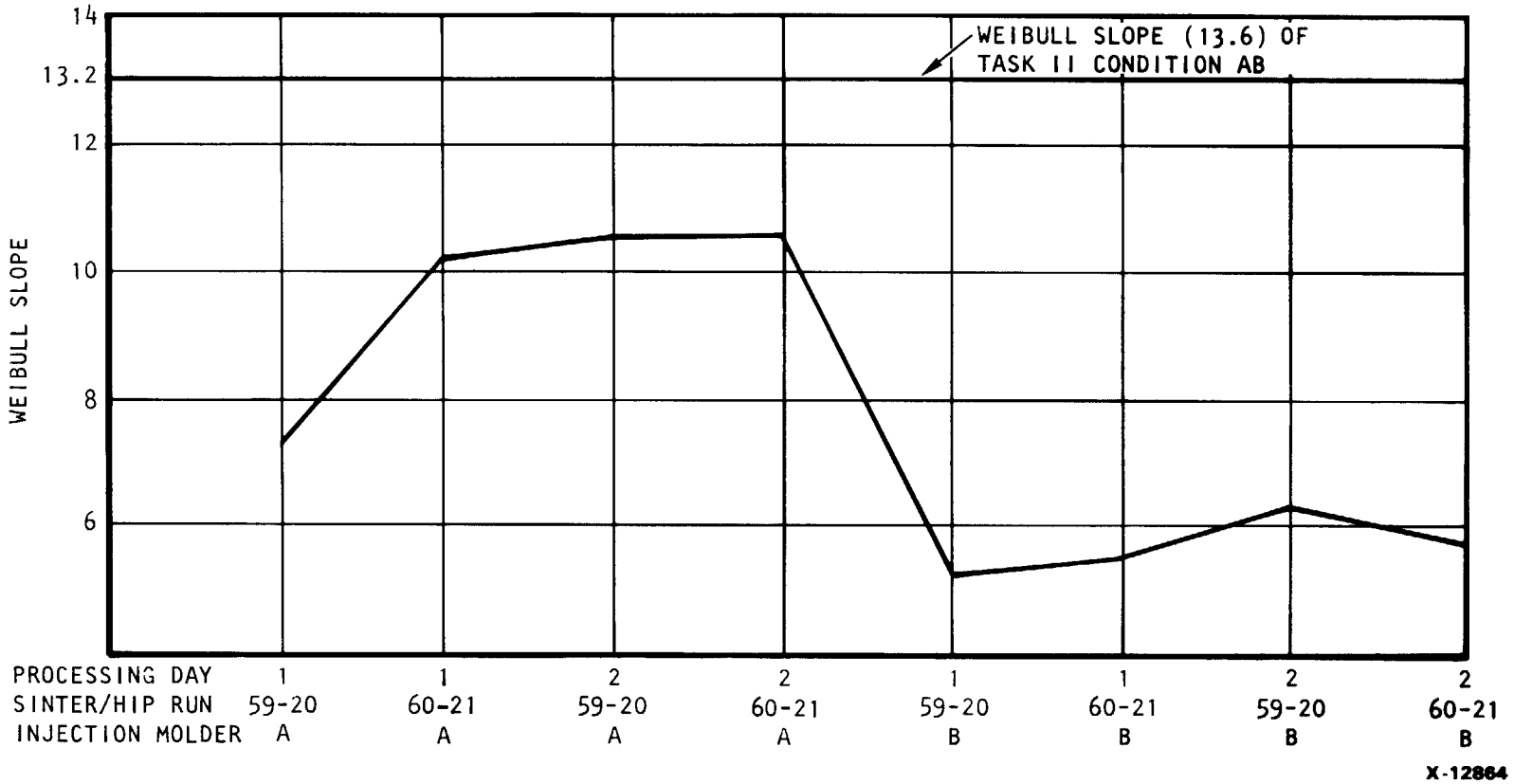

Figure 62.--Comparison of Weibull Slopes of "ab" Condition with Reproducibility Experiments.

TABLE 35.--COMPARISON OF SPECIMENS WITH DIFFERENT FRACTURE ORIGINS

Fracture Origins	Specimens from Arburg		Specimens from Battenfeld	
	Mean MOR, MPa (ksi)	Number	Mean MOR, MPa (ksi)	Number
Tensile face	631.1 (91.6)	76	679.4 (98.6)	33
Chamfer corner	593.9 (86.2)	13	627.7 (91.1)	35
Agglomerates	540.2 (78.4)	3	499.5 (72.5)	18
Voids	568.4 (82.5)	6	450.6 (65.4)	8
Others	632.5 (91.8)	3	581.5 (84.4)	7
(Total specimens)	620.1 (90.0)	101	604.3 (87.7)	101

The detail results are presented in Appendix C. In general, the original Matrix II-2 test bar had larger grains (average grain size was 1.39 microns) with higher aspect ratio (2.09 ±1.62).

Among the eight groups of processing conditions, the results of the four groups injection molded on Arburg were closer to the target MOR (641.2 MPa (93.0 ksi)) and Weibull slope (13.6) than those on Battenfeld. Furthermore, the scatter in average MOR within the Arburg group is narrower (29.0 MPa (4.2 ksi) or 4.6 percent) than that of Battenfeld (98.6 MPa (14.3 ksi) or 16.3 percent).
The results of the reproducibility experiment showed that in the case of the Arburg molder, good material/process reproducibility can be achieved using the same lot of Si_3N_4, processed on separate days (batches) and sinter/HIP'ed in separate runs. The reasons that the original "ab" results were not reproduced were most likely due to the difference in Si_3N_4 PSD (lot-to-lot variation) and the sinter/HIP cycle modification required by furnace limitation. Although the modified sinter/HIP cycle produced higher density, it may have resulted in microstructural differences which, in turn, affected the strength. The reason the Battenfeld molder produced more test bars containing defects, exhibiting lower strength and larger scatter, was possibly due to the molder not optimized for molding test bars.

A detailed statistical analysis was conducted to evaluate the effects of process day, sinter/HIP run and molder type effect on flexural strength (Appendix B). The results are summarized as follows:

(a) Effect of Day, Run, and Molder on Flexural Strength.--The analysis using specimen MOR data from both injection molders showed a statistically significant interaction between day, run,

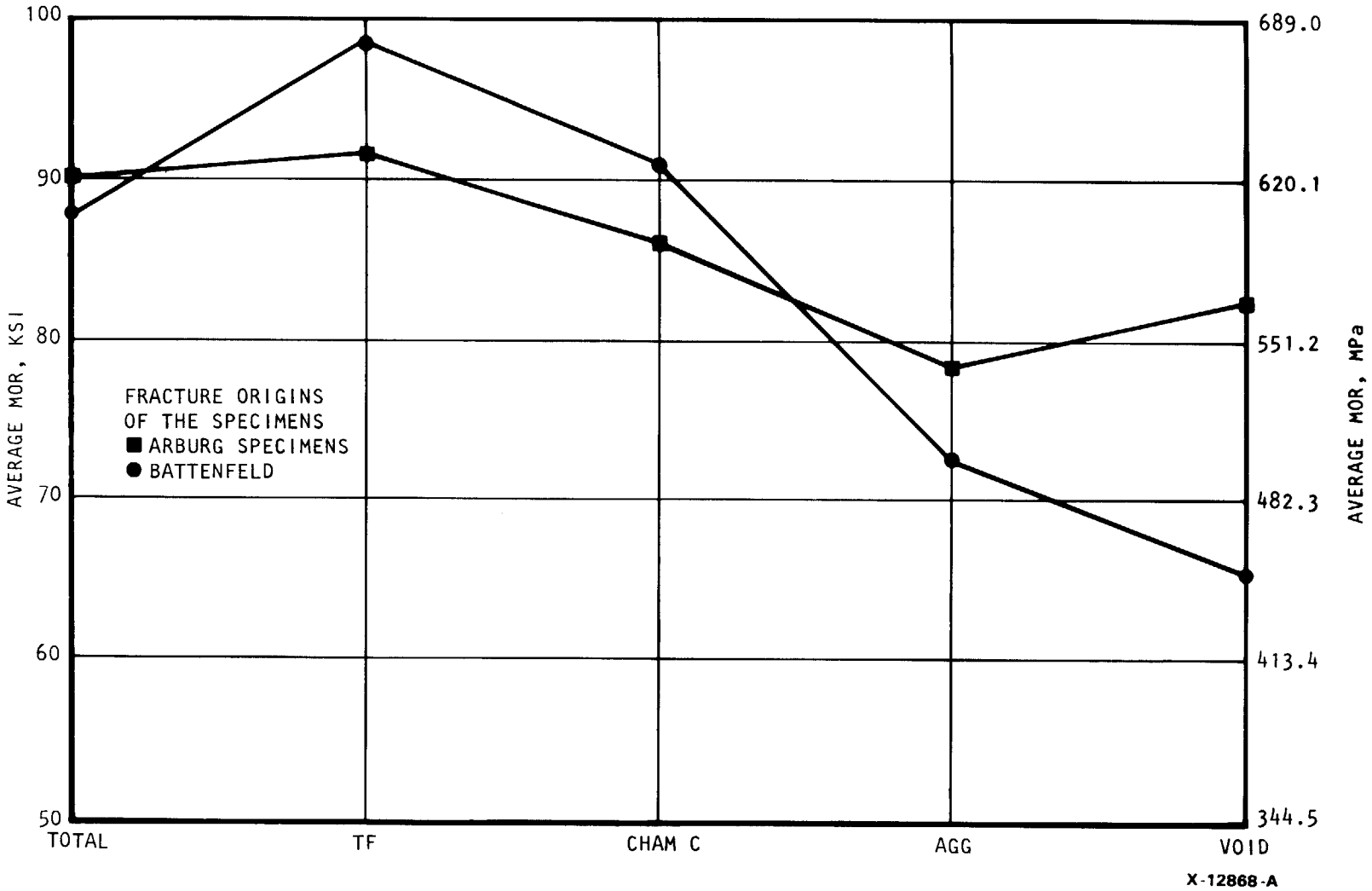

Figure 63.--MOR Comparison of Fracture Origins: Voids and Agglomerates Gave the Lowest MOR.

and molder, and between day and molder at the 90-percent confidence level. Due to the significant effects of the different injection molders, the data for each molder were analyzed separately so that the effect of day and run could be explored.

(1) Specimens Injected by Arburg Molder.--The small difference in MOR, 20.7 to 27.6 MPa (3 to 4 ksi), indicated that the process based on the Arburg injection molder was reproducible.

(2) Specimens Injected by Battenfeld Molder.--Statistical analysis showed that Battenfeld injection molder produced test bars that varied between runs, and between the combination of day and run.

(b) Effect of Sinter/HIP Layer on Flexure Strength.--During sinter/HIP, the specimens were placed on five separate layers inside a crucible in the furnace. The specimens sintered on layers 2 and 3 showed higher strength than the specimens sintered on layers 4 and 5.

The differences in MOR's were suspected to be caused by the potential differences in sinter/HIP temperature or atmosphere between layers.

(c) Effect of Test Bar Location on Flexure Strength.--The location of the test bars on each layer during sinter/HIP had no significant effect on flexure strength at 90-percent confidence for all layers.

(d) Correlation Between MOR and Density.--Within the range of high density achieved, no correlation was found between density and MOR for the test specimens. The correlation coefficients are small, with an absolute value of 0.36 or less (perfect correlation coefficient -1).

2.3 DEVELOPMENT OF HIGH-TEMPERATURE MATERIAL*

2.3.1 Summary/Introduction

The need for improved high-temperature property material for advanced gas turbine engines prompted Allied-Signal Aerospace Company to develop a new Si_3N_4 with an average flexure strength of 586.1 MPa (85 ksi) or more at 1399°C (2550°F). Two approaches were taken to achieve the goal: (1) reduce the amount of sintering aids in the baseline Y_2O_3 + Al_2O_3 system and (2) screen for alternate sintering aids.

The Y_2O_3 + Al_2O_3 system was selected because of Allied-Signal Aerospace Company's previous experience with the Code 1 (8 wt% Y_2O_3 + 4 wt% Al_2O_3) and Code 2 (6 wt% Y_2O_3 + 2 wt% Al_2O_3) materials. New compositions developed could be easily transferred to the existing fabrication process. Even though these two materials do not have the required high-temperature properties, they do show a trend of increasing high-temperature properties with decreasing sintering aid content.

A statistically designed experiment was used to evaluate the effect of composition/strength relationships in this system at room temperature, 1232°C (2250°F), and 1399°C (2550°F). A mathematical model was generated to produce a contour plot that describes the variation of flexure strength as a function of composition at each temperature. The contour plot identifies the optimum composition and shows trends that help in selecting compositions for future material development.

An experiment to screen various sintering aid systems for improved high temperature strength was performed simultaneously. The investigation revealed a material, GN-10 (90 wt% Si_3N_4 + 8 wt% Y_2O_3 + 2 wt% SrO composition), with excellent strengths of 890.1 MPa (129.1 ksi) at room temperature, 706.7 MPa (102.5 ksi) at 1232°C (2250°F), and 581.3 MPa (84.3 ksi) at 1399°C (2550°F). A follow-up optimization experiment using the modeling technique developed for the Y_2O_3 + Al_2O_3 system produced a new material with even higher strength (620.6 MPa (90 ksi)) at 1399°C (2550°F).

2.3.2 Y_2O_3 + Al_2O_3 Sintering Aid Optimization

A statistical optimization study of the Si_3N_4 + Y_2O_3 + Al_2O_3 system was performed to provide a better understanding of the strength/composition relationships at three temperatures.

Six cylindrical billets with different Y_2O_3 + Al_2O_3 + Si_3N_4 compositions, other than the baseline, were fabricated. Their Y_2O_3 content ranged from 4 to 6 wt% and the Al_2O_3 content ranged from 0 to 2 wt%. The billets were CIP'ed and then encapsulated HIP'ed in niobium cans. This fabrication route was adopted to reduce process variations and to maximize the chance of achieving full density. A HIP cycle with a maximum HIP'ing condition of 2 hours at 1900°C (3452°F) and

*Performed under revised Task II of the contract.

206.9 MPa (30 ksi) N_2 was used. All six billets achieved theoretical density. Standard 0.125 by 0.250 by 2.0 inch test bars were machined from the billets. Strength of the test bars was measured at room temperature, 1232°C (2250°F), and 1399°C (2550°F) in four-point flexure. (See Appendix D for compositions and strengths.)

Statistical modeling of the Y_2O_3 + Al_2O_3 compositions was performed to predict the optimum composition and the trends in strength/composition relationship. Using regression techniques, a model was derived to identify the strength vs material composition relationship at room temperature, 1232°C (2250°F), and 1399°C (2550°F). The model developed is useful for establishing trends within composition range and potentially identifies optimum compositions for each temperature. Properties outside of these ranges may not be accurately predicted. The model also does not account for the effect of flaw population, microstructure, and fabrication process. Furthermore, since a different optimum composition was predicted for each temperature, engineering judgement is needed to select the "best" material composition from the statistical modeling results.

2.3.3 Summary of Modeling Procedure

Only a summary will be presented in this section. The detailed analysis procedure and modeling results are presented in Appendix D.

The first stage of the optimization analysis involved developing a model or equation to predict, for a given test temperature, the composition/strength relationship between each individual experimental data point within the measured composition range. (Note: The individual experimental data points instead of the average strength for each composition were used in the analysis.) Three prediction methods were used in modeling: the method of least squares (LS), the method of weighted least squares (WLS), and the method of two-step prediction. Among these three methods, the two-step prediction method was found the most suitable because it combines the benefits of both the LS and WLS methods. It provides more accurate predictions than the LS method and is capable of predicting values outside the experimental data range where standard deviation data are not available. Since the WLS method requires standard deviation values as "weights," it cannot predict values outside the experimental range or when the standard deviations are nonuniform throughout this range. The third approach was utilized because in addition to the strength vs composition relationship, there appeared also to be a standard deviation vs composition relationship. Thus a two-step approach was utilized, first to model the standard deviation vs composition relationship, then to use this model to derive an accurate strength vs composition model.

The second stage of the optimization involved using the model developed to calculate more data points to describe the change in strength as a function of composition. The model can be described by the form of a three-dimensional surface projected above the Y_2O_3 + Al_2O_3 + Si_3N_4 compositional triangle. Figures 64, 65, and 66 shows the "contour maps" generated to represent these surfaces for the three different temperatures. Experimental data points are shown as dark dots. As shown, the experimental data are nearly, but not exactly, predicted by the model. Although the exact magnitudes are not accurate, the trend in strength vs composition has been accurately modeled. The model

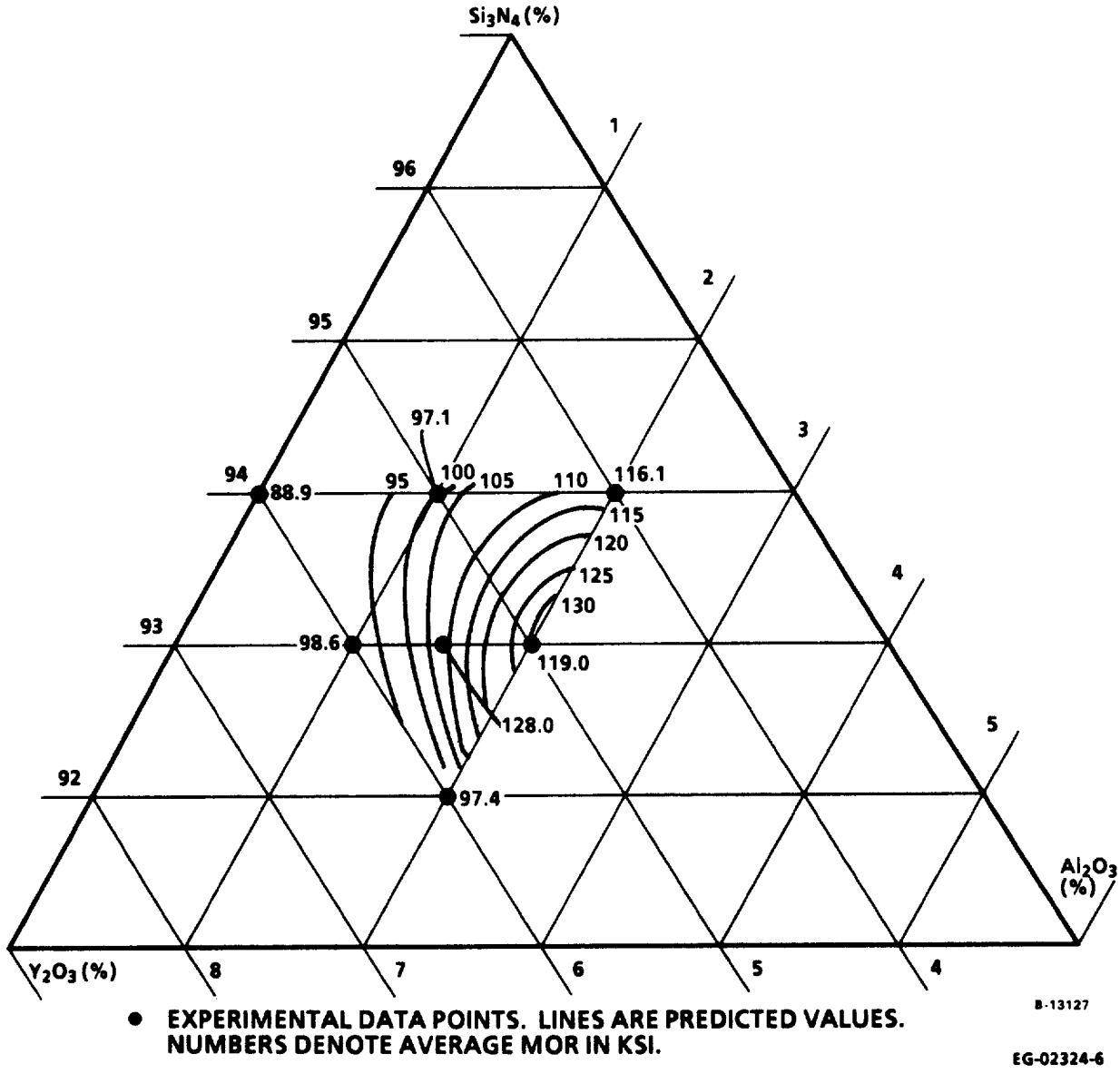

Figure 64.--Contour Plot of MOR vs Composition At Room Temperature.

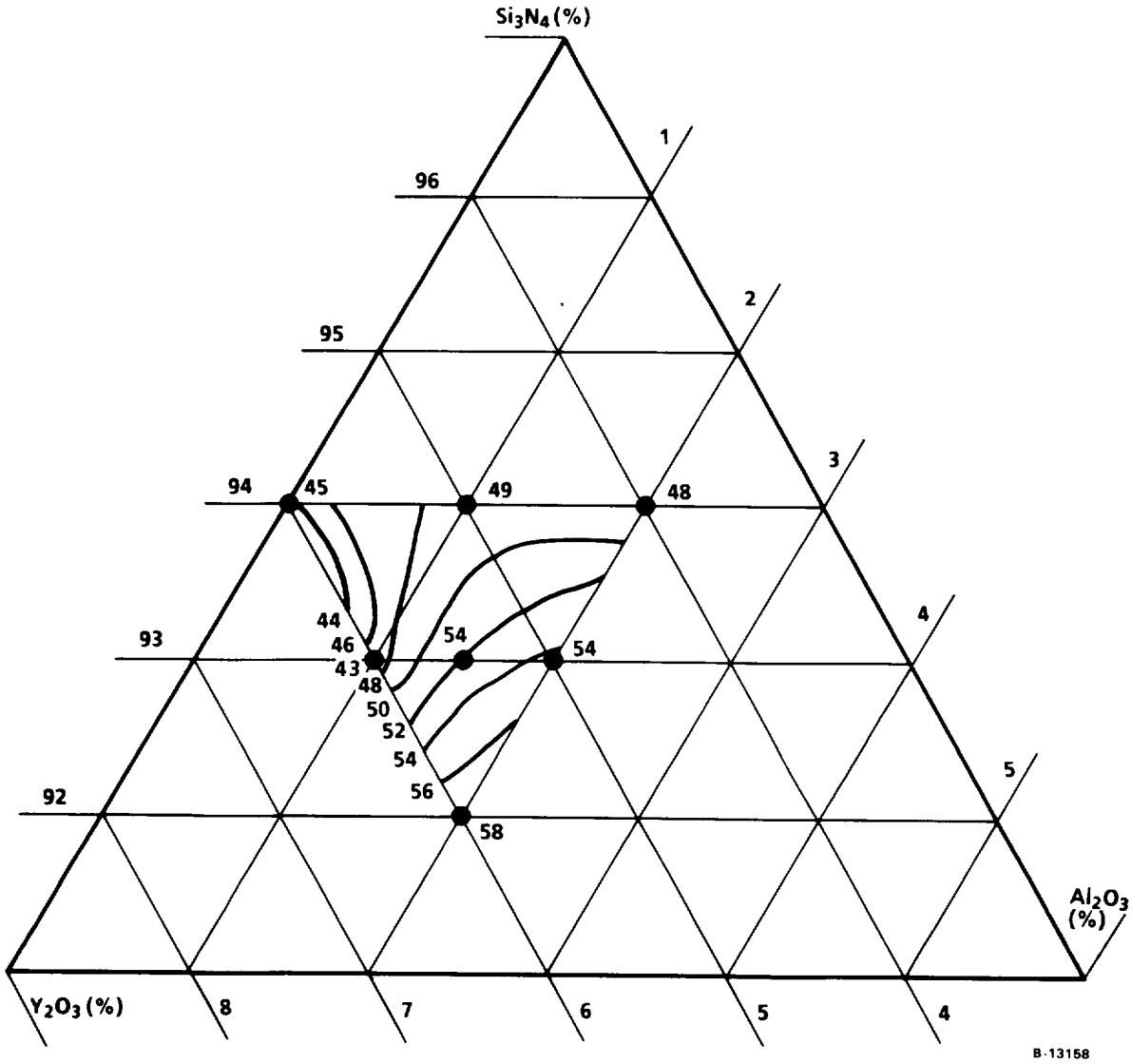

Figure 65.--Contour Plot of MOR vs Composition at 1232°C (2250°F).

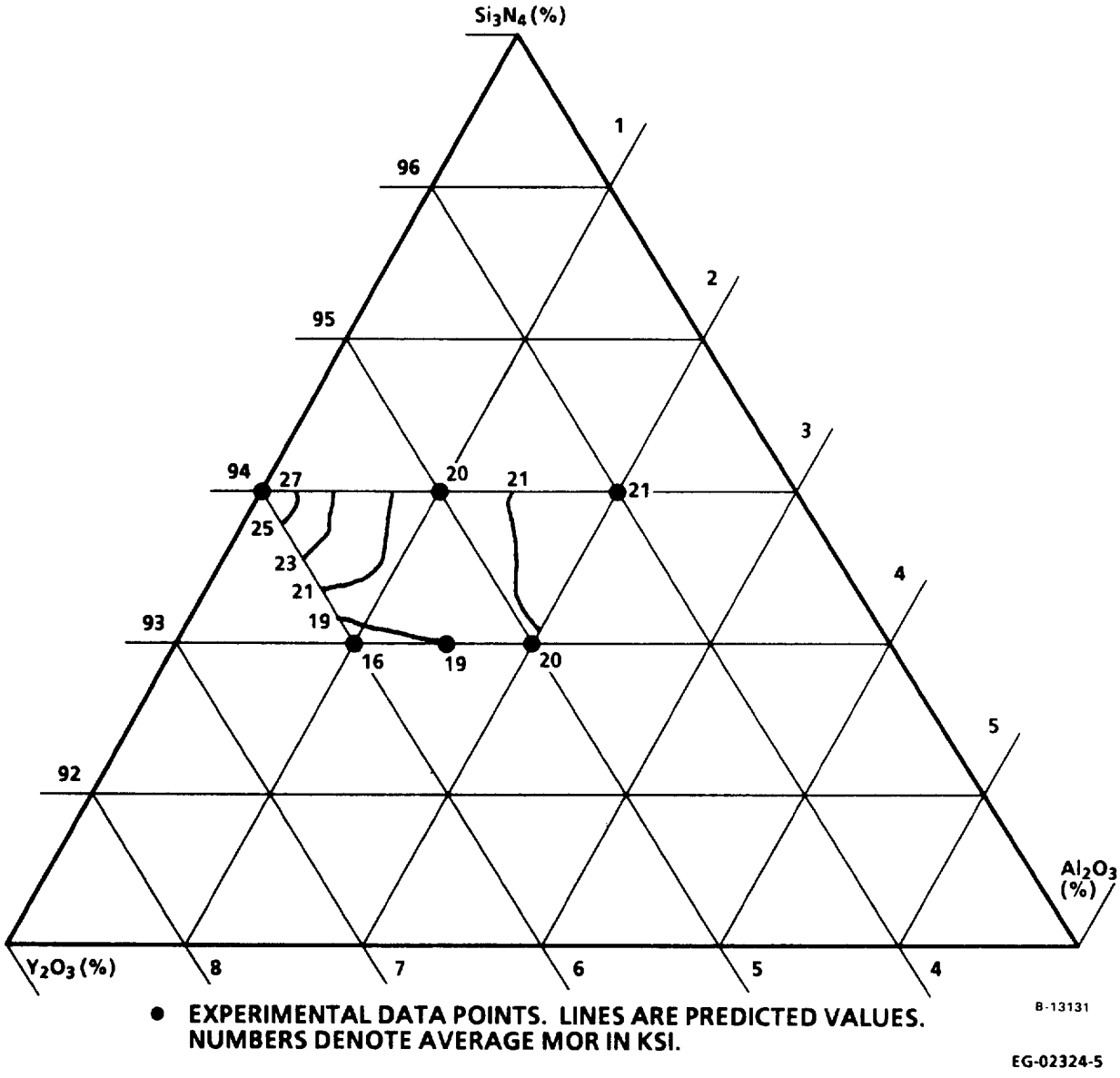

Figure 66.--Contour Plot of MOR vs Composition at 1399°C (2550°F).

predicts that increasing the Al_2O_3 content will increase the strength at room temperature and 1232°C (2250°F). At 1399°C (2550°F), the strength is predicted to decrease as the Al_2O_3 content increases. The predicted optimum compositions are listed below.

Material	Composition at 70°F (wt%)	Composition at 2250°F (wt%)	Composition at 2550°F (wt%)
Si_3N_4	93	92	94
Al_2O_3	2	2	0
Y_2O_3	5	6	6

2.3.4 Alternate Sintering Aids Evaluation

Alternate sintering aids were examined to identify the composition with improved high-temperature strength properties. The prospective sintering aids identified would then be optimized using the modeling technique developed for the Y_2O_3 + Al_2O_3 system. Ten billets with Y_2O_3 and different amounts of ZrO_2, SrO, CeO_2, or MgO were fabricated. Test bar fabrication and strength testing were the same as in the Y_2O_3 + Al_2O_3 optimization experiment. All 10 billets (compositions) achieved nearly theoretical density. Compositions and the HIP'ed densities of these 10 billets are listed in table 36. For comparison, the compositions and densities of the six billets containing Y_2O_3 + Al_2O_3 sintering aids (see para. 2.3.2) are also listed. For future reference, the compositions listed in Table 36 are coded GN-10 through GN-25.

Average flexure strengths of the test bars of these 10 billets (compositions) at room temperature, 1232°C (2250°F), and 1399°C (2550°F) are listed in table 37, in decreasing 1399°C (2550°F) strength order, and plotted as bar charts in figure 67. The strengths of the six new Y_2O_3 + Al_2O_3 composition materials are also included for comparison. Material GN-10 achieved significantly higher strength (95 percent confidence level) at 1232°C (2250°F) and 1399°C (2550°F) than the rest of the 15 compositions. Its average strengths were 890.1 MPa (129.1 ksi) at room temperature, 706.7 MPa (102.5 ksi) at 1232°C (2250°F), and 581.3 MPa (84.3 ksi) at 1399°C (2550°F). This material virtually meets the program goal of 586.1 MPa (85 ksi) at 1399°C (2550°F).

A statistical analysis was performed to compare the strength of these materials. The room temperature strengths of the individual test bars ranged from 482.7 to 1027.4 MPa (70 to 149 ksi), with an overall average of 730.9 MPa (106 ksi). At 95 percent confidence level, three of the materials (GN-10, GN-20, and GN-23) showed significantly higher strength than the other materials.

The strength of the individual test bars at 1232°C (2250°F) ranged from 144.8 to 779.1 MPa (21 to 113 ksi), with an overall average of 337.9 MPa (49 ksi). The individual strength of the test bars at 1399°C (2550°F) ranged from 69.0 to 600.0 MPa (10 to 87 ksi), with an overall average of 179.3 MPa (26 ksi). Material GN-10 showed significantly higher strengths than all of the other materials.

TABLE 36.--DENSITY AND COMPOSITION OF HIP'ED HIGH-TEMPERATURE Si_3N_4 BILLETS

Billet No.	Composition Code	Composition	Density (Meas.)/ Density (Theo.)
1	GN-10	90% Si_3N_4, 8.0% Y_2O_3, 2.0% SrO	3.32/3.31
2	GN-11	93% Si_3N_4, 4.0% Y_2O_3, 3.0% ZrO_2*	3.29/3.28
3	GN-12	93% Si_3N_4, 5.5% Y_2O_3, 0.5% MgO	3.27/3.26
4	GN-13	93% Si_3N_4, 5.0% Y_2O_3, 2.0% CeO_2	3.30/3.29
5	GN-14	93% Si_3N_4, 6.0% Y_2O_3, 1.0% MgO	3.28/3.27
6	GN-15	93% Si_3N_4, 3.0% Y_2O_3 2.0% SrO, 2.0% ZrO_2	3.28/3.28
7	GN-16	93% Si_3N_4, 5.0% Y_2O_3 1.5% SrO, 0.5% MgO	3.27/3.27
8	GN-17	93% Si_3N_4, 4.5% Y_2O_3 0.5% MgO, 2.0% CeO_2	3.29/3.28
9	GN-18	93% Si_3N_4, 30% Y_2O_3 3.0% ZrO_2*, 1.0% CeO_2	3.29/3.29
10	GN-19	93% Si_3N_4, 1.0% Y_2O_3 3.0% ZrO_2*, 3.0% CeO_2	3.29/3.30
11	GN-20	94% Si_3N_4, 6.0% Y_2O_3	3.28/3.26
12	GN-21	94% Si_3N_4, 5.0% Y_2O_3, 1.0% Al_2O_3	3.26/3.26
13	GN-22	94% Si_3N_4, 4.0% Y_2O_3, 2.0% Al_2O_3	3.24/3.25
14	GN-23	93% Si_3N_4, 6.0% Y_2O_3, 1.0% Al_2O_3	3.27/3.27
15	GN-24	93% Si_3N_4, 5.5% Y_2O_3, 1.5% Al_2O_3	3.27/3.27
16	GN-25	93% Si_3N_4, 5.0% Y_2O_3, 2.0% Al_2O_3	3.26/3.26

*Stabilized ZrO_2

TABLE 37.--HIGH-TEMPERATURE MATERIAL STRENGTH
(sorted in decreasing 1399°C (2550°F) strength)

Code	Average Flexure Strength, MPa (ksi)		
	Room	1232°C (2250°F)	1399°C (2550°F)
GN-10	889.5 (129.1)	706.2 (102.5)	580.8 (84.3)
GN-13	647.7 (94.0)	421.0 (61.1)	213.6 (31.0)
GN-15	699.3 (101.5)	314.2 (45.6)	201.9 (29.3)
GN-20	612.5 (88.9)	307.3 (44.6)	186.7 (27.1)
GN-16	659.4 (95.7)	386.5 (56.1)	166.0 (24.1)
GN-18	691.8 (100.4)	246.7 (35.8)	161.2 (23.4)
GN-17	668.3 (97.0)	292.1 (42.4)	159.8 (23.2)
GN-12	729.0 (105.8)	290.8 (42.2)	159.2 (23.1)
GN-11	667.0 (96.8)	281.8 (40.9)	152.3 (22.1)
GN-22	734.5 (106.6)	333.5 (48.4)	148.1 (21.5)
GN-14	888.1 (128.9)	232.2 (33.7)	142.6 (20.7)
GN-21	602.2 (87.4)	336.9 (48.9)	141.2 (20.5)
GN-25	819.2 (118.9)	373.4 (54.2)	139.9 (20.3)
GN-24	881.9 (128.0)	373.4 (54.2)	133.7 (19.4)
GN-19	764.1 (110.9)	288.7 (41.9)	133.7 (19.4)
GN-23	079.4 (98.6)	244.6 (35.5)	109.6 (15.9)

2.3.5 Stress Rupture

Five test bars of GN-10 were tested in stress rupture at 1371°C (2500°F.) Stress rupture properties are important for turbine engine materials, which need to sustain stress at elevated temperature. The results are listed below and plotted in figure 68.

Specimen	Applied Stress, MPa (ksi)	Percentage of Average Fast Fracture Stress	Time to Failure, hours
26388	379.0 (55)	65	0.65
26389	344.5 (50)	59	2.70
26390	310.1 (45)	53	4.75
26391	275.6 (40)	48	8.75
26392	275.6 (40)	48	11.00

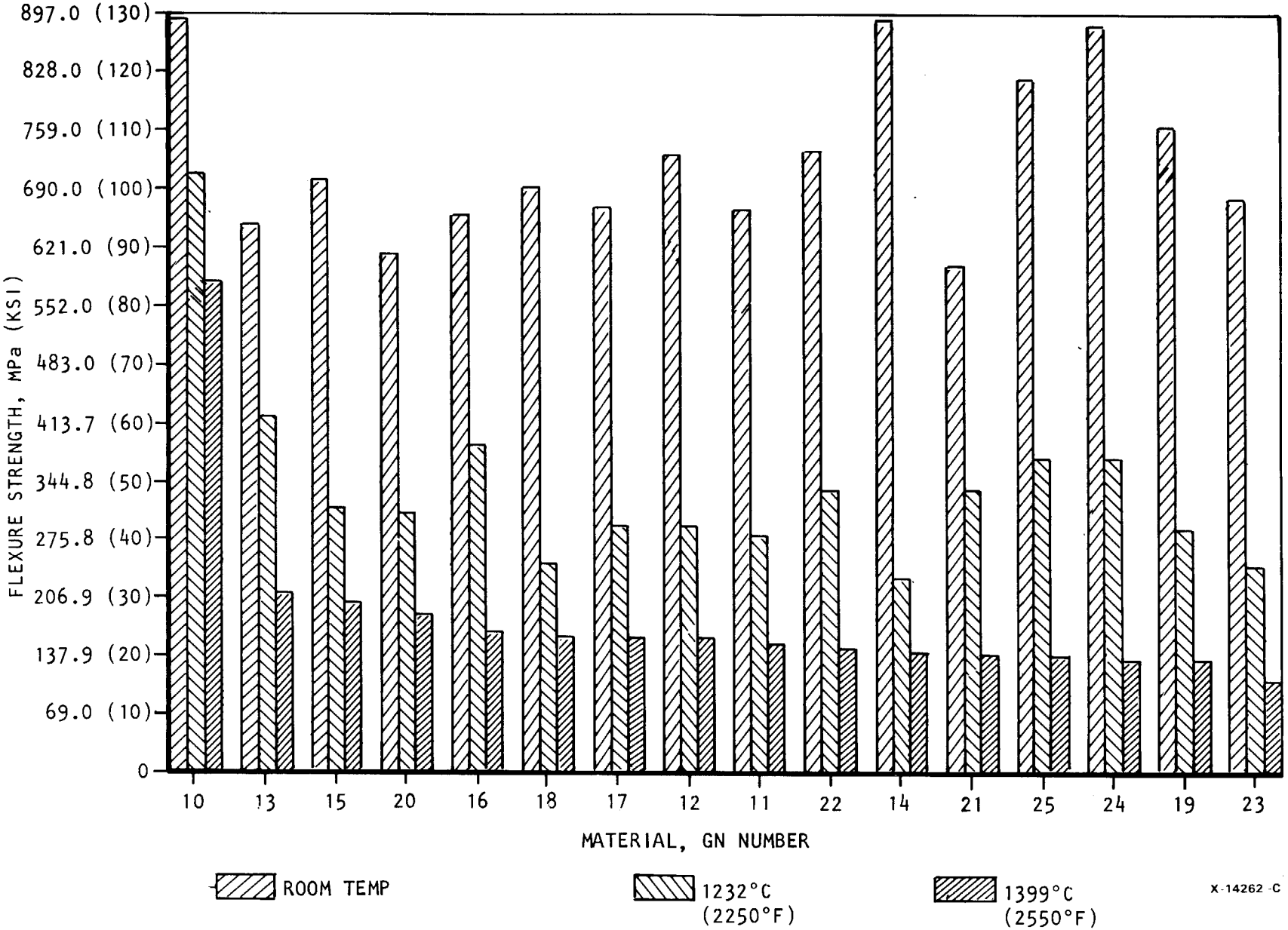

Figure 67.--Average Flexure Strengths of the High-Temperature Materials Investigated. (Sorted in Decreasing 1399°C (2550°F) Strength)

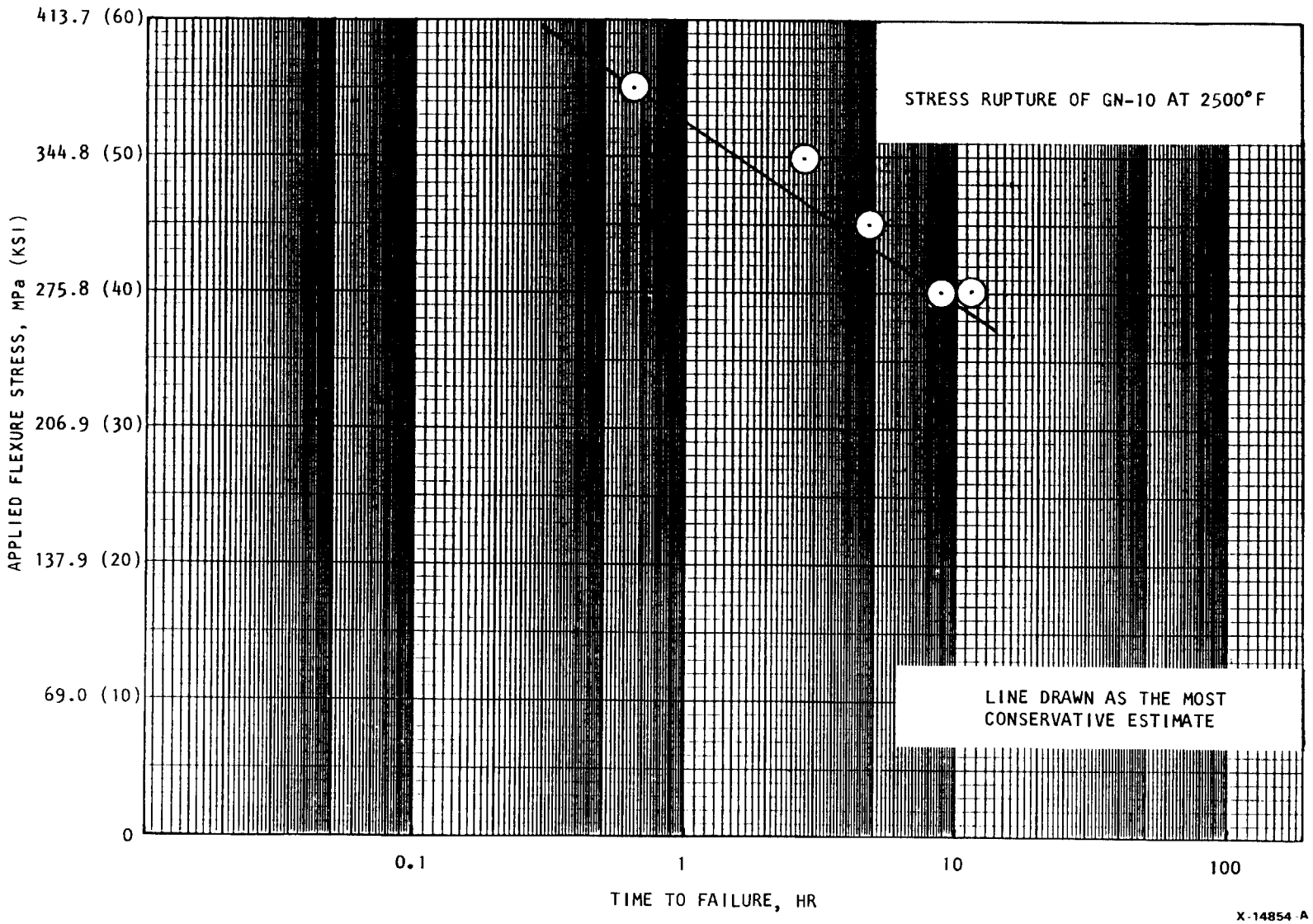

Figure 68.--Stress Rupture of GN-10 at 1371°C (2500°F).

Due to the limited number of specimens, testing was performed at only one temperature but at various loads to obtain an approximation of the stress rupture behavior. The test temperature of 1371°C (2500°F) was selected to provide a direct comparison with other similar materials tested at GAPD. All of the specimens failed from the surface and showed indications of slow crack growth. The specimens also showed permanent creep deformation after testing.

2.3.6 Optimization of the GN-10 Composition

This study was aimed at optimizing the GN-10 composition, which is composed of Si_3N_4 with two sintering aids, Y_2O_3 and SrO. Since only one composition in the Si_3N_4 + Y_2O_3 + SrO system was evaluated, it was essential to evaluate compositions close to GN-10. A better understanding of the property/composition relationship of this system will enable the material fabricator to select the best composition for a particular application. For example, if the amount of sintering aids needs to be changed, the effect on fast fracture strength can be predicted from the model. Lowering sintering aids has the potential of improving high-temperature strength, fast fracture, and possibly oxidation resistance. Higher sintering aid levels generally increase room temperature strength and promote sinter/HIP densification, which is important for fabricating net-shape components or incorporating SiC whiskers.

Eleven billets with ten different Y_2O_3 + SrO additive compositions (table 38) were CIP'ed and encapsulated HIP'ed in niobium cans. The billets were HIP'ped at GCC in three separate HIP runs in the 206.9 MPa (30 ksi) furnace using identical conditions as the first GN-10 billet (2 hours at 1900°C (3452°F) and 206.9 MPa (30 ksi)). Their compositions and respective locations in the Si_3N_4 + Y_2O_3 + SrO composition triangle are given in figure 69. Two GN-10 composition billets were made to demonstrate reproducibility of the material between HIP furnace runs.

TABLE 38.--BILLET COMPOSITION SELECTION FOR GN-10
GN-10 OPTIMIZATION STUDY

Billet No.	Composition (Wt %)		
	Si_3N_4	Y_2O_3	SrO
2	91	8	1
3	91	7	2
4	90.7	7.7	1.6
5	90	9	1
6A*	90	8	2
6B*	90	8	2
7	90	7	3
8	89.7	8.7	1.6
9	89.7	7.7	2.6
11	89	9	2
12	89	8	3

*GN-10 Composition

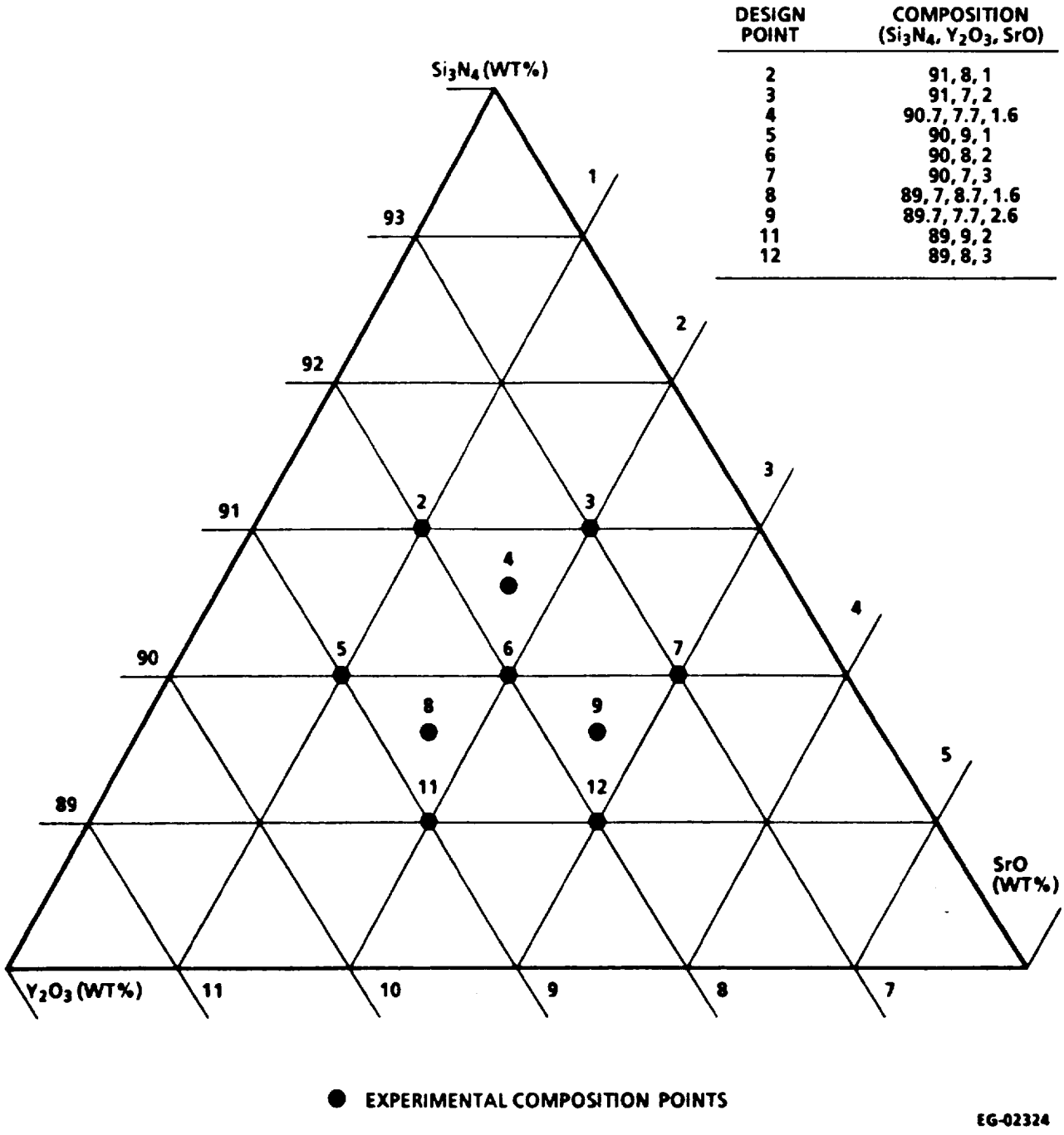

Figure 69.--Mixture Design for GN-10 Optimization.

The billets were successfully HIP'ed to theoretical density and machined into standard 0.125 by 0.250 by 2.0 inch flexure bars. Visual observation indicated a light-colored region on most test bars machined from the outer portion of the billet. Some test bars showed the mottled appearance of phase separation independent of location in the billet. For each billet, ten test bars were tested at room temperature: five at 1232°C (2250°F), and five at 1399°C (2550°F). When quantities permitted, the bars were selected from the inside of the billet and oriented to avoid testing the light-colored side in tension.

The strength results of the eleven billets (ten compositions) are summarized for each temperature in tables 39, 40, and 41. Overall, the average room temperature strengths are lower than the test bars from the original GN-10 composition billet, but some compositions (billets 4 and 8) achieved higher strength 634.3 and 661.9 MPa (92 and 96 ksi) at 1399°C (2550°F). Two billets, 6A and 6B, have the original GN-10 composition and were included to demonstrate process reproducibility. However, they showed a difference in strength, especially at 1399°C (2550°F), compared to both themselves and the original GN-10 results. Strength measurements at 1399°C (2550°F) were 530.9, 606.8, and 579.2 MPa (77, 88, and 84 ksi) for billets 6A, 6B, and the original GN-10 billet, respectively. The standard deviation of most of the billets was high due to some low-strength test bars as shown in tables 39, 40, and 41.

2.3.7 Statistical Modeling of Composition/Strength Relationship

The statistical modeling technique previously demonstrated from the Si_3N_4 + Y_2O_3 + Al_2O_3 system study was used to analyze the results. However, due to the large variation in the strength of test bars of the same composition, only the least squares prediction method was used in this study (i.e., the standard deviation vs composition was not modeled). The detailed analysis procedure and modeling techniques can be found in Appendix D.

The optimization experiment consisted of ten specific compositional points as shown in figure 69. Using regression techniques, a statistical model was derived to identify the strength vs material composition relationship for room temperature, 1232°C (2250°F), and 1399°C (2550°F). The model developed was then used to describe the change in strength as a function of composition in the form of a three-dimensional surface projected above the Y_2O_3 + SrO + Si_3N_4 compositional triangle. Figures 70, 71, and 72 show the "contour maps" generated to represent these surfaces for the three different temperatures. Although the magnitudes of the predicted strengths may not be precise, the trends in strength vs composition have been accurately modeled.

At room temperature, there was a pattern of increasing strength as a function of increasing SrO content up to approximately 2.5 wt% as shown in figure 70. At this SrO content, the strength can be increased by reducing the Y_2O_3 content.

The 1232°C (2250°F) strength results are shown in figure 71. The "contour map" indicates a maximum strength region along an SrO composition line. Changing the Y_2O_3 content in this region does not affect the strength. The contour plot in figure 72 shows that the maximum strength at 1399°C (2550°F) is about 620 MPa (90 ksi).

TABLE 39.--SUMMARY STATISTICS OF MOR AT ROOM TEMPERATURE

Billet No.	No. of Bars**	Observed MOR, MPa (ksi)				Predicted* MOR, MPa (ksi)
		Mean	S.D.	Min.	Max.	
2	10	554.0 (80.4)	154.6 (22.44)	270.1 (39.2)	760.0 (110.3)	519.5 (75.4)
3	10	785.5 (114.0)	82.4 (11.96)	597.4 (86.7)	906.7 (131.6)	807.5 (117.2)
4	10	701.4 (101.8)	58.6 (8.51)	635.3 (92.2)	837.1 (121.5)	717.9 (104.2)
5	9	543.6 (78.9)	140.0 (20.32)	355.5 (51.6)	791.7 (114.9)	582.9 (84.6)
6A	9	740.0 (107.4)	65.3 (9.48)	622.9 (90.4)	839.2 (121.8)	793.0 (115.1)
6B	10	825.4 (119.8)	96.8 (14.05)	636.6 (92.4)	908.1 (131.8)	793.0 (115.1)
7	10	853.0 (123.8)	123.1 (17.87)	601.5 (87.3)	1008.0 (146.3)	831.6 (120.7)
8	10	762.7 (110.7)	55.8 (8.10)	672.5 (97.6)	851.6 (123.6)	733.8 (106.5)
9	10	837.1 (121.5)	84.7 (12.29)	704.2 (102.2)	956.3 (138.8)	817.8 (118.7)
11	8	793.7 (115.2)	46.0 (6.68)	735.9 (106.8)	877.1 (127.3)	775.1 (112.5)
12	9	703.5 (102.1)	115.5 (16.76)	527.8 (76.6)	843.3 (122.4)	735.2 (106.7)

*By modeling technique

**Selected low-strength test bars excluded from analysis

TABLE 40.--SUMMARY STATISTICS OF MOR AT 1232°C (2250°F)

Billet No.	No. of Bars**	Observed MOR, MPa (ksi)				Predicted* MOR, MPa (ksi)
		Mean	S.D.	Min.	Max.	
2	5	584.3 (84.8)	98.1 (14.24)	468.5 (68.0)	704.2 (102.2)	562.9 (81.7)
3	5	643.5 (93.4)	22.7 (3.30)	613.2 (89.0)	664.9 (96.5)	657.3 (95.4)
4	5	624.9 (90.7)	101.9 (14.79)	494.0 (71.7)	730.3 (106.0)	649.7 (94.3)
5	5	487.1 (70.7)	114.8 (16.66)	388.6 (56.4)	674.5 (97.9)	518.1 (75.2)
6A	5	644.2 (93.5)	62.8 (9.12)	549.8 (79.8)	722.1 (104.8)	660.8 (95.9)
6B	5	670.4 (97.3)	103.1 (14.97)	541.6 (78.6)	807.5 (117.2)	660.8 (95.9)
7	5	535.4 (77.7)	136.4 (19.80)	390.7 (56.7)	748.3 (108.6)	509.9 (74.0)
8	5	682.8 (99.1)	77.3 (11.22)	579.4 (84.1)	768.2 (111.5)	634.6 (92.1)
9	5	620.8 (90.1)	119.5 (17.35)	430.6 (62.5)	718.6 (104.3)	615.3 (89.3)
11	5	668.3 (97.0)	135.0 (19.59)	460.3 (66.8)	791.7 (114.9)	665.6 (96.6)
12	5	535.4 (77.7)	123.9 (17.98)	401.0 (58.2)	726.2 (105.4)	562.9 (81.7)

*By modeling technique

**Selected low-strength test bars excluded from analysis

TABLE 41.--SUMMARY STATISTICS OF MOR AT 1399°C (2550°F)

Billet No.	No. of Bars**	Observed MOR, MPa (ksi)				Predicted* MOR, MPa (ksi)
		Mean	S.D.	Min.	Max.	
2	5	598.7 (86.9)	71.2 (10.34)	489.9 (71.1)	678.7 (98.5)	590.5 (85.7)
3	5	559.5 (81.2)	36.6 (5.31)	498.1 (72.3)	589.1 (85.5)	574.6 (83.4)
4	5	662.1 (96.1)	24.0 (3.49)	627.0 (91.0)	688.3 (99.9)	609.1 (88.4)
5	5	558.1 (81.0)	57.0 (8.27)	484.4 (70.3)	619.4 (89.9)	581.5 (84.4)
6A	5	610.5 (88.6)	71.5 (10.38)	520.2 (75.5)	684.9 (99.4)	595.3 (86.4)
6B	5	531.2 (77.1)	74.9 (10.87)	428.6 (62.2)	636.6 (92.4)	595.3 (86.4)
7	5	399.6 (58.0)	8.7 (1.26)	388.6 (56.4)	412.7 (59.9)	394.1 (57.2)
8	5	636.6 (92.4)	61.9 (8.98)	539.5 (78.3)	694.5 (100.8)	618.7 (89.8)
9	5	486.4 (70.6)	16.2 (2.35)	464.4 (67.4)	507.8 (73.7)	511.9 (74.3)
11	5	627.0 (91.0)	69.9 (10.15)	523.6 (76.0)	686.2 (99.6)	617.3 (89.6)
12	5	465.1 (67.5)	26.0 (3.78)	426.5 (61.9)	498.1 (72.3)	445.8 (64.7)

*By modeling technique

**Selected low-strength test bars excluded from analysis

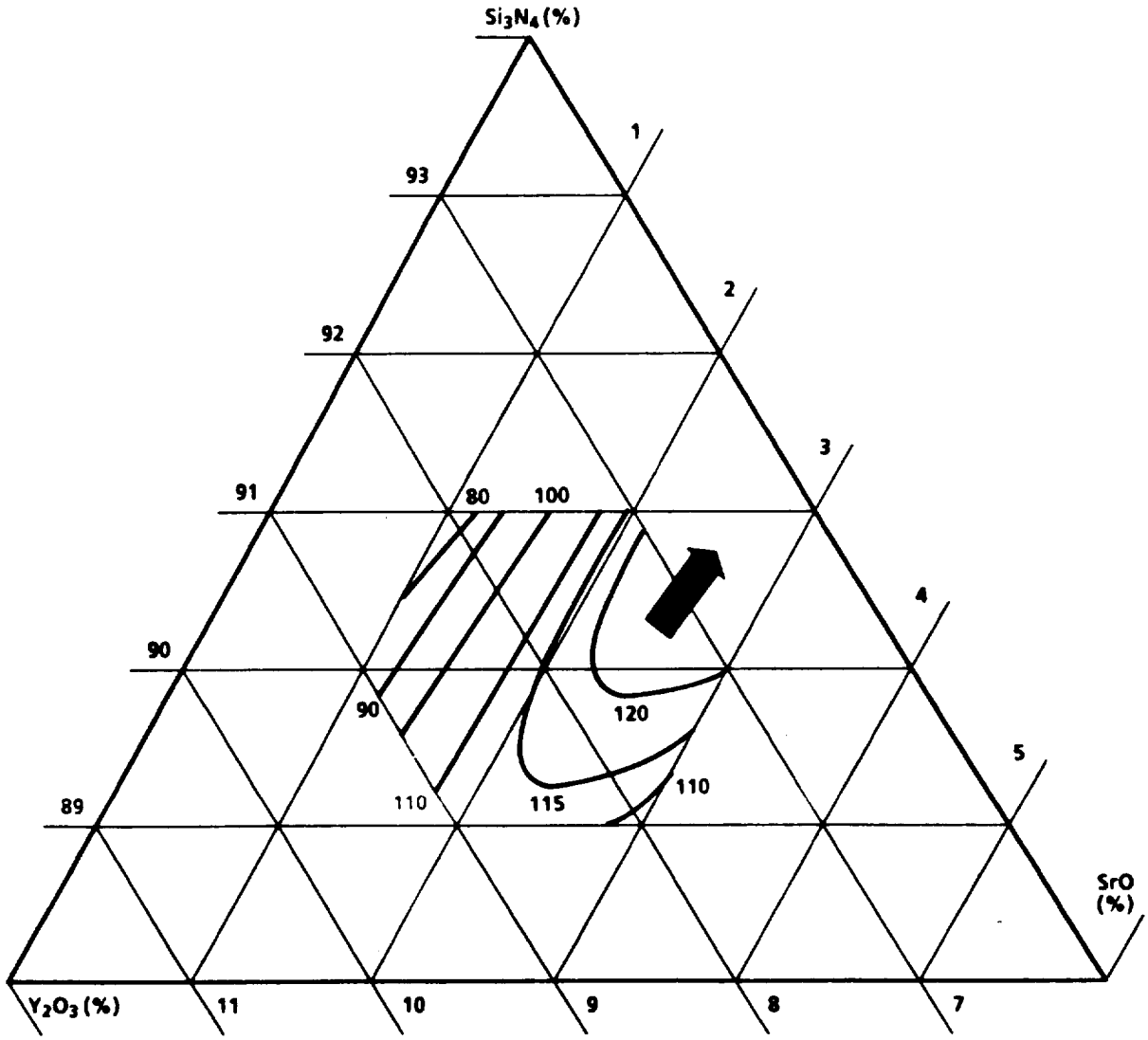

Figure 70.--Contour Plot of MOR (ksi) vs Composition at Room Temperature.

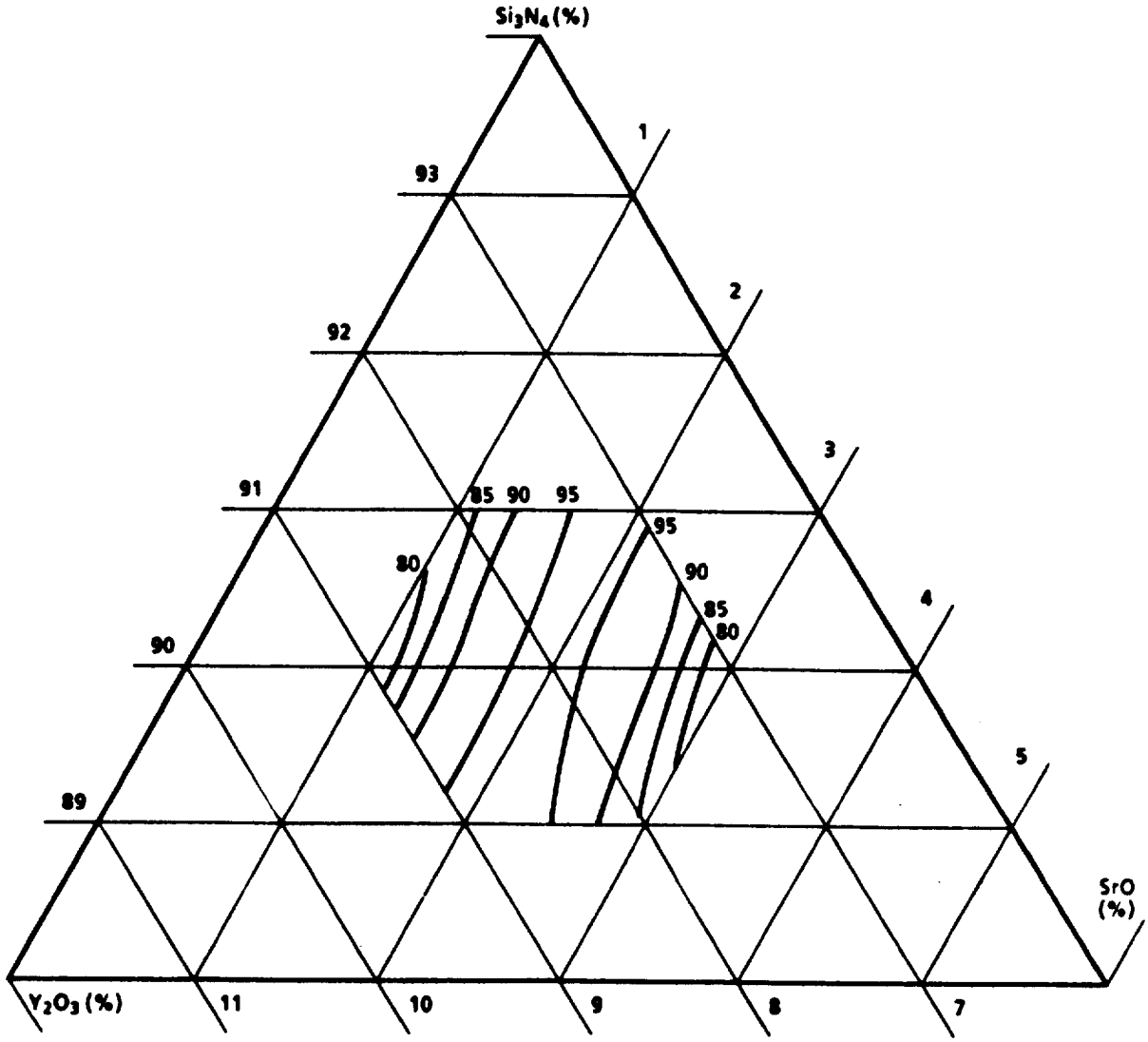

*CONTOUR LINES REPRESENT PREDICTED MOR VALUES
*NUMBERS DENOTE MOR IN KSI

EG-02324-4
B 12679

Figure 71.--Contour Plot of MOR (ksi) vs Composition at 1232°C (2250°F).

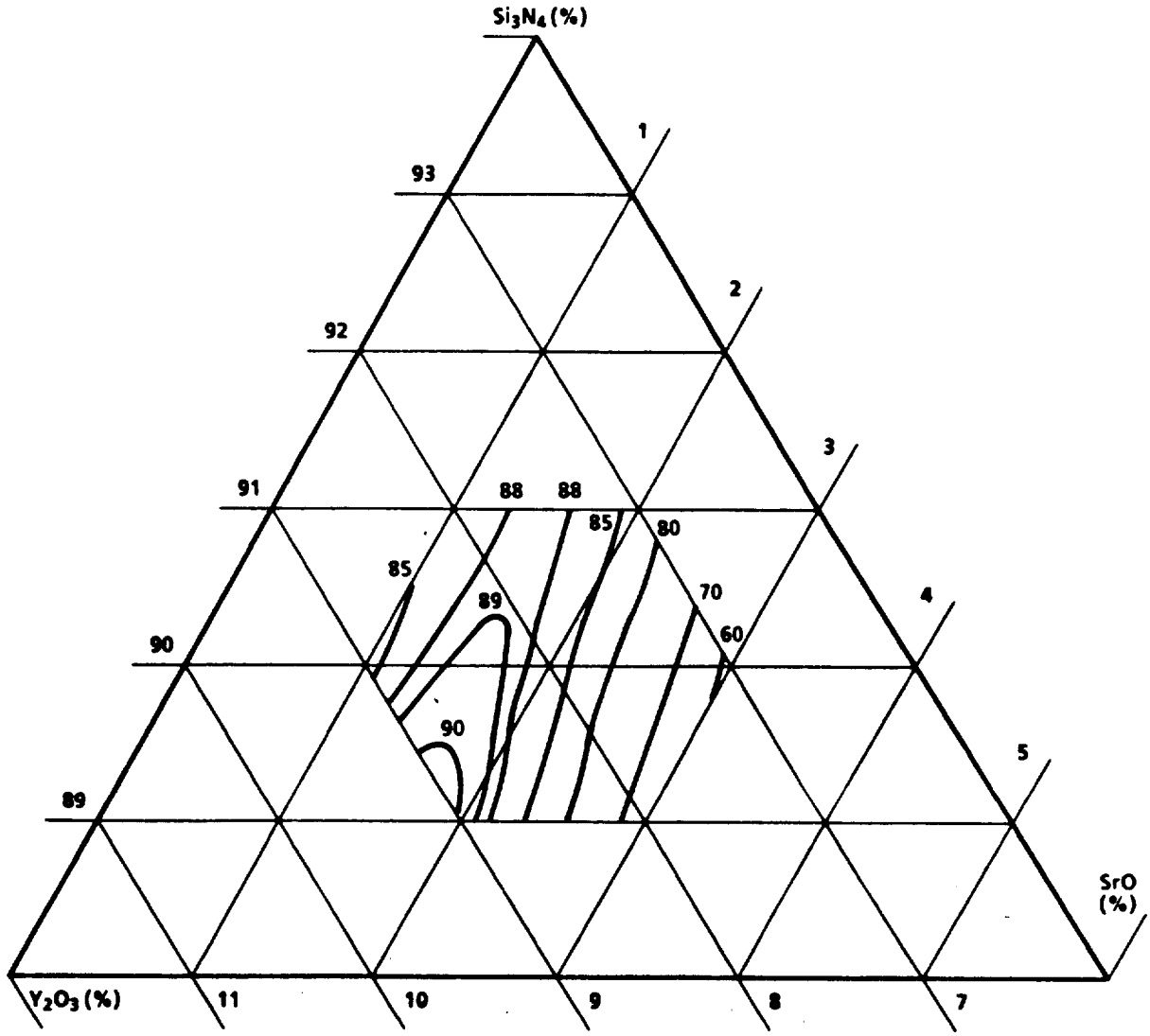

Figure 72.--Contour Plot of MOR (ksi) vs Composition at 1399°C (2550°F).

In general, the analysis showed that SrO plays a dominant role in the strength of the Si_3N_4. A region of optimal composition is shown in figure 73.

The large variation in strength of the test bars cut from the same billet and the inconsistent strength variations among billets made analysis difficult. Furthermore, billets 6A and 6B, which had the same composition but were HIP'ed in separate runs, showed different strength, especially at the 1399°C (2550°F) test temperature. The analysis was, therefore, performed by combining the strength of the two billets. This resulted in a larger strength variation and less accuracy in the predictions.

2.3.8 Fractography of Test Bars

Optical fractography using a 40X stereo microscope was performed on all of the fractured test bars. The fractography results presented in table 42 and figures 74, 75, and 76 summarize the average, maximum, and minimum strength of test bars as well as the flaw type and failure locations. Dark patches or inclusions were observed at the fracture origin of a large number of test bars (25 percent of total). These inclusions all appeared to be of the same type. SEM/EDX analysis of the inclusions showed the presence of Fe, Cr, and Ni, as indicated in the SEM micrographs and X-ray dot maps shown in figures 77, 78, and 79. One test bar failed from a void and one from an agglomerate. The rest of the test bars (65 percent) failed from the tensile surface with no identifiable flaws.

The large strength variation observed in these test bars cannot be accounted for by the flaws observed at the fracture origins. Test bars which failed from inclusions had strength value throughout the strength range. Also, test bars failing from inclusions had slightly higher strengths than those failing from the surface.

During pre-test inspection, some test bars with either damaged chamfer edges or edges with as-densified surfaces were discovered. The damaged chamfers were probably due to machining, while test bars with the as-densified surfaces on the edges were machined too close to the surface of the HIP'ed billets. Special efforts were made to select and exclude damaged bars from the tests. Only one test bar in the whole group failed from a chipped chamfer corner, as shown in the SEM micrograph in figure 80. The high strength (813.6 MPa (118 ksi)) of this test bar suggested that the damage was small enough to escape detection.

Fractography results for test bars tested at 1232°C (2250°F) are listed in table 42 and presented in figure 75. A large percentage (40 percent) of the test bars failed from the same type of dark inclusions that were observed in the room temperature test bars. The strength of test bars failing from the inclusions and from the tensile surfaces are similar (592.3 and 610.2 MPa) (85.9 and 88.5 ksi). Test bars that failed from inclusions were also scattered throughout the strength range. Two of the test bars from billets with the highest SrO content showed signs of slow crack growth.

Fractography results for test bars tested at 1399°C (2550°F) are listed in table 42 and presented in figure 76. A smaller percentage (16 percent) of test bars failed from the dark inclusions. Typical slow crack growth features of a large undulating fracture face and flat fracture surface were observed on 53 percent of the test bars. The load curve of these test bars also showed flattening near failure. Test bars which showed signs of slow crack growth had lower strength. The slow crack growth phenomena, indicating weakening of the intergranular phase, was observed only on test bars with certain sintering aids compositions.

The large variation in strength of the test bars cannot be accounted for by the type of flaws at the fracture origins. Machining damage does not appear to be the reason. Nonuniform mixing or phase separation that resulted in weaker regions in the material may be a possible explanation. The dark patches or inclusions found at the fracture origin of many test bars were probably not the cause of low strength based on fractography and strength results. The effect of SrO content on high-temperature and fracture behavior of test bars was observed. The results suggested that an optimal amount of SrO is needed so that the viscosity of the liquid phase is low enough for proper sintering, but not excessively low to cause strength degradation at the test temperatures.

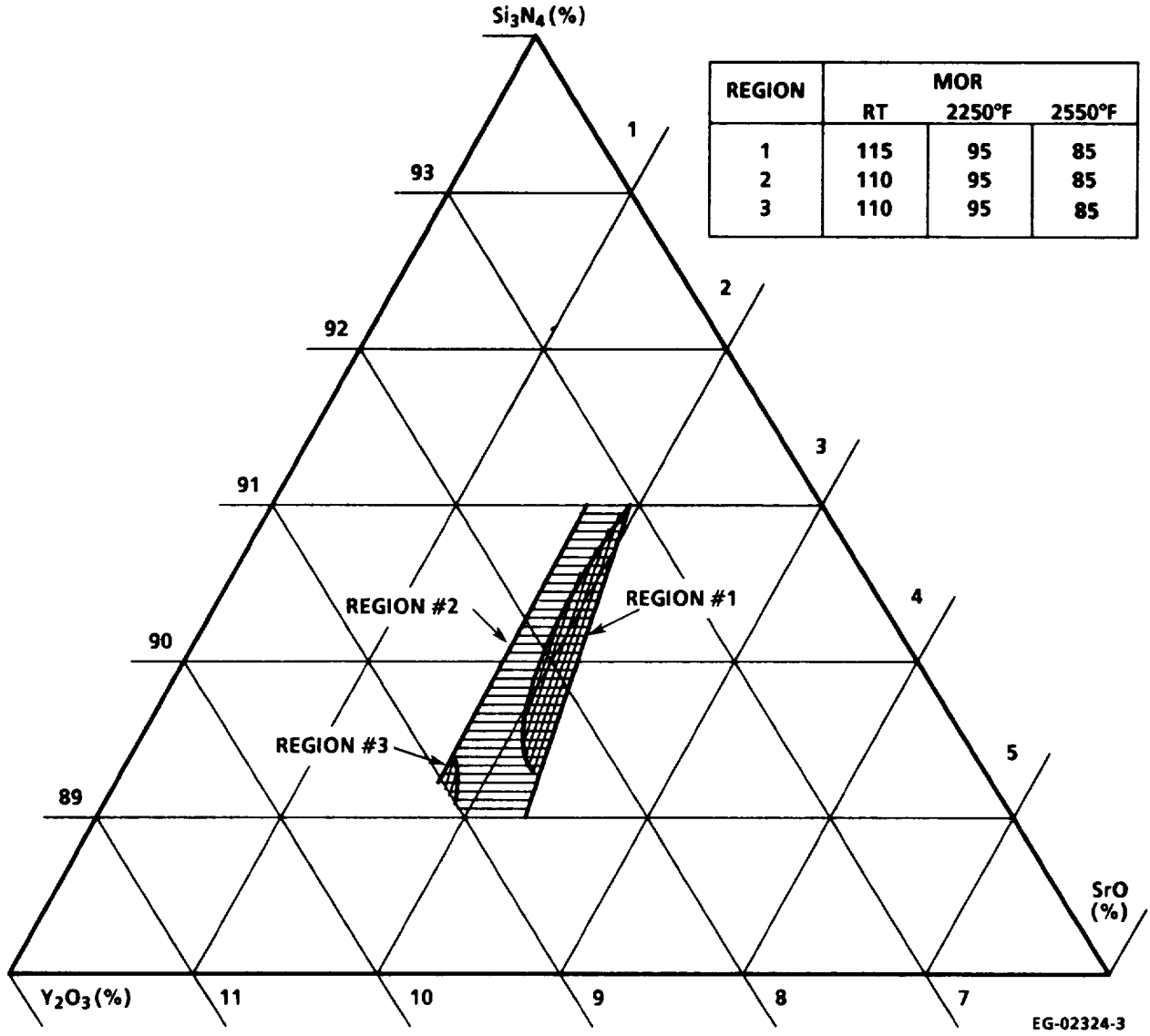

REGION	MOR		
	RT	2250°F	2550°F
1	115	95	85
2	110	95	85
3	110	95	85

Figure 73.--Plot of Optimal Region vs Composition.

TABLE 42.--CORRELATION OF FLEXURE STRENGTH WITH IDENTIFIED FRACTURE ORIGIN FLAWS

Flow Origin Description	Test Temperatures								
	Room Temp			1232°C (2250°F)			1399°C (2550°F)		
	Avg.	Max.	Min.	Avg.	Max.	Min.	Avg.	Max.	Min.
Tensile surface	100.4 (48)	138.8	51.6	87.5 (24)	114.0	56.4	81.6 (23)	100.8	56.4
Corner surface	103.7 (23)	146.3	35.7	93.5 (5)	105.4	60.8	77.1 (16)	97.3	59.9
Surface (total)	101.5 (71)	146.3	35.7	88.5 (29)	114.0	56.4	79.7 (39)	100.8	56.4
Surface inclusion	113.2(2)	116.6	109.7	81.1 (9)	97.9	56.7	68.0 (2)	74.0	61.9
Near surface inclusion	116.8 (12)	131.9	97.6	89.7 (3)	104.3	74.0	74.5 (2)	91.0	57.9
Internal inclusion	115.0 (8)	135.4	82.7	89.1 (10)	114.9	58.2	92.2 (4)	99.6	78.3
Side inclusion	92.0 (5)	115.2	58.8						
Corner inclusion	113.5 (1)							85.0 (1)	
Inclusion (total)	111.5 (28)	135.4	58.8	85.9 (22)	114.9	56.7	82.1 (9)	99.6	57.9
Void	130.5 (1)			102.4 (3)	117.2	84.1			
Agglomerate	102.5 (1)								
Slow crack growth				68.0 (2)	77.8	58.2	74.4 (29)	98.5	56.4

NOTE: Numbers for average, maximum, and minimum strength values are in ksi.
Numbers in parentheses indicate number of test bars identified.

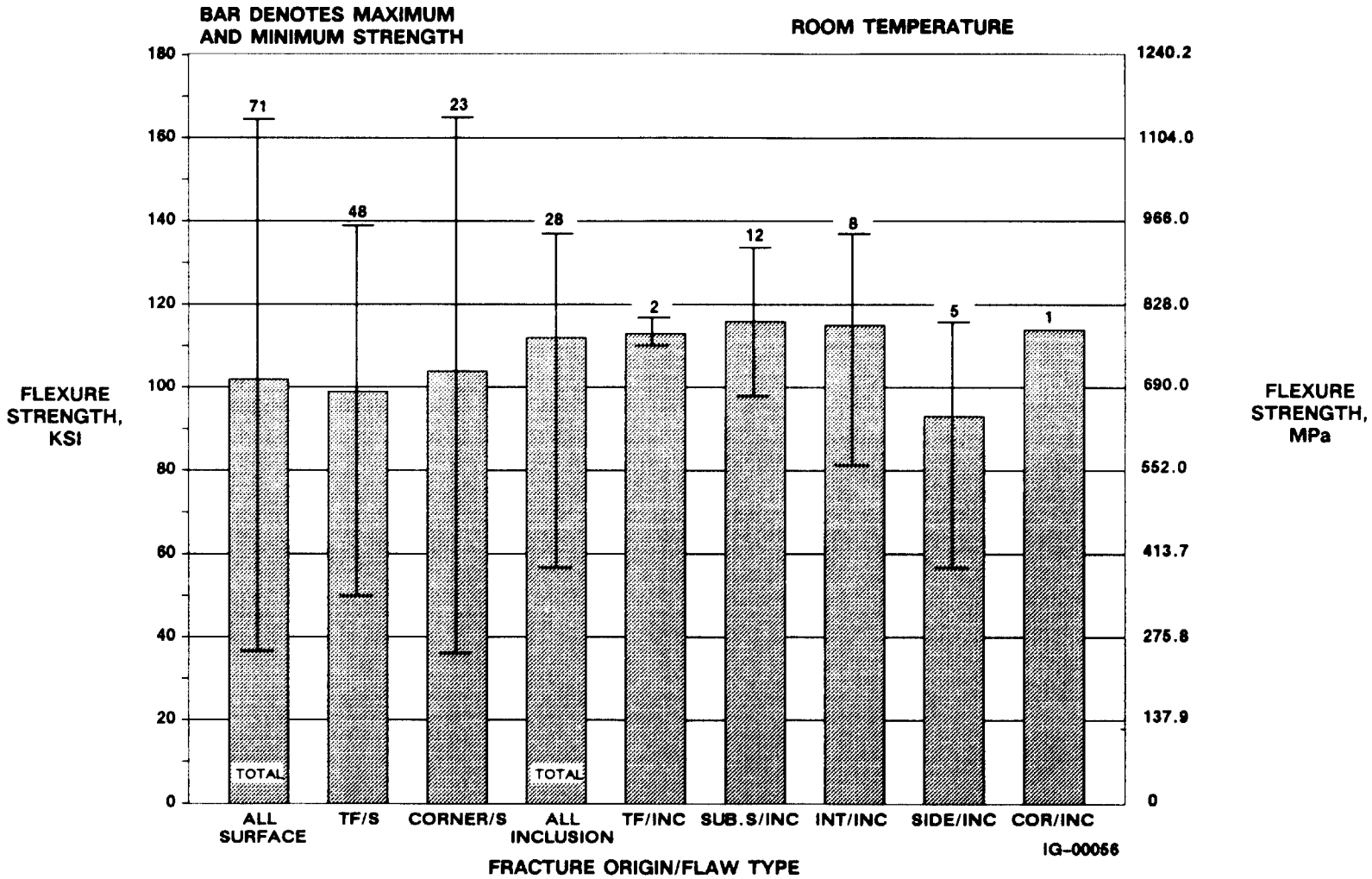

Figure 74.--Fractography Results for Test Bars Tested at Room Temperature.

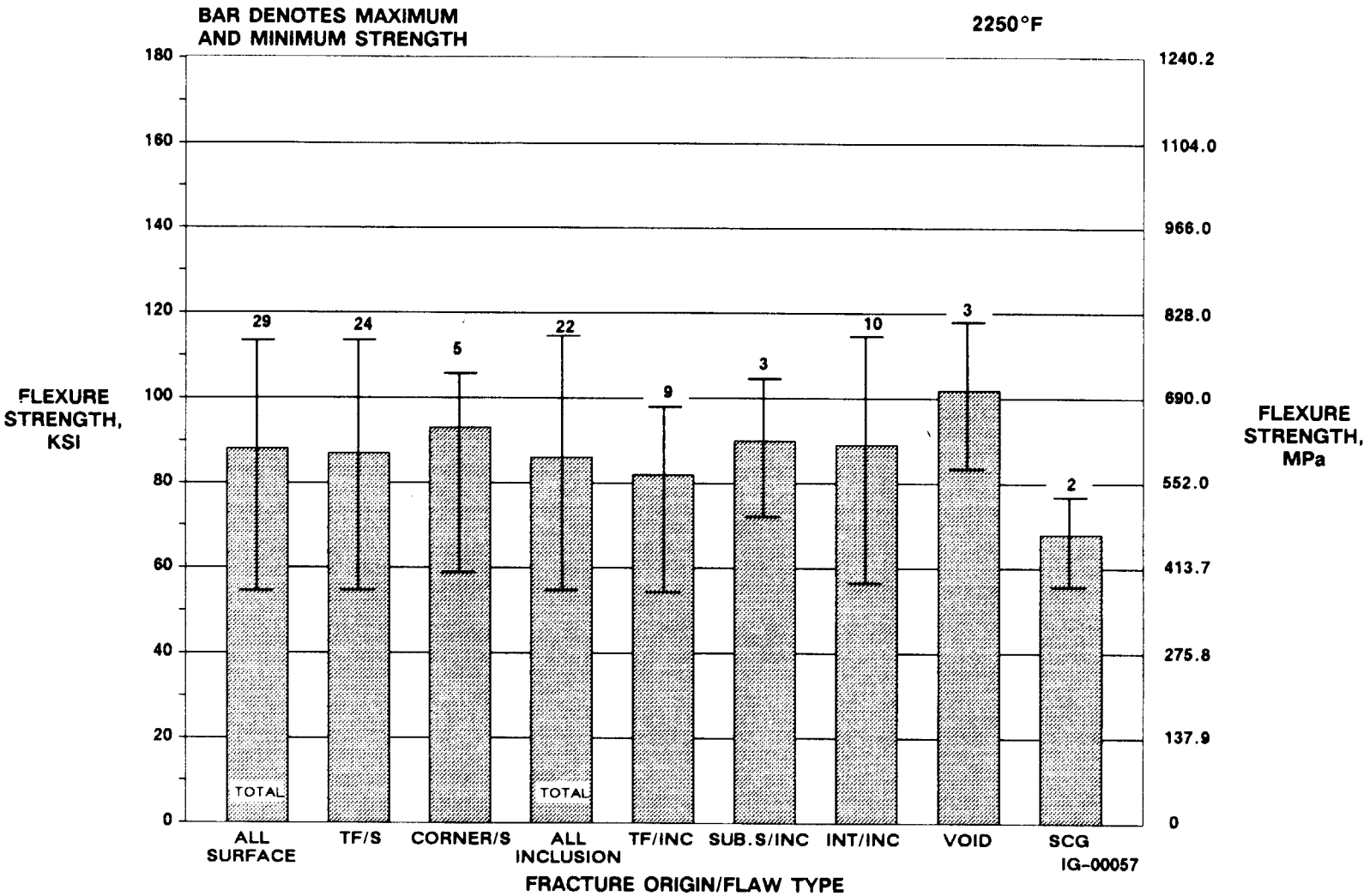

Figure 75.--Fractography Results for Test Bars Tested at 1232°C (2250°F).

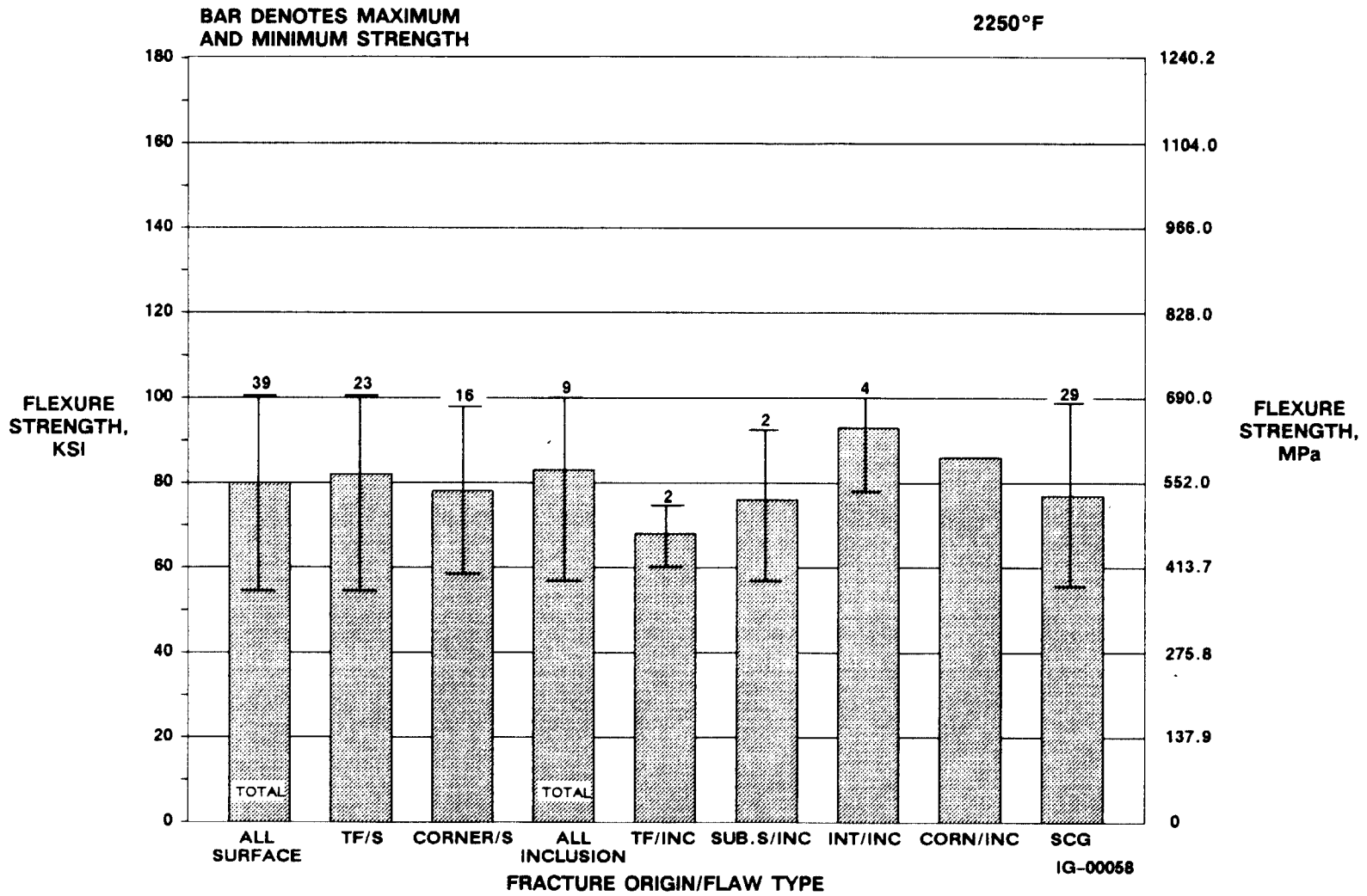

Figure 76.--Fractography Results for Test Bars Tested at 1399°C (2550°F).

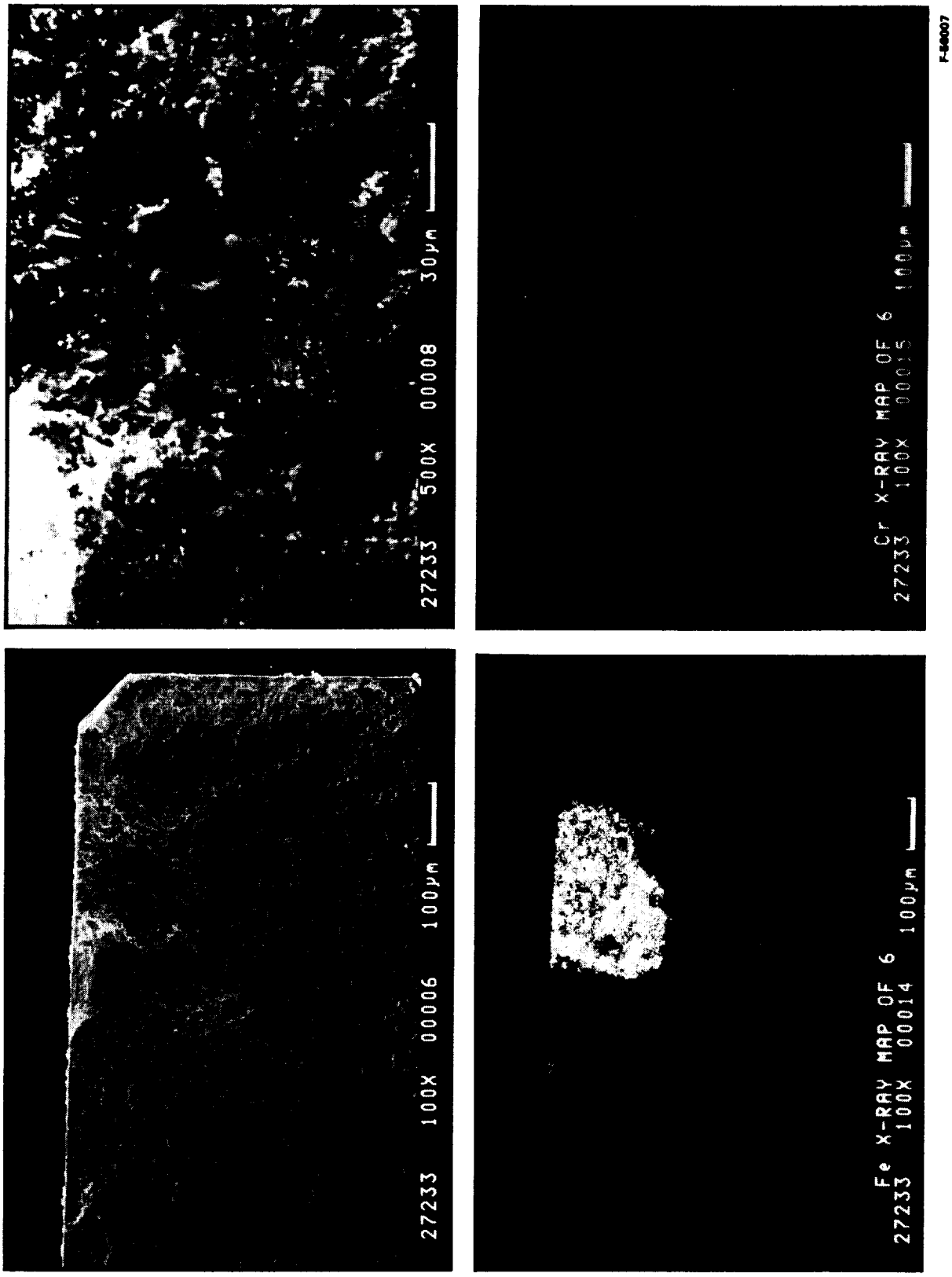

Figure 77.--A Large Surface Inclusion Containing Fe and Cr at the Fracture Origin of Specimen 27233.

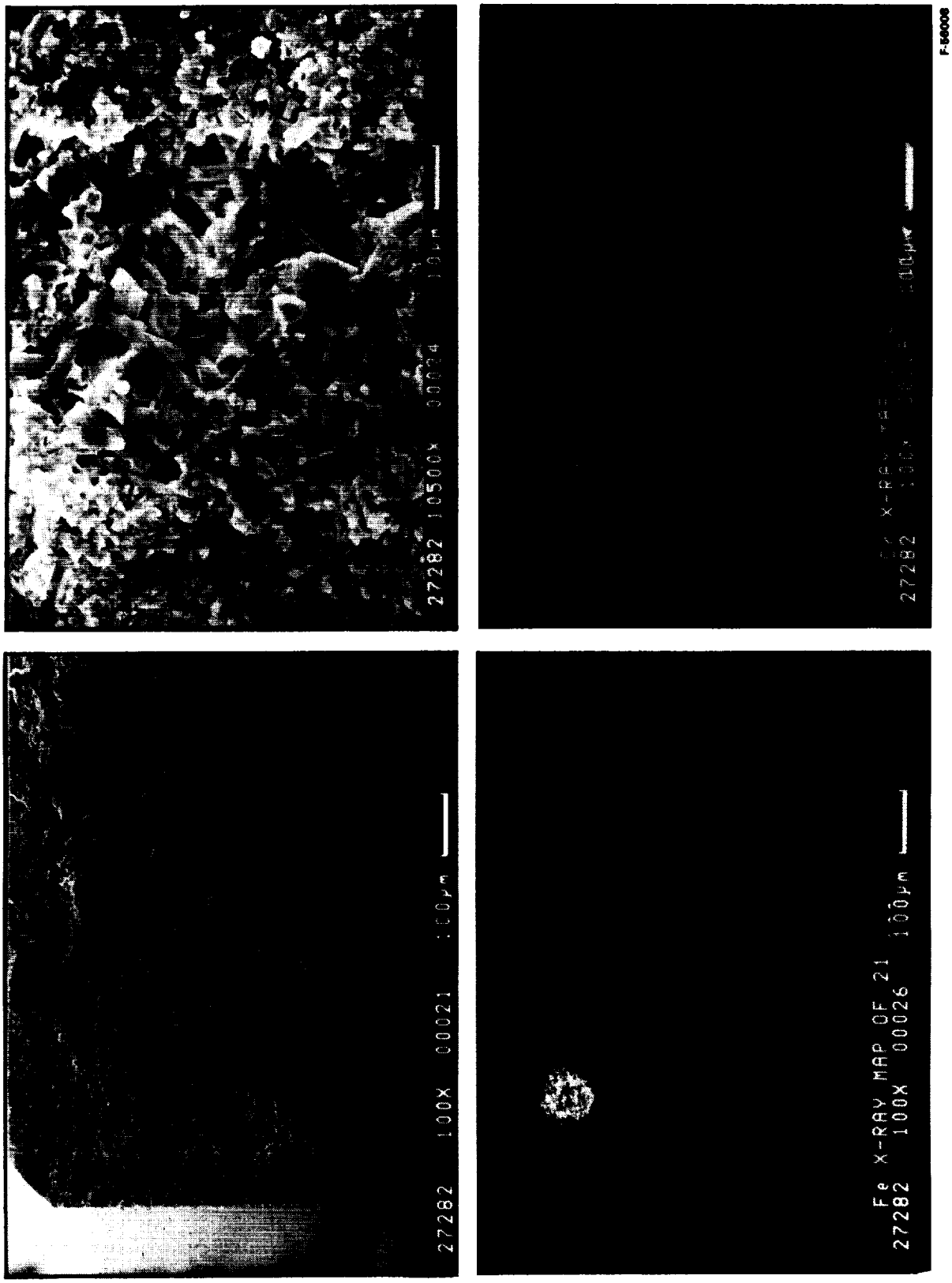

Figure 78.--An Internal Inclusion Containing Fe and Cr at the Fracture Origin of Specimen 27282.

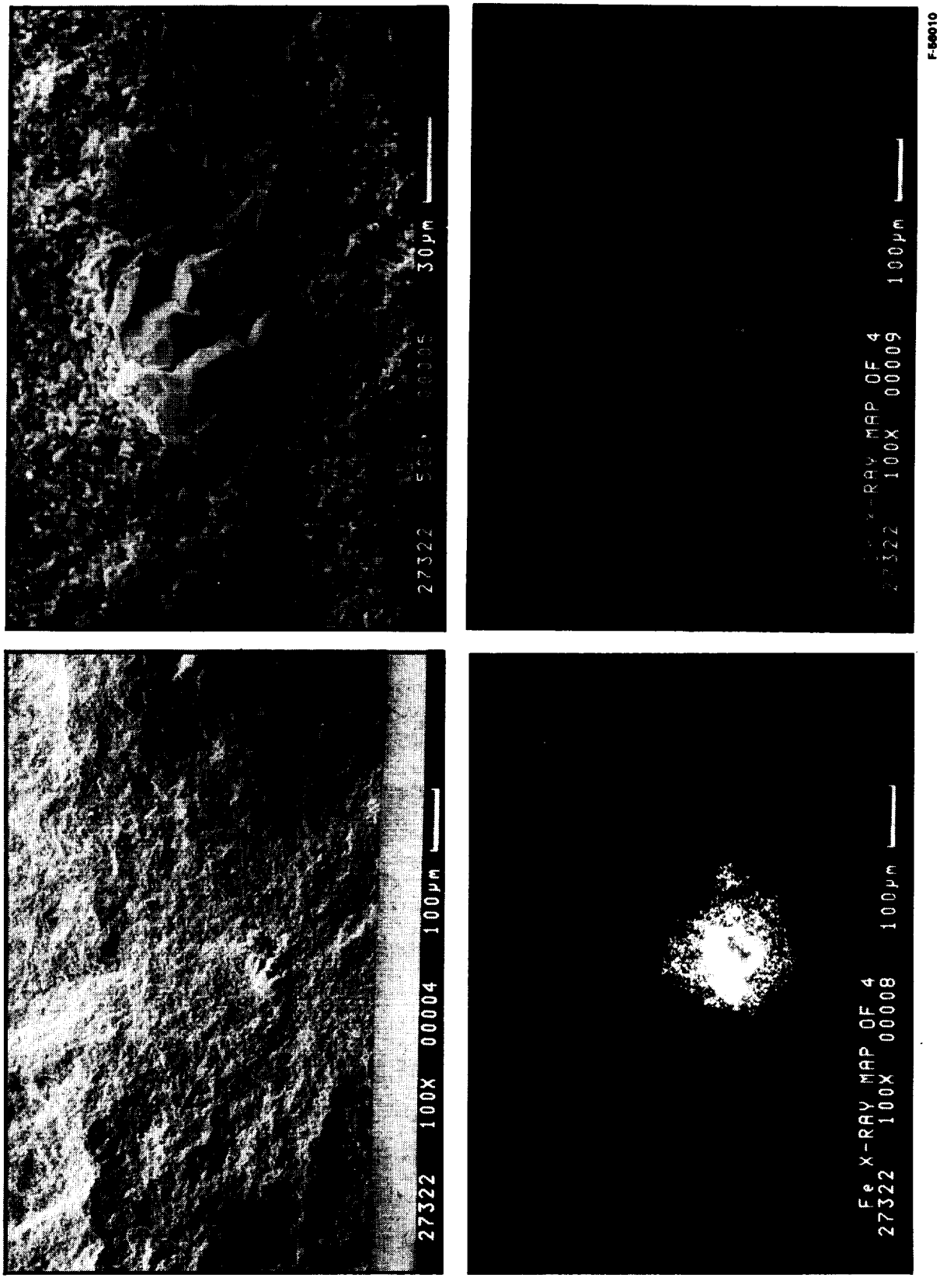

Figure 79.--An Internal Inclusion Containing Fe and Cr at the Fracture Origin of Specimen 27322.

ORIGINAL PAGE
BLACK AND WHITE PHOTOGRAPH

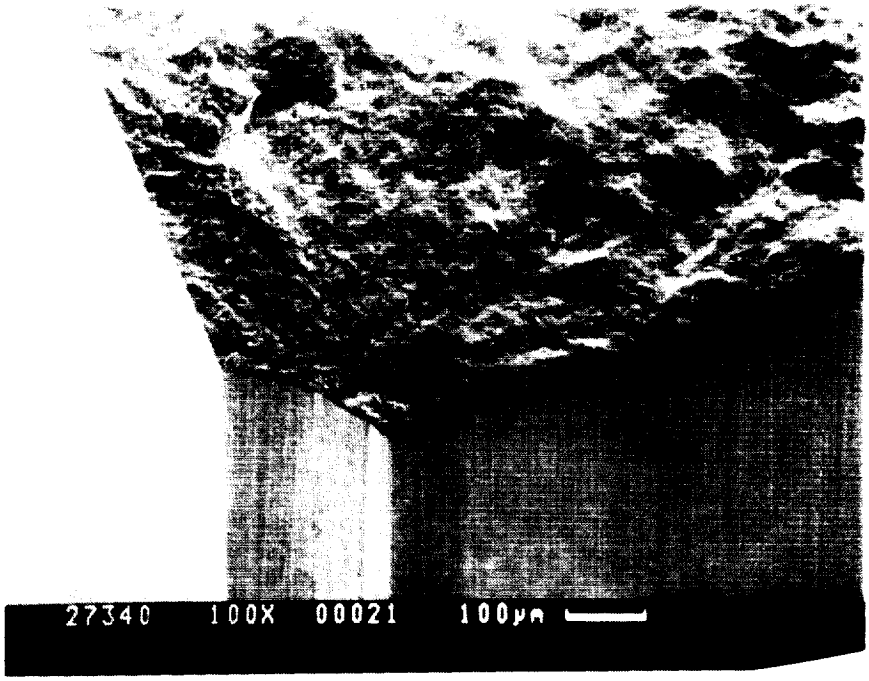

Figure 80.--Failure Originated from Improperly Machined Chamfer.

2.4 PROCESS DEVELOPMENT FOR IMPROVED MATERIAL (GN-10) RELIABILITY AND STRENGTH*

2.4.1 Summary/Introduction

The excellent flexure strength of the GN-10 material was demonstrated in section 2.3 of this report with test bars machined from Nb canned and HIP'ed billets. However, HIP'ed materials tend to have a more uniform flaw distribution and higher strength. Efforts in this section focused on developing the GN-10 composition into a reproducible material using a fabrication process with shape capability, i.e., injection molding and sinter/HIP.

Additional efforts were also made to fabricate this material with high strength and Weibull slope by eliminating the more severe fabrication flaws and improving the sinterability of the material. Previous effort with the "ab" material indicated that the major flaws were metallic inclusions and planar voids near the chamfer corners. Alternate processing approaches aimed at eliminating these defects were evaluated:

(1) Avoid powder contact with equipment that may introduce metallic inclusions.

(2) Use alternative blending methods and mixers.

(3) Modify existing blending parameters.

(4) Polish injection molding die for better surface finish.

(5) De-air the injection molder during molding to collapse voids.

The best processing combination, which included using a different mixer (Henschel), polished die, de-airing mechanism on the Arburg injection molder, and a mixture of ball-milled and attrition-milled powder was identified. A batch of 50 test bars was fabricated with this combination and tested at room and elevated temperatures. Fractography results showed that the metallic inclusions and planar voids at the chamfer corners were successfully eliminated and no identifiable flaws were found. However, due to furnace complications, the effect of defect elimination on flexure strength could not be analyzed due to the low density of these test bars.

2.4.2 Defect Elimination Study of Injection-Molded Material

Five different methods of preparing injection molding mixes were evaluated in an attempt to eliminate flaws and improve the homogeneity of the injection molding powder and binder mix. Test bars representative of each of the approaches were sintered and inspected after each processing step. A brief summary of each approach is listed below.

*Performed under Revised Task II of the contract.

(1) Standard method.--This was the blending method used for all previous test bars. A 4.5-kg batch of powder and wax binder was blended in a Sigma mixer. The wax was first melted in the mixer, then the powder was added to make up a total batch of 4.5 kg containing 14.5 percent wax. The blending action was provided by the counterrotating Sigma-shaped blades in the mixer. The blended material is usually in the form of chunks and is later pelletized using a pelletizer. The pellets were then fed to the Arburg injection molder and molded into test bars for evaluation.

(2) Batch 1.--Same as the standard method, except the powder was heated first in the mixer, and then the wax was added in small chunks. The mixing action was started before all the wax was melted.

(3) Batch 2.--Same as Batch 1, except additional material was added to make up a full load of 6.1 kg to investigate the effect of batch size. However, due to the lack of available powder, about 3.9 kg of previously blended and pelletized material from Batch 1 had to be used.

(4) Solvent Mix.--The wax binder was first dissolved in toluene and the solution was blended with powder in a ball mill. After blending, the toluene was evaporated and the solid material further blended by passing it through the Arburg injection molder.

(5) Henschel Mixer.--The Henschel mixer was used to blend and pelletize the material. A 2.0-kg mixing load was selected.

(6) De-airing.--This process was included during the injection molding process to collapse large voids and prevent the formation of air bubbles in the mix. This was accomplished by connecting a vacuum system to the feeding section of the injection molder to create a partial vacuum in the injection molding chamber. Material from injection molding batches blended by the standard method was used for this study.

Evaluations of the blending methods included visual and x-ray inspection, density, dewaxed weight loss, and MOR and fractography of as-injection-molded and sinter/HIP'ed test bars. The sinter/HIP parameters which produced satisfactory density (3.28 g/cc) GN-10 test specimens during trial sintering runs were selected. However, due to a furnace malfunction, the required sinter/HIP conditions were not met and the test bars only achieved an average density of 3.07 g/cc. The low density accounted for the lower strength (average MOR = 516.1 MPa (74.9 ksi)), but the MOR and fractography results of these test bars were still adequate for comparing the blending methods.

2.4.3 Characterization

Injection-molded, dewaxed, and sintered test bars were tested in four-point blending at room temperature. Fractography was performed on the test bars to characterize the flaws for each of the three conditions.

The MOR and fractography results of the test bars for each blending method are presented in tables E-1, E-2, and E-3 of Appendix E. Overall, the difference due to the blending methods is small, about 10 percent between groups having the highest and lowest MOR. The average MOR is 2.1 MPa (1.03 ksi) for the injection-molded bars, 2.1 MPa (0.302 ksi) for the dewaxed bars, and 516.1 MPa (74.9 ksi) for the sinter/HIP'ed bars.

In order to select the best blending method from these three sets of data, the average MOR, the standard deviation, and the maximum and minimum strength in each group are ranked from 1 to 6, with 1 being the best. The best blending method should be the highest ranked in every group and category. The combined ranking data listed in table 43 show that the new methods are either equal to or better than the standard method. The Batch 1 method appeared to be the best method (see Combined Rank (1)). However, it was felt that the strength data of the injection-molded test bars should not be included in the analysis because the higher strength of the wax binder overshadows the effect of the powder. After excluding the injection-molding data from the analysis (Combined Rank (2)), the Henschel mixer appears to be the best blending method.

Fractography results of the test bars were not included in the ranking analysis because of the difficulty in quantifying the data. However, several significant observations were made. The injection-molded test bars typically failed from the surface or agglomerates. The results are not very useful for identifying flaws that will affect the strength of sinter/HIP'ed bars, because inclusions and binder agglomerates which later become voids are not easily detectable at this stage. Fractography of the dewaxed test bars is useful for characterizing inclusions that are later decomposed during sintering. Examples are the organic fiber and the flaky crystals seen, which are probably left-over polymer components of the wax binder that resisted decomposition during the dewax cycle. The disadvantage of the dewaxed test bars is the difficulty in preserving the fracture surface, because they are very fragile.

2.4.4 Sinter/HIP and Reproducibility of GN-10

A 2^2 factorial experimental matrix (table 44) was used to evaluate the effect of particle size distribution (PSD) and injection molder. The PSD difference was produced by milling procedure difference. In table 44, GN-10 designates the GN-10 formulation powder prepared by the standard ball milling procedure; PM-4 designates the GN-10 formulation powder consisting of a mixture of standard ball-milled and finer attrition-milled powder. The effort was directed toward fabricating high-strength and high-Weibull-modulus injection-molded GN-10 Si_3N_4 test bars. The matrix requires a total of 200 test bars fabricated using two different powder batches (GN-10 and PM-4) and injection molded by two different molders (table 44). Additional test bars were used in trial sintering cycles to develop the proper sinter/HIP parameters that will produce GN-10 test bars with a minimum sintered density of 3.20 g/cc.

PM-4 starting powder and Arburg injection molder was found to be the best processing combination for the highest strength test bars based on flexure strength results.

TABLE 43.--STRENGTH RANKING COMPARISON OF DIFFERENT BLENDING METHODS

Blending Methods	Standard	Solvent	Henschel	De-Air	Batch 1	Batch 2
Injection molded						
Average MOR	3*	5	6	4	1	2
Std. Dev.	6	1	3	2	4	5
Highest MOR	3	5	6	4	1	2
Lowest MOR	4.5	3	6	4.5	2	1
Group Rank	5	3	6	4	1	2
Dewaxed						
Average MOR	3	6	1	5	2	4
Std. Dev.	4	5	6	3	2	1
Highest MOR	4	3	1	5.5	2	5.5
Lowest MOR	6	5	4	3	1	2
Group Rank	5	6	2	4	1	3
Sinter/HIP'ed						
Average MOR	6	3	1	5	4	2
Std. Dev.	5	6	1	4	3	2
Highest MOR	3	2	6	4	1	5
Lowest MOR	3	4	1	5	5	2
Group Rank	5	4	1	6	3	2
Combined Rank (1) Injection molded, dewaxed, and sinter/HIP'ed	6	4	3	5	1	2
Combined Rank (2) Dewaxed and sinter/HIP'ed	4	4	1	2	3	4

*Numbers denote rank in each category (1=best, 6=worst).

2.4.4.1 Injection Molding and Sinter/HIP

Two different batches of powders, GN-10 and PM-4, were used. The chemical composition and the median (50 percentile) particle size of these two batches of powders are the same. However, the GN-10 batch consisted of 100 percent ball-milled powders, while PM-4 consisted of 25 percent ball-milled powder and 75

TABLE 44.--2^2 FACTORIAL MATRIX

	Powder Batch	
Injection Molder	GN-10	PM-4
Arburg	50*	50
Battenfeld	50	50

*Number of test bars required

percent attrition-milled powder. The attrition-milled powder had a narrower particle size distribution. The powders and binders were mixed in a rotating blade mixer (Henschel) and the mix injection molded into test bars by two injection molders. The test bars were subsequently CIP'ed in rubber bags after dewaxing to increase the green density.

The first sinter/HIP run of the experimental matrix was performed using optimized sinter/HIP parameters developed from the trial sintering runs. Among the 120 test bars sintered, 92 test bars with acceptable density, surface condition, and specimen geometry (i.e. not severely warped) were obtained for flexure strength testing at room temperature, 1232°C (2250°F), and 1399°C (2550°F). The strength results were used to decide which combination of processing conditions should be used to fabricate the Task III confirmation test bars.*

2.4.4.2 Strength Results

A summary of the room temperature, 1232°C (2250°F), and 1399°C (2550°F) flexure strength of the test bars is listed in table 45. The individual test bar data are presented in Appendix F. Table 45 shows the average, maximum, and minimum strength for each processing group. The individual room temperature test bar strengths are also plotted in figure 81 to show their distribution. The data showed large variations of strength in each group.

Table 45 also shows that test bars made from PM-4 powders and injection molded by the Arburg injection molder have the highest strength. In fact, there is a noticeable trend of higher strengths from test bars made with the PM-4 powders and/or from the Arburg molder. The narrower particle size distribution of the PM-4 powders and the de-airing feature on the Arburg molder may have contributed to the higher strength. The strength difference becomes insignificant at high temperature where the strength is insensitive to processing flaws.

*Fabrication of test bars using optimized parameters to demonstrate reproducibility.

TABLE 45.--SUMMARY OF STRENGTH OF TEST BARS FABRICATED IN DIFFERENT POWDER/MOLDER COMBINATIONS

Powder/Molder	Strength, ksi								
	Room Temperature			2250°F			2550°F		
	Avg.	Max.	Min.	Avg.	Max.	Min.	Avg.	Max.	Min.
PM-4/Arb	94.0 (14)	116.0	81.9	71.6 (6)	76.3	59.6	51.9 (4)	54.5	46.8
PM-4/Bat	88.3 (13)	115.4	57.9	70.1 (5)	80.8	52.5	51.2 (5)	53.5	48.5
GN-10/Arb	87.8 (13)	110.0	70.7	67.8 (5)	79.8	47.5	49.7 (5)	51.5	47.7
GN-10/Bat	82.4 (10)	97.7	69.5	64.7 (5)	71.6	53.4	50.2 (5)	53.1	42.9

Note: Numbers in parentheses indicate number of test bars tested.

PM-4: A mixture of attrition-milled and regular ball-milled GN-10 powder.
GN-10: Regular ball-milled GN-10 powder.
Arb: Arburg injection molder.
Bat: Battenfeld injection molder.

2.4.4.3 Fractography

Optical fractography was performed on all of the test bars to identify fracture origins. The results are presented in Appendix E and summarized in table 46. Most of the test bars failed from the surface of chamfer corners, while some failed from the tensile surface. Only one inclusion and three voids were observed at the fracture origins. The results indicate that the fabrication process has improved and successfully eliminated the metallic inclusions that were frequently observed in previous test bars.

There were large variations in the room temperature strength of these test bars. Some test bars had low strengths around 482.3 MPa (70 ksi). Optical fractography showed that they all failed from chamfer corners, but no distinct flaws were observed. The large number (62 percent) of test bars failing from the chamfer corners is of concern, especially since their average strength is lower than those failing from the tensile surface (590.5 MPa (85.7 ksi)) compared with 654.6 MPa (95.0 ksi) for all the room temperature test bars).

Test bars that failed at 1399°C (2550°F) exhibited slow crack growth, as indicated by the load chart and fracture surface features.

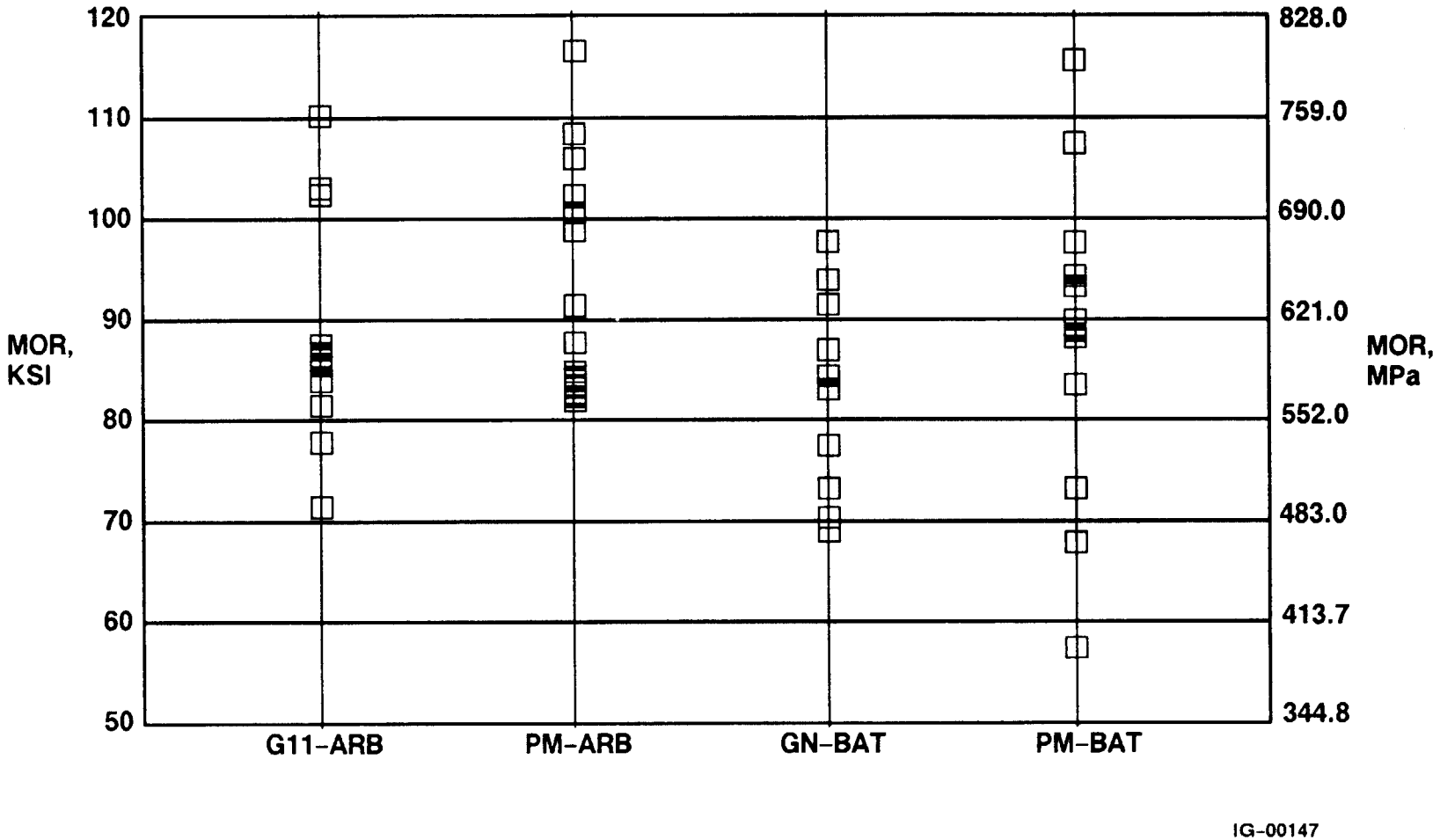

Figure 81.--Room Temperature MOR Comparison of Test Bars, Injection Molded, Sinter/HIP, at 1900°C (3452°F) and 10.3 MPa (1500 psi).

TABLE 46.--CORRELATION OF FLEXURE STRENGTH WITH IDENTIFIED FRACTURE ORIGIN FLAWS

Powder/ Molder	Flaw Origin Description	Strength, ksi								
		Room Temperature			1232°C (2250°F)			1399°C (2550°F)		
		Avg.	Max.	Min.	Avg.	Max.	Min.	Avg.	Max.	Min.
PM-4 Arb.	Tensile surface	96.1 (7)	108.8	81.9	71.6 (6)	76.3	59.6	51.1 (3)	53.9	46.8
	Corner surface	91.9 (7)	116.0	92.2	(0)			54.5 (1)		
PM-4 Bat.	Tensile surface	92.7 (4)	115.4	73.0	70.1 (5)	80.8	52.5	51.2 (5)	53.3	48.5
	Corner surface	86.3 (9)	108.1	57.9	(0)			(0)		
GN-10 Arb.	Tensile surface	95.3 (6)	110.0	85.2	72.8 (4)	79.8	64.5	49.7 (5)	51.5	47.7
	Corner surface	81.3 (7)	87.6	70.7	(0)			(0)		
GN-10 Bat.	Tensile surface	(0)	108.8	81.9	69.0 (3)	71.6	67.6	50.2 (5)	53.1	42.9
	Corner surface	83.7 (9)	97.7	69.5	(0)			(0)		
Total	Tensile surface	95.0 (17)	115.4	73.0	71.0 (18)	80.8	52.5	50.4 (18)	53.9	42.9
	Corner surface	86.7 (32)	116.0	57.9	(0)			54.5 (1)		

Note: Numbers in parentheses indicate number of test bars tested.

In conclusion, the fabrication process using attrition-milled powders, Henschel mixer, and the de-airing injection molding technique resulted in test bars without detectable defects at the fracture origin. However, the flexure strength is lower than the HIP'ed material, probably due to the difference in microstructure.

2.5 DEVELOPMENT OF SIC WHISKER/Si_3N_4 MATRIX COMPOSITE*

2.5.1 Introduction/Summary

The widespread use of high-temperature Si_3N_4 for heat engine applications requires not only high strength and high reliability but also high toughness. One approach to improve the toughness is to reinforce the matrix with a high-temperature phase such as SiC whiskers (SiC_w). In this effort, exploratory experiments were conducted to fabricate dense SiC_w/Si_3N_4 composites and to characterize their properties.

Both the improved baseline Si_3N_4 formulation ("ab") and the newly developed high-temperature GN-10 were used as matrix materials. The goal was to develop a composite with both high-temperature strength and high toughness. Whiskers from two suppliers were evaluated as reinforcements: one from Tokai Carbon Company, the other from Advanced Composite Materials Company (ACMC, formerly ARCO). A uniform dispersion of whiskers in Si_3N_4 was achieved with both dry and wet blending techniques. Green samples were successfully fabricated by cold isostatic processing (CIP'ing) and injection molding. Whisker loadings investigated ranged from 10 through 30 wt%. A series of sinter/HIP experiments were conducted to determine the feasibility of densifying SiC_w/Si_3N4 composites without encapsulation. The best density achieved was 2.60 g/cc (80 percent theoretical). Experimental data indicated that SiC whiskers reacted with the N_2 sintering atmosphere to become Si_3N_4, thereby losing their identity. Also, the presence of SiC whiskers in the matrix powder probably retarded the conventional sintering mechanisms. The conclusion was reached that encapsulated HIP was necessary in order to achieve full density. One such experiment was conducted using ASEA glass encapsulation, a technique with net-shape potential. Full density was achieved for both 20 percent Tokai SiC whisker/GN-10 matrix and 20 percent ACMC SiC whisker/GN-10 matrix samples. Relative to the co-processed monolithic GN-10, up to 14 percent improvement in toughness was achieved; however, the flexural strength of the composites was lower. Between the two whiskers evaluated, the ACMC whisker was superior in achieving reinforcement.

2.5.2 Fabrication

2.5.2.1 Materials

The improved baseline Si_3N_4 (92% Denka Si_3N_4, 6% Moly Corp. Y_2O_3, and 2% Linde A Al_2O_3) and the newly developed GN-10 were selected as the matrix materials. They were milled using the procedures established for the improved baseline and GN-10, respectively. The baseline formulation (Code 2) was selected for its relative ease of densification and wide data base available; the GN-10 was selected for its high-temperature strength.

The Tokawhisker SiC whisker from Tokai Carbon Co. and ACMC SC-9 SiC whisker were selected for investigation. The Tokawhisker SiC whisker was selected because its chemistry and morphology appeared to be the most promising among all the commercially available SiC whiskers. The ACMC SC-9 whisker was selected

*Performed under Task II of the contract.

because it was found to be the best SiC whisker among all the SiC whiskers evaluated under an ORNL/DOE composite program conducted at GCC. However, the ACMC SC-9 SiC whisker was not available in unblended form at the time the selection was made. The composite mixture containing 20 percent SC-9 SiC_w and 80 percent GN-10 used in this study was blended at ACMC by a proprietary technique with GN-10 matrix powder supplied by GCC. Consequently, most of the green processing studies were conducted only with the Tokawhisker SiC whisker.

2.5.2.2 Green Forming

The Tokawhisker was cleaned by a sedimentation technique prior to blending with the matrix powder. Both dry milling and wet slip blending methods were used to blend Tokawhisker SiC whisker with either Code 2 or GN-10 powders. The blended composite mixtures were formed into billets by cold isostatic pressing or test bars by injection molding. The billets (2.5 inches dia by 3 inches high) were formed by CIP'ing in a rubber die at 379.0 MPa (55 ksi). The billets often exhibited lamination (or cracking) after CIP'ing. The problem was solved by high compaction of the composite mixture into the die prior to CIP'ing. For injection molding of composite test bars, higher binder contents were required as the whisker loading was increased. The baseline dewax cycle was satisfactory for binder removal from composite test bars.

2.5.2.3 Densification

Most whisker-reinforced ceramic composites reported in the literature were densified by hot pressing. It is more desirable to densify composites by net-shape methods such as unencapsulated sinter/HIP and glass-encapsulated HIP. Both of these techniques were evaluated in this study.

A series of sinter/HIP experiments were performed using injection-molded test bars which consisted of Code 2 matrix with 10, 20 and 30 percent Tokawhisker SiC_w. These test bars were dewaxed using the baseline cycle prior to sinter/HIP. The concept of sinter/HIP is first to form a closed pore structure in the matrix by conventional sintering and then to HIP the composite compact to high density. High N_2 overpressure (0.69 to 2.07 MPa (100 to 300 psi)) is required to achieve sintering of the Si_3N_4 matrix. The initial experiments were conducted in a sinter/HIP furnace (1033.5 MPa (1500 psi max.)), starting with the cycle established for the "ab" material/process. The results consistently showed low densities and high weight gains of the samples. The highest density achieved was only 2.60 g/cc (80 percent theoretical). The density decreased with increasing SiC whisker loading, while the amount of weight gain increased with SiC whisker loading. Table 47 shows the results of one of the sinter/HIP experiments. The trend in weight gain with SiC_w loading along with X-ray diffraction data suggested that SiC whiskers had the tendency to react with the N_2 atmosphere to form Si_3N_4. This is supported by thermodynamic calculations as shown by the stability diagram (between SiC and Si_3N_4) in figure 82. The high-temperature, high-N_2 overpressure required for achieving sintering of Si_3N_4 in the initial stage of the sinter/HIP run favored the conversion of SiC to Si_3N_4. Subsequent experiments with the introduction of Argon or a mixture of N_2/Argon in sinter/HIP did not enhance densification. Results

TABLE 47.--SUMMARY OF SINTER/HIP OF Si_3N_4 AND SiC COMPOSITES

Sinter/HIP condition: 1750°C, 1 hr hold, 100 psi N^2
1800°C, 4 hr hold, 1500 psi N^2

Bar Number	Composition	Layer Number**	Density, g/cc	Weight Change, percent
6002	20% SiC (dry)*	2	2.06	+ 5.49
6004A	20% SiC (dry)	2	2.20	+ 4.97
6042	10% SiC (wet)	2	2.25	+ 1.72
6043A	10% SiC (wet)	2	2.45	+ 1.05
6067	20% SiC (wet)	2	1.97	+ 5.68
6066A	20% SiC (wet)	2	2.12	+ 5.18
6110	30% SiC (wet)	2	1.78	+ 9.96
6098A	30% SiC (wet)	2	1.96	+ 9.10
6004	20% SiC (dry)	4	2.12	+ 4.68
6043	10% SiC (wet)	4	2.23	+ 0.73
6066	20% SiC (wet)	4	2.02	+ 4.76
6098	30% SiC (wet)	4	1.91	+ 8.99

*Mixing method.
**Number 2 is lower than number 4.

described in the recent literature indicate that densification of whisker-reinforced ceramic composites by unencapsulated sinter/HIP requires either an excessive amount of liquid phase during sintering or the limitation of whisker contents to 10 percent. Matrix compositions that form a large amount of liquid phase during sintering normally have inferior high-temperature strength, while composites with whisker loadings of 10 percent or lower do not exhibit the desired toughening effect. Based on the above information, it was concluded that densification of SiC whisker-reinforced Si_3N_4 with sintering aid compositions appropriate for good high-temperature strength can only be densified by either hot pressing or encapsulated HIP.

Glass-encapsulation/HIP was chosen in this investigation because of its good potential for net-shape forming of engine components. Composite billets containing 20 percent Tokawhisker SiC and 80 percent GN-10 matrix, and 20 percent ACMC SiCw and 80 percent GN-10 matrix were glass-encapsulated/HIP'ed at 1800°C (3272°F), 192.9 MPa (28 ksi) for 4 hours at ASEA. A glass-encapsulated monolithic GN-10 billet was glass-encapsulated/HIP'ed in a separate run using identical cycle parameters. All billets achieved full density. The billets were ultimately machined into MOR and fracture toughness (K_{IC}) bars for characterization.

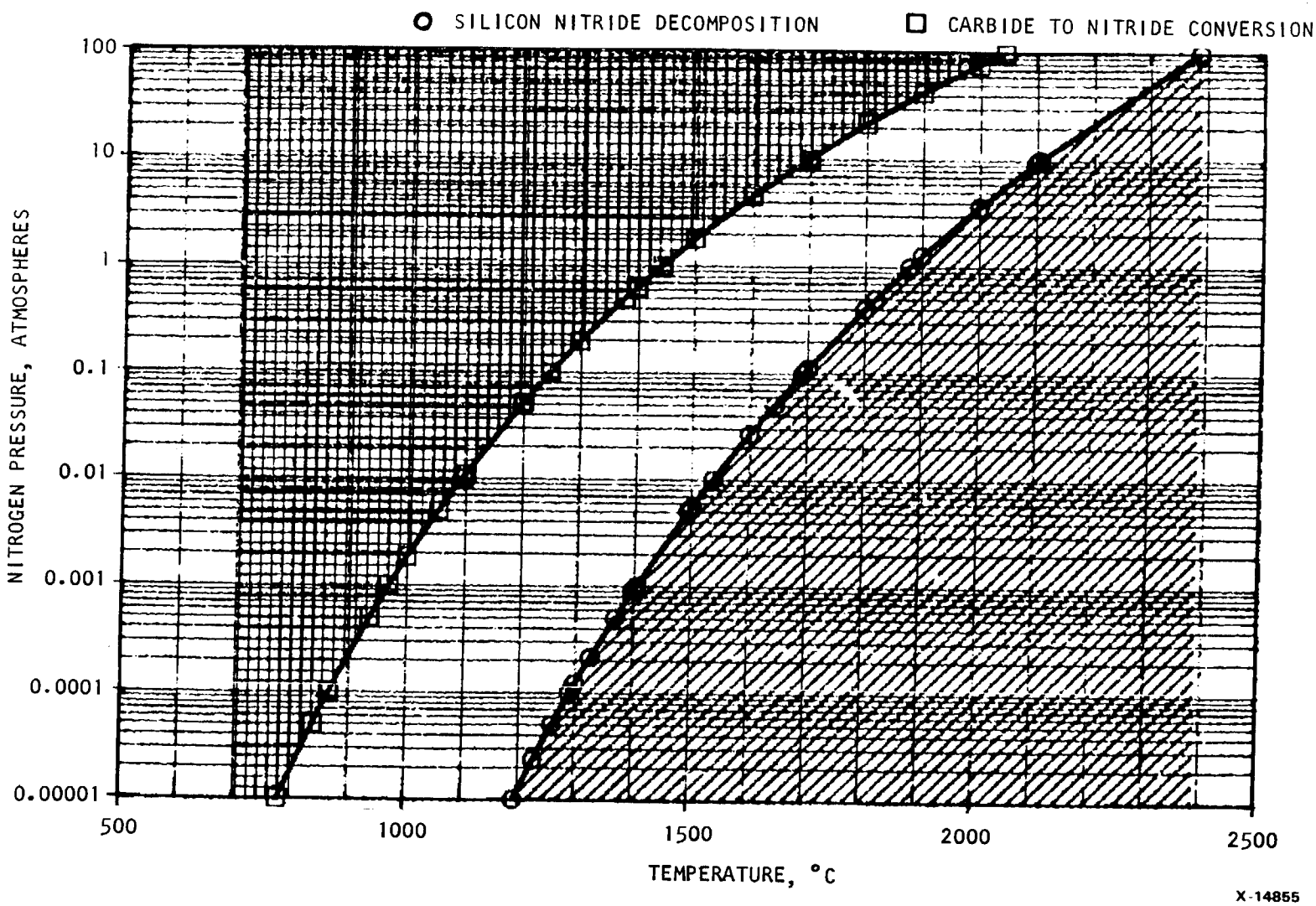

Figure 82.--Silicon Carbide/Nitride Stability Diagram.

2.5.2.4 Characterization

No characterization was conducted on ACMC SC-9 SiC_w used in this investigation because these whiskers were not available in unblended form. SEM micrographs of the as-received Tokai SiC whiskers (Tokawhiskers) are shown in figures 83 through 85. The whiskers form agglomerates (figure 83) with diameters ranging from about 20 to 200 microns. Detailed micrographs of the loose whiskers, indicated by arrow A in figure 83, and whiskers from an agglomerate, indicated by arrow B in figure 83, are shown in figures 84a through 84c, and figures 85a through 85c, respectively. Both sets of micrographs show that the whiskers vary greatly in length, between about 3 and 40 microns, and contain many kinked or crooked whiskers.

The milled Si_3N_4 matrix powders were mixed with 10-, 20-, and 30-wt% SiC whiskers by either dry milling or liquid mixing. The fracture surface of a typical 20-wt% whisker/powder mixture is shown in figures 86a through 86d. This mixture was prepared by liquid mixing and shows good whisker dispersion in the powder matrix. A mixture of the same composition but prepared by 30 minutes of dry milling is presented in figures 87a through 87d. The mixture is also well dispersed and appears identical to the liquid mixed mixture.

Injection molding mixtures with 10, 20, and 30 wt% of whisker content were examined by SEM to evaluate whisker dispersion. For the 20-wt% whisker content mixture, liquid mixing and dry milling samples were included. The fracture surfaces of the samples are shown in figures 88 through 91. All of the surfaces appeared identical, with whiskers projecting from a relatively flat fracture surface. The whiskers and the powders were covered with the wax binder.

Figure 83.--As-Received SiC Tokai Tokawhiskers Showing Whiskers (Indicated by Arrow A) and Whisker Agglomerate (Indicated by Arrow B).

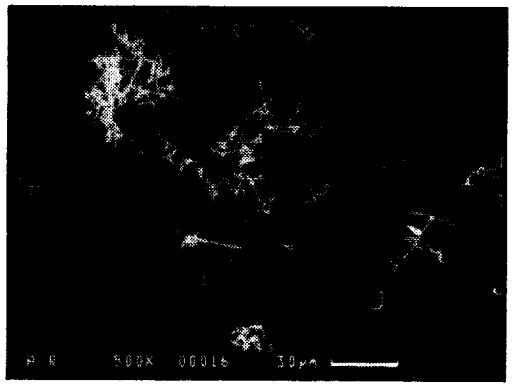

(a)

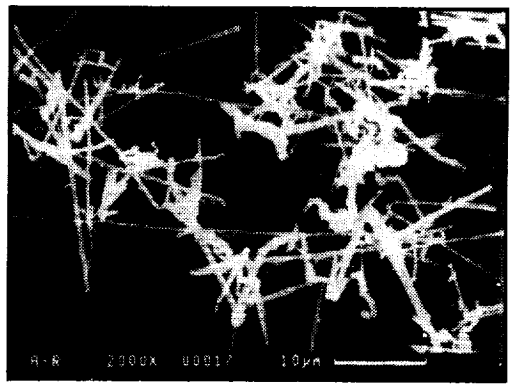

(b)

(c)

F-52456

Figure 84.--As-Received SiC Tokai Tokawhiskers (Indicated by Arrow A in Figure 83).

ORIGINAL PAGE
BLACK AND WHITE PHOTOGRAPH

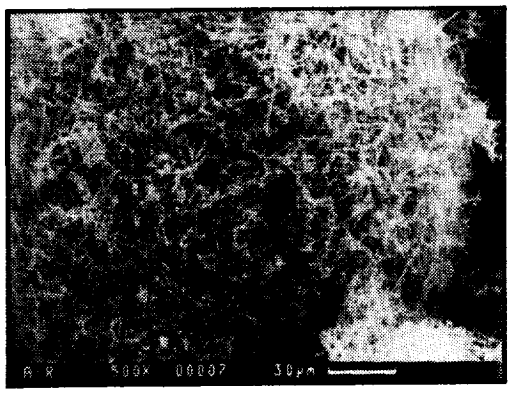

(a)

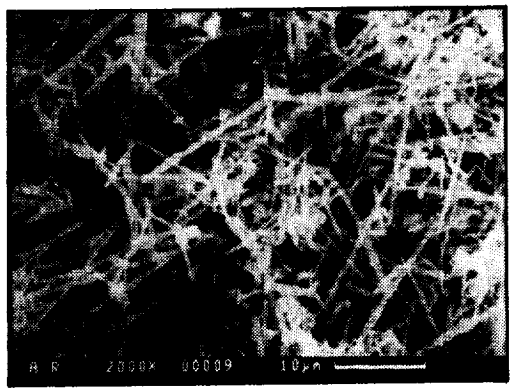

(b)

(c)

F-52457

Figure 85.--As-Received SiC Tokai Tokawhisker Whisker Agglomerate (Indicated by Arrow B in Figure 83).

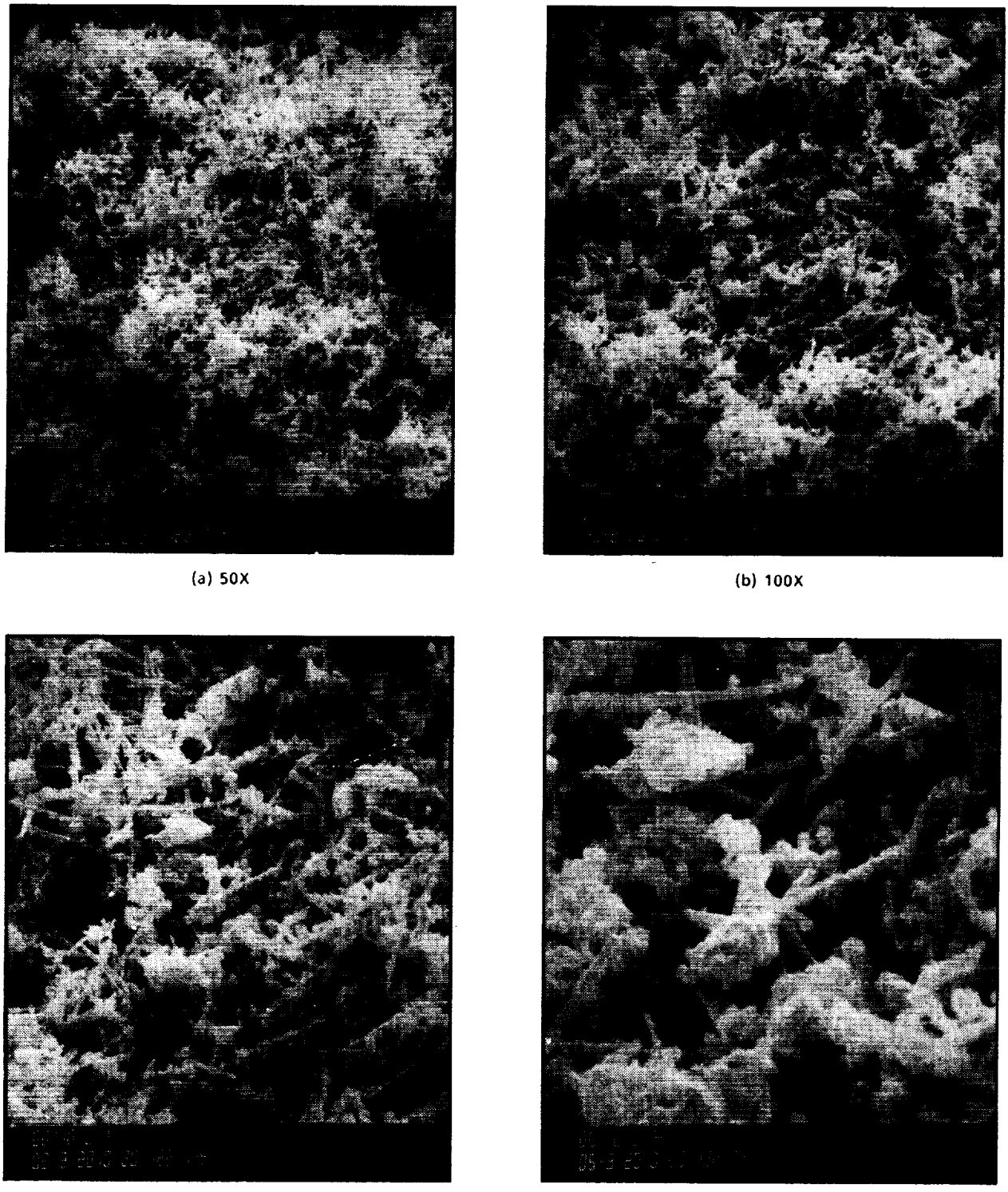

(a) 50X

(b) 100X

(c) 2000X

(d) 5000X

F-52462

Figure 86.--Fracture Surface of a 20-wt% Tokawhisker Powder Mixture Mixed by Liquid Mixing.

ORIGINAL PAGE
BLACK AND WHITE PHOTOGRAPH

(a) 50X

(b) 100X

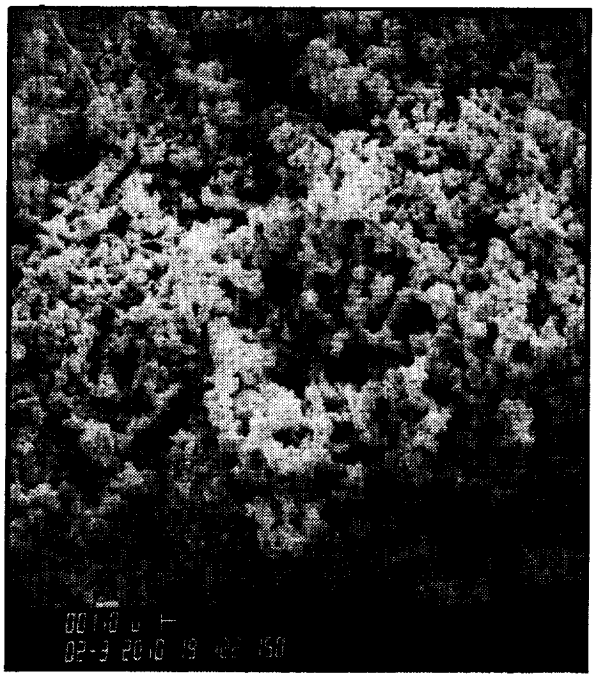

(c) 2000X

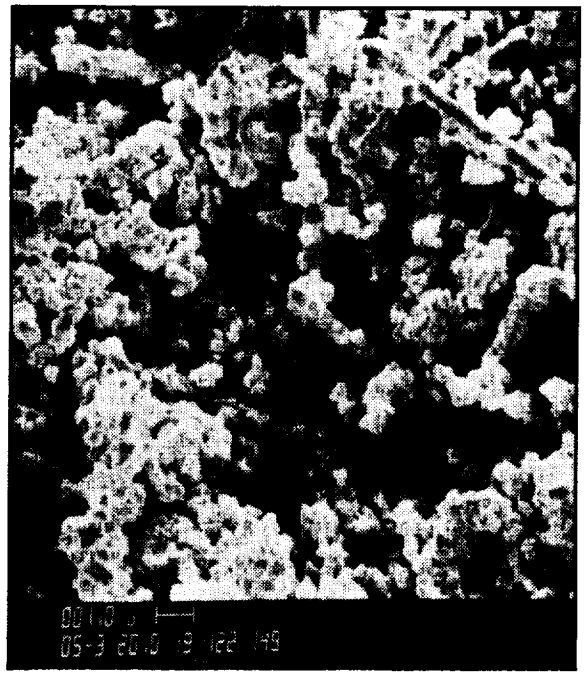

(d) 5000X

F-52463

Figure 87.--Surface of a 20-wt% Tokawhisker/Powder Mixture. (The sample was mixed by 30 minutes of dry milling. Note agglomerates in (a) and (b).)

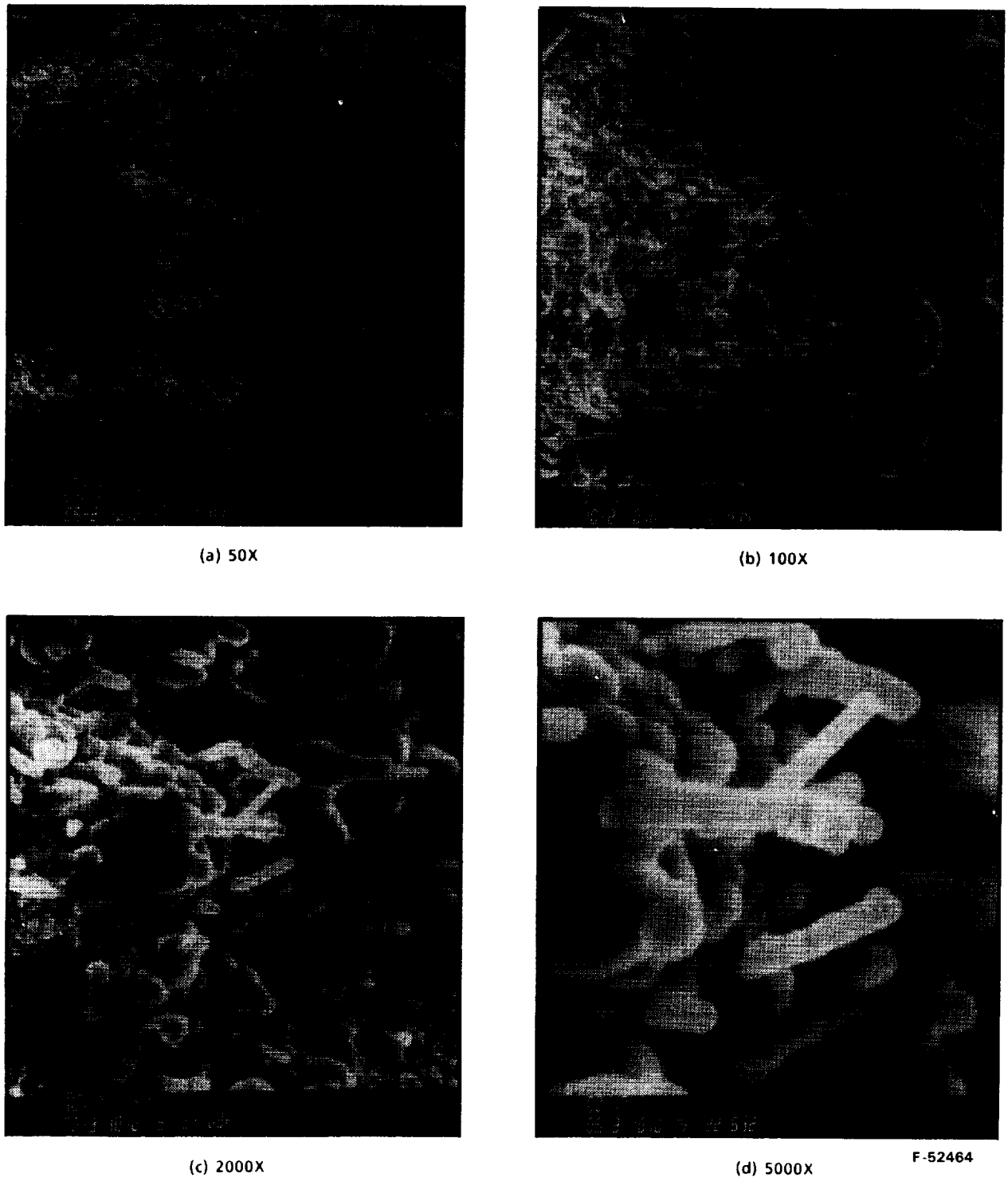

(a) 50X

(b) 100X

(c) 2000X

(d) 5000X

F-52464

Figure 88.--Fracture Surface of a 10-wt% Whisker Content Injection Molding Mix with 19.0-wt% Wax. (The whisker/powder was mixed by liquid mixing.)

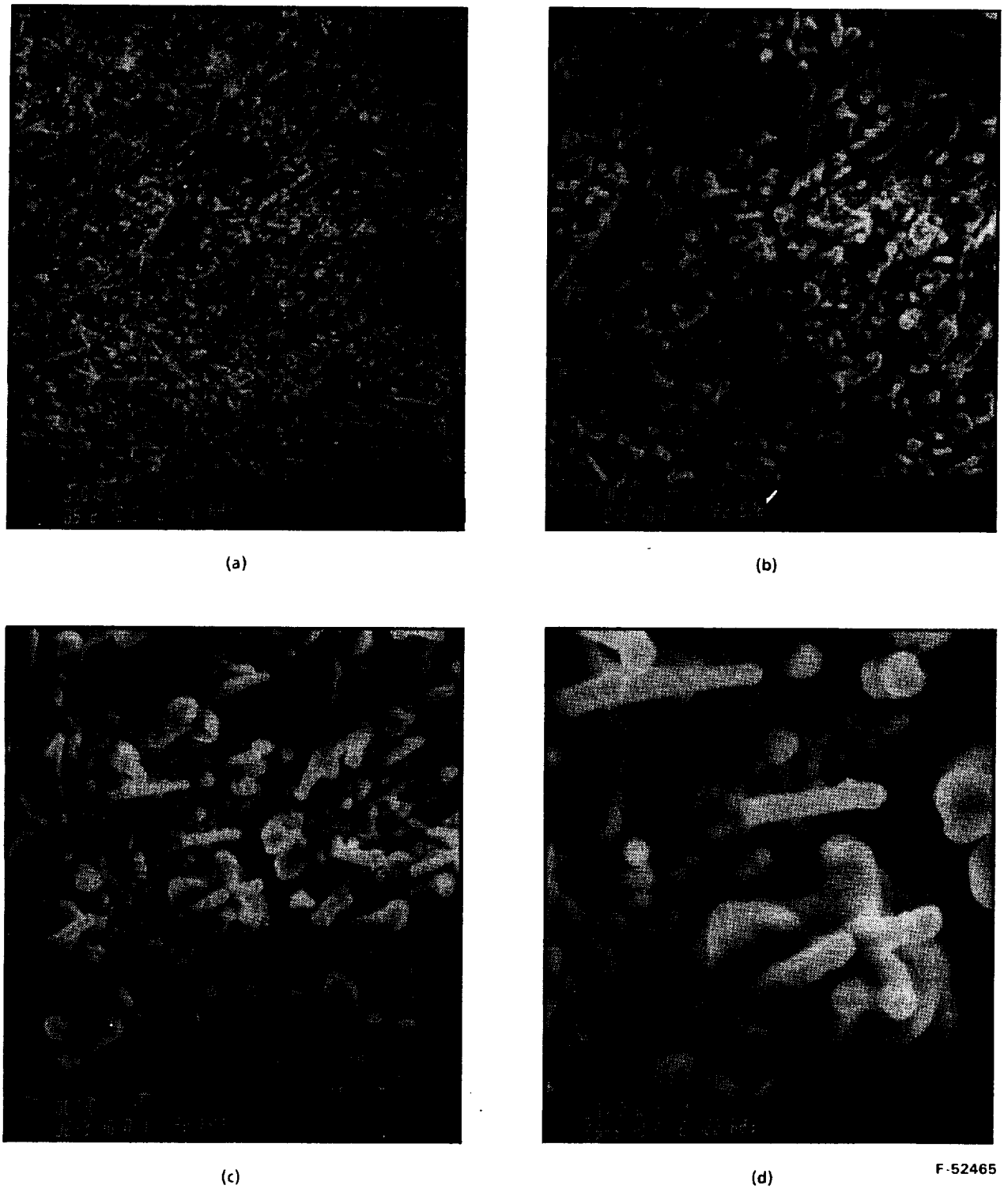

Figure 89.--Fracture Surface of a 20-wt% Whisker Content Injection Molding Mix with 19.0-wt% Wax. (The whisker/powder was mixed by dry milling.)

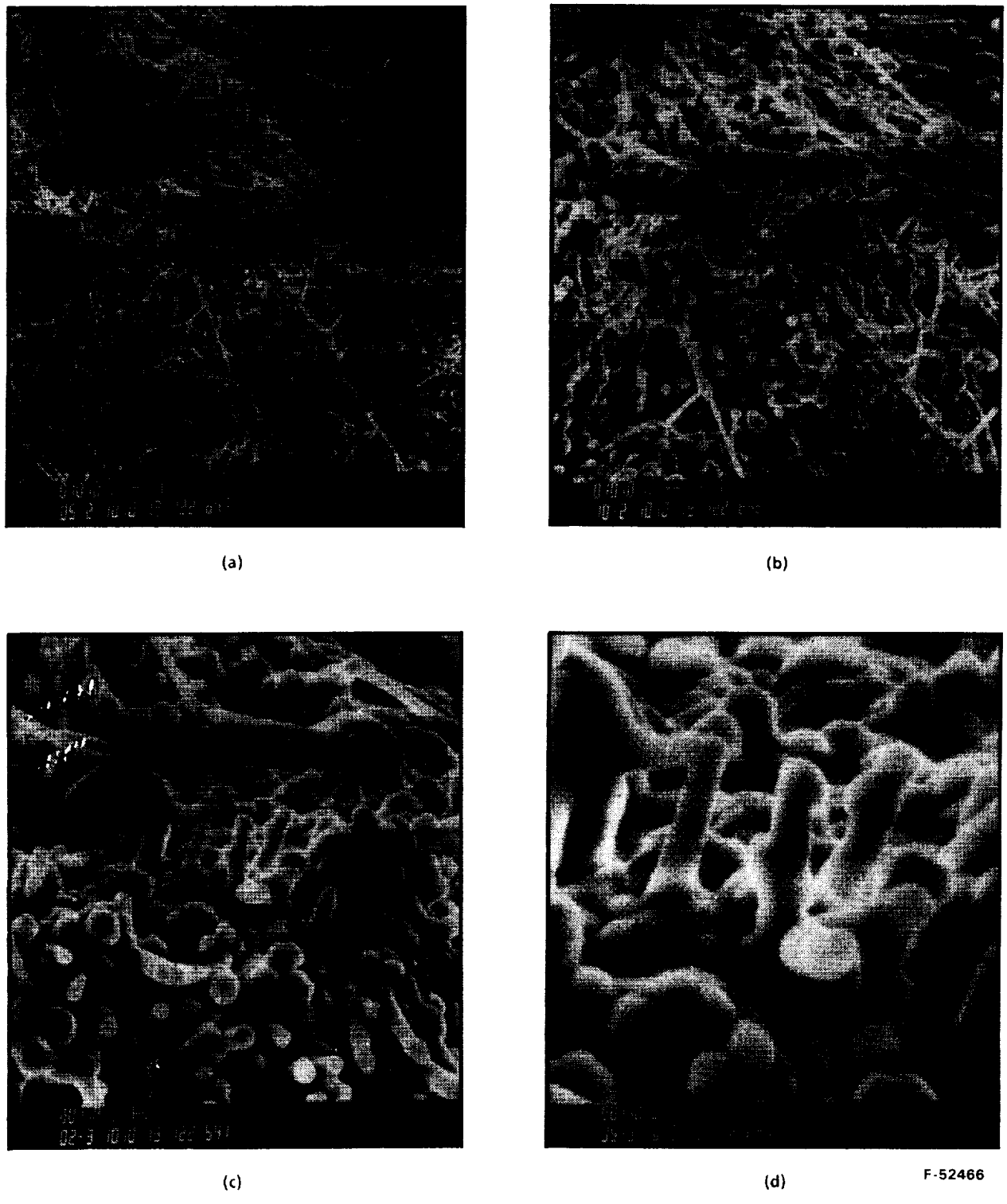

Figure 90.--Fracture Surface of a 20-wt% Whisker Content Injection Molding Mix with 21.5-wt% Wax. (The whisker/powder was mixed by liquid mixing.)

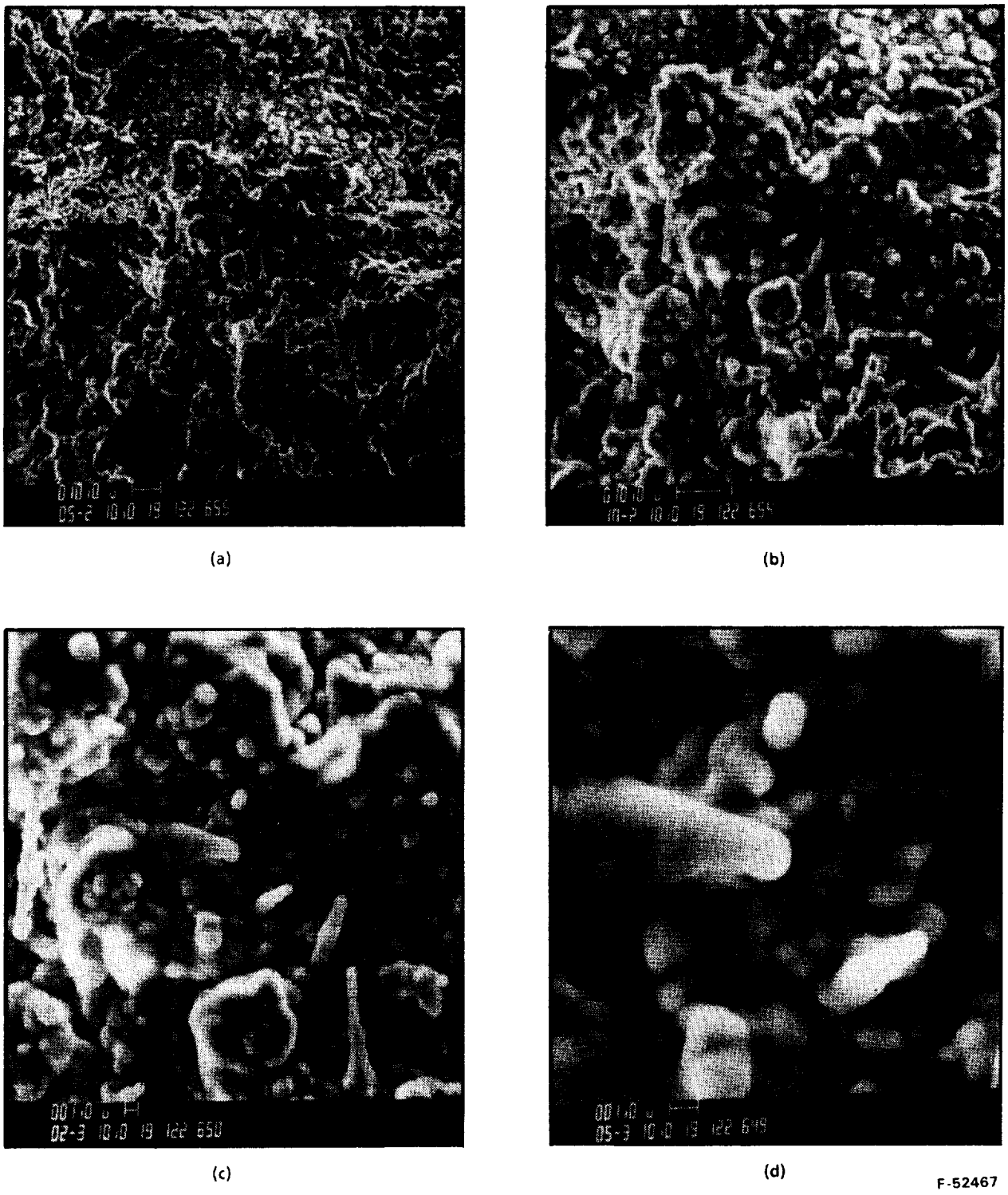

(a) (b) (c) (d)

F-52467

Figure 91.--Fracture Surface of a 30-wt% Whisker Content Injection Molding Mix with 24.0-wt% Wax. (The whisker/powder was mixed by liquid mixing.)

Selected dewaxed composite test bars with 10-, 20-, and 30-wt% whisker content were examined by optical microscope and SEM to evaluate whisker dispersion and alignment. For SEM, the test bars were broken by hand and the fresh fracture surface was immediately coated and examined. The micrographs are shown in figures 92 through 95. The whiskers appeared to be well dispersed in the matrix and the amount of whisker observed is in accordance with the batched whisker content. No distinct difference could be observed between test bars with the same SiC whisker content that were made with the starting material and liquid mixed, as shown in figure 93, or mixed by ball milling, as shown in figure 94.

Polished samples of the dewaxed test bars were examined with reflected light. Two sections from each test bar were selected. The longitudinal sections are shown in figures 96a through 96c, and the transverse sections are shown in figures 97a through 97c. The whiskers appear as the small needle-shaped bright phase in the micrographs and show a tendency toward alignment parallel to the axis of the test bars. The alignment is most probably due to the flow of material during injection molding. It is not certain whether some of the larger bright phases indicate agglomeration of whiskers.

STEM analyses were performed on HIP'ed GN-10 Si_3N_4 composites reinforced with ACMC and Tokai SiC whiskers, respectively. Figures 98 and 99 show the typical microstructure with SiC whiskers dispersed in the Si_3N_4 matrix. In general, very little degradation of the SiC whiskers was observed. A typical SiC whisker degradation due to Fe impurity is shown in figure 100.

Flexural strength and toughness results at room temperature, 1232°C (2250°F), and 1399°C (2550°F) of the test bars machined from a 20-percent ACMC SiC_w/GN-10 Si_3N_4 and a 20-percent Tokai SiC_w/GN-10 Si_3N_4 are shown in table 48 and figure 101. Both composite materials are weaker than the monolithic material, possibly because:

(1) Damaging flaws formed from whisker degradation or whisker agglomeration.

(2) The addition of SiC whisker diluted the concentration of sintering aids (20 percent less) in the matrix. This might result in a weaker grain boundary phase.

The strengths of the ACMC whisker composites were higher than the Tokai whisker composites. Polished sections of the materials (figures 102 and 103) showed that the ACMC whiskers are more uniformly distributed and appear to be longer. The Tokai whisker composites have more agglomerates, which implies nonuniform mixing. The agglomerates are the gray patches shown in figure 100. The Tokai whisker composites also contain black shiny inclusions seen on either the polished surface (figures 103a and 103c), or the fracture surfaces of some test bars.

The fracture toughness results of glass-encapsulated/HIP'ed monolithic GN-10 and GN-10 composites are presented in table 49. At room temperature, the ACMC whisker composite showed a 14-percent increase over the monolithic matrix

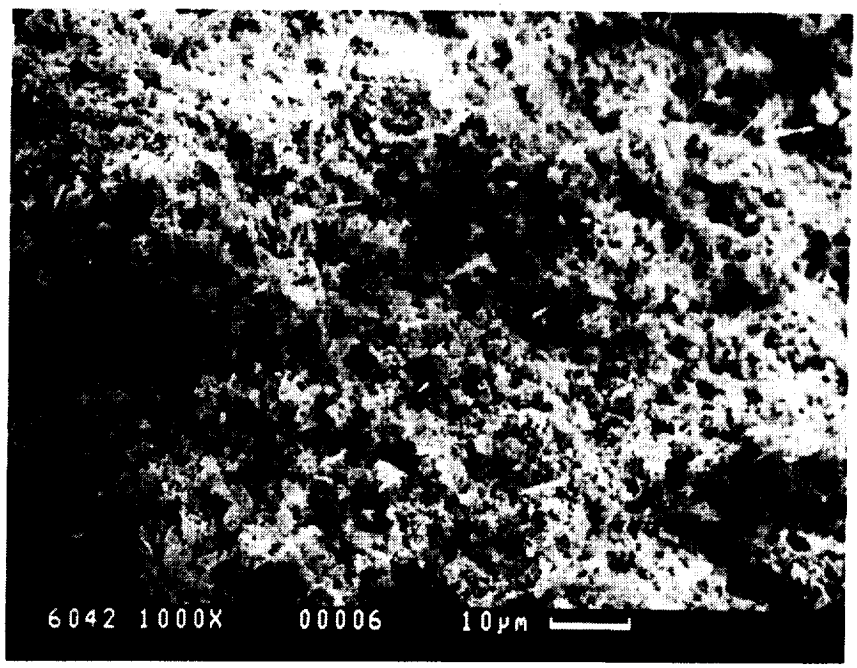

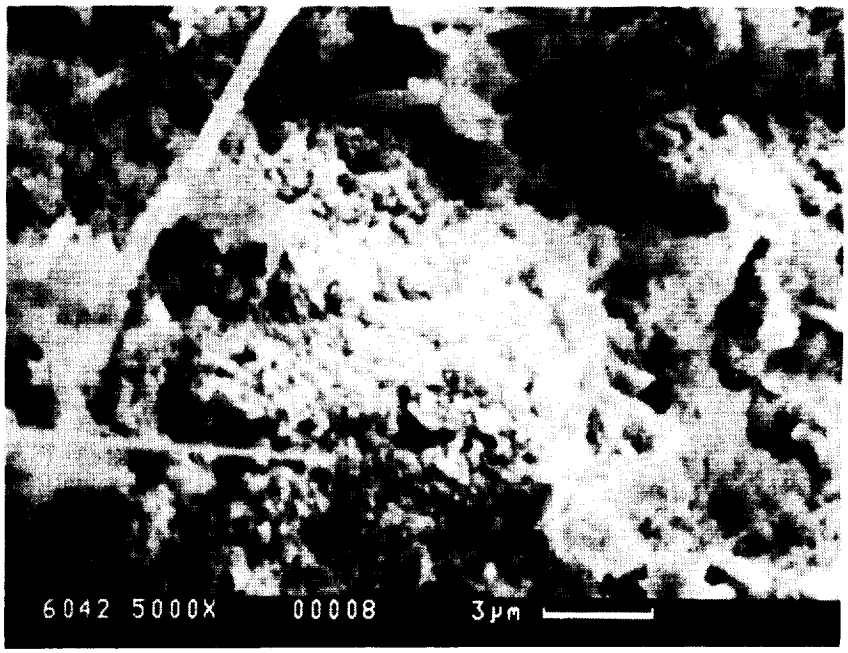

K-11702

Figure 92.--Fracture Surface of Dewaxed Test Bar with 10-Percent SiC Whisker Content (Whiskers and Powders Mixed in Liquid).

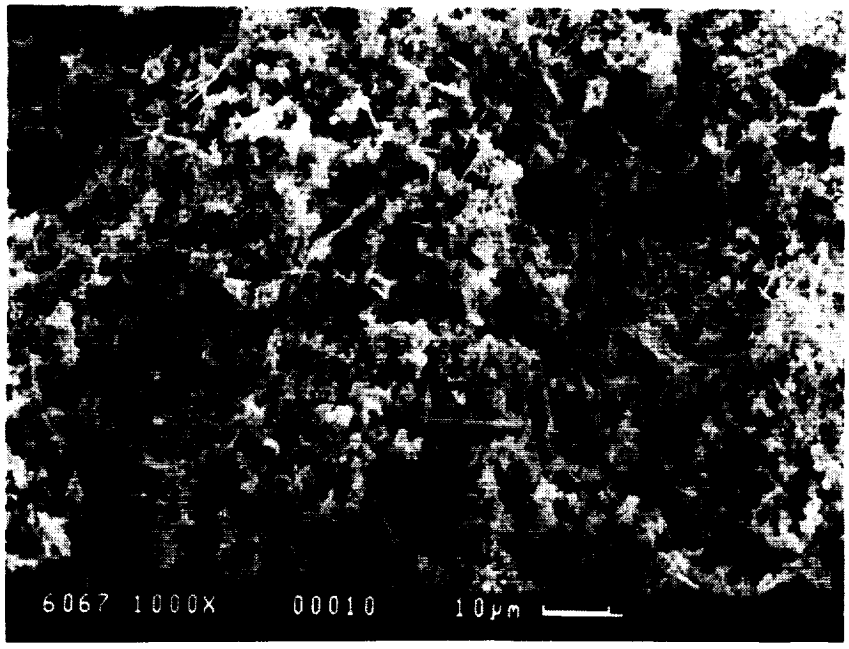

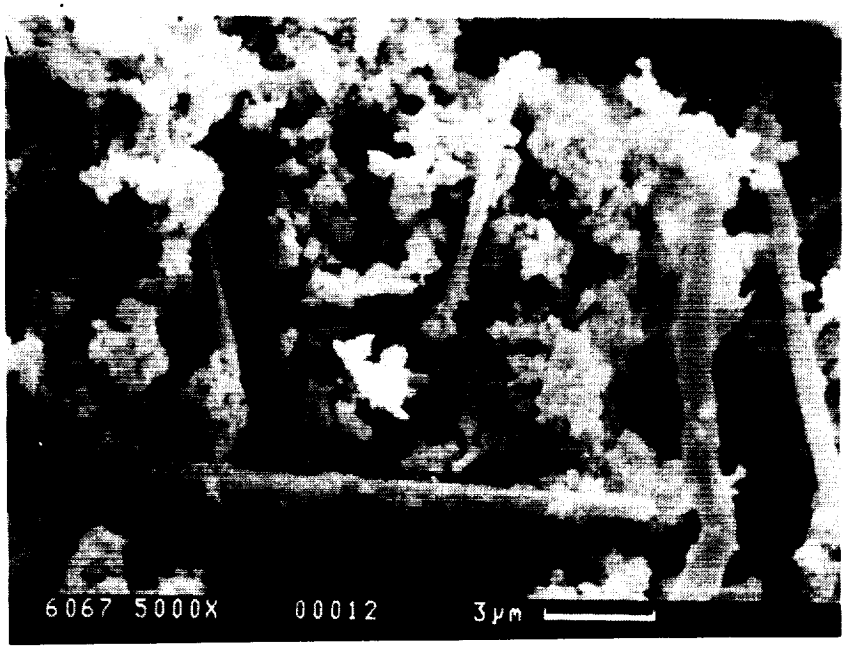

K-11703

Figure 93.--Fracture Surface of Dewaxed Test Bar with 20-Percent SiC Whisker Content (Whiskers and Powders Mixed in Liquid).

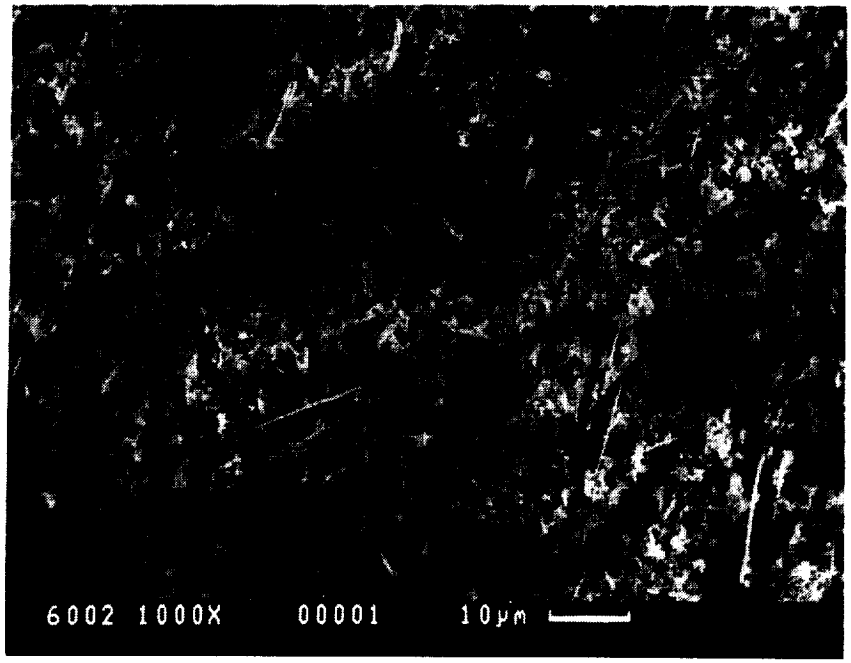

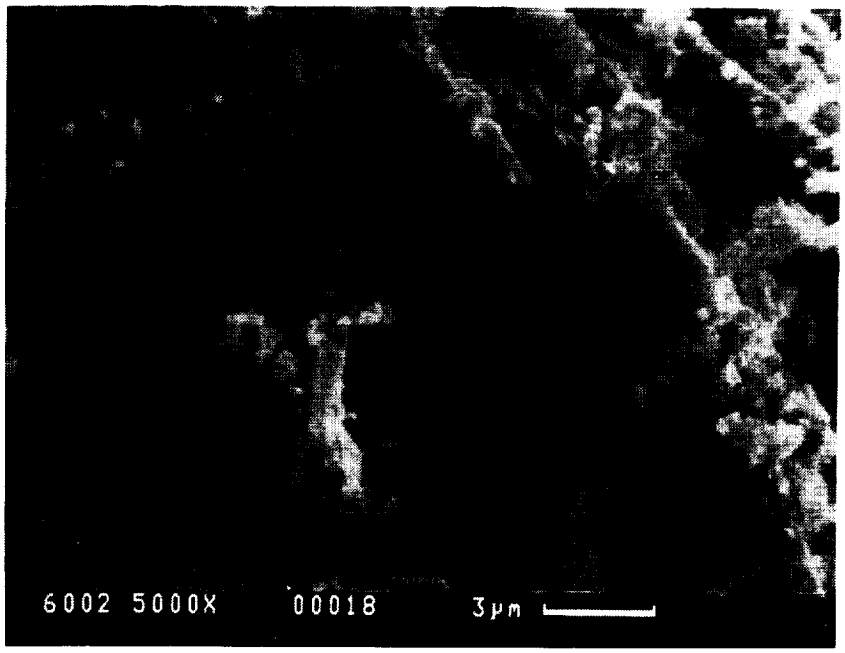

K-11704

Figure 94.--Surface of Dewaxed Test Bar with 20-Percent SiC Whisker Content (Whiskers and Powders Mixed by Ball Milling).

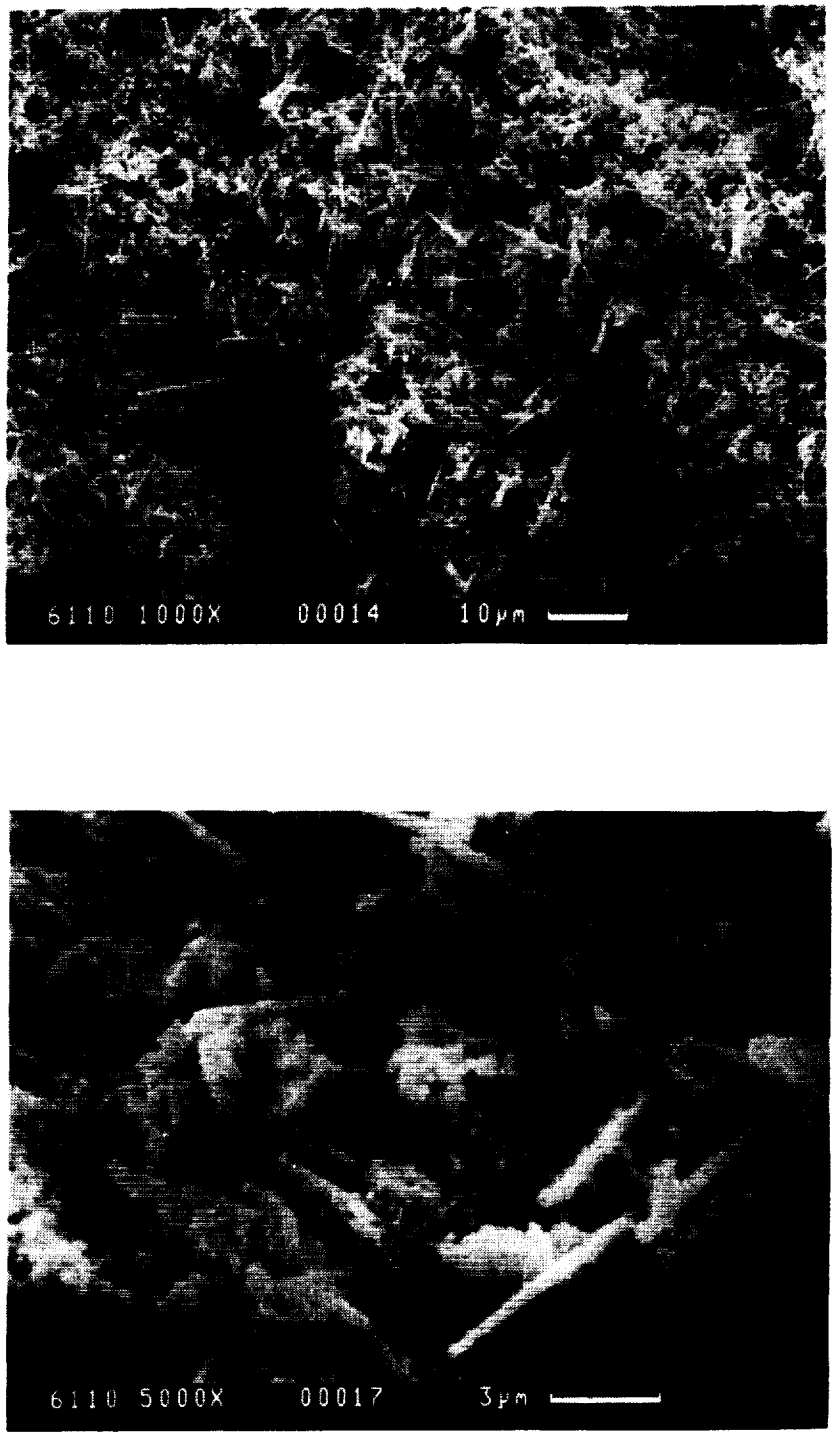

Figure 95.--Fracture Surface of Dewaxed Test Bar with 30-Percent SiC Whisker Content (Whiskers and Powders Mixed in Liquid).

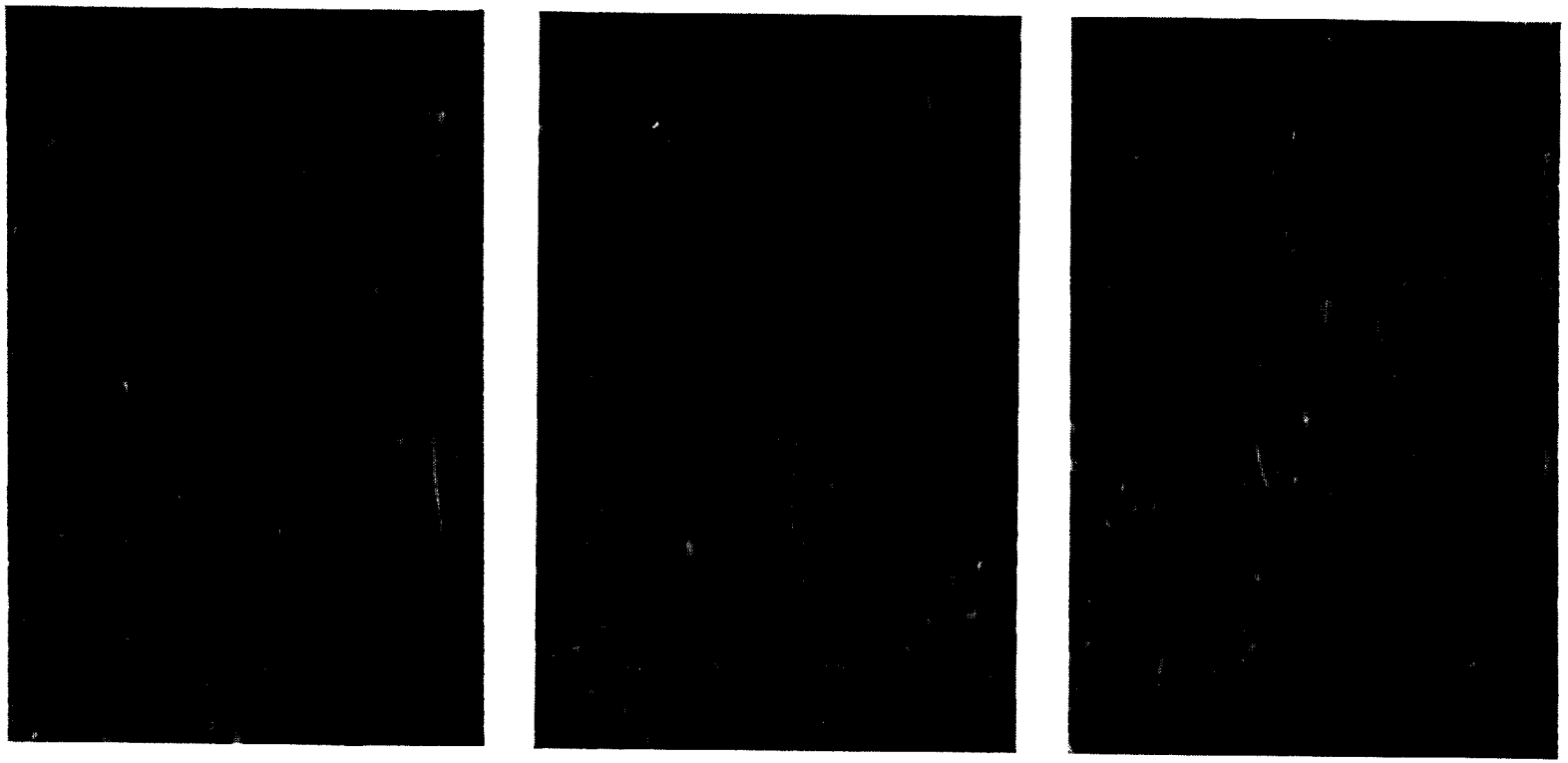

Figure 96.--Polished Longitudinal Sections of Dewaxed Composite Test Bars with 10 to 30 wt% SiC Whisker Content. (Magnification 1000X.)

Note: The whiskers shown as the bright needle-shaped phase appear to be aligned in the longitudinal direction of the test bars.

Figure 97.--Polished Transverse Sections of Dewaxed Composite Test Bars with 10 to 30 wt% SiC Whisker Content. (Magnification 1000X.)

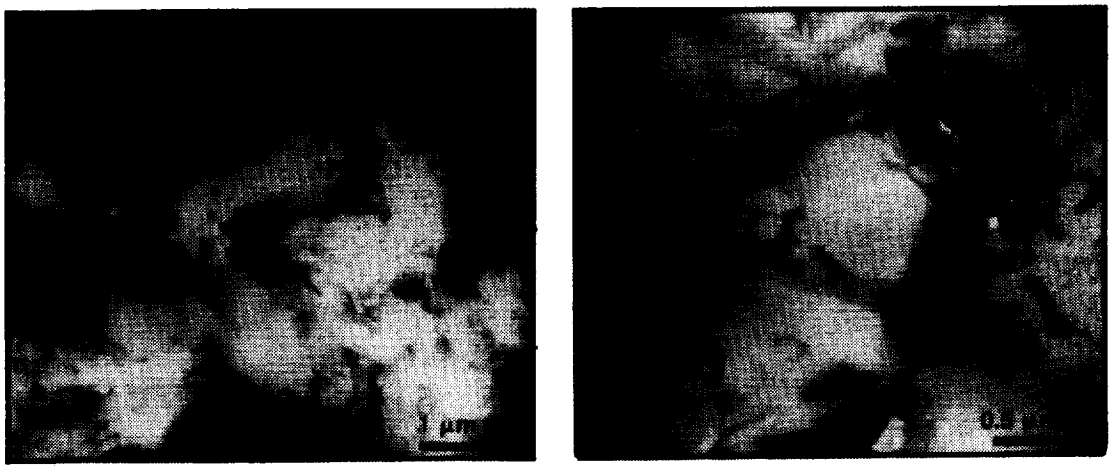

Figure 98.--Typical STEM Microstructure for GN-10/ACMC SiC Whiskers Composite.

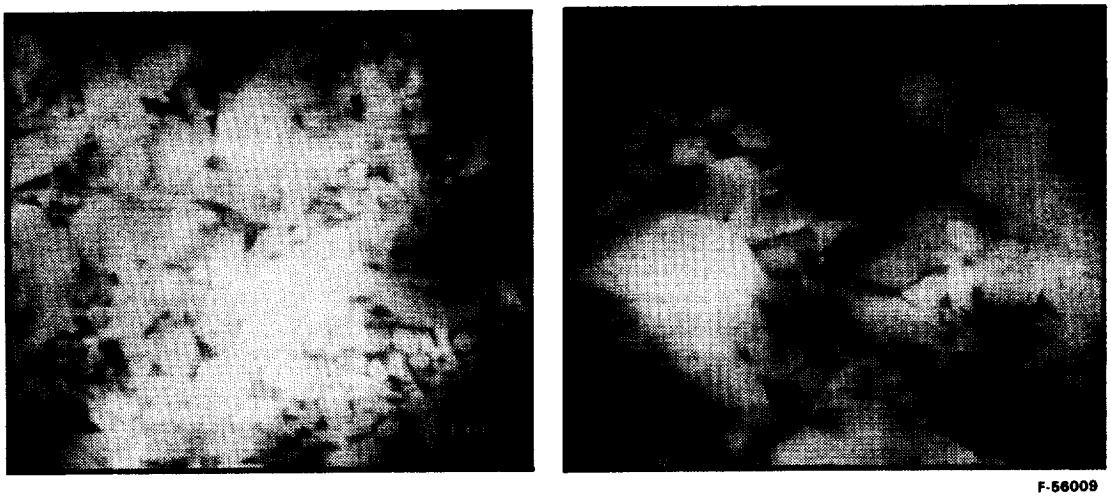

Figure 99.--Typical STEM Microstructure for GN-10/Tokai SiC Whiskers Composite.

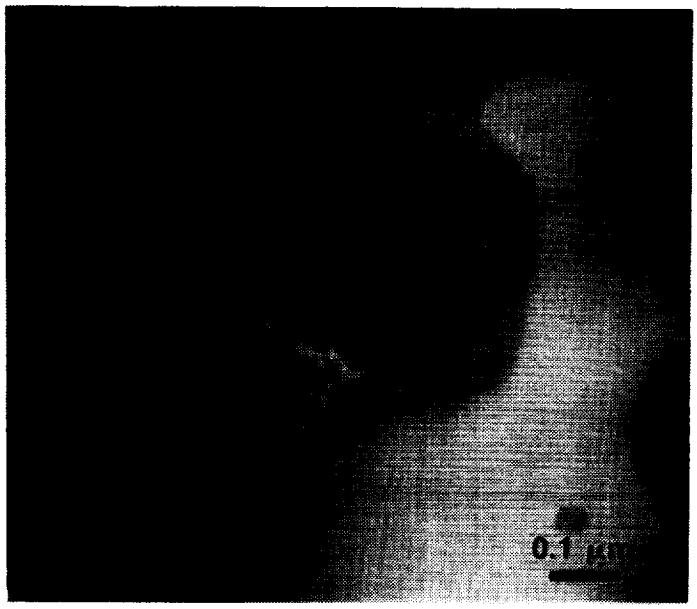

Figure 100.--Degradation of Tokai Silicon Carbide Whisker. (Arrow points to Fe impurity; next to Fe impurity are degradation products.)

material, while the Tokai whisker composite did not show any significant increase. The shorter length of the Tokai whiskers and the possibility of whisker degradation could be the reason for the lack of toughness increase.

The change in K_{IC} of the materials at 1232°C (2250°F) cannot be fully explained at this time due to insufficient data. The increase in K_{IC} at 1399°C (2550°F) was probably due to the increase in viscous flow of the grain boundary phase, which caused crack blunting.

2.5.3 Conclusion

In conclusion, the toughness of Si_3N_4 can be improved by SiC whisker reinforcement. Encapsulation HIP is necessary to densify net-shape composite parts of GN-10 composition. The use of SiC whiskers with high purity and large aspect ratio is necessary for high strength and toughness.

F-54965

TABLE 48.--FLEXURE STRENGTH OF GN-10 AND GN-10 COMPOSITES

Material	Green Forming Method	Encapsulation Technique	Maximum HIP Temperature	Flexure Strength, MPa (ksi)*		
				Room Temp.	1232°C (2250°F)	1399°C (2550°F)
GN-10 monolithic	CIP billet	Glass (ASEA)	1800°C	777.2 (112.8)	597.4 (86.7)	428.6 (62.2)
GN-10/20-percent ACMC whisker composite	CIP billet	Glass (ASEA)	1800°C	548.4 (79.6)	472.0 (68.5)	410.0 (59.5)
GN-10/20-percent Tokai whisker composite	CIP billet	Glass (ASEA)	1800°C	407.2 (59.1)	366.5 (53.2)	339.7 (49.3)

*Ten bars tested at room temperature and five bars at elevated temperature.

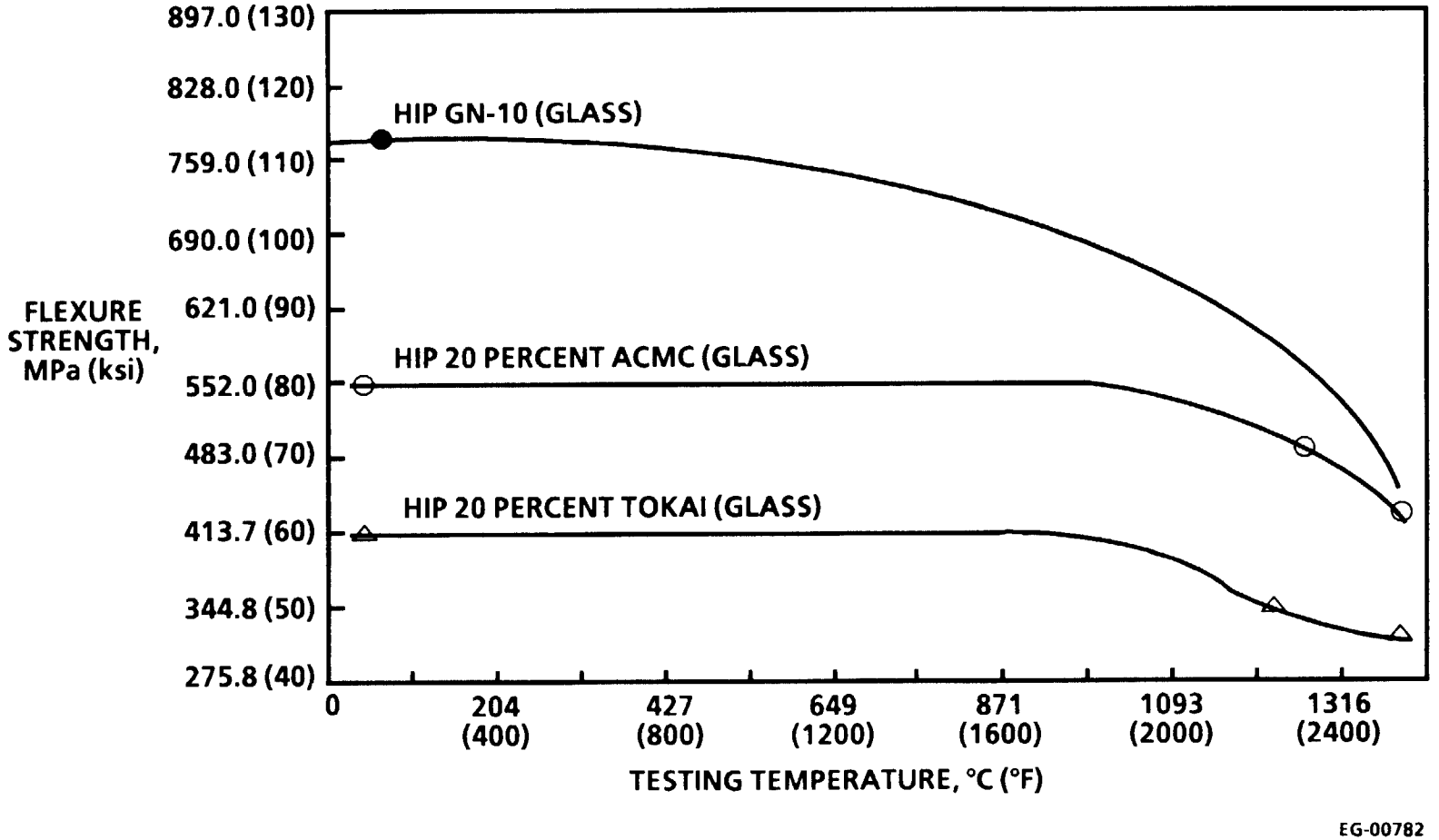

Figure 101.--Four-Point Flexure Strength Comparison of GN-10 Matrix and 20-Percent Whisker Composites.

ORIGINAL PAGE
BLACK AND WHITE PHOTOGRAPH

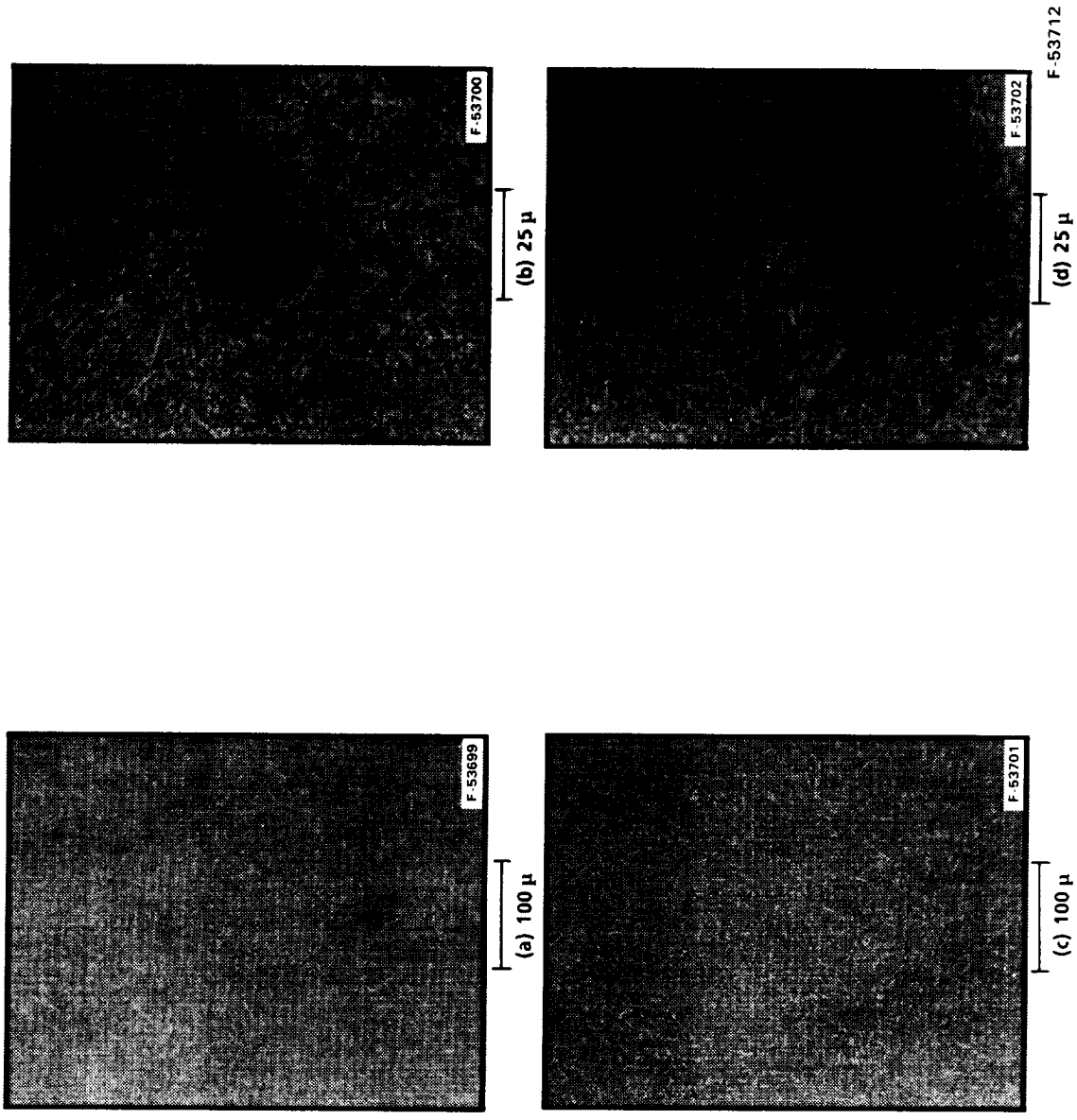

Figure 102.--Polished Sections of GN-10 Matrix 20-Percent ACMC Whisker Composite Showing Uniform Whisker (White Phase) Distribution--No Distinct Differences can be Seen Between the Center of the Billet, (a) and (b), and the Edge of the Billet, (c) and (d).

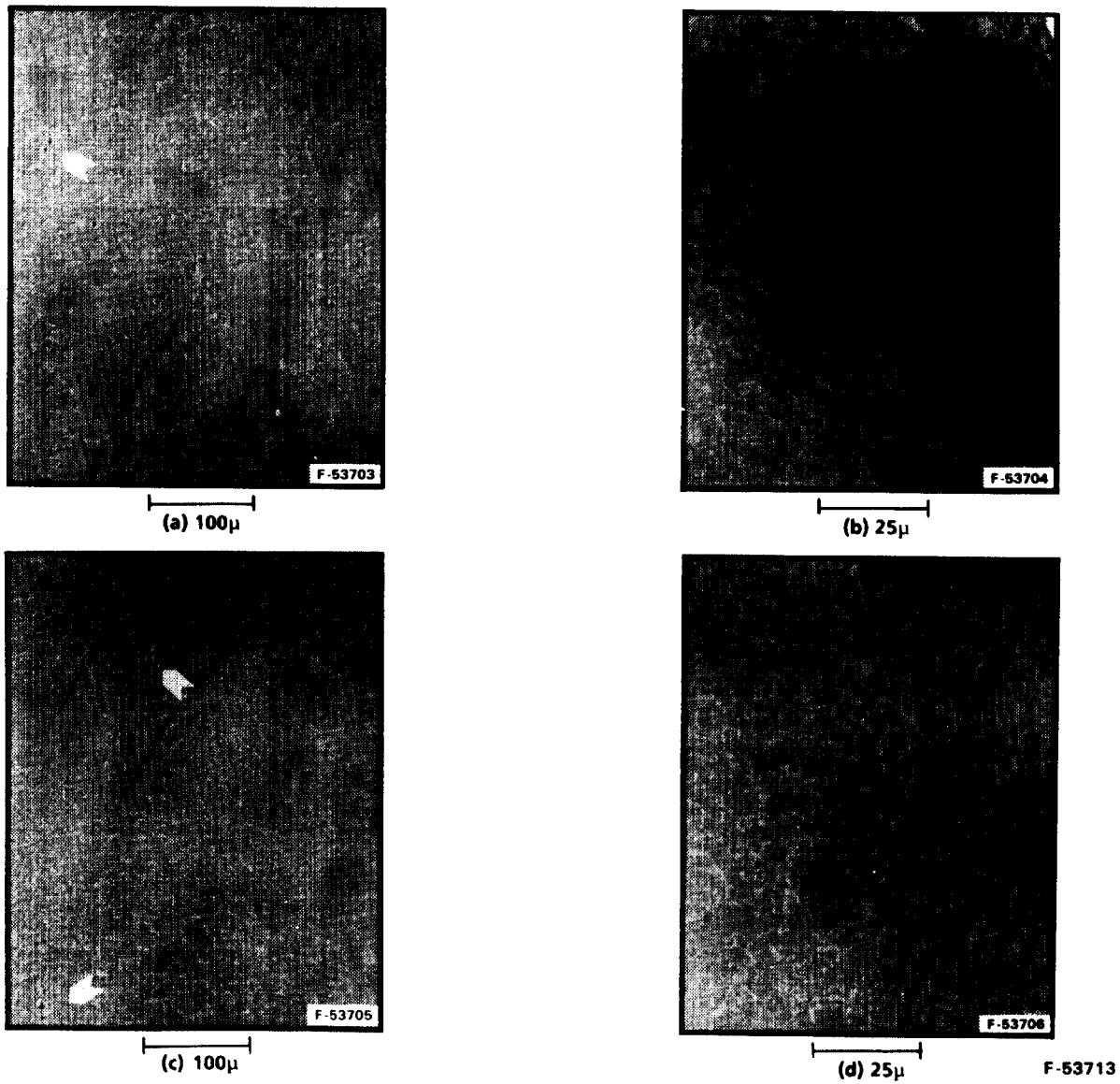

Figure 103.--Polished Sections of GN-10 Matrix 20-Percent Tokawhisker Composite Showing Possible Inclusions (Pointed by Arrows), and Large Agglomerates (Gray Patches)--No Distinct Difference can be Seen From the Center, (a) and (b), and the Edge, (c) and (d), of the Billet.

TABLE 49.--FRACTURE TOUGHNESS (K_{IC}) OF GN-10 AND GN-10 COMPOSITES

Material	Green Forming Method	Encapsulation Technique	Maximum HIP Temperature	Flexure Strength*, MPa x $in.^{1/2}$ (ksi x $in.^{1/2}$)		
				Room Temp.	2250°F	2550°F
GN-10 monolithic	CIP billet	Glass (ASEA)	1900°C	6.06 (5.51)	6.46 (5.87)	8.02 (7.29)
GN-10/20-percent ACMC whisker composite	CIP billet	Glass (ASEA)	1800°C	6.93 (6.30)	5.67 (5.15)	9.20 (8.36)
GN-10/20-percent Tokai whisker composite	CIP billet	Glass (ASEA)	1800°C	6.19 (5.63)	5.31 (4.83)	9.39 (8.54)

* Five specimens used for each testing condition

2.6 NET-SHAPE COMPONENT FABRICATION

2.6.1 Introduction/Summary

The ability to fabricate ceramic components to net shape is extremely important to the cost-effective use of ceramics in heat engines. With presently practiced machining techniques, machining ceramics to close tolerances increases the component cost beyond commercial viability. Consequently, only net-shape fabrication is economically feasible.

Injection molding is considered to be one of the most practical methods for mass production of net-shape ceramic components. The ultimate goal of this program was to apply the fabrication technology learned through injection-molded test bars to net-shape fabrication. The decision was made to evaluate how much of the material/process data base learned from the "ab" material/process could be transferred to the fabrication of net-shape components.

Molds were available in-house for two different size turbocharger rotors, T-2 and T-25. These molds were originally made for injection molding wax patterns to be used ultimately for the fabrication of metal turbocharger rotors. Either of these shapes was sufficiently complex to evaluate net-shape forming capability of ceramics. T-25, the larger of the two, was selected for initial evaluation in this study.

It was found that the molding parameters established for producing good quality test bars did not satisfy the requirements for producing similar quality rotors. However, the test bar study was meaningful in establishing compositions and processing parameters through blending and pelletizing, and in serving as a starting point in injection molding and dewaxing. The test bar sintering cycle was thought to be directly applicable to the rotors. Injection-molding parameter adjustments were necessary to make the transition from test bars to large, complex net-shape components, and these adjustments were found to depend upon size, shape, and molder characteristics. Significant progress was made through the correlation between defects and molding parameters. Defect types and location were identified and fully characterized. Several defect causes were identified. It was concluded from this study that total elimination of defects in T-25 rotors would require molding tool design changes to take into account the unique needs of injection-molded ceramics. The tooling used to produce wax patterns for metal castings cannot be used as a direct replica for molding ceramics. Thicker blades and a smooth transition from shaft to hub are examples of some of the modifications needed. This illustrates the need for an interdisciplinary approach at the onset between engine designer, tool engineer, ceramic process engineer, and die manufacturer.

The T-2 tool had previously been modified to provide the smoother transition between shaft and hub (tapered shaft) and also had slightly thicker blades. Modifications to the T-2 tool included improved venting, ejector pin addition, and a steel collar which resolved the mismatch problem at the exducer end. With these modifications, the injection-molding parameters were successfully optimized to achieve defect-free molded rotors.

*Performed under Task II of the contract.

2.6.2. Fabrication of Turbocharger Rotors

The raw materials and material composition selected for this evaluation were identical to those of "ab" material/process, i.e., 92 percent Denka 9FW Si_3N_4, 6 percent Linde A Al_2O_3, and 2 percent Molycorp Y_2O_3. Standard batches of material were prepared through pelletizing using "ab" process parameters. The Battenfeld injection molder was selected over the Arburg because of its larger capacity, which is needed for T-25 size, and microprocessor controls that the Arburg lacked. Injection-molding parameters for test bars were optimized for the Battenfeld molder as a starting point.

Two turbocharger rotor molds were available for this evaluation: T-2 and T-25. The T-25 was selected for its higher potential for commercial benefits. The first group of rotors injected, based upon the optimized test bar injection-molding parameters, contained a large amount of defects. The locations determined by visual inspection are shown in figure 104. For example, stress cracks in the exducer portion of the rotor were observed, and unfilled tips on most blades of each rotor were noted. A summary of the visual inspection of the initial group (iteration 1) is shown in figure 105. After several iterations of molding experiments, a significant reduction of defects in as-injected rotors was achieved, as shown in figure 106 compared to figure 105. This was accomplished by a systematic improvement of the molding parameters. Table 50 lists the molding parameter changes from iteration 1 through iteration 4. Each iteration was preceded by five or more test runs, which were used to pre-evaluate the effects of scheduled parameter changes. Once the parameters were selected, a minimum of ten rotors were molded using the selected set of parameters, from which the percent of defects of each type was determined. The results are presented in figures 105 and 106.

One of the parameter settings involved in molding the initial group of rotors is known as time-dependent (listed in table 50). In this setting, the injection time is preset and full pressure is maintained throughout the set time. It was found that many defects such as cracks, broken blades, knit lines, etc. could be attributed to this procedure. Subsequent runs were conducted on a stroke-dependent setting. In this setting, the stroke distance of the plunger is preset. Full pressure is maintained until the set distance is reached. At this point, the pressure is immediately reduced. Rotors molded after the initial group (iteration 1), using the stroke-dependent setting, showed considerable improvement.

In addition to changing to stroke-dependent injection molding, other parameters were varied such as raising the zone temperature to the nozzle temperature (104°C (220°F)), which resulted in producing rotors with fewer exducer cracks; however, severe pull-out and broken blades still existed.

After five test runs using iteration 2 parameters, injection speed, injection pressure, material temperature, amount of mold release, and cooling rate were found to be critical to the quality of the rotors. A new set of process parameters was established for the third iteration. Higher injection speed (100 percent) and pressure (3.2 MPa (460 psi)) were used to obtain better mold filling and to reduce knit lines and unfilled blades. The cooling rate was controlled by replacing the metal sprue with a nylon sprue and by adjusting the mold temperature. A lower cooling rate after injection resulted in less thermal

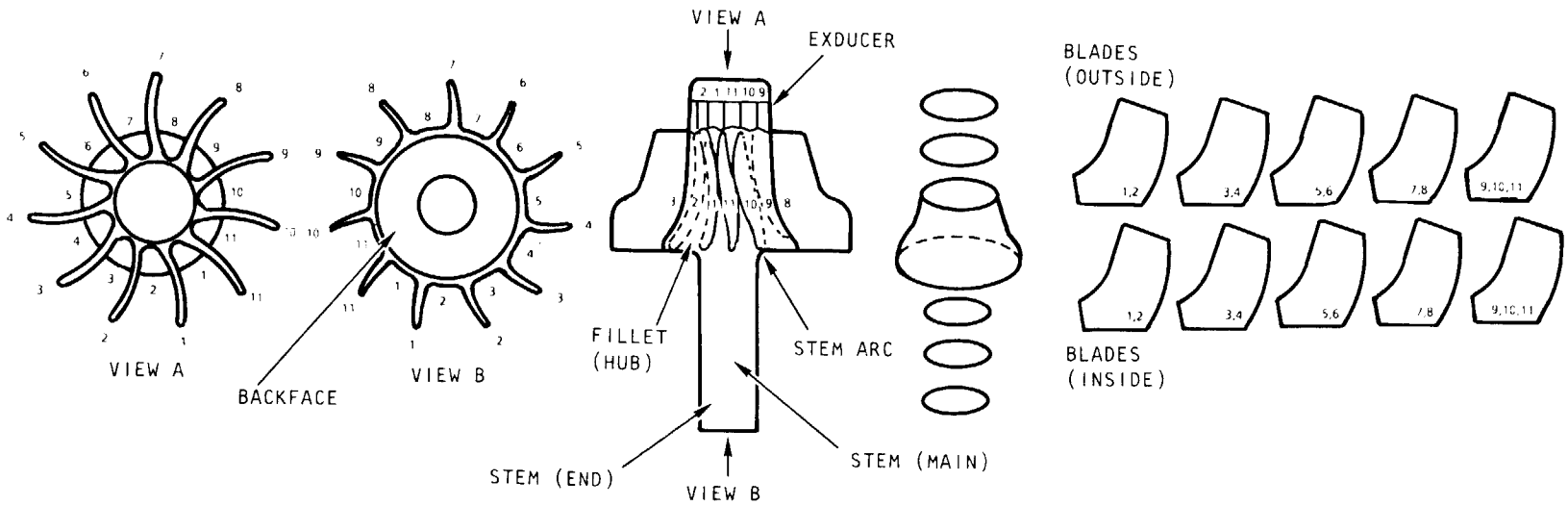

Figure 104.--Schematic Breakdown of a Rotor Showing All Locations Visually Inspected for Defects.

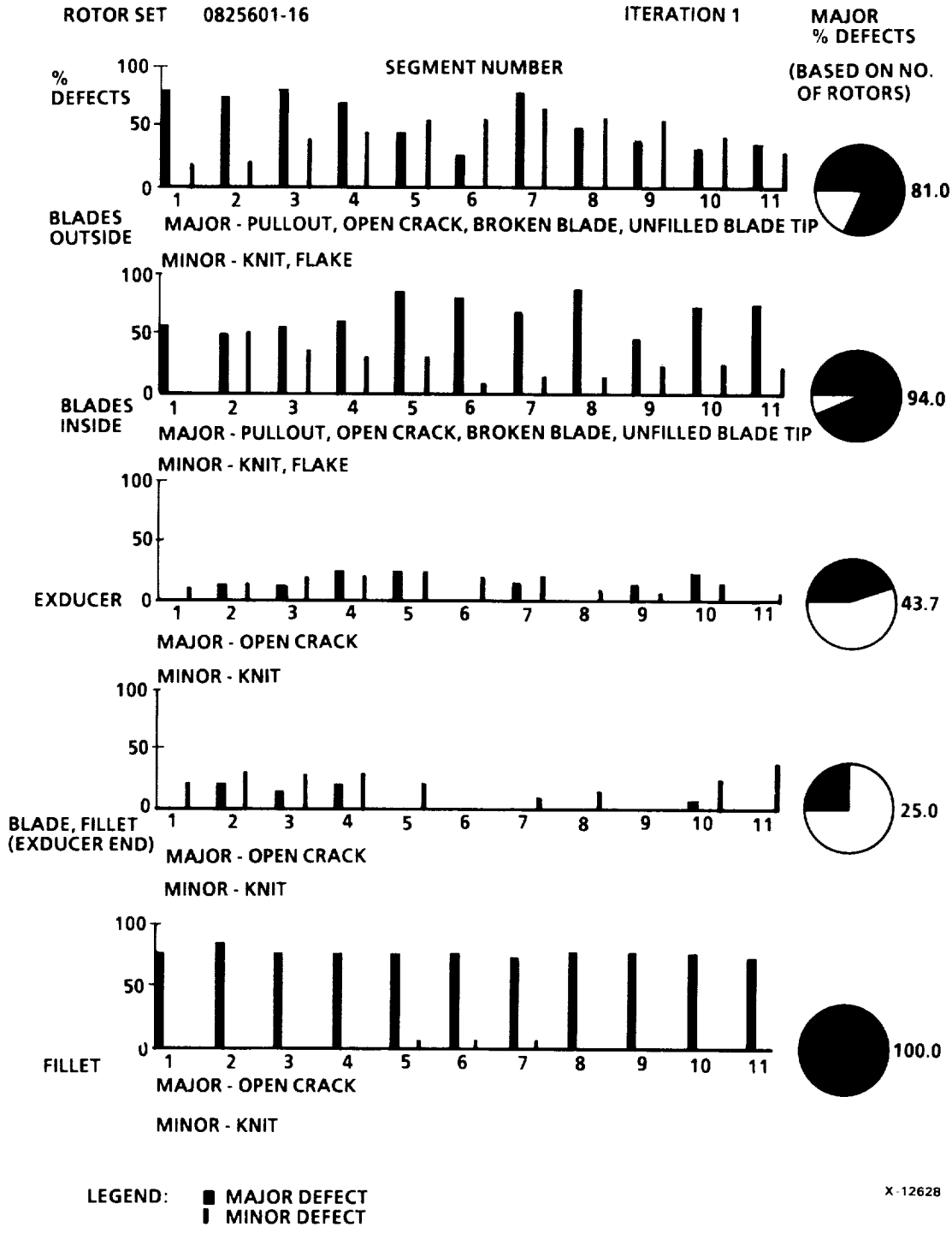

Figure 105.--Summary of Visual Inspection of 16 As-Injected Rotors in Initial Run Using Test Bar Optimized Parameters.

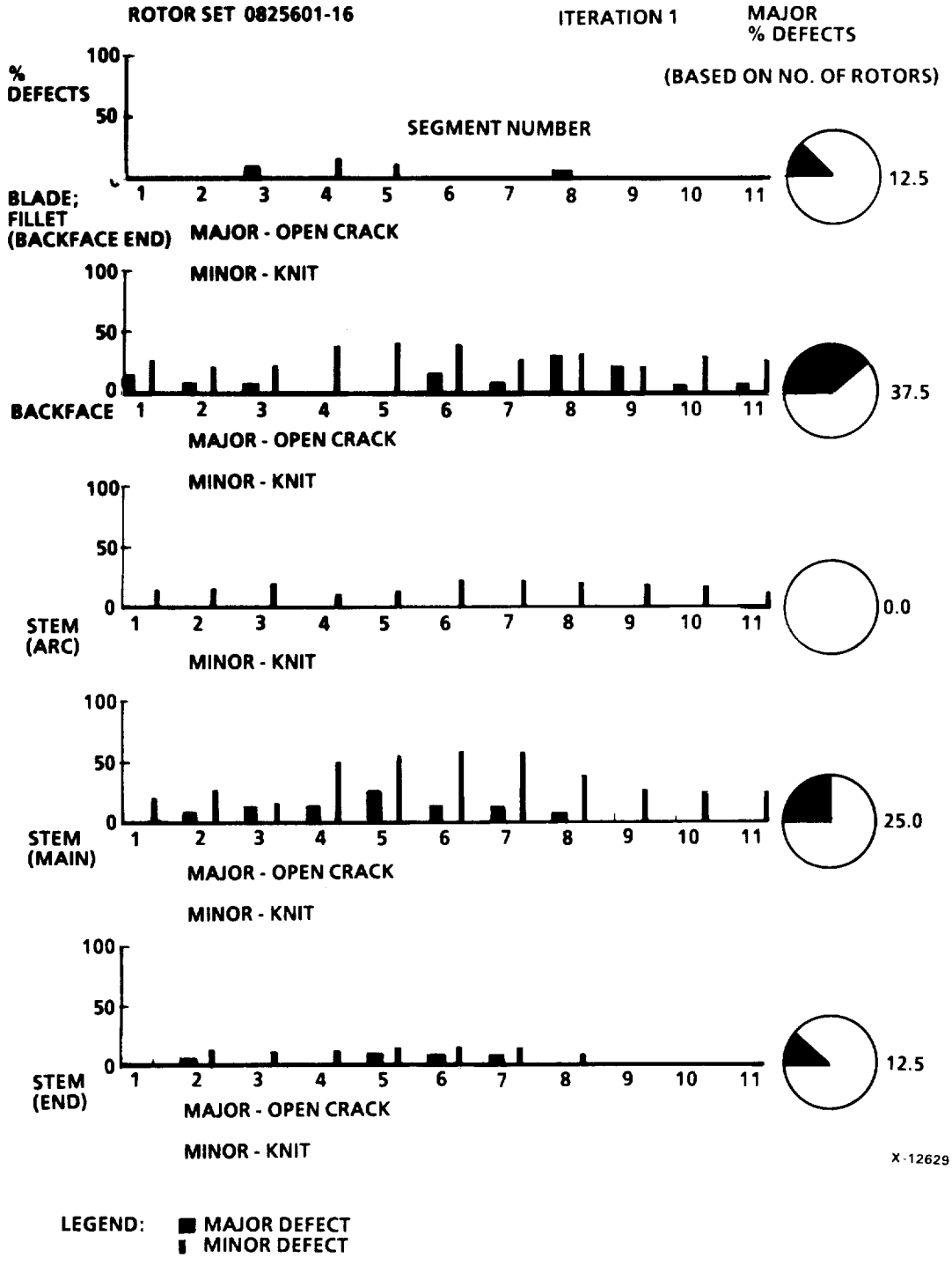

Figure 105.--(Continued).

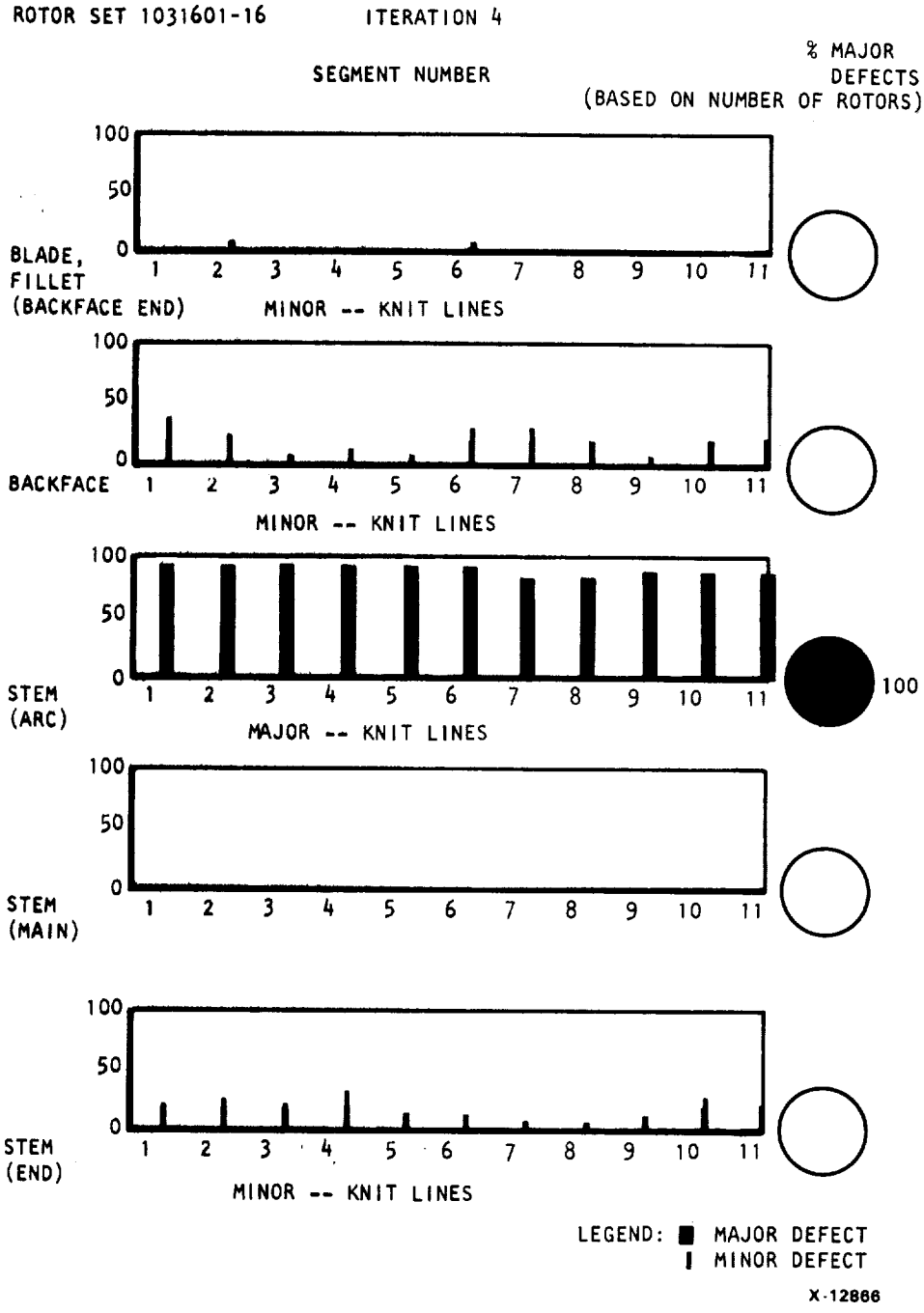

Figure 106.--Summary of Visual Inspection of 16 As-Injection-Molded Rotors, with Final Parameter Variations Showing Considerable Improvement over Initial Evaluation.

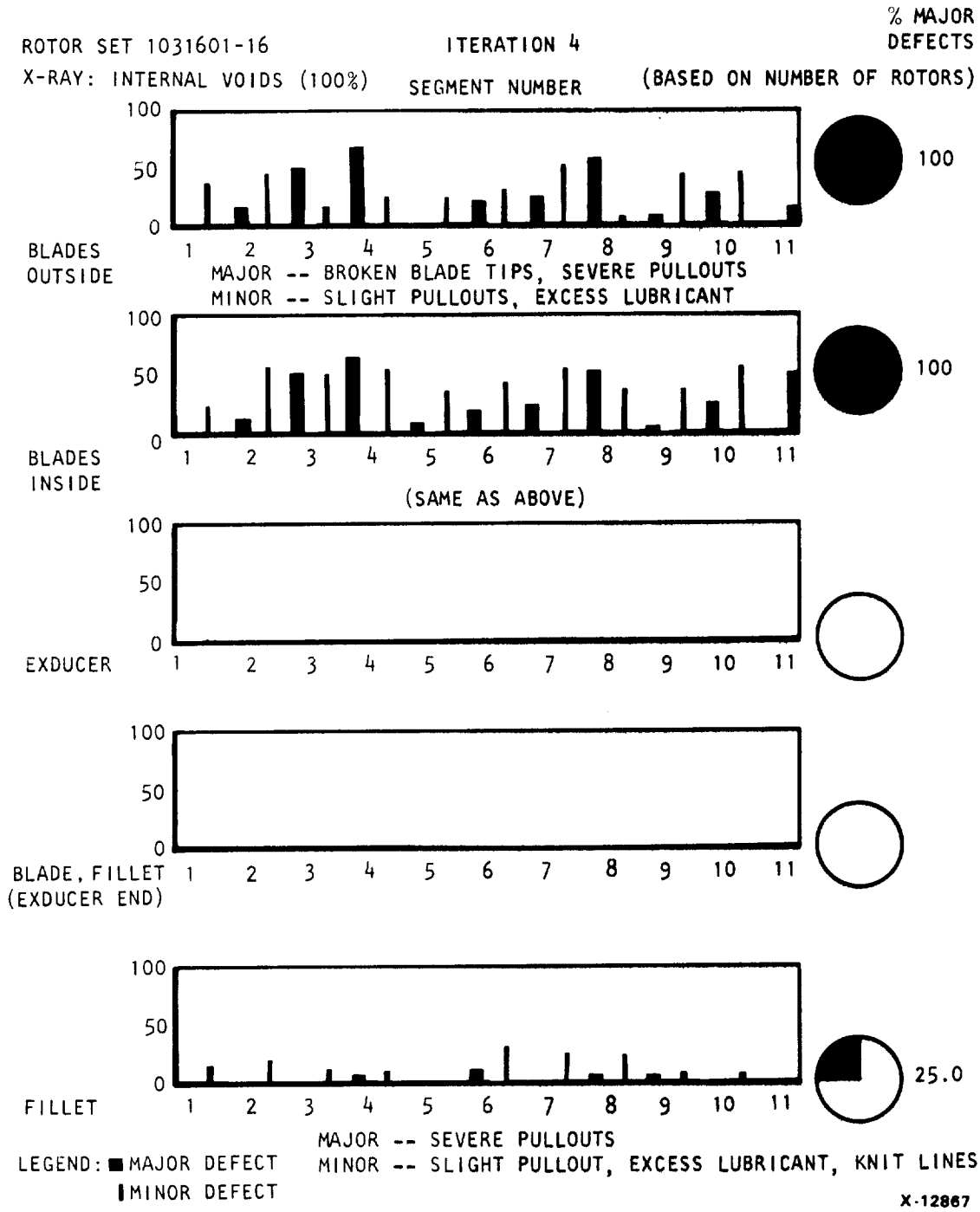

Figure 106.--(Continued).

TABLE 50.--INJECTION-MOLDING PROCESS PARAMETERS

Process Parameters	Injection Molding Parameter Variations--T-25 Rotor			
	1	2	3	4
Temp (nozzle)	104°C (220°F)	104°C (220°F)	93°C (200°F)	93°C (200°F)
Temp (Zone 1)	82°C (180°F)	104°C (220°F)	93°C (200°F)	104°C (220°F)
Temp (Zone 2)	66°C (150°F)	79°C (173°F)	78°C (172°F)	78°C (172°F)
Temp (Zone 3)	66°C (150°F)	66°C (150°F)	66°C (150°F)	66°C (150°F)
Temp (mold)	36.7°C (98°F)	38°C (100°F)	34.4°C (94°F)	34.4°C (94°F)
Injection pressure	0.689 MPa (100 psi)	0.689 MPa (100 psi)	3.169 MPa (460 psi)	3.169 MPa (460 psi)
Follow-up pressure	0.689 MPa (100 psi)	0.689 MPa (100 psi)	0.041 MPa (60 psi)	0.041 MPa (60 psi)
Injection speed	7% on all five speed zones	7% on all five speed zones	100% full speed on all five speed zones	50% on all five speed zones
Time- or stroke-dependent	Time Stroke	Stroke Stroke		

NOTE: Nylon sprue and more mold-release lubrication were used for all iterations.

stress and cracking. More mold release lubricant was applied to the mold to reduce pull-out. Significant quality improvement was achieved.

Finally, for the fourth iteration, two additional changes were made in process parameters. Material temperature was increased from 93° to 104°C (200° to 220°F) and injection speed was reduced from 100 percent to 50 percent.

In summary, higher material temperature helped to reduce exducer cracks, and lower injection speed reduced open cracks on the backface and knit lines on the fillets. However, more severe pullout on the blades and fillets resulted, and knit lines around the stem persisted. In addition, knit lines formed on the backface due to lower injection speed. An internal void was shown in the X-ray radiography on all of the final group of injected T-25 rotors. High material temperature is believed to have caused improper cooling after injection, and a shrinkage void was formed.

Although the quality of the as-injection-molded rotors from first and second groups was also found to improve after the injection of eight rotors, the total volume of those eight rotors is about the same as the volume of material passages inside the injection molding machine. This fact suggests that material left in these cavities over a length of time between operations may be unsuitable for injection molding into rotors.

In order to reduce/eliminate the defects remaining on the third iteration of T-25 rotors, an intensive study on process parameters, including material temperature, injection speed, and injection pressure, was conducted. It was found that when the material temperature exceeded 93°C (200°F), an internal shrinkage void formed in the hub of the rotor. This problem was reduced by lower injection speed and higher injection pressure. If the injection pressure and speed were too high, stress-related cracks and knit lines in the areas of the stem arc, the exducer end, and the top of the blades formed. This appeared to be caused by overpacking and insufficient venting. However, when the injection speed was too low (i.e., 30 percent setting or lower), knit lines formed on the backface, because the large volume of the hub cannot be filled quickly enough due to low speed. The problem of broken blade tips during removal from the die was reduced by higher injection pressure. Higher pressure was believed to improve material packing at the blade tips, resulting in higher green strength in the blade.

The stress-related cracks and knit lines could be completely eliminated with the current T-25 die design. The configuration of a stem arc with a sharp 90-degree bend must be modified to allow a smoother material flow and to reduce stress. A larger nozzle is also needed to allow a higher material flow rate to fill the die cavity faster. To verify these points, the existing T-2 rotor die, which has a tapered shaft (stem) and a smaller cavity with thicker blades, replaced the T-25 tool.

A series of experiments on the injection molding of T-2 size turbocharger rotors was conducted. Because of its tapered shaft design and thicker blades, the problems of stress cracks/knitlines on the stem arc and blade breakage experienced on the T-25 rotors were not observed. This confirmed the requirement to modify the T-25 die. The approach of using a higher injection

speed (75 percent setting on the control) to solve the knitline problem on the backface was tested. The results showed that the number of knitlines was reduced. However, some stress cracks were found on the exducer end. Past experience suggested that improved venting in the die would reduce or eliminate this problem. Tooling modification to improve venting was initiated.

The modification of the T-2 rotor mold included the addition of an ejector pin similar to that in the T-25 mold to facilitate removal of the rotor after injection molding. Also, a new steel collar was built to resolve the mismatch problems at the exducer end.

An optimum set of injection-molding parameters was developed for T-2 rotors. The visual and X-ray radiograph inspection results of the as-injected rotors indicated that 75 to 80 percent of the rotors contained no detectable defects.

In conclusion, most of the processing data base established for test bars can be transferred to net-shape forming such as raw materials, sintering aids, milling, mixing, and sintering. However, the molding parameters require extensive modification. The modifications made to the T-2 rotor tool indicated that most of the defects evident in the injection-molded T-25's can be eliminated. It is reasonable to expect that similar modifications to the T-25 tooling would eliminate most defects. Binder systems and/or dewax cycles may need to be re-evaluated with changes in tooling. The experience gained in this effort illustrates the need for an interdisciplinary approach to component fabrication involving the engine designer, tool engineer, ceramic process engineer, and tool manufacturer.

3. CONCLUSIONS AND RECOMMENDATIONS

Significant advances in processing and property improvements of Si_3N_4 materials for heat engine applications were made during the course of this program. The following are the conclusions along with recommendations for future work:

(1) Statistical experimental design is an effective tool in ceramic processing optimization. Using this tool, the as-processed baseline Si_3N_4 flexural strength (MOR) was increased 20 percent at both room temperature and 1232°C (2250°F) to 668.8 MPa (97 ksi) and 403.4 MPa (58.5 ksi), respectively. The Weibull slope was increased by 72 percent to 13.6. Statistical experimental design is recommended to be employed whenever possible in future ceramic processing work.

(2) More significant improvements in high-temperature strength of Si_3N_4 require grain boundary/microstructure control. A new high-temperature Si_3N_4 material was developed which exhibited MOR values of 889.5 MPa (129 ksi) at room temperature, 725.4 MPa (105.2 ksi) at 1232°C (2250°F), and 581.2 MPa (84.3 ksi) at 1399°C (2550°F). These strengths were achieved with a material densified by encapsulated HIP. Additional in-depth process investigation supported by extensive STEM grain boundary study is needed in order to further improve the property of this HIP'ed material, and, more importantly, to develop an unencapsulated sinter/HIP densification process to achieve a material with strength equal to that of the HIP'ed one.

(3) The mathematical modeling for optimizing material property within a selected range of composition is useful. A model was developed to predict the optimum compositions in the two sintering aid systems investigated in this program. Additional experimental work is needed to apply this model to further develop the new high-temperature material system. This investigation should be augmented by phase diagram study and microstructure evaluations.

(4) Reproducibility of process/property can be achieved when raw materials with consistent properties and reliable equipment are used. It is necessary to use Si_3N_4 powder with a narrow scatter band in property, especially PSD and chemistry, from lot to lot. Equally important are well-designed and reliable high-temperature sinter HIP furnaces. Both factors are needed to achieve fully densified material with consistent properties.

(5) The toughness of Si_3N_4 can be improved by SiC whisker reinforcement. Encapsulation HIP is necessary to densify net-shape composite parts of GN-10 compositions. The use of SiC whiskers with high purity and large aspect ratio is necessary for high strength and toughness. The phenomenon of whisker alignment observed in injection-molded composites required additional investigation.

(6) A significant portion of the processing technology learned from test bar MOR evaluation can be transferred to net-shape component

fabrication. The two processing steps that are most size- and shape-dependent are injection molding and dewaxing. These two steps need major adjustment. Computer modeling of material flow during molding of a particular component size and shape is needed. Die design may have to be modified to make it more compatible with the characteristics of material rheology and dewax behavior. It is recommended that an interdisciplinary team address the issue, including engine designers, tool makers, and ceramic process engineers.

APPENDIX A

EXPLORATION EXPERIMENTS (TASK VII)

1. INTRODUCTION

The purpose of this task is to explore new concepts in processing, to investigate the impact of major processing parameters on material properties, and to study the interactions between major processing parameters. This task is cost shared by GCC. In the first year, following eight major parameters were selected for evaluation:

(1) Alternate raw materials (Si_3N_4)

(2) Alternate binder system

(3) Binder extraction cycle (dewax)

(4) Injection molding parameters

(5) Alternate powder preparation (PSD)

(6) Additive composition (sintering aids)

(7) Sintering cycles

The evaluations were conducted iteratively. Two or more processing parameters were investigated in a statistically designed experimental matrix to determine possible interactions between those parameters. Prior experience and efficiency of experimental work were used to guide the selections of parameters included in a particular matrix.

Table A-1 shows the parameters chosen for evaluation and the combinations of these parameters in Matrixes 1 through 6. The design and rationale of each matrix will be explained in the subsequent sections.

2. MATRIX 1 - RAW MATERIALS/SINTERING TEMPERATURES

As the first iteration, four commercial Si_3N_4 powders were selected for comparison. These four materials were processed through the dewax cycle using baseline processing. The last step, sintering, was carried out at two different peak temperatures to assess the interaction between raw materials and peak sintering temperature. Figure A-1 shows the experimental matrix design.

Experimental procedures: Figure A-2 is a flowchart showing the major processing procedures and guidelines. The silicon nitride powders chosen for study were GTE SN-502 (baseline), Denka 9S, UBE SN-EN, and Starck H-1. The powders were prepared by baseline milling procedures described in Task I. Each milled powder was blended with a 15.5 percent GCC standard binder (identified as B_1) using a HAAKE Rheomix model 600 mixer. This unit was used instead of the baseline mixer (double-arm, sigmabladed) which requires a minimum of 4000 g of

TABLE A-1.--RELATIONSHIP BETWEEN PROCESS SUBTASKS AND EXPERIMENTAL MATRIXES

	Experimental matrix number						
	1	2	3	4	5	6	7
Subtask 1 Raw material	X				X	X	
Subtask 2 Binder		X			X	X	X
Subtask 3 Binder extraction			X			X	X
Subtask 4 Injection molding			X			X	
Subtask 5 Powder preparation (milling)			X		X		
Subtask 6 Composition				X			
Subtask 7 Sintering cycle	X			X		X	

	M_1	M_2	M_3	M_4
S_1	10 MOR	10 MOR	10 MOR	10 MOR
S_2	10 MOR	10 MOR	10 MOR	10 MOR

M_1 = GTE SN-502 Si_3N_4 powder + 6% Y_2O_3 + 2% Al_2O_3

M_2 = DENKA 9S Si_3N_4 powder + 6% Y_2O_3 + 2% Al_2O_3

M_3 = UBE SN-EN Si_3N_4 powder + 6% Y_2O_3 + 2% Al_2O_3

M_4 = STARCK H-1 Si_3N_4 powder + 6% Y_2O_3 + 2% Al_2O_3

S_1 = Baseline sintering temperature and conditions

S_2 = Baseline plus 50°C

Figure A-1.--Experiments Designed to Investigate the Interaction Between Raw Materials and Sintering Cycles.

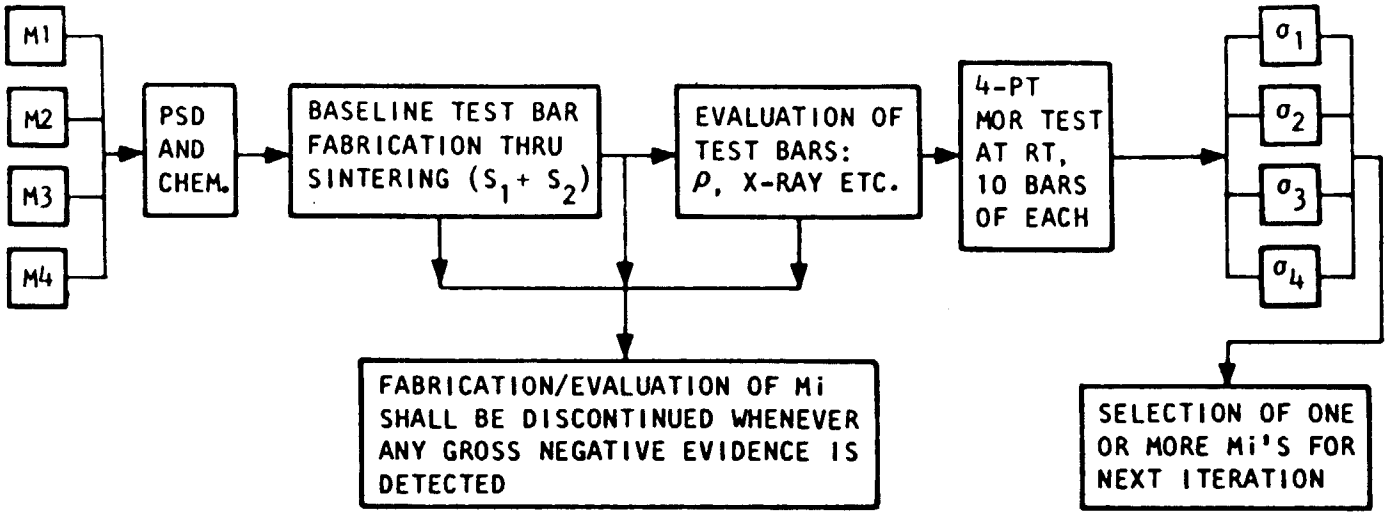

NOTE:

M1 = BASELINE Si_3N_4
(SN 502 + 6% Y_2O_3 + 2% Al_2O_3)

Mi = ALTERNATE Si_3N_4.
where i = 2, 3 AND 4

B_1 = BASELINE BINDER

B_i = ALTERNATE BINDER SYSTEMS

DC_i = DEWAX CYCLES

S_i = SINTERING CYCLES

σ_i = STRENGTHS

A-70733

Figure A-2.--Flowchart Showing the Experimental Approach of Matrix I Alternate New Materials/Sintering Temperature.

materials to achieve an adequate mixing action. The HAAKE Rheomix 600 requires only 107 g of material, and the mixing parameters are more readily controlled and monitored.

A new set of mixing parameters, "HAAKE baseline", was chosen for blending powder and binder for this matrix. Any subsequent experiments in Task VII that require only a small amount of blended injections mix also will be processed in this manner.

Results and discussion: All above-mentioned powders, except UBE SN-EN, were blended successfully using the new baseline blending procedures. Slow wetting of the UBE powder by the binder and the very high mixing torques required indicated that this powder, milled by the "HAAKE baseline" process, was not suitable for injection molding. Therefore, processing of UBE SN-EN beyond blending was discontinued.

The three successfully blended materials were injection molded by baseline injection molding procedures (see Task I) after the materials were pelletized. No difficulty was encountered during injection molding, and all test bars appeared acceptable by visual inspection.

Binder was removed from 84 bars using the baseline cycle. Bars of baseline material, M_1, appear to be in good condition; however, the other two materials, M_2 and M_4, exhibited cracking.

The test bars subsequently were sintered in two sintering runs, 1850°C (3360°F) and 1900°C (3450°F) at 0.68 MPa (95 psig) nitrogen. Sintered densities are reported in table A-2. A small density increase was observed at the increased sintering temperature for M_1 and M_4 powders, but a slight decrease occurred for M_2. Blistering was observed on M_2 bars sintered at the higher temperature but not on the other bars.

Sintering shrinkage was measured on each bar. M_3 and M_4 bars showed isotropic shrinkage, but baseline M_1 bars demonstrated higher shrinkage in thickness than in length, 16.3 percent compared with 13.9 percent.

This anisotropic shrinkage was probably due to a small amount of needle-like materials, that remained in the milled GTE SN-502 Si_3N_4 powder.

Visual and X-ray radiography inspection of the sintered bars showed that the quality of M_1 bars was comparable to that of the Task 1 bars; however, the M_2 and M_4 bars had a high rejection rate, 96 and 75 percent, respectively.

Room temperature MOR measurement data correlated well with the quality of test bars. The MOR values for M_1 bars ranged from 515 to 570 MPa (75 to 83 ksi), while the values for M_2 and M_4 were mostly below 345 MPa (50 ksi). The low MOR's for M_2 and M_4 are clearly due to lower sintered densities and the presence of defects.

The M_2 material exhibited large internal voids on the fracture surfaces, often associated with large blisters. The M_4 material exhibited some large

TABLE A-2.--SINTERED DENSITIES USING DIFFERENT Si_3N_4 STARTING POWDERS

	Density and standard deviation, g/cc			
	1850°C (3360°F)		1900°C (3450°F)	
Starting powder	ρ	Δ	ρ	Δ
M_1	3.18	0.03	3.21	0.01
M_2	3.06	0.04	2.99	0.03
M_4	2.99	0.02	3.05	0.01

ρ: average density
Δ: standard deviation

internal porosity on the fracture surface, but the porosity was less common and smaller than that of the M_2 material. Some specimens also exhibited internal cracking.

The low strength and excessive defects observed in the M_2 and M_4 test bars suggest either that these two materials are intrinsically poor or that they require a set of processing parameters significantly different from the baseline processing parameters that were used.

3. MATRIX 2 - BINDER/WETTING AGENT/MIXING

The degree and homogeneity of ceramic powder dispersion in the binder are believed to be very important to the quality of injection-molded ceramic parts. Figure A-3 shows the design of a matrix which combines binder system, wetting agents, and mixing conditions.

Experimental procedures: The baseline binder, B_1, and an alternate binder, B_2, in conjunction with several wetting agents, and different ways of mixing the wetting agents with the powder/binder were investigated. Baseline powder was used throughout the matrix.

All mixing was carried out on the Rheomix 600 using the "HAAKE baseline" procedures. The mixer chamber was heated (80°C/175°F) to melt the binder, then the powder was added to the mixer. A wetting agent was added 5 minutes after the onset of each mixing run. The twin mixing rotors were run at 60 and 15 rpm at the end of the mixing cycle in order to evaluate the rheology dependency on shear rate of the mixed material.

An initial mixing process study was completed using binders B_1 and B_2 with wetting agents WA_1, WA_2, WA_3, and WA_4, all of which are proprietary.

Figures A-4 and A-5 show examples of torque and temperature curves plotted by the HAAKE Rheomix mixer.

	TB_1	TB_2	TB_3
WA_1	B_{11}	B_{22}	B_{21}
WA_2	B_{12}	B_{21}	B_{22}
WA_3	B_{21}	B_{11}	B_{12}
WA_4	B_{22}	B_{12}	B_{11}

TB_i = Blending temperature, where i = 1, 2, and 3

WA_i = Wetting agent, where i = 1, 2, and 3

B_{11} = Binder system 1 at level 1

B_{12} = Binder system 1 at level 2

B_{21} = Binder system 2 at level 1

B_{22} = Binder system 2 at level 2

Figure A-3.--Matrix 2 Design.

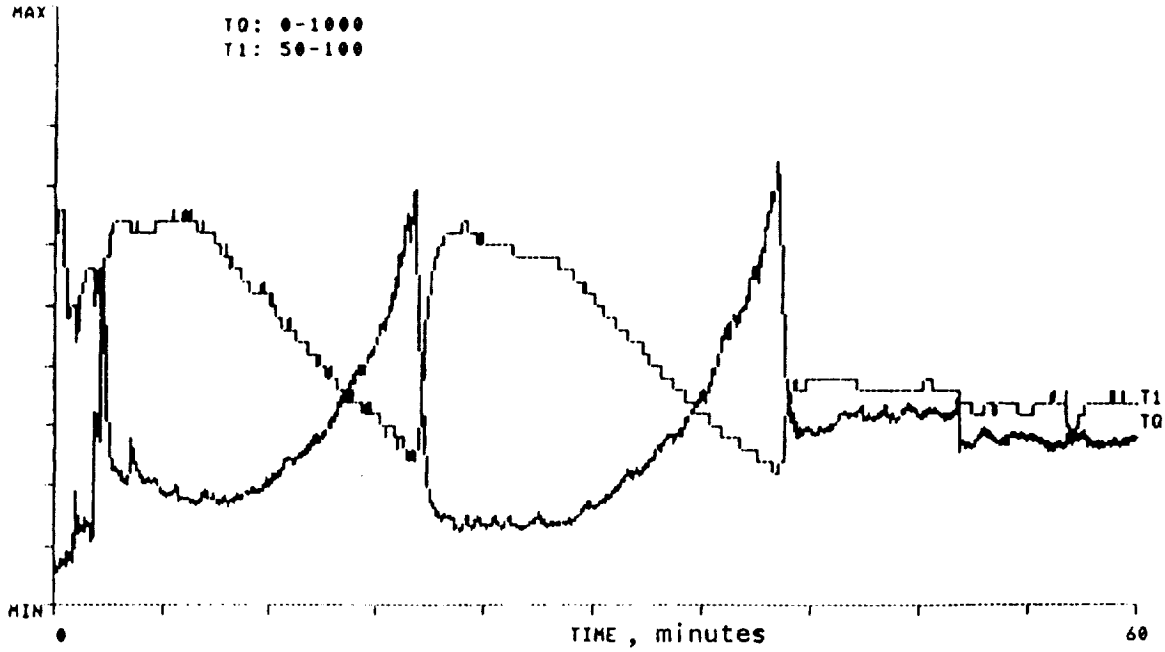

Figure A-4.--Mixing Torque and Temperature Curves for Baseline Powder and B_1 Binder.

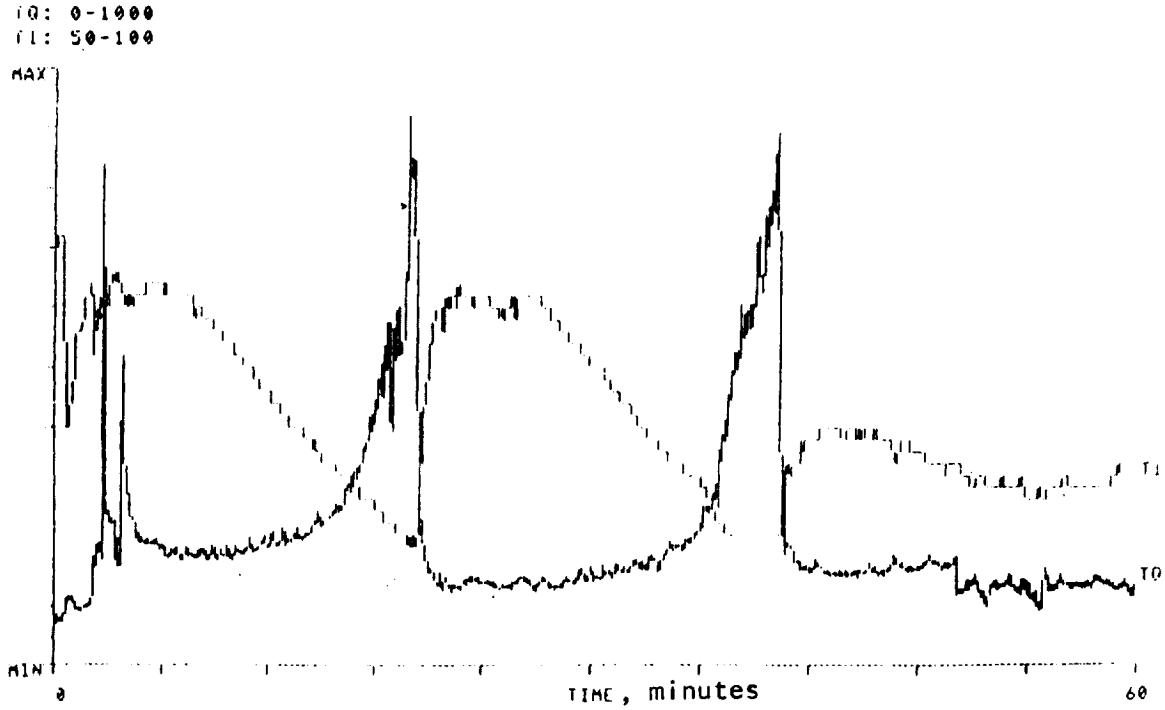

Figure A-5.--Mixing Torque and Temperature Curves for Baseline Powder and B_2 Binder.

Results and discussion: The results of the experiments are shown in the matrix blocks in table A-3. The response of each treatment is the measured torque at high and low shear rates and their ratio. A detailed analysis of Matrix 2 was conducted and only the highlights are summarized here.

The results of the data analyses indicated that interaction may exist among the variables included in this matrix.

(1) Judging from the data in the matrix, the calculated values of the variances (S^2) are significantly high thereby making the numbers of critical statistics (w) unreasonably higher than the differences of the main effects.

(2) From figures A-6, A-7, and A-8, the combined effects of mixing temperature, wetting agent, and binder (B_{xy}) to torque exhibited the same pattern of effect. These figures illustrate a significant interaction between the binder (B_{xy}) and the wetting agent.

When interaction exists, the nature of the main effect being unknown (it depends on the level of other variables), and the significant test to estimate the difference of any effect will draw a misleading result.

The identified interaction probably results from specific, proprietary binder (B_{xy}) components and wetting agents. Significance of this behavior, with regard to test bar fabrication, will be determined in separate experiments.

TABLE A-3.--MATRIX 2 EXPERIMENTS BINDER/WETTING AGENT/MIXING TEMPERATURE

WETTING AGENT	Blending Temperature			Total
	TB_1	TB_2	TB_3	
WA_1	B_{11} $\frac{305}{300} = 1.107$	B_{22} $\frac{170}{110} = 1.545$	B_{21} $\frac{130}{115} = 1.130$	Ratio R_1 = 3.692 H Shear R_1 = 605 L Shear R_1 = 525
WA_2	B_{12} $\frac{340}{350} = 0.97$	B_{21} $\frac{220}{150} = 1.47$	B_{22} $\frac{120}{100} = 1.20$	Ratio R_2 = 3.64 H Shear R_2 = 680 L Shear R_2 = 600
WA_3	B_{21} $\frac{160}{125} = 1.29$	B_{11} $\frac{640}{750} = 0.853$	B_{12} $\frac{295}{240} = 1.23$	Ratio R_3 = 3.363 H Shear R_3 = 1095 L Shear R_3 = 1115
WA_4	B_{22} $\frac{280}{240} = 1.167$	B_{12} $\frac{700}{800} = 0.875$	B_{11} $\frac{380}{350} = 1.086$	Ratio R_4 = 3.128 H. Shear R_4 = 1360 L. Shear R_4 = 1390
Total	Ratio C_1 = 4.434 H Shear C_1 = 1085 L Shear C_1 = 1015	Ratio C_2 = 4.743 H Shear C_2 = 1730 L Shear C_2 = 1810	Ratio C_3 = 4.646 H Shear C_3 = 925 L Shear C_3 = 805	Ratio G = 13.823 H Shear G = 3740 L Shear G = 3630

B_{xy} = Binder Type x at y level

Response is torque ratio of high shear rate (at 60 rpm) and low shear rate (at 15 rpm)

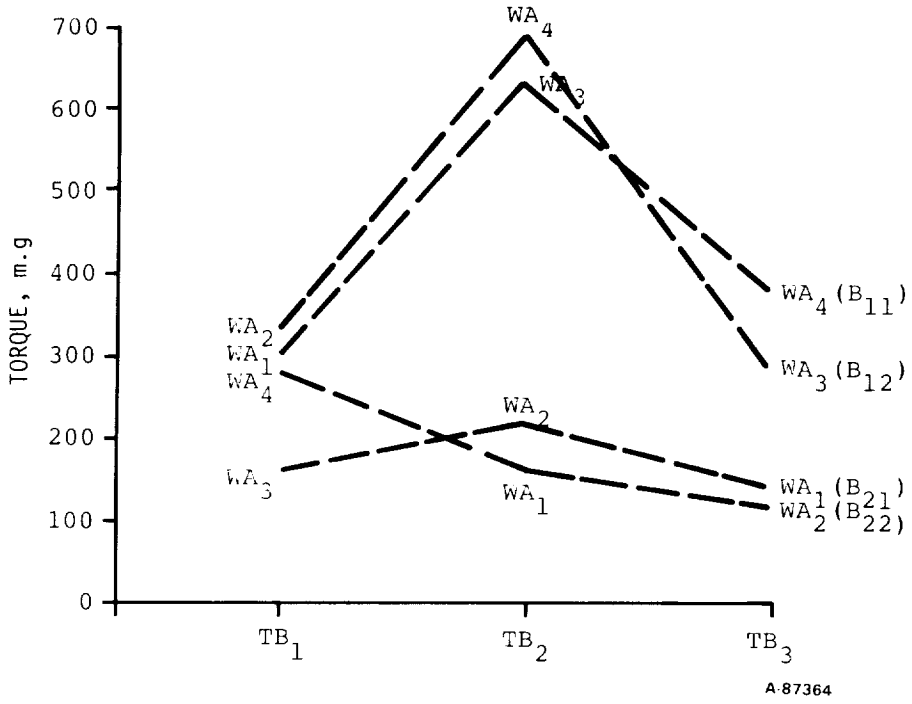

Figure A-6.--Mixing Torque at High Shear Rate (60 rpm).

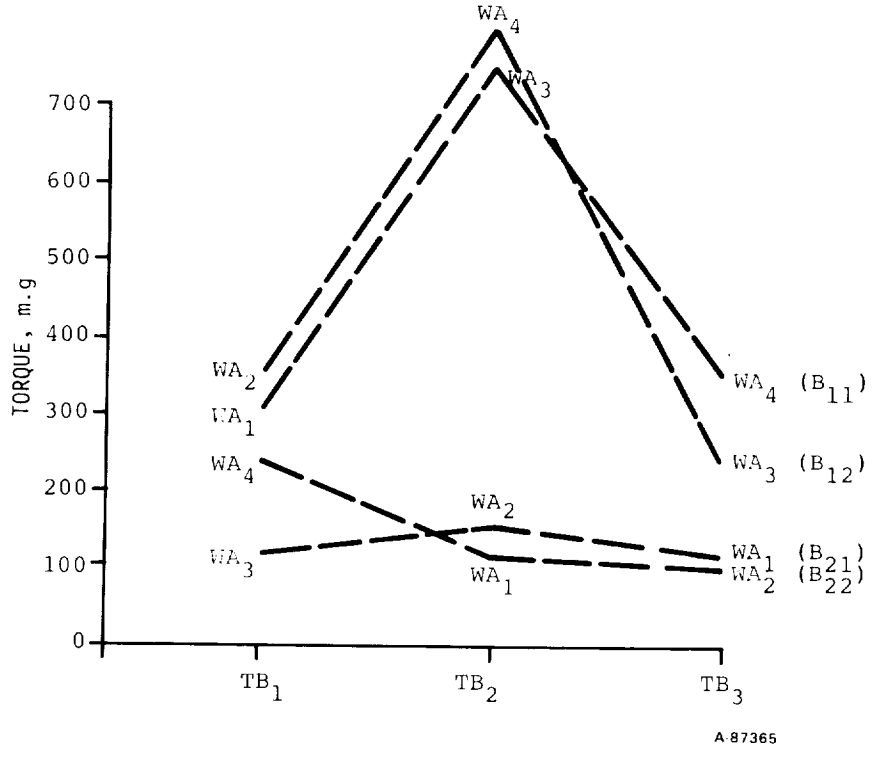

Figure A-7.--Mixing Torque at Low Shear Rate (15 rpm).

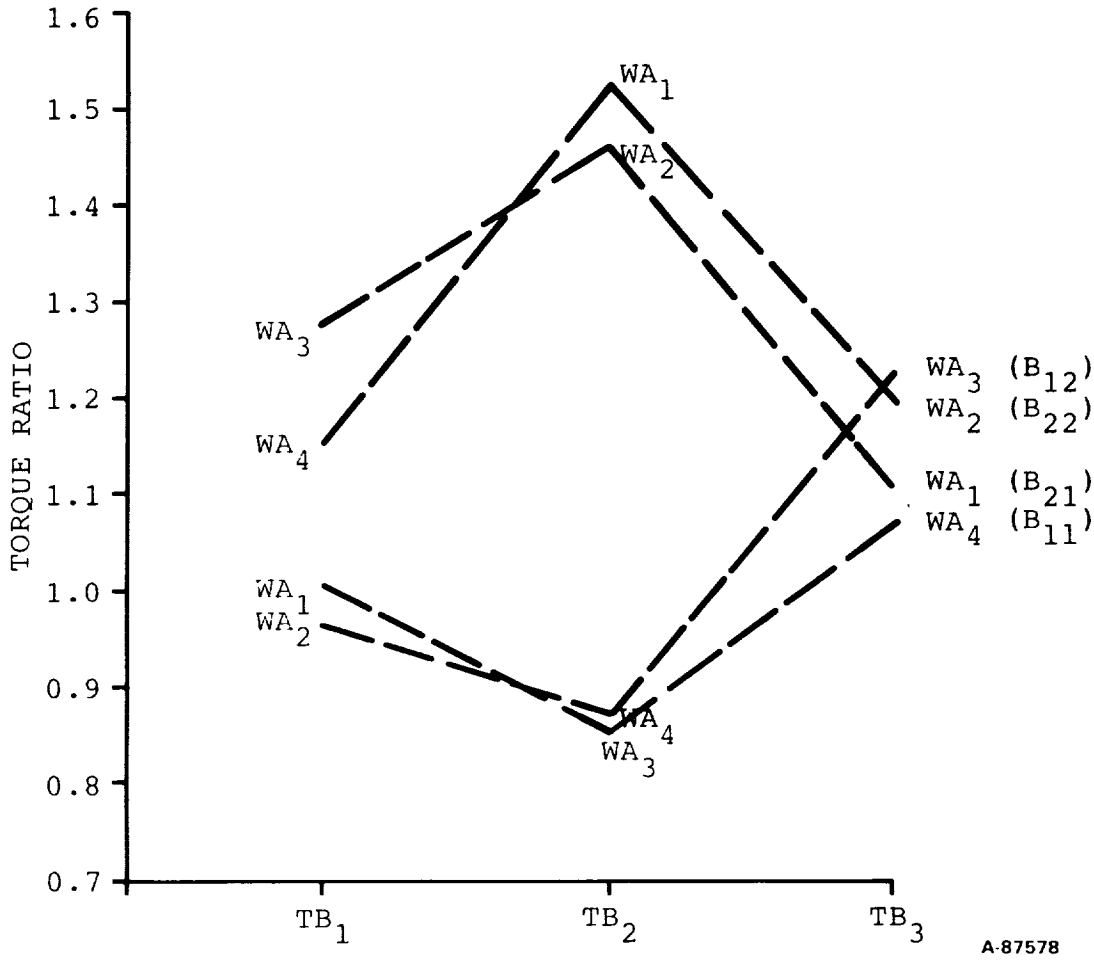

Figure A-8.--Mixing Torque Ratio (High Shear Rate/Low Shear Rate).

4. MATRIX 3 - BINDER EXTRACTION/INJECTION MOLDING/POWDER PREPARATION

This matrix was designed to study the relationship between dewax cycle, molding material temperature, and milling time (i.e., PSD). Figure A-9 illustrates the matrix design which is known as the Youden square design. Due to experimental difficulties, certain treatments in the matrix could not be carried to injection molding, and therefore, the intended statistical analysis of variance could not be conducted. However, even though the originally planned statistical analysis could not be conducted, several simpler analyses and observations could be performed and meaningful conclusions were obtained.

Experimental procedures: The baseline material (GTE SN-502 + 6% Y_2O_3 + 2% Al_2O_3) was used throughout the matrix. The processing procedures, milling through sintering, were part of the matrix evaluation and are more conveniently described along with results relating to the evaluation of the particular processing parameters to be followed. The baseline process was used as one of the experimental variations in this experiment.

	DC_1	DC_2	DC_3	DC_4
T_1	PSD_1	PSD_2	PSD_3	PSD_4
T_2	PSD_2	PSD_3	PSD_4	PSD_1
T_3	PSD_3	PSD_4	PSD_1	PSD_2
T_4	PSD_4	PSD_1	PSD_2	PSD_3

DC_i = Binder extraction at different thermal cycles, where i = 1, 2, ...

PSD_i = Particle size distribution

T_i = Injection molding temperature

Figure A-9.--Matrix 3 Design.

Results and discussion:

(1) Powder milling (PSD) effect on mixing.--In order to evaluate the effect of powder particle size distribution on mixing (with a binder) and injection molding of the mix, the baseline powder was milled for 8, 24, 48, and 96 hours. These milled powders subsequently were mixed with a fixed quantity of the baseline binder (B_1) in a HAAKE Rheomix under a programmed temperature profile (figure A-10a) at 60 rpm rotor rotation speed. The temperature profile and rotor speed were selected to provide good mixing and an appropriate torque output for rheological evaluation. It is demonstrated (see figure A-10b) that throughout the 40-minute mixing period, the torque output level systematically varied inversely with milling time. Also, it is evident that for a given mix, the torque level varied inversely with the programmed temperature profile.

The above rheological variation data are to be used as guidelines for injection molding parameter studies in the future.

(2) Injection molding behavior map.--A series of injection molding experiments were performed to investigate the molding behavior variation of mixes. It was found that when all other molding parameters were held constant, the material molding temperature required to obtain visually good test bars depended strongly on the PSD of the powder. The molding material temperatures required for 8-, 24-, and 48-hr milled materials were 93°, 77°, and 71°C (200°, 170°, and 160°F), respectively.

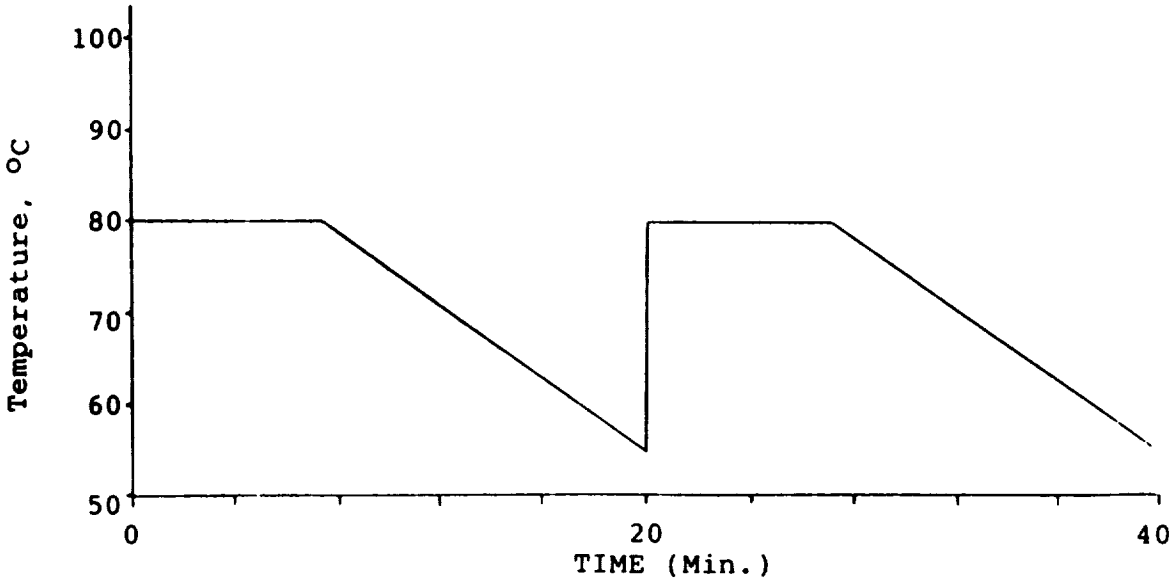

A. Programmed temperature profile for mixing.

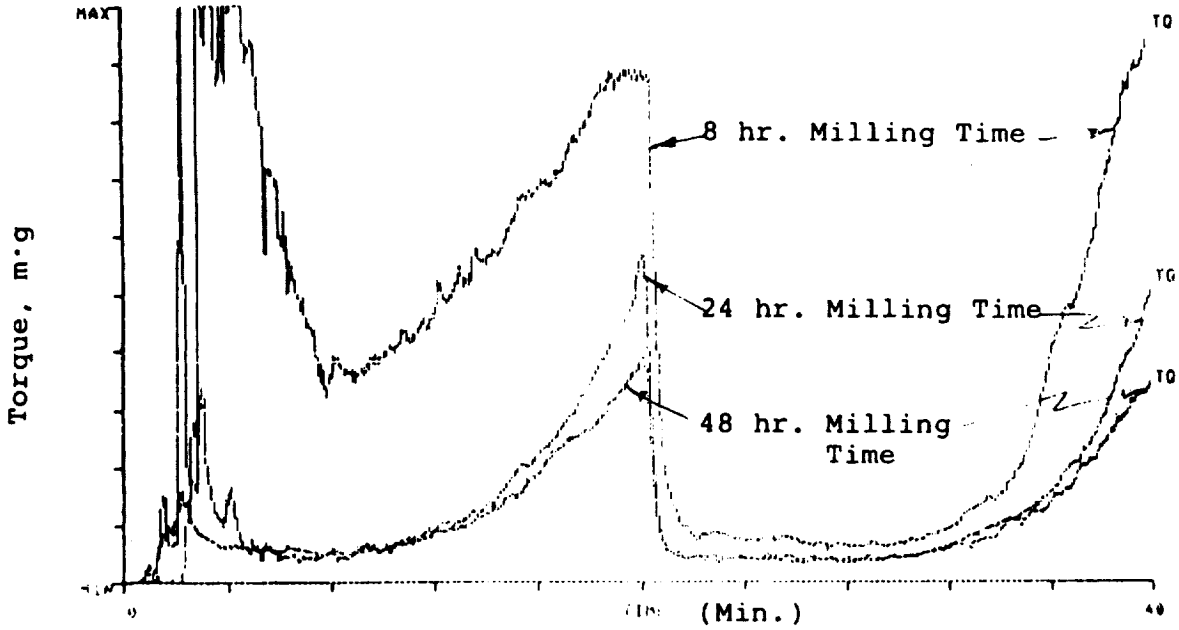

B. Mixing torque curves under the programmed temperature profile at 60 rpm rotor rotation speed.

Figure A-10.--Mixing Torque Curves from Powders of Various Milling Times.

The general flow behavior observed for 18 different milling time/molding temperature combinations is illustrated in figure A-11. As the graph indicates, high molding temperatures (i.e., greater than 93°C) are required to obtain satisfactory test bars for powder milled for 8 hours. Bars which appeared to be satisfactory by visual and X-radiographic inspection were injected at 71°C material temperature with powders milled for 48 or 96 hours. The following process step, binder removal, resulted in cracks and shrinkage in bars with 48- or 96-hour-milled powder; this was attributed to excess binder.

In figure A-11, "insufficient fluidity" describes the condition at which the material does not flow smoothly but tends to break up as it fills and conforms to the die cavity. "Excess fluidity" describes the condition at which leakage within the injection molding machine prevents maintaining full pressure during the forming of the test bar.

(3) Dewax experiments--Four thermal cycles are used for the experiments in this matrix. Weight loss, dimensional change, and surface quality inspection were evaluated and correlated with PSD (or milling time) and injection molding parameters. The observations and results are described in the following paragraphs.

(a) Weight loss analysis--Table A-4 shows the treatments in Matrix 3 and the experimental results of the dewax weight loss. The data in table A-4 can not be analyzed by using the Latin square or Youden square methods as was originally planned. Rather, data from bars which have been through dewax are point estimated for several selected treatments of dewax cycle, material temperature, and milling time instead of investigated in a three-dimensional space of these variables. Therefore, the statistical analysis is conducted to compare the results between two points (or treatments).

Table A-5 shows the comparison of two groups of treatments with the same dewax cycles, and table A-6 shows the comparison of two groups of treatments with the same molding material temperature. From these results it is observed that:

(1) With the same dewax cycles, the difference in dewax weight loss between treatments is significant in most cases. The difference is more likely influenced by milling time (or PSD) than by material molding temperature.

(2) With the same material molding temperature, the difference in dewax weight loss between treatments is also significant in most cases. The difference is also more likely influenced by milling time (PSD) than by dewax cycle.

(3) With the same molding material temperature, the influence of different dewax cycles is not significant.

(b) Dimensional change--The thickness of a selected group of dewaxed bars was measured and compared with the thickness of these bars before

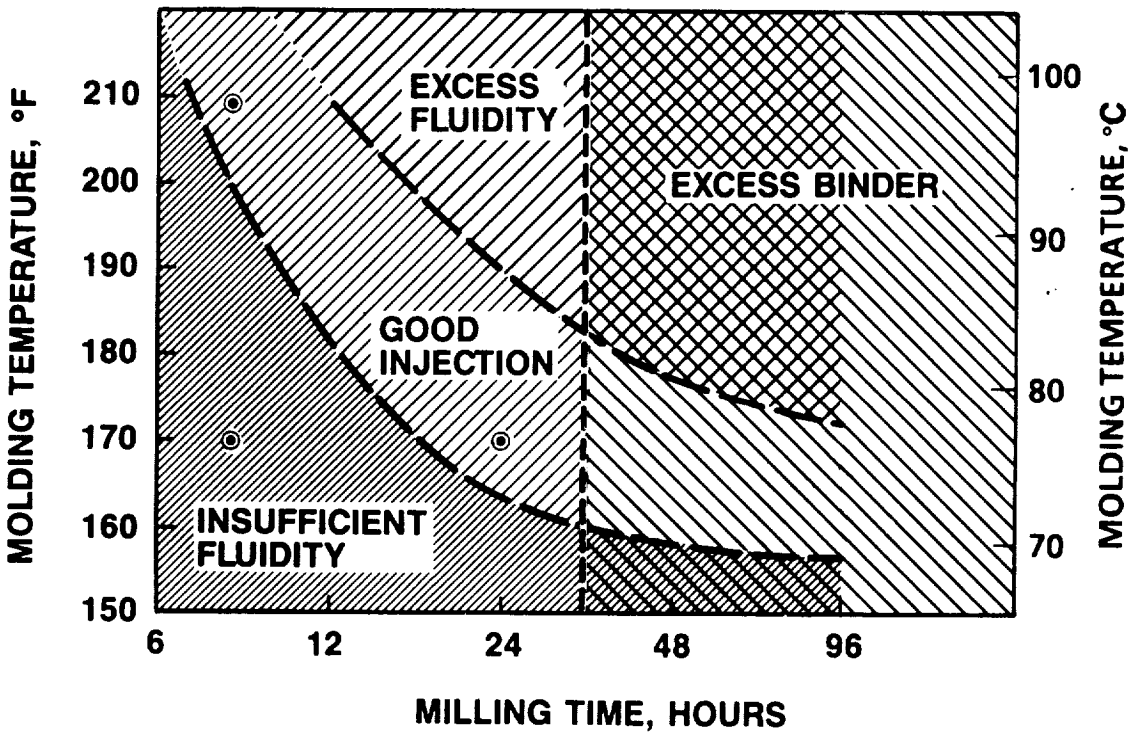

Figure A-11.--Flow Characteristics of Injection Molding Materials as a Function of Powder Milling Time, Material Temperature During Molding, and Mixing Torque at 65°C (149°F) (GTE SN-502 Powder was Used).

being dewaxed. These dimensional changes are listed in table A-7 along with the bars' weight loss as a function of milling time. The dimensional change data are also plotted in figure A-12. It is obvious that the dimensional change is a function of milling time (PSD), ranging from an expansion of 0.5 percent to a shrinkage of 1.5 percent. This has a significant implication in understanding the cracking behavior of a dewaxed part. The significance of the increase in weight loss with milling time (table A-5) observed on the same set of test bars can not be interpreted at the present time.

TABLE A-4.--MATRIX 3, DEWAX WEIGHT LOSS DATA

MOLDING MATERIAL TEMPERATURE	DEWAX CYCLES			
	DC1 132 HR 850°F	DC 2 40 HR 850°F	DC3 20 HR 850°F	DC4
155°F	N=4 MILLING TIME 48 HR $\bar{X}$=15.275% σ=0.05			
160°F		12 48 HR $\bar{X}$=15.375 σ=0.0866	12 96 HR #2 $\bar{X}$=15.5 σ=0.0853	16 24 HR #1 $\bar{X}$=15.07 σ=0.0704
170°F	23 24 HR #2 $\bar{X}$=15.37 σ=0.0703	4 24 HR #2 4 96 HR #1 2 8 HR $\bar{X}$=15.45 σ=0.10 $\bar{X}$=15.57 σ=0.058 $\bar{X}$=15.0 σ=0	12 48 HR $\bar{X}$=15.308 σ=0.0996	24 96 HR #1 $\bar{X}$=15.571 σ=0.0751
180°F	8 48 HR $\bar{X}$=15.4 σ=0.0926	12 96 HR #2 $\bar{X}$=15.533 σ=0.065	16 24 HR #1 $\bar{X}$=15.131 σ=0.0602	4 8 HR $\bar{X}$=15.05 σ=0.0577
190°F	12 96 HR #2 $\bar{X}$=15.45 σ=0.0904	10 24 HR #2 $\bar{X}$=15.17 σ=0.0675	8 8 HR $\bar{X}$=14.963 σ=0.0517	
200°F				4 8 HR $\bar{X}$=15.05 σ=0.0577
210°F		4 8 HR $\bar{X}$=14.975 σ=0.0958		

A 81092

N=NUMBER OF SAMPLES

MILLING TIME IN HOURS

$\bar{X}$=MEAN DEWAX WEIGHT LOSS
σ=STANDARD DEVIATION

TABLE A-5.--MATRIX 3, DEWAX WEIGHT LOSS DATA SUMMARY ARRANGED BY DEWAX CYCLE

DC1 (132 hr to 454°C/850°F)			DC2 (40 hr to 454°C/850°F)			DC3 (20 hr to 454°C/850°F)			DC4 (10 hr to 454°C/850°F)		
Groups	$\bar{x}$	σ	Groups	$\bar{x}$	σ	Groups	$\bar{x}$	σ	Groups	$\bar{x}$	σ
(1) 155°F 48 hr	15.275	0.05	(1) 160°F 48 hr	15.375	0.0704	(1) 160°F 95 hr #2	15.5	0.0853	(1) 160°F 24 hr	15.07	0.0704
(2) 170°F 24 hr #2	15.37	0.07	(2) 170°F 24 hr	15.45	0.10	(2) 170°F 48 hr	15.31	0.0996	(2) 170°F 96 hr #1	15.57	0.075
(3) 180°F 48 hr	15.40	0.093	(3) 170°F 96 hr #1	15.37	0.058	(3) 180°F 24 hr #1	15.13	0.0602	(3) 180F 8 hr	15.05	0.0577
(4) 190°F 96 hr	15.45	0.09	(4) 170°F 8 hr	15.0	0	(4) 190°F 8 hr	14.96	0.0517	(4) 200°F 8 hr	15.05	0.0577
			(5) 180°F 96 hr #2	15.533	0.065						
			(6) 190°F 24 hr #2	15.17	0.0675						
			(7) 210°F 8 hr	14.975	0.096						
Comparison between groups	P-value		Comparison between groups	P-value		Comparison between groups	P-value		Comparison between groups	P-value	
(1) (2)	0.0169		(1) (2)	0.1693		(1) (2)	0.000		(1) (2)	0.000	
(1) (3)	0.0323		(1) (3)	0.0033		(1) (3)	0.000		(1) (3)	0.630	
(1) (4)	0.0027		(1) (4)	0.0001		(1) (4)	0.000		(1) (4)	0.630	
(2) (3)	0.339		(1) (5)	0.000		(2) (3)	0.000		(2) (3)	0.000	
(2) (4)	0.0084		(1) (6)	0.000		(2) (4)	0.000		(2) (4)	0.000	
(3) (4)	0.246		(1) (7)	0.000		(3) (4)	0.000		(3) (4)	1.000	
			(2) (3)	0.1345							
			(2) (4)	0.0039							
			(2) (5)	0.0714							
			(2) (6)	0.000							
			(2) (7)	0.0005							
			(3) (4)	0.0009							
			(3) (5)	0.435							
			(3) (6)	0.000							
			(3) (7)	0.0002							
			(4) (5)	0.000							
			(4) (6)	0.0065							
			(4) (7)	0.745							
			(5) (6)	0.000							
			(5) (7)	0.000							
			(6) (7)	0.0009							

TABLE A-6.--DEWAX WEIGHT LOSS DATA SUMMARY ARRANGED BY MOLDING TEMPERATURE

71°C (160°F)			77°C (170°F)			82°C (180°F)			88°C (190°F)		
Groups	$\bar{X}$	σ	Groups	$\bar{X}$	σ	Groups	$\bar{X}$	σ	Groups	$\bar{X}$	σ
(1) DC2 48 hr	15.375	0.0866	(1) DC1 24 hr #2	15.37	0.0703	(1) DC1 48 hr	15.4	0.0926	(1) DC1 96 hr #2	15.45	0.0904
(2) DC3 96 hr	15.50	0.0853	(2) DC2 24 hr #2	15.45	0.10	(2) DC2 96 hr #2	15.53	0.065	(2) DC2 24 hr #2	15.17	0.0675
(3) DC4 24 hr #1	15.07	0.0704	(3) DC2 96 hr #1	15.567	0.058	(3) DC3 24 hr #1	15.13	0.0602	(3) DC3 8 hr	14.96	0.0517
			(4) DC2 8 hr	15.0	0.0	(4) DC4 8 hr	15.05	0.0577			
			(5) DC3 48 hr	15.308	0.0996						
			(6) DC4 96 hr #1	15.57	0.0751						
Comparison between groups	P-value		Comparison between groups	P-value		Comparison between groups	P-value		Comparison between groups	P-value	
(1) (2)	0.0017		(1) (2)	0.0572		(1) (2)	0.0013		(1) (2)	0.000	
(1) (3)	0.000		(1) (3)	0.0001		(1) (3)	0.000		(1) (3)	0.000	
(2) (3)	0.000		(1) (4)	0.000		(1) (4)	0.000		(2) (3)	0.000	
			(1) (5)	0.042		(2) (3)	0.000				
			(1) (6)	0.0001		(2) (4)	0.000				
			(2) (3)	0.134		(3) (4)	0.0258				
			(2) (4)	0.0039							
			(2) (5)	0.0275							
			(2) (6)	0.356							
			(3) (4)	0.0009							
			(3) (5)	0.001							
			(3) (6)	0.850							
			(4) (5)	0.0012							
			(4) (6)	0.000							
			(5) (6)	0.002							

TABLE A-7.--MILLING TIME EFFECT ON BINDER EXTRACTION OF TEST BARS

Milling time, hr	Test bar thickness change[1,2], %	Weight loss[1], %
8	+0.5	15.00
24	+0.2	15.10
48	-0.1	15.35
96	-1.0	15.56

Notes:

1. $\frac{\text{Thickness after binder extraction-thickness before binder extraction}}{\text{thickness before binder extraction}}$

2. Average of a minimum of 10 test bars

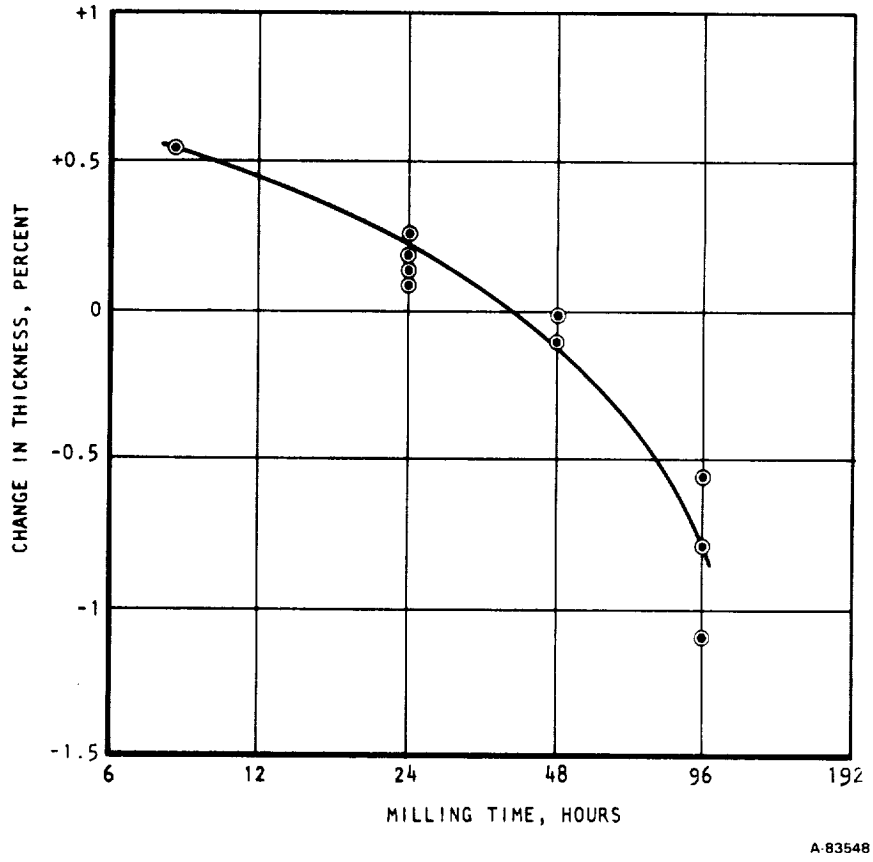

Figure A-12.--Dimensional Change During Binder Removal, using a Constant Binder Content and GTE SN-502 Powder.

(c) Surface quality--A selected number of samples were examined under a microscope after dewaxing. It was found that:

(1) Binder-extracted specimens often revealed additional defects not seen on injection-molded test bars. An example is shown in figure A-13.

(2) The visual surface quality of the binder-extracted test bars also depends on the injection molding temperature and PSD (milling time) as shown in figures A-14 and A-15.

(4) Sintering--Sintering was completed on 144 test bars representative of 4 PSD's and 4 dewax cycles. Weight loss was comparable to Task I resintered bars. Higher weight loss bars (located in the outer position of the sintering tray) appeared darker and somewhat grainy. They are relatively free, however of the pitting which was extensive in earlier bars (shown in figure A-16 near the bottom edge).

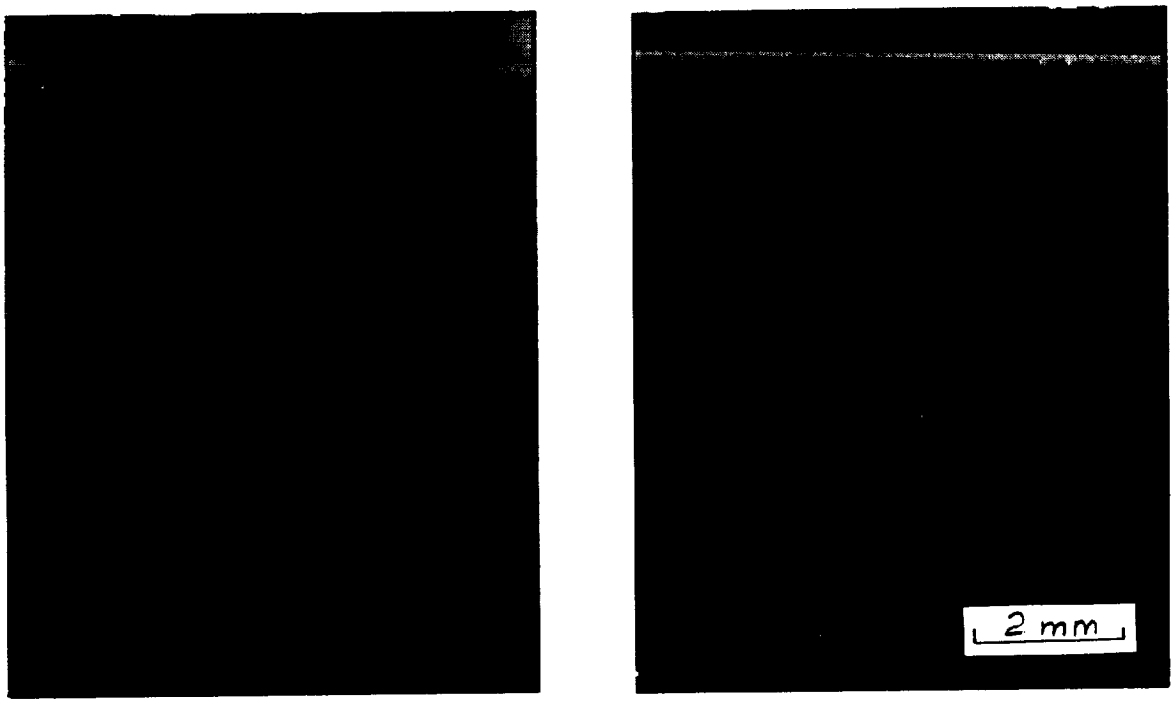

F-47248

A. Injection molded

B. Dewaxed

Figure A-13.--Injection-Molded and Dewaxed Surfaces of Test Bar 904 (76.6°C/170°F Injection) using Powder Milled 96 Hours.

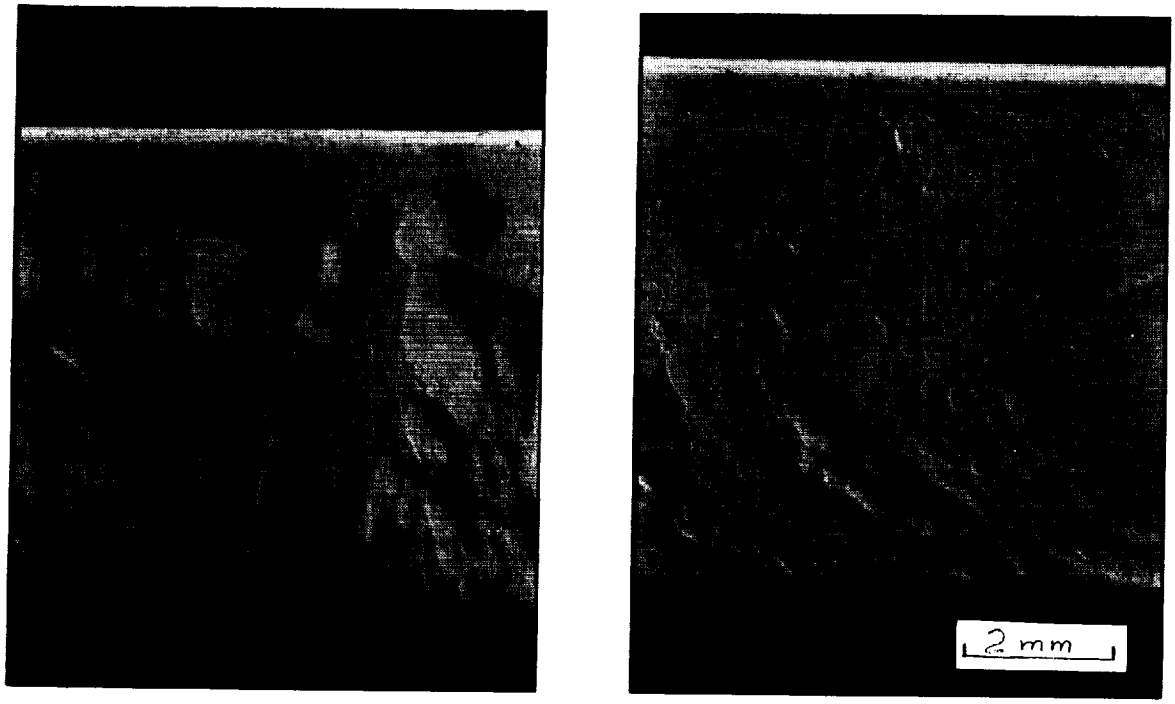

A. Bar no. 1054 (71°C/160°F injection)

B. Bar no. 1072 (77°C/180°F injection)

Figure A-14.--Dewaxed Test Bar Surfaces from Two Molding Temperatures using Powder Milled 96 Hours.

Densities after sintering were generally higher than Task I results. Data are presented in table A-8.

Some improvements were seen in surface finish during sintering as compared with dewax (see figure A-17). Existing cracks were not healed, however. It is not clear if a smoother surface results in any flaw healing.

Three-way plots of the MOR data vs two process variables at fixed dewax run or molding temperature were made. From these plots the following observations are made.

(1) At a fixed dewax run, or a fixed material molding temperature, each PSD has its own specific dewax weight loss region and that PSD affects MOR significantly. For the same PSD, dewax weight loss does not affect MOR. At this time, it is concluded that PSD has the primary effect.

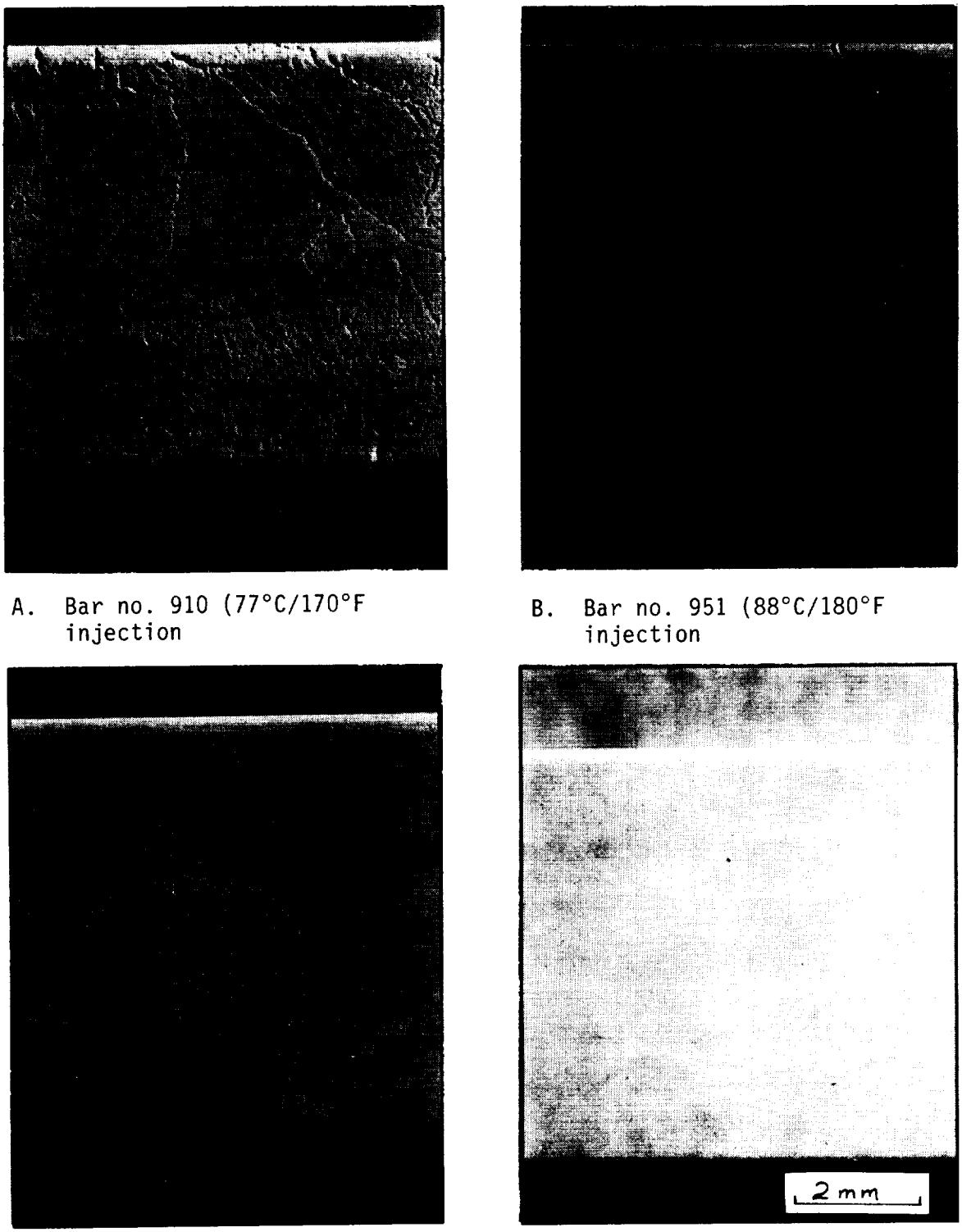

A. Bar no. 910 (77°C/170°F injection

B. Bar no. 951 (88°C/180°F injection

C. Bar no. 942 (93°C/200°F injection)

D. Bar no. 948 (99°C/210°F injection)

Figure A-15.--Dewaxed Test Bar Surfaces from Four Molding Temperatures using Powder Milled 8 Hours.

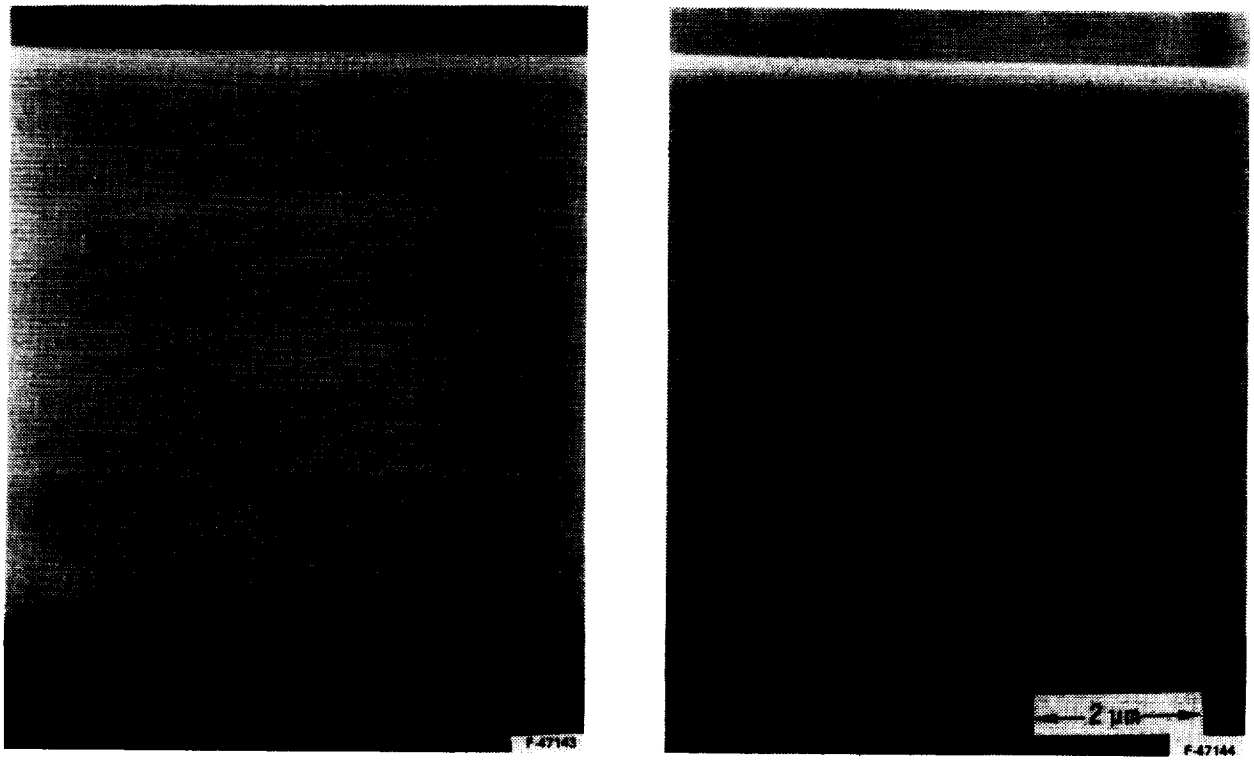

F-47173

Figure A-16.--Sintered Test Bars with High Weight Loss.

TABLE A-8.--MATRIX 3, SINTERING DATA SUMMARY

Milling time, hours	Average density, g/cc	Average weight loss, %	Number of samples weighed
8	3.22	1.44	21
24	3.25	1.65	57
48	3.25	2.14	32
96	3.23	2.17	29

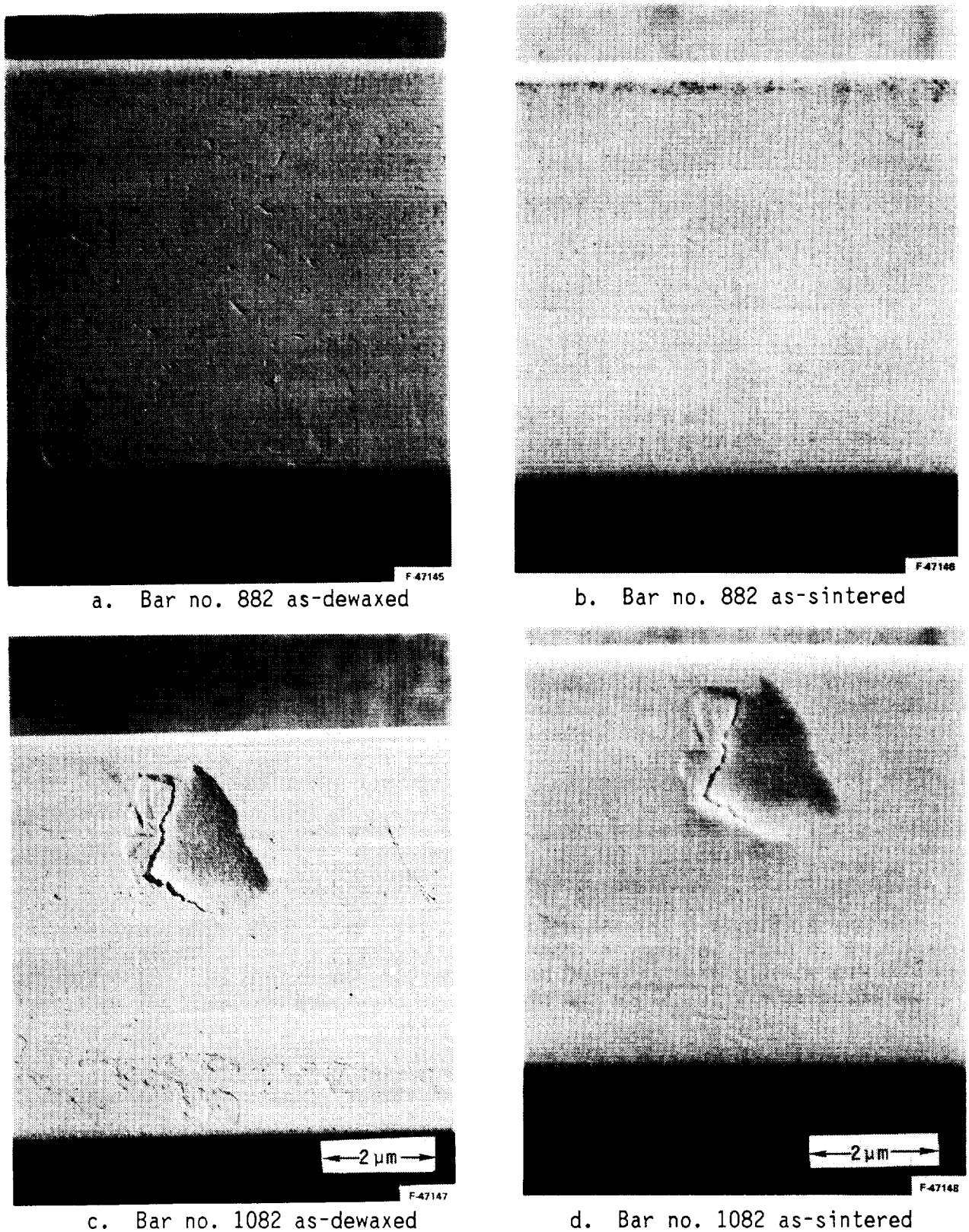

a. Bar no. 882 as-dewaxed

b. Bar no. 882 as-sintered

c. Bar no. 1082 as-dewaxed

d. Bar no. 1082 as-sintered

F-48900

Figure A-17.--Surface Changes in Sintering.

(2) At a fixed dewax run or a fixed material molding temperature, different PSD significantly affects MOR and sintering weight loss. For some dewax runs and some fixed PSD's, the higher the sintering weight loss, the higher the MOR.

(3) At a fixed dewax run or a fixed material molding temperature, different PSD has a distinguishable but not significant region of density. Different PSD significantly affects MOR. At a fixed PSD, the higher the density, the higher the MOR.

5. MATRIX 4 - SINTERING AIDS/SINTERING CYCLE

In order to improve the high temperature strength of the test bars, modification of the type and quantity of sintering aids is planned. In the first iteration, Y_2O_3 and Al_2O_3 levels will be varied with the goal of reducing the Al_2O_3 content. The baseline composition uses 6% Y_2O_3 and 2% Al_2O_3. Alternate levels were selected as follows: 6% and 1%, 6% and 0.5%, and 8% and 1%, Y_2O_3 and Al_2O_3, respectively. Sintering aid, sintering cycle, and heating rate are combined to form Matrix 4, as shown in figure A-18. Hot isostatic pressing (HIP) cycle is also included in this Matrix.

Experimental procedures: Baseline powder (GTE SN-502 Si_3N_4) was milled for 24 hours with the appropriate sintering aids. The milled powders were then blended with the baseline binder (B_1) at the baseline level (15.5 percent) using the "HAAKE baseline" procedures.

Results and discussion: Because of the variation in sintering aids, the mixing behavior of the mixes in the HAAKE 600 mixer also varied as reflection by the mixing torque summarized in table A-9. Correspondingly, the injection molding behavior using the baseline parameters also differs as reflected by the surface finish of the injection bars (see the last two columns of table A-9). This suggests that in order to fabricate good quality test bars, with different sintering aids, the injection parameters have to be readjusted.

6. MATRIX 5 - RAW MATERIALS, MILLING TIME, AND MILLING AID

Matrix 5 (figure A-19) was designed to provide a range of processing conditions in order to identify appropriate parameters for evaluating new powders and milling aids (MA_1 and MA_2). The results in Matrix 1 indicated that it may be necessary to change the processing parameters when evaluating a new powder.

Based on the results of Matrix 5 efforts, the range of processing conditions was narrowed to provide a limited number of materials for test bar fabrication and evaluation in Matrix 6.

Experimental procedure: Each powder and milling aid combination was milled at a minimum of two different milling time periods. Each of the milled powders was mixed with binder on the torque rheometer, using a fixed binder ratio, to determine the mixing and flow behavior.

	S1				S2			
	SA1	SA2	SA3	SA4	SA1	SA2	SA3	SA4
HR1								
HR2								
HIP								

S = Sintering peak temperature

HR = Heating rate

SA = Sintering aid

HIP = Hot isostatic pressing

Figure A-18.--Matrix 4.

TABLE A-9.--MIXING AND MOLDING BEHAVIORS OF MATERIALS CONTAINING DIFFERENT SINTERING AIDS

Code	Composition, %			Mixing Torque (m·g) at 65°C		Number of bars injected	Surface finish of as-injected test bars
	Si_3N_4	Y_2O_3	Al_2O_3	Average*	Standard deviation		
SA_1	92	6	2	400	40	44	Good
SA_2	93	6	1	507	60	52	Marginal
SA_3	93.5	6	0.5	510	52	32	Bad
SA_4	91	8	1	380	35	32	Some good, some marginal

*Average of 5 or 6 values

	MA_0	MA_1	MA_2
M_1	PSD_1PSD_2	PSD_3PSD_4	
M_4	PSD_5PSD_6		
M_5			
M_6			

M = Si_3N_4 raw material

MA_0 = No milling aid

MA_X = Proprietary milling aid

PSD_X = Particle size distribution variations for each powder

Figure A-19.--Matrix 5 - Milling Study on Various Raw Materials.

Materials M_5 (Starck LC-1), M_6 (KermaNord P95M), and MA_2 had no prior processing history. The experiment plan was modified after finding that MA_2 appeared to yield inconsistent milling results, increased mixing torque, and increased dewax residue. Use of MA_2 was discontinued until benefits are shown in further processing of M_1/MA_2 and M_4/MA_2 combinations.

Results and discussion: Processing conditions evaluated in Matrix 5 are shown in table A-10. Seventeen batches were milled and mixed on the torque rheometer. Torque results shown were taken from one mixer run for materials not selected for further processing. Materials chosen for further processing required additional mixing and provided up to six mixes for torque data averaging. The standard deviation was typically 10 percent of the average value indicating the level of uncertainty of data based on one run. In nearly all cases where milling time was increased for a given composition, the torque value dropped.

Powder M_1 was initially milled as follows: 48 hours with no milling aid MA_0, 24 hours with milling aid MA_1, and 24 hours with milling aid MA_2. Even with shorter milling times, the use of milling aids provided a finer powder as shown by the data in table A-10.

New milled batches were prepared using milling aids MA_1 and MA_2. Milling was performed with these materials until the median particle size (50 percent on

TABLE A-10.--PROCESSING RESULTS--RAW MATERIALS AND MILLING VARIATIONS

Material	Milling aid	Milling time, hours	Particle size at 50%, m	Mixing torque[1] at 65°C, m·g	Bars molded[2] for Matrix 6
M_1	MA_0	48	0.87	281	Yes
	MA_1	24	0.80	290	
	MA_1	14	0.87	481	Yes
	MA_2	24	0.80	310	
	MA_2	26	0.87	479	Yes
M_4	MA_0	2	1.05	416	
	MA_0	8	0.95	452	Yes
	MA_1	2	1.05	1107	
	MA_1	8	0.93	569	Yes
	MA_2	2	1.03	1771	
	MA_2	8	0.92	1264	Yes
M_5	MA_0	2	1.06	946	
	MA_0	8	0.93	765	Yes
	MA_1	8	0.92	1083	Yes
M_6	MA_0	8		1900	
	MA_0	48	1.03	660	Yes
	MA_1	24		1500	Yes

Notes:

1. Cooling rate 2°C/hr

2. The mixing torque data for materials selected for bar production is an average of five mixer runs

the cumulative volume curve) matched that of the baseline at 0.87 m. Inconsistent milling behavior was observed when MA_1 was used; this is not yet understood. The longer milling time resulted in a coarser powder as indicated by the PSD measurement and supported by the torque behavior.

Powder M_4 (Starck H-1) is finer than M_1 and has a greater surface area. Shorter milling times--2 and 8 hours--were selected for evaluation. The median particle size for all 8-hour-milled powders ranged from 0.92 to 0.95 m in diameter. The 8-hour-milled powders were selected for test bar fabrication in Matrix 6.

Material M_5 (Starck LC-1) was reported by the manufacturer to be physically similar to M_4. The milling parameters chosen for M_5 were based on M_4 results. The eight-hour-milled powders were selected for further processing in Matrix 6.

Initially, material M_6 (KemaNord P95M) was milled eight hours and mixed. However, very high torque values indicated that more milling was required. The milling time was increased to 48 hours and a significant reduction in mixing torque was observed. The effect of MA_1 observed with powder M_1 was assumed to provide a similar effect with powder M_6. Powders milled for 48 hours with no milling aid and 24 hours with a milling aid were selected for further processing.

Increased milling time for all M/MA combinations generally showed reduced mixing torque. Exceptions to this were small (M_4/MA_0) or from a milling anomaly (M_1/MA_2) and could also result in the uncertainty of the torque rheometry reading. This behavior is consistent with Matrix 3 results.

Milling aids proved to accelerate the particle reduction rate during milling for powders M_1 and M_4. The use of milling aids, however, resulted in a higher torque, at the same or finer PSD, than for those mixes with no milling aid. Milling with an effective milling aid is not equivalent to increasing the milling time.

7. MATRIX 6 - RAW MATERIALS, MOLDING PARAMETERS, BINDER REMOVAL, AND SINTERING

Matrix 6 was designed to provide a range of processing conditions in order to identify appropriate parameters for evaluating new materials (M_4, M_5, and M_6) and milling aids (MA_1 and MA_2). Powders were milled and evaluated for suitable processing behavior in Matrix 5. Materials that did not process well in Matrix 1 (M_2 blistered in sintering and M_3 mixed with great difficulty) were not studied here. Processing which appeared detrimental in Matrix 1 was avoided (M_4 cracked upon dewax similar to excessively milled GTE SN-502 in Matrix 3).

Experimental procedure: A statistically designed experiment was planned to include five variables: four Si_3N_4 powders, three milling aids, two molding temperatures, two binder removal cycles, and two sintering cycles. The large matrix was a combination of four 1/2 replicate 2^5 fractional designed matrixes. The detailed original plan was presented (Monthly Report No. 7) and is not shown here due to required modifications.

The revised matrix is shown in figure A-20. Modifications were required after recognizing the sintering temperature required for densification was similar for M_1 and M_6 and similar for M_4 and M_5 but is very different for the two pairs. The configuration of the submatrixes was reduced by the elimination of M_5/MA_2 and M_6/MA_2 as discussed in Matrix 5.

Results and discussion: Molding temperatures were selected based on visual examination of molded test bars. A good correlation exists between mixing torque and required molding temperature as seen in table A-11. Combination M_4/MA_2 had high mixing torque but was injected prior to establishing the torque molding temperature relationship. The 77°C (170°F) molded M_4/MA_2 bars did show evidence of insufficient flow.

Inspection of dewaxed bars showed no effect from the two different binder removal (dewax) cycles. This is consistent with Matrix 3 results (Matrix 6, DC_1, and DC_2 are the same as Matrix 3, DC_2 and DC_3, respectively). Cycle DC_1 is currently being used in the program as the standard cycle. Matrix 6 cycle DC_2 doubles the heating rate, apparently with no damage to thin section test bars.

Dewax weight loss indicated that a significant residue resulted from the use of MA_2. Sintering trails have been run on spare bars representing Matrix 6 materials. (Spare bars resulted from molding trials for identifying proper molding temperatures which resulted in less-than-optimum surfaces.) A sample run included 27 test bars and the data are presented in table A-12. Run parameters were approximately 1975°C for 4 hours. M_1 baseline material went to 100 percent theoretical density but demonstrated significant weight loss. M_6 yielded one 100 percent theoretically dense sample and indicated low weight loss. This material will be further evaluated in subsequent experiments.

Silicon nitride M_4, Starck H-1, also showed lower weight loss. Higher temperatures or pressures are required to fully densify M_4-based samples. These data provide useful input to establishing processing conditions for Task II, Matrix 1. Successful processing of M_4 powder was achieved in Matrixes 5 and 6 because of understanding gained in Matrix 3 and the iterative approach used here. The same material in Matrix 1 yield poor results.

8. MATRIX 7 - DEWAX LOAD SIZE

The requirements of processing large numbers of bars in Task II suggested the need to evaluate the effect of increasing the number of test bars within the closed system of the binder removal cycle. As many as 100 test bars had been processed in a single cycle (Matrix 1) with no detrimental effects attributed to the large furnace load. However, the furnace that was used had a processing capacity that was significantly larger.

Experimental procedure: Test bars were injected in parallel with Matrix II-1 (Task V) for use in optimization experiments. Dewax run 101 consisted of 36 bars, while run 102 contained 216 bars. Bars from each of the eight groups injected in Matrix II-1 were distributed uniformly throughout the furnace in run 102. These included bars with 14.5 percent and bars with 15.5 percent binder. Only three groups were used in run 101 to provide a statistically significant

	MA_0								MA_1								MA_2							
	T_1				T_2				T_1				T_2				T_1				T_2			
	DC_1		DC_2		DC_1		DC_2		DC_1		DC_2		DC_1		DC_2		DC_1		DC_2		DC_1		DC_2	
	S_1	S_2	S_1	S_2	S_1	S_2	S_1	S_2	S_1	S_2	S_1	S_2	S_1	S_2	S_1	S_2	S_1	S_2	S_1	S_2	S_1	S_2	S_1	S_2
M_1	ABCDE			ABC		ABD	ABE			ACD	ACE		ADE			A								
M_6		BCD	BCE		BDE			B	CDE			C		D	E									

a. M1 AND M6

	MA_0								MA_1								MA_2							
	T_1				T_2				T_1				T_2				T_1				T_2			
	DC_1		DC_2		DC_1		DC_2		DC_1		DC_2		DC_1		DC_2		DC_1		DC_2		DC_1		DC_2	
	S_3	S_4	S_3	S_4	S_3	S_4	S_3	S_4	S_3	S_4	S_3	S_4	S_3	S_4	S_3	S_4	S_3	S_4	S_3	S_4	S_3	S_4	S_3	S_4
M_4																								
M_5																								

b. M4 AND M5

NOTES:

1. M = Si_3N_4
2. MA = MILLING AID
3. T = MOLDING TEMPERATURE
4. DC = DEWAX CYCLE
5. S = SINTERING CYCLE

A-87181

Figure A-20.--Matrix 6 Submatrixes; Shaded Areas to be Performed.

TABLE A-11.--TORQUE AT 65°C (150°F) AND MOLDING TEMPERATURES FOR MATRIXES 5 AND 6

	MA_0		MA_1		MA_2	
	Torque at 65°C, m·g	Molding temperature, °C (°F)	Torque at 65°C, m·g	Molding temperature, °C (°F)	Torque at 65°C, m·g	Molding temperature, °C (°F)
M_1	281	77, 82 (170, 180)	481	77, 82 (170, 180)	479	82, 88 (180, 190)
M_4	452	77, 82 (170, 180)	569	77, 82 (170, 180)	1264	77, 82 (170, 180)
M_5	765	82, 88 (180, 190)	1083	82, 88 (180, 190)		
M_6	660	82, 88 (180, 190)	1500	88, 93 (190, 200)		

Notes:

1. Mixer cooling rate was 2°C (3.6°F) per minute.
2. Torque values given are averages from 5 mixer runs.

M = Si_3N_4 raw material

MA = Milling aid

m·g = meter·gram

number of bars in each group. Evaluation was performed on load size, tray stacking, and location within a tray. A three-day dewax cycle was used, which proved acceptable in Matrixes 3 and 6, instead of the Task I, baseline seven-day cycle.

Results and discussion: Table A-13 shows the dewax weight loss from three sets of similar bars from dewax runs 101 and 102. The t test was used to compare individual sets of bars and indicated a difference between like sets of bars in different runs. Some sets, however, indicate more residue in run 101 while others indicate more residue in run 102. When combining the data from all sets, the difference is actually beyond the range of precision of the balances used for obtaining the data. Very little difference, if any, can be detected between the runs based on dewax weight loss data.

TABLE A-12.--MATRIX 6--SINTERED DENSITIES FROM TRIAL RUN[1]

Material	Number of bars	Density range[2], g/cc	Weight loss range[2], %
M_1	10	3.25-3.26	3.1-4.0
M_4	10	3.06-3.16	2.3-2.8
M_5	3	3.16-3.23	2.5-2.7
M_6	4	3.15-3.26	0.8-2.0

Note:

1. Bars were sintered at 1950°C/4 hr/0.68 MPa (100 psi).
2. Broad range is due to variables including BN powder bed, sintering position, milling time, and binder residue.

TABLE A-13.--DEWAX WEIGHT LOSS - EVALUATION OF LOAD SIZE

Run 101 (36 bars, one layer)				Run 102 (216 bars, 3 layers)			
Bar number	N	Ave. weight loss, %	σ	Bar number	N	Ave. weight loss, %	σ
1548-1559	12	15.39	0.05	1560-1579	20	15.32	0.07
2343-2354	12	14.32	0.07	2383-2402	10	14.41	0.03
2943-2954	11	14.44	0.05	2974-2993	20	14.40	0.04
All bars (sets)	3	14.72		All bars (sets)	3	14.71	

No test bar location was identified in run 102 with three layers of test bars. Figure A-21 shows the average residue measured for eight bars in each location shown. All groups of eight bars consist of one bar from each of the eight groups processed in Matrix II-1. The observed range is 0.08 to 0.16 percent, but this does not appear to correspond to any trend related to location.

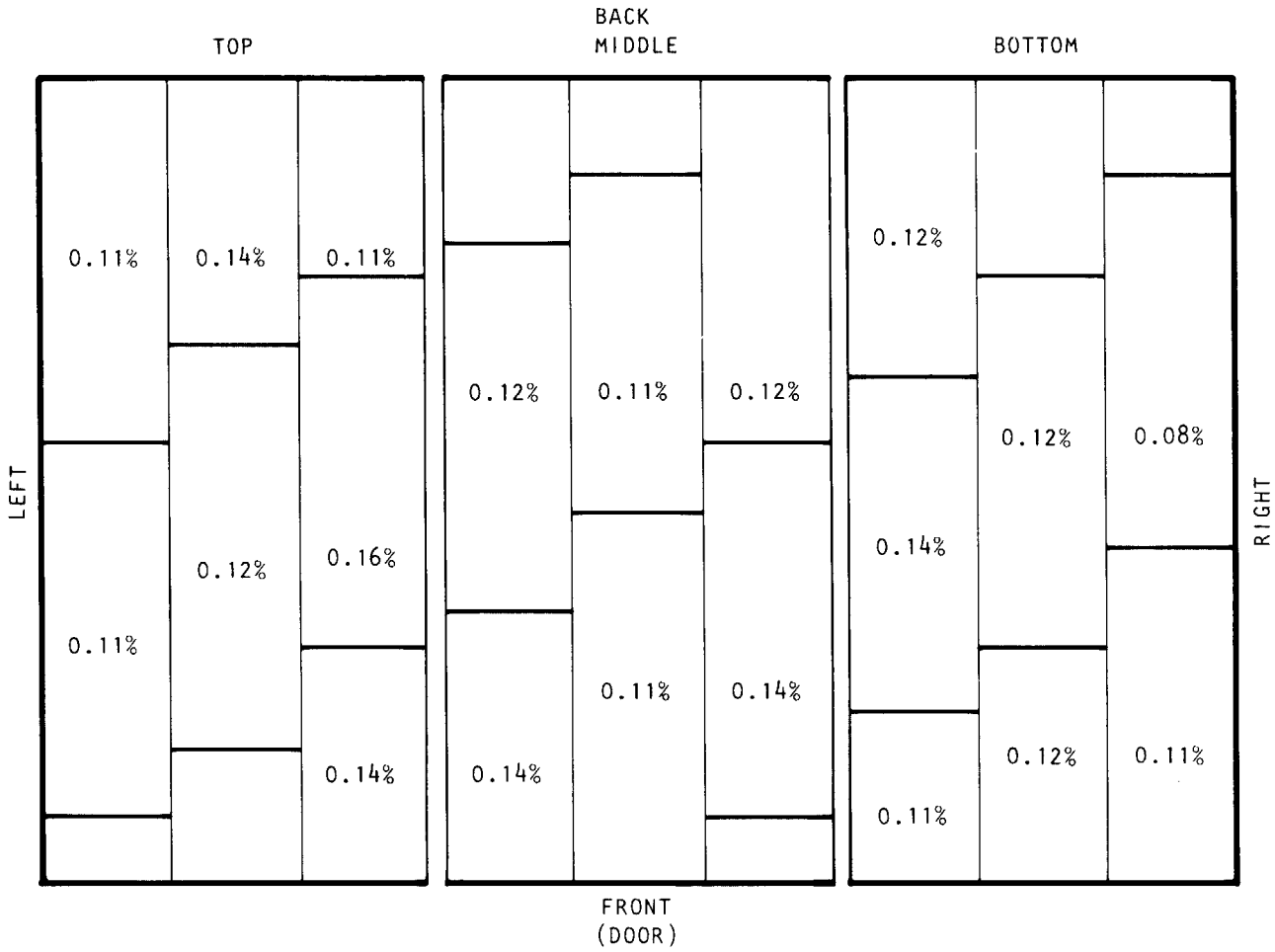

Figure A-21.--Residue after Dewax in Run 102.

Twelve bars from each of the dewax runs were sintered. A total of 24 bars, consisting of 4 bars from each of the groups identified in table A-14, yielded the sintering results shown in table A-13. Only a small difference is indicated in density and no difference in weight loss. The low densities shown here result from a nonoptimum sintering cycle, and are especially noticeable for bars with a reduced level of sintering aids.

TABLE A-14.--SINTERING RESULTS - EVALUATION OF DEWAX LOAD SIZE

Parameter	Dewax run 101		Dewax run 102	
Density, g/cc	2.93	= 0.04	2.96	= 0.04
Weight loss, %	2.0	= 0.3	2.0	= 0.2

APPENDIX B

STATISTICAL ANALYSIS OF REPRODUCIBILITY EXPERIMENTS

1. INTRODUCTION

Statistical analyses were carried out on the following:

(1) The effect of day, molder, and run on flexure strength.

(2) The effect of test specimen position in the sintering furnace (i.e., layer, location, and spot) on flexure strength.

(3) The correlation between density and MOR.

2. EFFECT OF DAY, RUN, AND MOLDER ON FLEXURE STRENGTH

Initial analysis using specimen MOR data from both injection molders showed statistically significant three-factor interaction (day/run/molder) and two-factor interaction (day/molder) at the 90-percent confidence level. Results of the statistical analyses are summarized in tables B-1 through B-13. Because of the possible effects of the different injection molders, the data for each molder were analyzed separately so that the effect of day and run could be explored.

2.1 SPECIMENS INJECTED BY ARBURG

The flexure strength of the 101 specimens injected by Arburg ranged from 357.4 to 751.0 MPa (51 to 109 ksi), with an average of 620.1 MPa (90 ksi). Forty-five percent of the specimens were considered high-strength, with an MOR equal to or higher than 640.8 MPa (93 ksi), the minimum flexure strength determined for this reproducibility experiment. The differences in MOR due to the various factors were low, ranging from 2.1 to 27.6 MPa (0.3 to 4 ksi), as shown in tables B-4 through B-6. The differences were also statistically insignificant at the 90-percent confidence level, as shown in table B-3. These results indicated that the process based on the Arburg injection molder was reproducible.

2.2 SPECIMENS INJECTED BY BATTENFELD

The flexure strength of the 101 specimens injected by Battenfeld ranged from 330.7 to 806.1 MPa (48 to 117 ksi), with an average of 606.3 MPa (88 ksi). Forty-eight percent of the specimens had an MOR of 640.1 MPa (93 ksi) or higher, as shown in table B-7. The average difference in MOR due to different days is 68.9 MPa (10 ksi), and the difference due to different runs is 41.3 MPa (6 ksi). The average MOR for Day 2 specimens did not show any difference between runs, as shown in table B-9 through B-11. Statistical analysis showed that the difference in MOR between days is significant at a 99-percent confidence level, and that at a lower confidence level (90 percent) the difference in MOR between runs and between the combination of day and run is significant, as shown in table B-8.

TABLE B-1.--ANALYSIS OF VARIANCE IN MOR, ksi

Source of Variation	Degrees of Freedom	Mean Square	F	Probability
Day	1	1762	10	0.001*
Molder	1	192	1	0.293
Day/Molder	1	489	3	0.092*
Run	1	360	2	0.151
Day/Run	1	174	1	0.316
Molder/Run	1	305	1	0.186
Day/Molder/Run	1	540	3	0.079*

*Confidence level = (1-Probability) x 100 percent.

TABLE B-2.--DESCRIPTIVE STATISTICS
(Summary of MOR for Arburg Bars)

Number of bars	101
Minimum MOR, MPa (ksi)	351.4 (51)
Maximum MOR, MPa (ksi)	751.0 (109)
Mean MOR, MPa (ksi)	620.1 (90)
Percentage bars with MOR $\geq$ 640.1 MPa (93 ksi)	45

TABLE B-3.--ANALYSIS OF VARIANCE IN MOR, ksi
(Summary of MOR for Arburg Bars)

Source of Variation	Degrees of Freedom	Mean Square	F	Probability
Day	1	196	1.76	0.18
Run	1	1	0.01	0.92
Day/Run	1	50	0.45	0.50
Error	97	112	--	--

TABLE B-4.--MEAN MOR OF DIFFERENT DAY AND RUN COMBINATIONS
(Summary of MOR for Arburg Bars)

	MOR, MPa (ksi)	
Run	Day 1	Day 2
59-20	614.6 (89.2)	624.2 (90.6)
60-21	606.3 (88.0)	635.3 (92.2)

Maximum difference in MOR = 28.9 MPa (4.2 ksi)

TABLE B-5.--MEAN MOR OF DIFFERENT DAYS
(Summary of MOR for Arburg Bars)

	Day 1	Day 2
Mean MOR, MPa (ksi)	610.5 (88.6)	629.7 (91.4)

Difference in MOR between days = 19.3 MPa (2.8 ksi)

TABLE B-6.--MEAN MOR OF DIFFERENT RUNS
(Summary of MOR for Arburg Bars)

	Run 59-20	Run 60-21
Mean MOR, MPa (ksi)	618.7 (89.8)	620.8 (90.1)

Difference in MOR between runs = 2.1 MPa (0.3 ksi)

TABLE B-7.--DESCRIPTIVE STATISTICS
(Summary of MOR for Battenfeld Bars)

Number of bars	101
Minimum MOR, MPa (ksi)	695.9 (48)
Maximum MOR, MPa (ksi)	806.1 (117)
Mean MOR, MPa (ksi)	606.3 (88)
Percentage bars with MOR $\geq$ 640.1 MPa (93 ksi)	48

TABLE B-8.--ANALYSIS OF VARIANCE IN MOR, ksi
(Summary of MOR for Battenfeld Bars)

Source of Variation	Degrees of Freedom	Mean Square	F	Probability
Day	1	2059	8.79	0.003*
Run	1	665	2.83	0.09**
Day/Run	1	665	2.83	0.09**
Error	97	234		

*The factor day has a significant effect on MOR at 99 percent confidence level.

**The factor run and the day/run interaction have a significant effect on MOR only at 90 percent confidence level.

TABLE B-9.--MEAN MOR OF DIFFERENT DAY AND RUN COMBINATIONS
(Summary of MOR for Battenfeld Bars)

Run	MOR, MPa (ksi)	
	Day 1	Day 2
59-20	537.4 (78)	640.1 (93)
60-21	613.2 (89)	640.1 (93)

Maximum difference in MOR = 103.4 MPa (15 ksi)

TABLE B-10.--MEAN MOR OF DIFFERENT DAYS
(Summary of MOR for Battenfeld Bars)

	Day 1	Day 2
Mean MOR, MPa (ksi)	571.9 (83)	640.1 (93)

Difference in MOR between days = 69.0 MPa (10 ksi)

TABLE B-11.--MEAN MOR OF DIFFERENT RUNS
(Summary of MOR for Battenfeld Bars)

	Run 59-20	Run 60-21
Mean MOR, MPa (ksi)	585.7 (85)	627.0 (91)

Difference in MOR between runs = 41.3 MPa (6 ksi)

TABLE B-12.--AVERAGE MOR OF EACH LAYER

Molder	MOR, MPa (ksi)			
	Layer 2	Layer 3	Layer 4	Layer 5
Arburg	654.6 (95)	638.9 (92)	578.8 (84)	599.4 (87)
Battenfeld	647.7 (94)	620.1 (90)	565.0 (82)	571.9 (83)
Average of each layer	654.6 (95)	627.0 (91)	571.9 (83)	571.9 (85)

TABLE B-13.--CORRELATION COEFFICIENT BETWEEN MOR (ksi) AND DENSITY

Molder	Day 1		Day 2	
	Run 59-20	Run 60-21	Run 59-20	Run 60-21
Arburg	-0.05	-0.22	-0.36	0.05
Battenfeld	0.07	-0.01	0.33	-0.16

Note: Perfect correlation = 1.0

3.2 EFFECT OF SINTER/HIP LAYER ON FLEXURE STRENGTH

During sinter/HIP, the specimens were placed on separate layers inside a crucible in the furnace. The specimens sintered on Layers 2 and 3 showed higher strength than the specimens sintered on Layers 4 and 5. The maximum difference in average MOR was 82.7 MPa (12 ksi) between Layer 2 and Layer 4. The average MOR of the specimens on different sinter/HIP layers is listed in table B-12 and shown as a plot in figure B-1. Note that the two curves for the two molders are almost parallel, showing the same trend in MOR and sintering layers. The highest MOR corresponds to Layer 2, while the lowest MOR corresponds to layer 4. The differences in MOR's were suspected to be caused by the difference in sinter/HIP temperature or atmosphere/powder bed between layers. A furnace temperature survey was performed with additional thermocouples at the top and bottom of the crucible. It was found that the temperature difference was very small, i.e., 5°C (41°F) between these two additional thermocouples, which were at the center of the hot zone. However, the temperature at the center of the hot zone is 20° to 30°C (68° to 86°F) lower than the temperature at the side, which is closer to the heating elements.

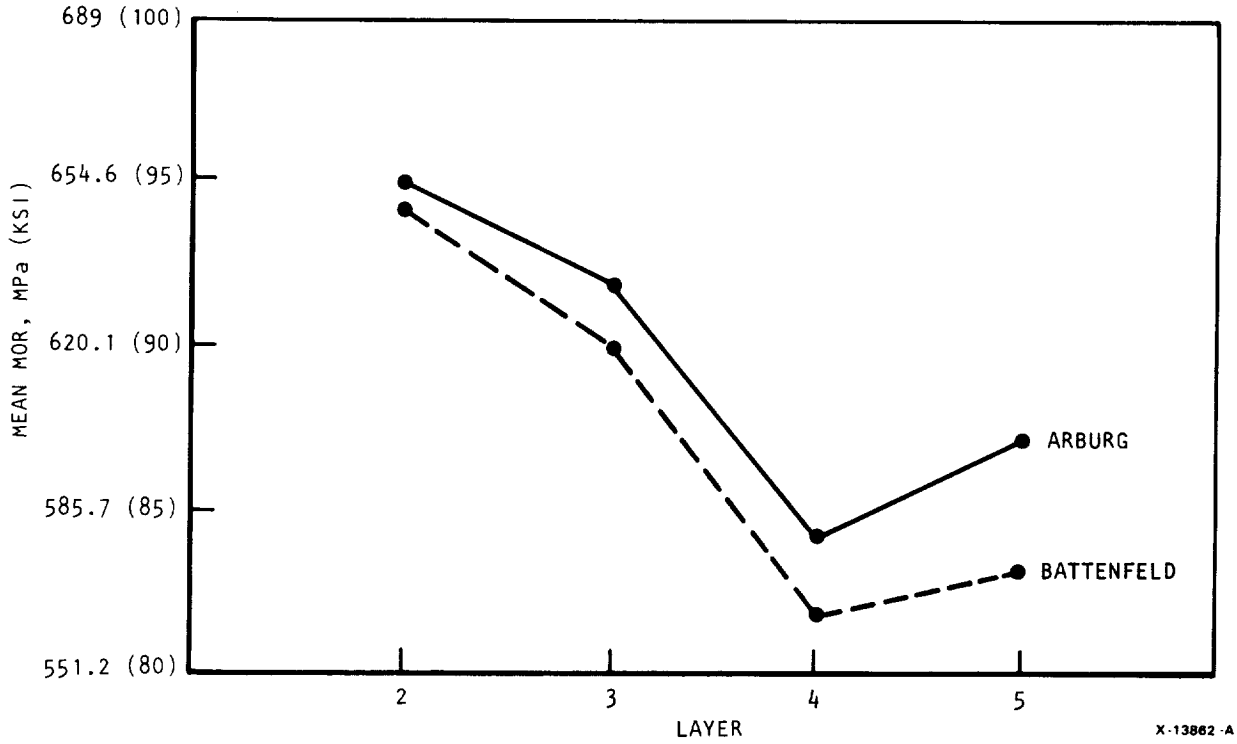

Figure B-1.--Average MOR of Each Layer for Arburg and Battenfeld Injection Molders.

4. EFFECT OF TEST BED LOCATION ON FLEXURE STRENGTH

The findings from the sinter/HIP layer analysis suggested that the location of the test bars on each layer had a possible effect on the test results. A statistical analysis was performed and the results indicated that the location of the test bars has no significant effect on flexure strength, at 90-percent confidence level, for all layers. However, due to the limited number of test bars in some locations, the accuracy of this study is less than desired.

5. CORRELATION BETWEEN MOR AND DENSITY

No correlation was found between density and MOR for the test specimens. The correlation coefficients for each group of specimens were calculated and listed in table B-13. All of the correlation coefficients are small, with an absolute value of 0.36 or less (perfect correlation coefficient = 1). It is interesting to note that the average MOR of the specimens for the Arburg molder decreases with decreasing density, as indicated by the negative correlation coefficient.

APPENDIX C

REPRODUCIBILITY SAMPLES ("ab")

1. INTRODUCTION

The potential utilization of silicon nitride monolithic ceramics as production components requires that different lots of the component have identical properties. To achieve this goal, the Improved Silicon Nitride for Advanced Heat Engines Program established a technology base for the fabrication of silicon nitride components. Mechanical properties of sintered injection-molded test bars was found to depend upon such processing parameters as powder particle size distribution, injection molding parameters, and binder systems (ref. 1). Further work using a statistically designed matrix experiment concluded that the consolidation environment, consolidation method, sintering aid content, consolidated environment/sintering aid content, consolidation environment/mixing component, and mixing component/sintering aid content factors controlled the room temperature mechanical properties (ref. 2). Characterization of samples consolidated by the same cycle showed the importance of sintering aid content and mixing on altering the microstructure (ref. 3). Reproducibility experiments were conducted for a given process scheme in order to evaluate lot-to-lot variations. The process sequence selected was very similar to that producing sample "ab" of the Matrix II-2 program (ref. 2, 3). The processing included a sintering aid composition of 6 wt% Y_2O_3 and 2 wt% Al_2O_3, binder content of 15.5 percent, no extra extruding of the blended powders and binder, a consolidation environment of a BN powder bed, and a sinter/HIP consolidation method. The only difference was that the sintering temperature was lowered from 1950° to 1900°C (3542° to 3452°C) and the time extended from 4.8 to 6 hours. Samples processed per this "ab" sequence in the Matrix II-2 program had the highest room temperature modulus of rupture in the study. Four samples fabricated at different times at GCC were characterized and compared to Sample 3349, a similarly processed specimen from the Matrix II-2 program (ref. 3). Table C-1 illustrates the production parameters that were varied and the resulting properties.

2. SUMMARY

All of the reproducibility samples examined had a fairly similar microstructure and composition. The reproducibility samples had a finer grain size, but areas lacking grain boundary phase were larger than noted for Sample 3349 from the Matrix II-2 program. The aspect ratio for Sample 3349 was somewhat greater. Grain boundary pocket composition was similar, but the Y level decreased at the interface for the reproducibility samples. Smaller amounts of inclusions were still found.

3. EXPERIMENTAL TECHNIQUES

Microstructural characterization was performed with the Vacuum Generator HB-5 dedicated scanning transmission electron microscope (STEM). Sample preparation and experimental details were as reported previously (ref 3).

TABLE C-1.--TASK II, SUBTASK A, REPRODUCIBILITY EXPERIMENTS

Sample	Powder Preparation Day	Molder	Furnace	MOR, MPa (ksi)	Density, g/cm^3
5093	1	A	60	549.8 (79.8)	3.27
5173	2	A	59	494.0 (71.7)	3.27
7070	1	B	59	583.6 (84.7)	3.25
5054	1	A	59	529.2 (76.8)	3.26
3349 [3]	-	-	-	707.6 (102.7)	3.19

Note: A - Arburg Injection Molder
B - Battenfeld Injection Molder

TABLE C-2.--MICROSTRUCTURAL ANALYSIS

Sample	Average Grain Size, μm	Aspect Ratio	Volume Fraction Grain Boundary Phase, percent
5093	0.88	1.74 ±0.87	10 1
5173	0.92	1.74 ±0.78	10.3
7070	1.03	1.65 ±0.71	7.1
5054	0.98	1.67 ±0.69	8.1
3349*	1.39	2.09 ±1.62	6.7

*Ref. 3.

TABLE C-3.--COMPOSITION FROM GENERAL FIELDS OF VIEW

Sample	Al_2O_3, wt%	Y_2O_3, wt%	CaO, wt%
5093	2.4 ±0.2	5.6 ±0.7	0.1
5173	2.5 ±0.4	6.1 ±0.5	0.1
7070	2.4 ±0.3	5.8 ±0.7	0.1
5054	2.2 ±0.3	6.1 ±1.1	0.1
3349*	2.3 ±0.3	6.9 ±1.1	0.1

4. RESULTS AND DISCUSSION

The cross-sectional microstructure had an equiaxed appearance (figures C-1a through C-1d); randomly oriented elongated grains were also found throughout for all samples (figures C-2a through C-2d). The average grain size as measured by the intercept method for these samples was smaller than observed for the Matrix II-2 Sample 3349 (table C-2). This is attributed to the lower sintering temperature or finer starting powder. The aspect ratio as calculated from the STEM micrographs was obtained by measuring and then dividing the thickness by the longest length of a cross-section grain. Since a cross-sectional analysis is used, this is not a true aspect ratio, but is quite useful for comparative purposes. The breadth of the deviation indicates the presence of the elongated grains. For the reproducibility specimens, the aspect ratio is somewhat less than for Sample 3349. The reduced processing temperature and resulting lower viscosity of the liquid phase tend toward globularization of particles from the liquid phase (ref. 4). Heinrich and Bohmer (ref. 5) suggest that a greater aspect ratio increases the strength and fracture toughness, while a finer grain size only raises the fracture strength. The poorer mechanical properties of the reproducibility samples may have some contribution from the lower aspect ratio; counteracting that effect is the finer grain size.

As with all of the samples from the program, the intergranular component has filled virtually all of the gaps between the silicon nitride grains. This indicates that sintering was by a liquid phase mechanism. Volume fraction of grain boundary phase was somewhat greater for Samples 5093 and 5173 (Table II). Grain boundaries were quite narrow in width, generally about 2 nm. No α-Si_3N_4 was detected by x-ray diffraction.

Sintering aid levels as determined from general fields of view were fairly consistent with the nominal concentrations (table C-3). Ca impurity is from the Denka 9FW starting silicon nitride powder.

In silicon nitride materials from various vendors, lot-to-lot variations were most noticeable in the grain boundary pocket composition (ref. 6, 7). For these reproducibility samples, the noncrystalline grain boundary pocket composition was virtually identical to that of Sample 3349 (table C-4). The noncrystalline nature of the grain boundary pockets was verified by microdiffraction and illustrated by photographing the grain boundary pockets at two different tilt angles (figures C-3a through C-3b). No attempt was made to determine whether these grain boundary pockets would devitrify upon a post-heat treatment as was previously observed with Sample 3349 (ref. 3).

For all of the samples, a lack of grain boundary phase was noted in some areas (figures C-4a through C-4d). Some of these regions were quite large, with one extending 30 μm in diameter. An occasional area void of grain boundary phase was found for Sample 3349, but the size was substantially smaller. These flaws may contribute to the lower strength, particularly if they are located at the surface.

Several large grain boundary pockets (figure C-5) were observed. Similarly sized grain boundary pockets were found in the skin region of Sample 3349 (ref. 8). All sections here were taken from the interior of the test bar, precluding any skin effect.

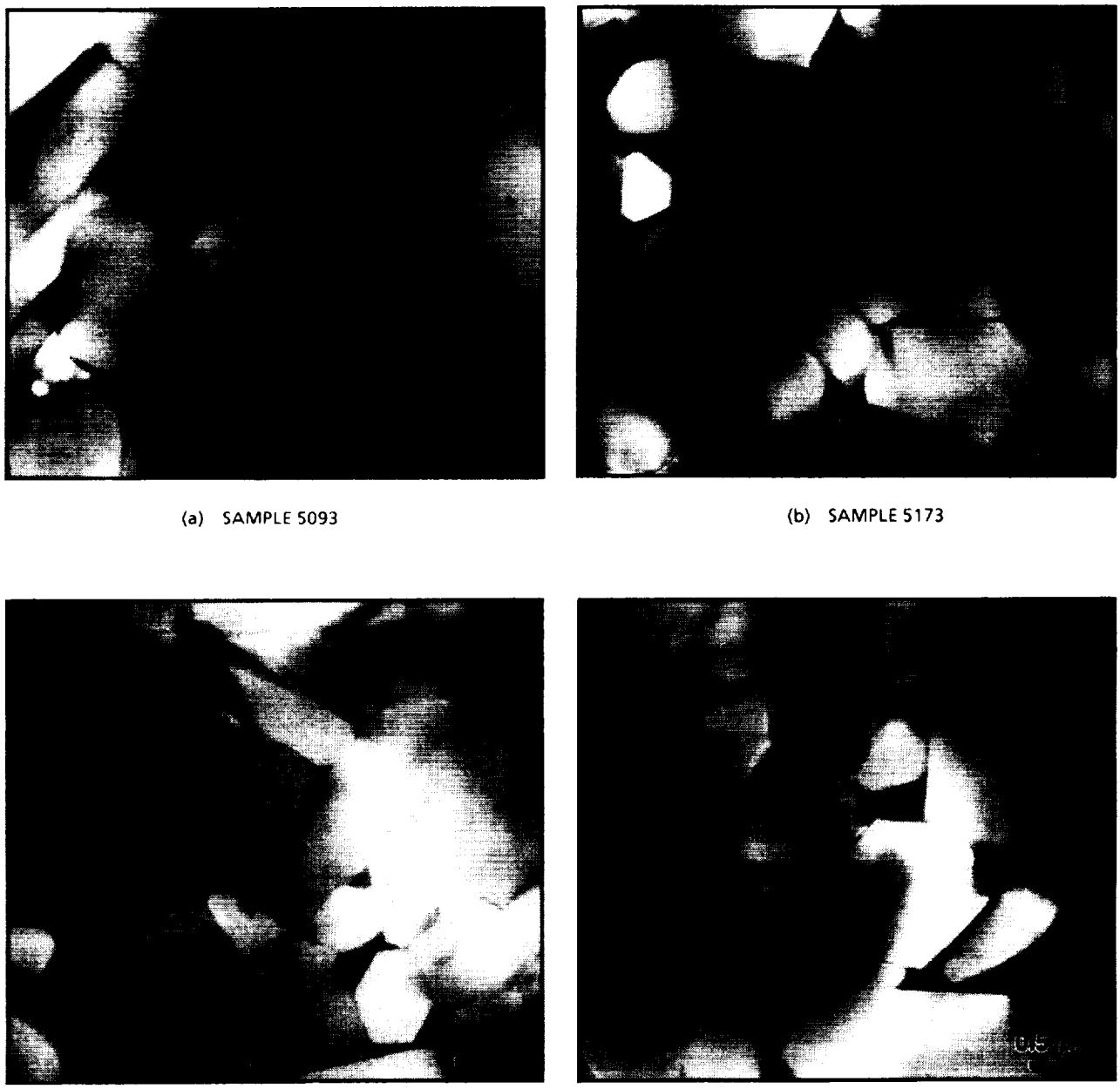

(a) SAMPLE 5093

(b) SAMPLE 5173

(c) SAMPLE 7070

(d) SAMPLE 5054

F-56023

Figure C-1.--General Microstructure for Samples. (Marker is 0.5 μm)

F-58026

BLACK AND WHITE PHOTOGRAPH

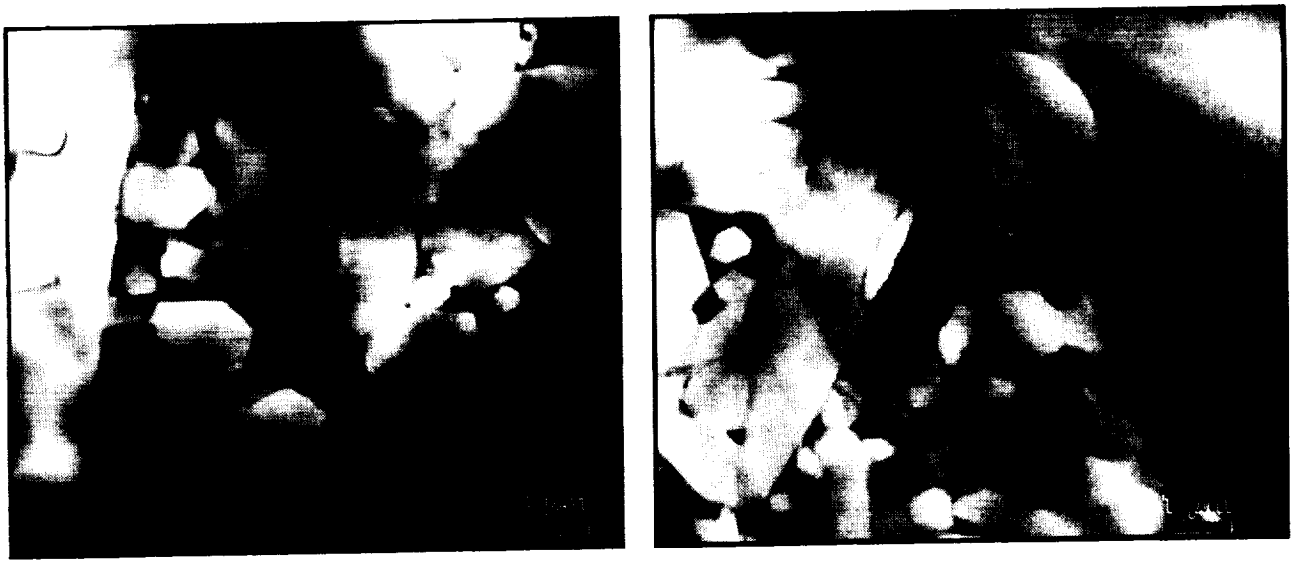

(a) SAMPLE 5093

(b) SAMPLE 5173

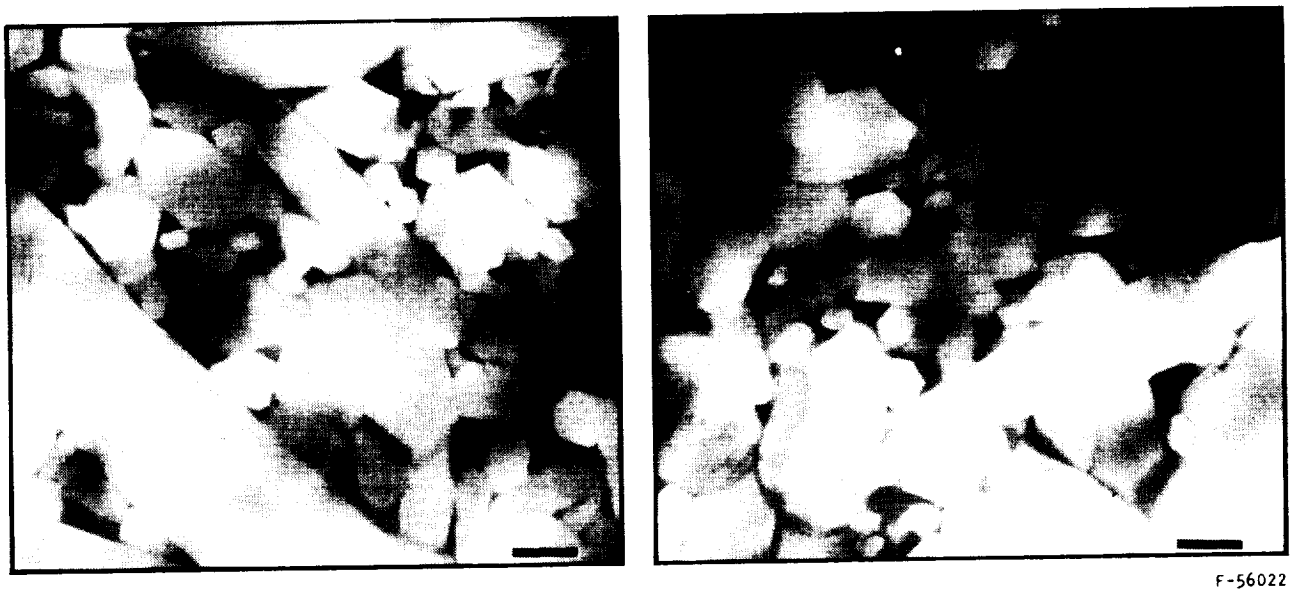

F-56022

(c) SAMPLE 7070

(d) SAMPLE 5054

Figure C-2.--Presence of Some Elongated Grains for Samples.
(Marker is 1 μm)

F-56025

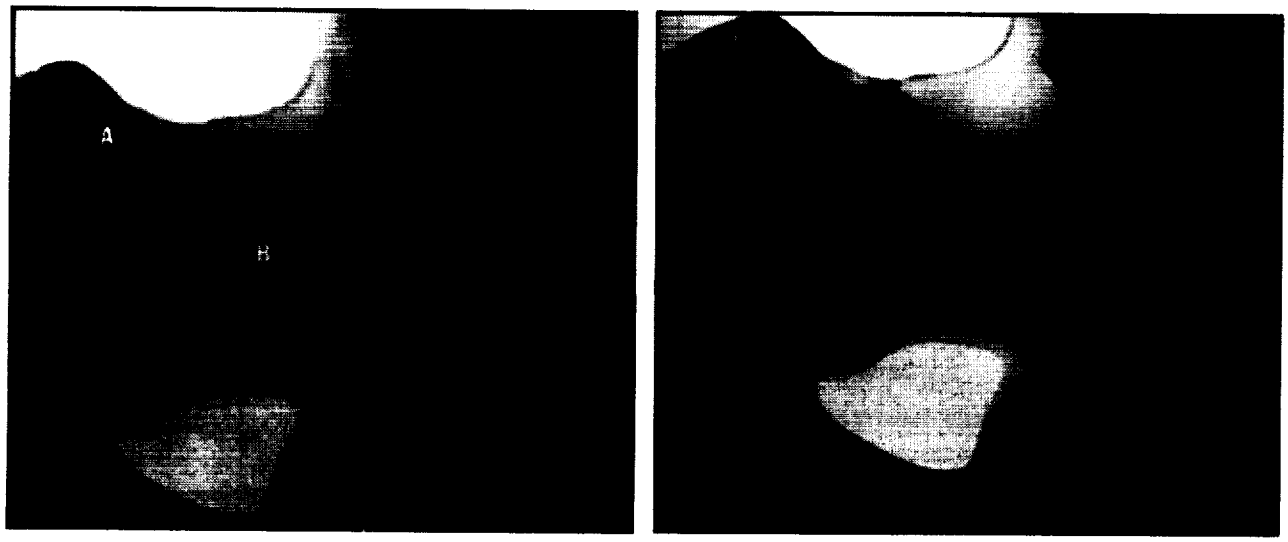

(a) SAMPLE 5093 (COMPOSITION OF A IS 15.7 AT% Al, 51.7 AT% Si, 1.1 AT% Ca, AND 31.5 AT% Y; AND FOR B IS 18.6 AT% Al, 47.3 AT% Si, 1.5 AT% Ca, AND 32.6 AT% Y. MARKER IS 0.2 μm)

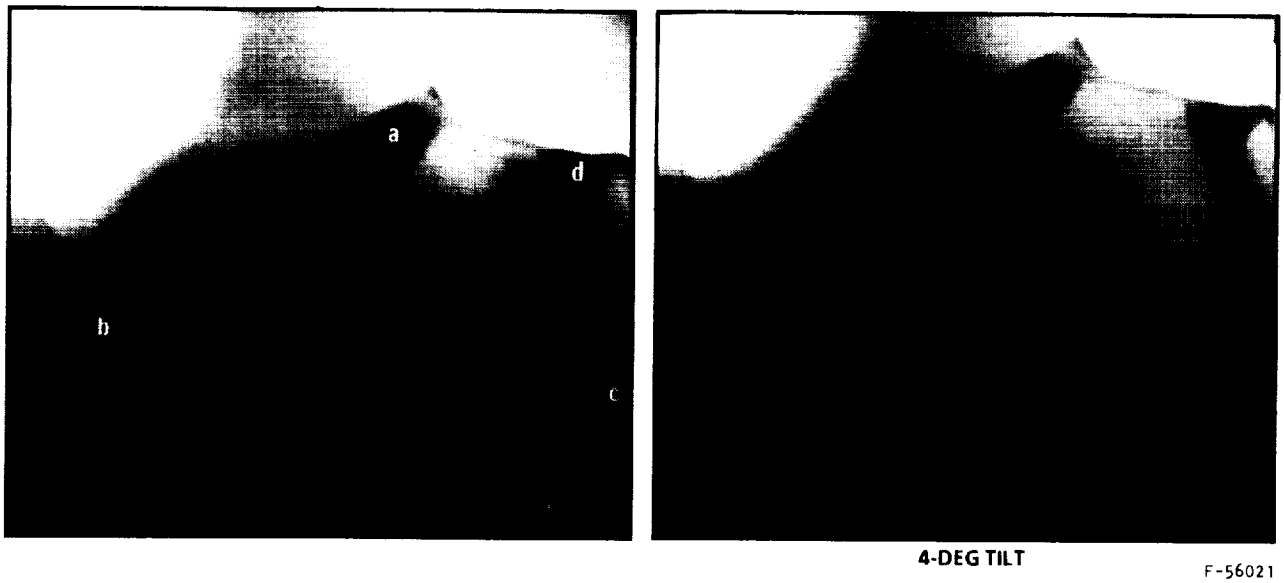

(b) SAMPLE 5173 (COMPOSITION OF a IS 15.9 AT% Al, 51.1 AT% Si, 1.5 AT% Ca, AND 31.6 AT% Y; FOR b IS 16.3 AT% Al, 47.3 AT% Si, 1.4 AT% Ca, AND 35.0 AT% Y; FOR c IS 15.1 AT% Al, 52.5 AT% Si, 1.3 AT% Ca, AND 31.1 AT% Y; AND FOR d IS 16.0 AT% Al, 52.6 AT% Si, 1.1 AT% Ca, AND 30.4 AT% Y.)

Figure C-3.--Noncrystalline Grain Boundary Pockets as Demonstrated by Tilting.

F-56027

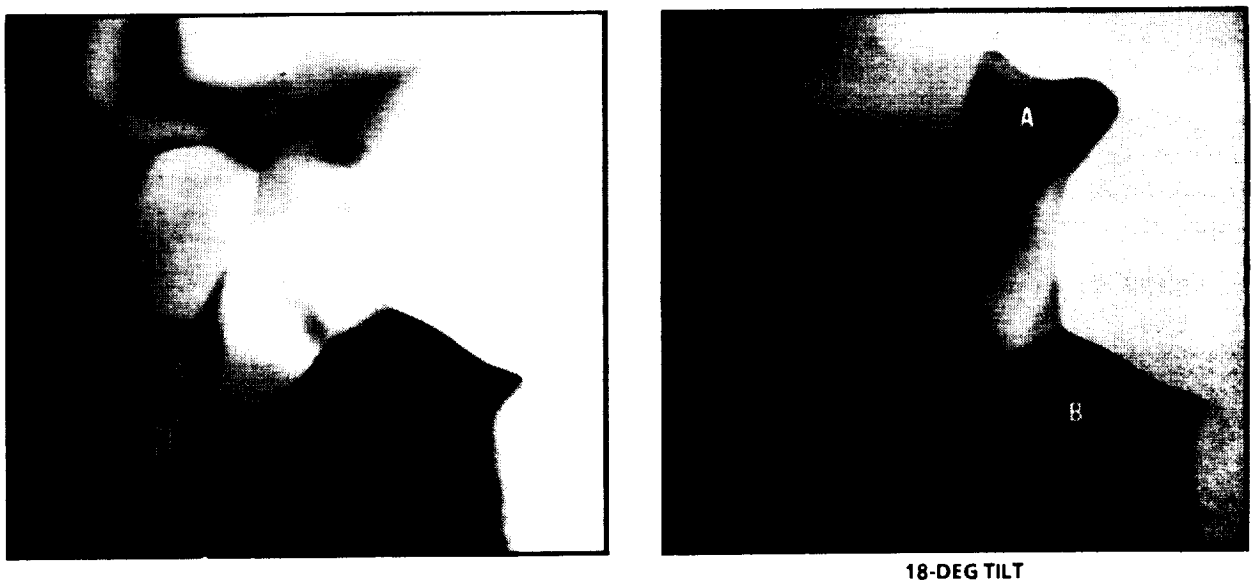

18-DEG TILT

(c) SAMPLE 7070 (GRAIN BOUNDARY POCKET COMPOSITION FOR A IS 15.3 AT% Al, 52.1 AT% Si, 1.0 AT% Ca, AND 31.6 AT% Y; AND FOR B IS 15.1 AT% Al, 51.6 AT % Si, 0.7 AT% CA, AND 32.6 AT% Y.)

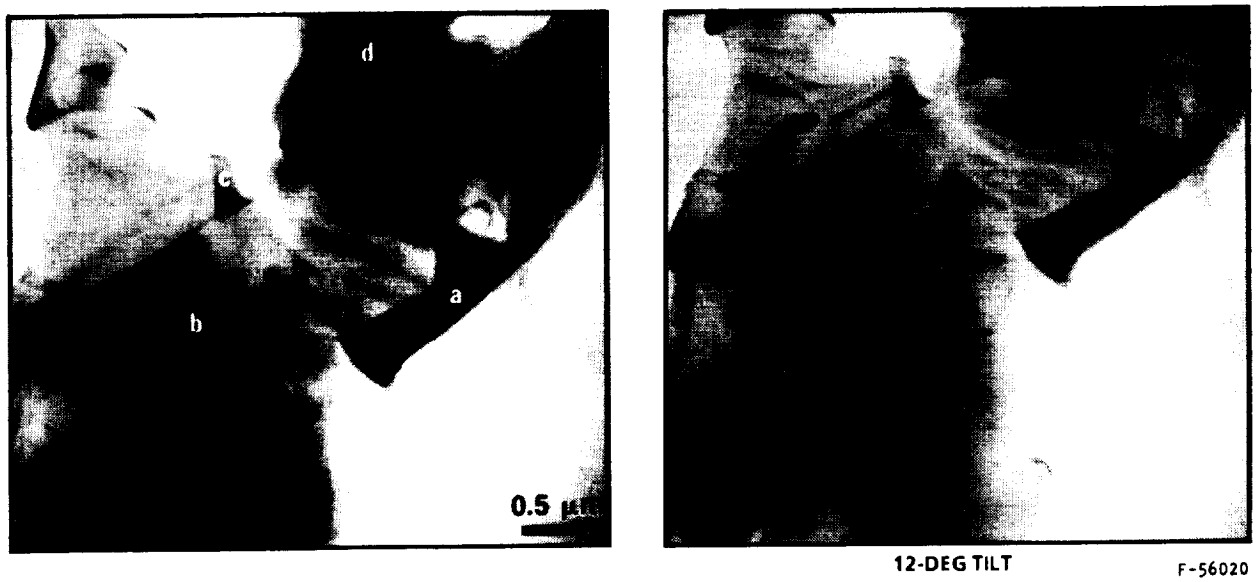

12-DEG TILT

F-56020

(d) SAMPLE 5054 (COMPOSITION FOR a IS 14.9 AT% Al, 52.4 AT% Si, 1.0 AT% Ca, AND 31.7 AT% Y; FOR b IS 17.6 AT% Al, 49.6 AT% Si, 1.1 AT% Ca, AND 31.7 AT% Y; FOR c IS 16.3 AT% Al, 48.8 AT% Si, 0.7 AT% Ca, AND 34.1 AT% Y; AND FOR d IS 16.6 AT% Al, 49.0 AT% Si, 0.9 AT% Ca, AND 33.4 AT% Y.)

Figure C-3.--(Continued).

F-56030

(a) SAMPLE 5093 (VOIDS EXTEND 30 μm.)

(b) SAMPLE 5173 (MARKER IS 1 μm.)

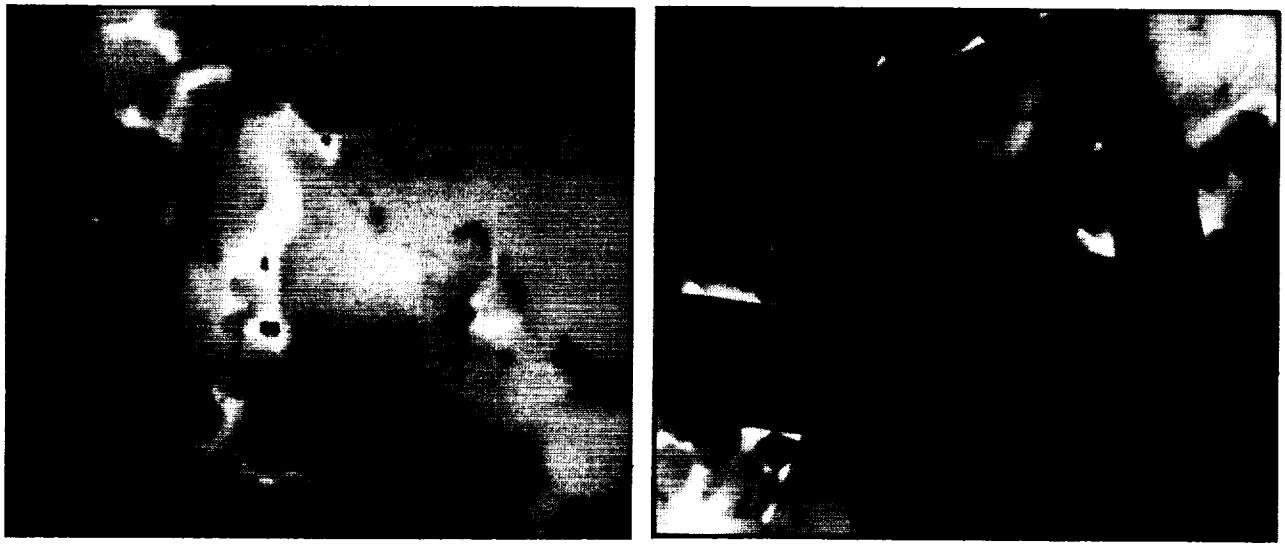

(c) SAMPLE 7070 (MARKER IS 1 μm.)

(d) SAMPLE 5054

F-56019

Figure C-4.--Evidence of (a) Grain Boundary Pocket Voids and (b) Lack of Grain Boundary Phase for Samples.

F-56024

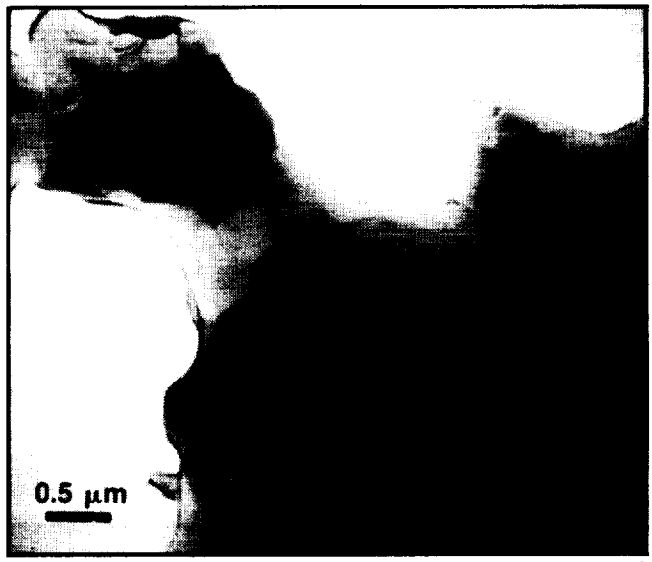

F-56018

Figure C-5.--Large Grain Boundary Pocket for Sample 5173.

F-56029

Inclusion particles of various compositions were found in all samples (figures C-6a through C-6c). Most of the particles were Fe- or Fe-Cr-rich and had reacted with Si and Y. One Ti V-rich particle was found as well.

Composition of the grain/grain boundary pocket interface was examined in order to evaluate the homogeneity of the grain boundary pockets. The technique used in this analysis has been described elsewhere (ref. 9). As shown in figures C-7 through C-10, the Y seems to be lower at the interface and increases to a plateau level 10 to 15 nm from the interface. This is in contrast to the observation of Sample 3349 (ref. 3), where it is relatively constant throughout. The cause of the increased Si level near the interface may be associated with the longer processing times. Variation in Al concentration within the plateau region was slightly less for these samples, while the data scatter for Y was rather similar.

The lower Y content at the interface is supported by the lower Y level found within the grain boundary (table C-5). On the other hand, the Al content of the grain boundary is somewhat similar to the average grain boundary pocket composition, with the exception of Sample 5054, where both Y and Al are low. Samples 5054 may be low because of a slight stage drift. The Y/Al ratio for all samples was rather similar.

As found previously (ref. 3), small concentrations of Al were found in the Si_3N_4 grains (table C-6). No variation in Al level based on Si_3N_4 grain size could be established.

5. CONCLUSIONS

The longer sintering times and lower sintering temperatures resulted in a finer grain size and a somewhat less elongated grain structure when compared to the process conditions for the Matrix II-2 samples. A finer starting powder size may have had an affect also. The longer sintering times also produced a more Si-rich grain boundary and grain/grain boundary pocket interface.

The parameters that were varied during the reproducibility study did not significantly alter the microstructure or grain boundary chemistry. Lot-to-lot variation based upon changing the injection molding equipment or furnace should not be anticipated.

The poorer mechanical properties of the reproducibility samples cannot be attributed to microstructure chemistry, but may be associated with the areas lacking grain boundary phases acting as flaw initiation sites. This will be particularly critical when these flaws are near the surface.

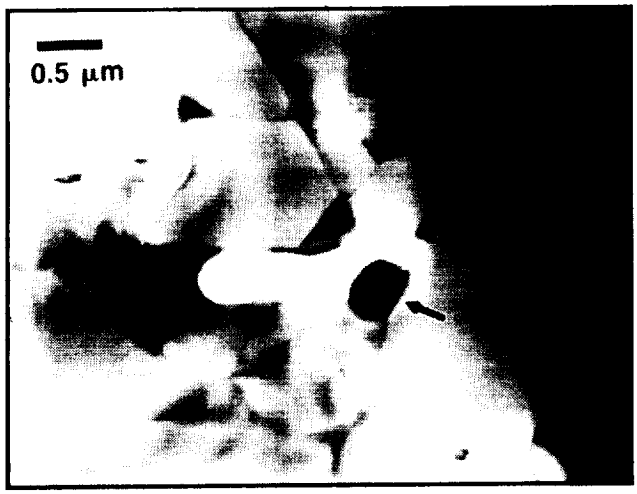

(a) Cr, Fe, V, Si PARTICLE IN SAMPLE 5173. COMPOSITION IS 53.0 AT% Cr, 31.9 AT% Si, 14.1 AT% Fe, AND 1.0 AT% V.

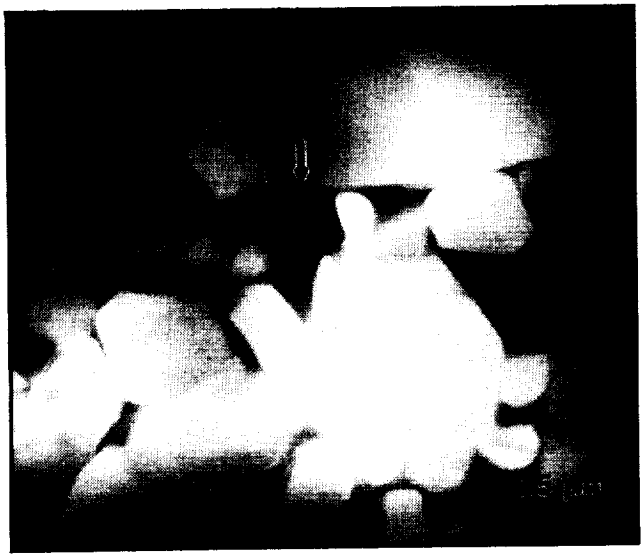

(b) Fe, Cr, Ni PARTICLE IN SAMPLE 7070. COMPOSITION IS 46.4 AT% Si, 46.5 AT% Fe, 4.7 AT% Y, 1.9 AT% Cr, AND 0.6 AT% Ni.

(c) Ti V PARTICLE IN SAMPLE 5054. COMPOSITION IS 41.7 AT% Si, 36.4 AT% Ti, 16.1 AT% V, 4.7 AT% Y, 2.3 AT% Mo, 2.0 AT% Cr, AND 0.6 AT% Fe.

F-56018

Figure C-6.--Particles in Samples.

F-56028

TABLE C-4.--GRAIN BOUNDARY POCKET COMPOSITION

Sample	Al, at%	Si, at%	Y, at%	Ca, at%
5093	16.3 ±1.3	50.3 ±3.0	32.2 ±2.2	1.2 ±0.3
5173	16.5 ±1.1	51.5 ±2.3	30.7 ±2.0	1.3 ±0.2
7070	16.0 ±1.0	51.1 ±2.3	32.0 ±1.6	0.9 ±0.3
5054	15.9 ±1.3	49.9 ±2.5	33.1 ±1.7	1.1 ±0.2
3349 [3]	16.8 ±1.1	48.2 ±1.8	34.4 ±2.0	0.8 ±0.3

TABLE C-5.--GRAIN BOUNDARY COMPOSITION

Sample	Al, at%	Y, at%
5173	12.9	25.8
7070	15.2	23.6
5054	7.2	18.1
3349*	15.1	30.1

*Ref. 3.

TABLE C-6.--Al_2O_3 SOLUBILITY

Sample	A, at%
5093	3.2 ±0.2
5173	3.2 ±0.2
7070	3.2 ±0.3
5054	3.0 ±0.3
3349*	3.2 ±0.3

*Ref. 3.

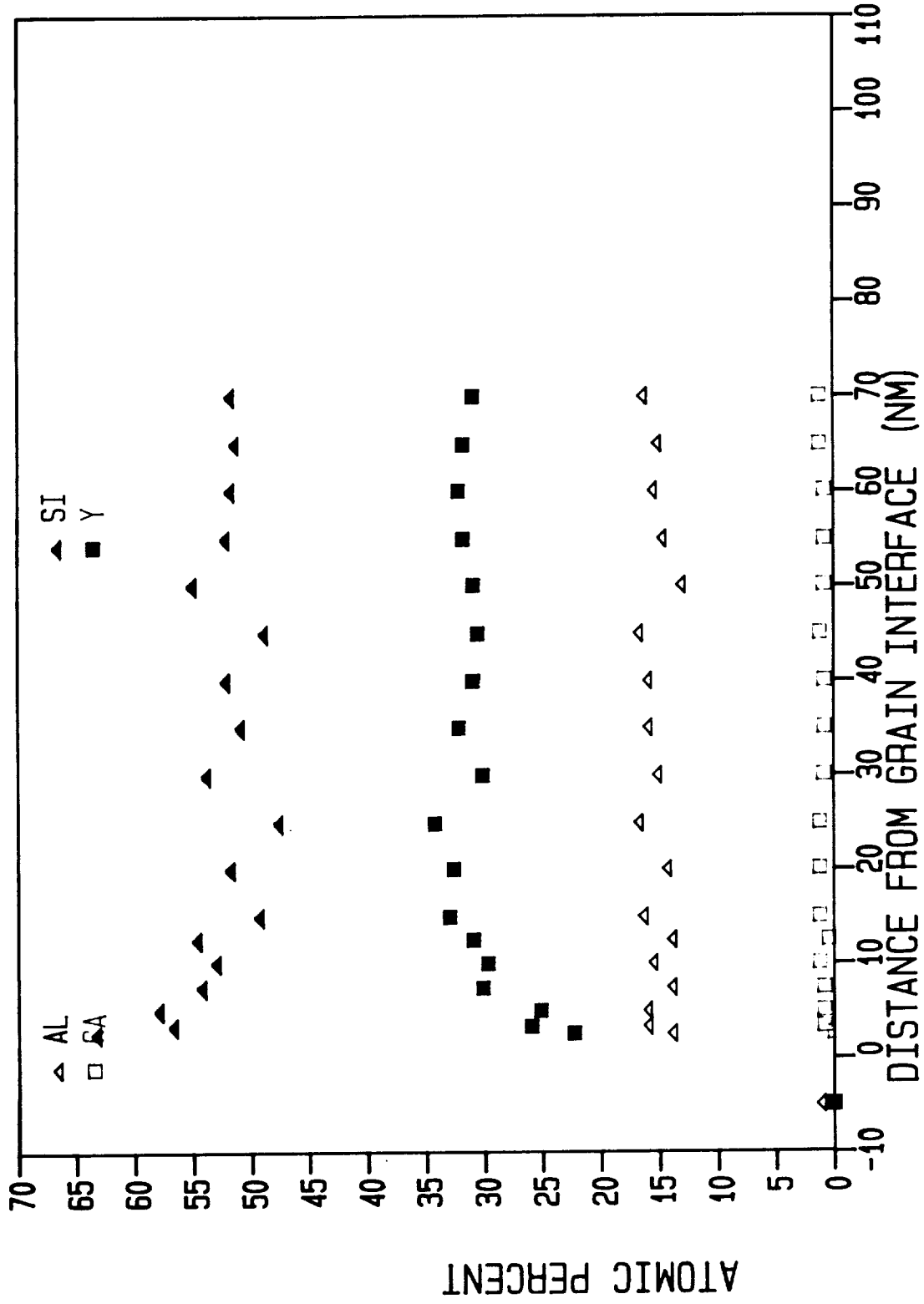

Figure C-7.--Distribution of Additives in Grain Boundary 5093.

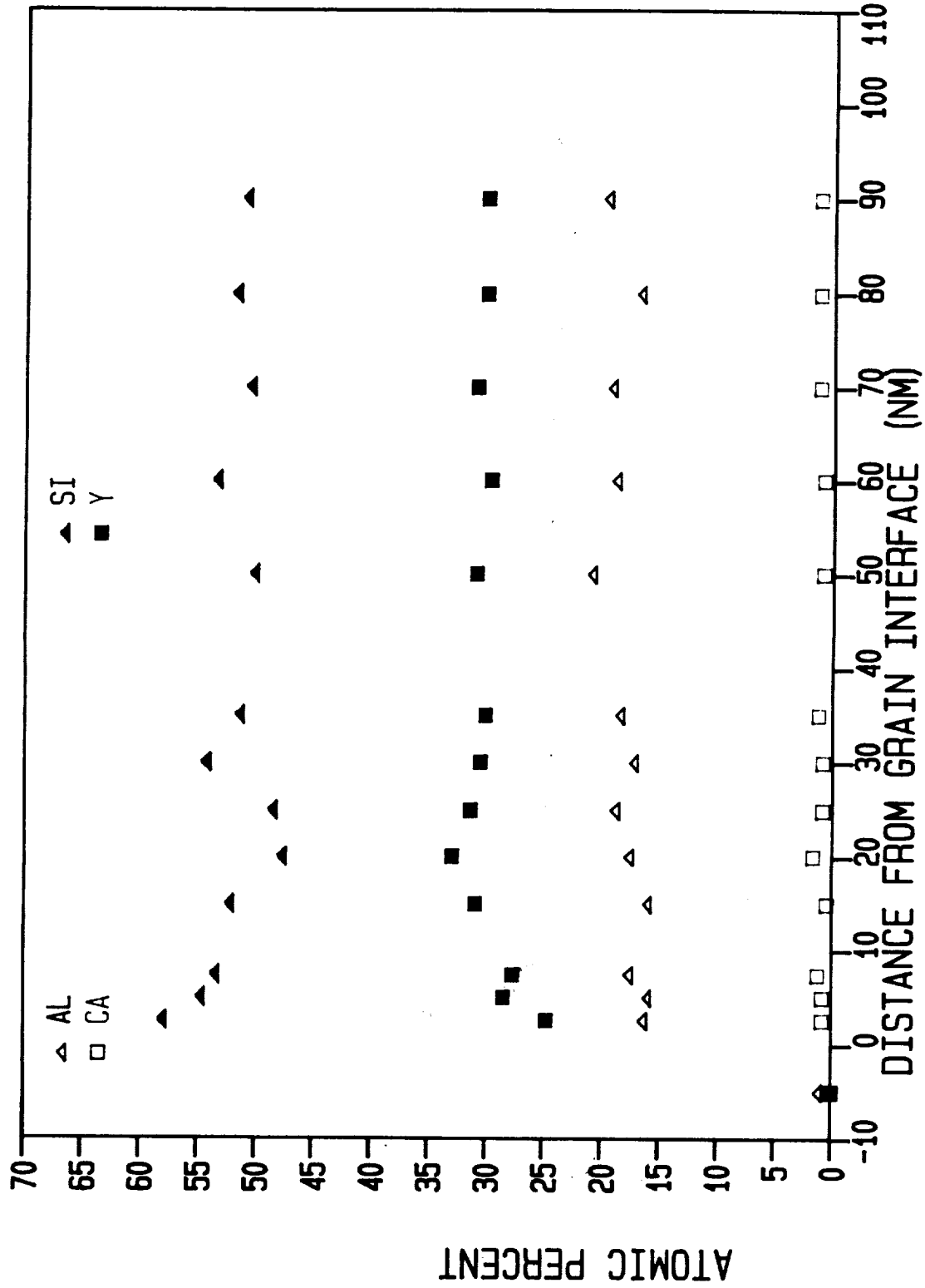

Figure C-8.--Distribution of Additives in Grain Boundary 5173.

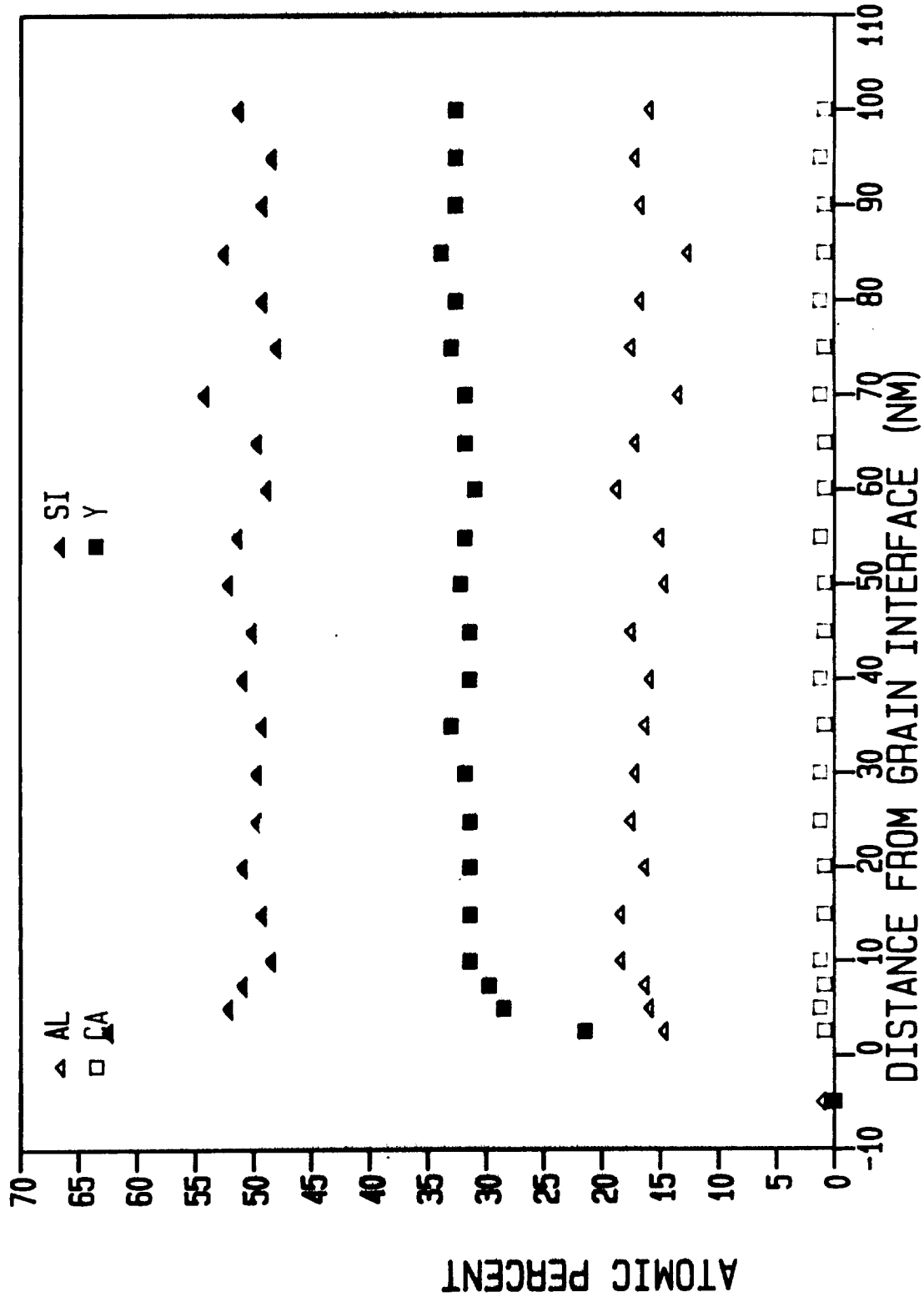

Figure C-9.--Distribution of Additives in Grain Boundary 7070.

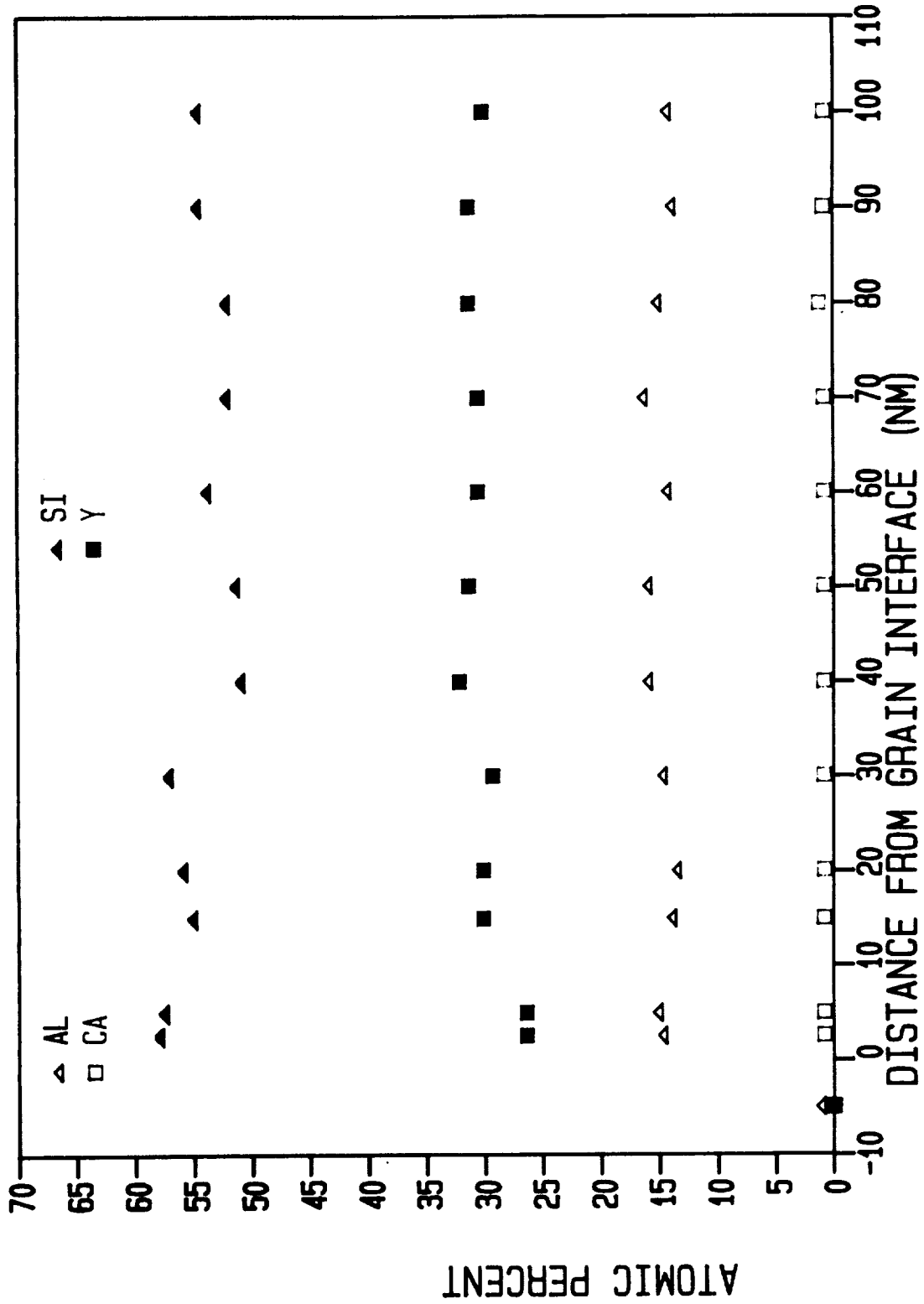

Figure C-10.--Distribution of Additives in Grain Boundary 5054.

REFERENCES

1. Rorabaugh, M.E., and H. Yeh, Paper Presented at 1985 SAE Aerospace Technology Conference.

2. Yeh, H.C., and H.T. Fang, NASA Contractor Report 179525, 1986.

3. Bradley, S.A., and K.R. Karasek, Allied-Signal Engineered Materials Research Report 66-68-40.

4. Wotting, G., and G. Ziegler, Science of Ceramics 12, 361 (1983).

5. Heinrich, J. and M. Bohmer, J. Amer. Ceram. Soc. 67, C-75 (1984).

6. Bradley, S.A. and K.R. Karasek, Allied-Signal Engineered Materials Research Report 66-68-41.

7. Memo from S.A. Bradley and K.R. Karasek to J. Wimmer, entitled "Characterization of Kyocera Rotors SN 251 and 253," dated March 16, 1987.

8. Memo from S.A. Bradley and K.R. Karasek to S.T. Gonczy, entitled "Skin Layer of 3349," dated December 17, 1986.

9. Bradley, S.A. and K.R. Karasek, Proceedings of the 45th Annual Meeting of Electron Microscopy Society of America, G.W. Bailey, ed., 162 (1987).

APPENDIX D

STATISTICAL MODELING OF THE $Si_3N_4 + Y_2O_3 + Al_2O_3$ SYSTEM

1. MODELING PROCEDURE

The statistical design consists of seven composition points, which allows a second-order model to be fitted to the MOR data. This model is derived from a complete second-order model in three variables. A complete second-order model in three variables is of the form:

$$Y = \beta_0 + \beta_1X_1 + \beta_2X_2 + \beta_3X_3 + \beta_{12}X_1X_2 + \beta_{13}X_1X_3 + \beta_{23}X_2X_3 + \beta_{11}X_1 + \beta_{22}X_2 + \beta_{33}X_3 + \varepsilon \quad (D1)$$

where Y = the measured MOR,
X_1 = the percentage of Si_3N_4 in a mixture,
X_2 = the percentage of Y_2O_3 in a mixture,
X_3 = the percentage of Al_2O_3 in a mixture,
β_0 = the intercept,
β_1, β_2, and β_3 are the linear coefficients,
β_{12}, β_{13}, and β_{23} are the interaction coefficients, and
β_{11}, β_{22}, and β_{33} are the quadratic coefficients.

In order to fit data to the complete second-order model, at least ten compositions are required. However, because the total percentage of Si_3N_4, Y_2O_3, and Al_2O_3 in a mixture is 100 percent, the above model can be reduced to fewer terms, and hence an experiment consisting of seven compositions is sufficient for modeling. A number of reduced models can be generated based on the complete second-order model.

In the process of determining the best model to fit the data, the method of least squares (LS), the method of weighted least squares (WLS), and several model selection criteria were used. The computer program used for the modeling procedure is the BMDP statistical computer package procedure P9R on GAPD's CDC Cyber computer. The LS method determines the regression coefficients by minimizing the sum of squares of errors. The WLS method determines the regression coefficients by minimizing the sum of squares of weighted errors. The model selection criteria used are R^2, adjusted R^2, and Mallows' Cp.

A key assumption in LS estimation is that the variation of random error is the same for all mixtures. When there is a lack of consistent variation, the remedy is to use the WLS method using standard deviations as weights.

A comparison of the results based on LS and WLS reveals improvements in the prediction of MOR measured at room temperature, 1232°C (2250°F), and 1399°C (2550°F) when using WLS. To use WLS, the standard deviations must be known. This can yield accurate predictions at the design points where the standard deviation is known, but no predictions can be made for points other than the design points where the standard deviations are unknown.

To resolve the problem of no predictions in the region of the unknown standard deviations, a two-step prediction process was utilized. Using this method, the standard deviation for a given composition of Si_3N_4 + Y_2O_3 + Al_2O_3 was modeled at each temperature. This standard deviation model was then used as the weight in predicting MOR in the WLS analysis.

A good prediction of MOR can be obtained by this two-step prediction method when a precisely predicted standard deviation is available. Since the predicted standard deviation is used as the weight in predicting MOR, the accuracy of the standard deviation prediction is very critical in getting a good prediction of MOR. An accurate prediction of the standard deviation would result in an accurate prediction of MOR, and a less accurate prediction of the standard deviation would lead to an unreliable prediction of MOR.

2. RESULTS

The following are the results for each of the three temperatures--room temperature, 1232°C (2250°F), and 1399°C (2550°F). In each section, the experimental results, a comparison of the three methods of estimation, and the final model selected for that temperature will be presented.

No billet was made of the 92% Si_3N_4, 6% Y_2O_3, 2% Al_2O_3 composition. Data used for "billet 17" is Task II Matrix A "ab condition" data. Only room temperature and 1232°C (2250°F) data were available for this composition; therefore, no predictions in the area of this composition can be made for MOR measured at 1399°C (2550°F).

2.1 ROOM TEMPERATURE

2.1.1 Experimental Results

Table D-1 presents a summary of the experimental MOR data. The standard deviations of MOR among the compositions vary from 29.22 to 73.86 MPa (4.24 to 10.72 ksi).

2.1.2 Comparison of Three Prediction Methods

Figure D-1 is a plot comparing the experimental values of MOR to the predicted values obtained using least squares. As can be seen, at 4% and 6% Y_2O_3, the predictions are fairly close (within 34.5 MPa (5 ksi)). At 5% and 5.5% Y_2O_3, the predictions were less accurate. The differences between the experimental and predicted MOR ranged from 69.0 to 138.0 MPa (10 to 20 ksi). The predicted 94% Si_3N_4 line does not appear to curve in the correct direction when compared to the experimental results. This is due to the influence of the 92% and 93% Si_3N_4 data points. The model predicts that the 94% Si_3N_4 line should curve in the same direction as the 93% Si_3N_4 line. This deviation from experimental results demonstrates the shortcomings of the LS method.

The weighted least square model using the observed standard deviations as weights is the second model fit to the MOR data. As shown in figure D-2, the predictions are very close (within 20.7 MPa (3 ksi)), yet no predictions can be made in the region where the standard deviations are unknown.

TABLE D-1.--SUMMARY STATISTICS OF EXPERIMENTAL MOR AT ROOM TEMPERATURE

Billet No.	Composition (%)			No. of Test Bars	Mean, MPa (ksi)	Standard Deviation, MPa (ksi)	Minimum, MPa (ksi)	Maximum, MPa (ksi)
	Si_3N_4	Y_2O_3	Al_2O_3					
11	94	6	0	9	613.0 (88.9)	29.23 (4.24)	572.3 (83.0)	674.3 (97.8)
12	94	5	1	9	669.5 (97.1)	47.99 (6.96)	595.7 (86.4)	740.5 (107.4)
13	94	4	2	7	800.5 (116.1)	66.95 (9.71)	710.2 (103.0)	879.8 (127.6)
14	93	6	1	8	679.8 (98.6)	32.68 (4.74)	635.7 (92.2)	722.6 (104.8)
15	93	5.5	1.5	9	882.6 (128.04)	73.91 (10.72)	759.1 (110.1)	965.3 (140.0)
16	93	5	2	9	820.5 (118.98)	72.05 (10.45)	692.9 (100.5)	905.3 (131.3)
17	92	6	2	29	671.6 (97.4)	76.40 (8.18)	502.6 (72.9)	749.5 (108.7)

The third model fitted to the MOR data is a model which first estimates the standard deviation and then uses that estimate to predict the MOR. Figure D-3 compares the predictions resulting from this method to the experimental values. This model predicts the values at 92% and 94% Si_3N_4 very well, but is not as accurate at 93% Si_3N_4. Figure D-4 compares the experimental and predicted standard deviation values. It can be seen from these two figures that poor standard deviation predictions are associated with poor MOR predictions.

In this method, the standard deviation plays a major role in predicting MOR. For a precisely predicted standard deviation, the predicted MOR is usually very close to the observed MOR. For example, the best predicted standard deviation is for billet 17, where both the predicted and experimental standard deviations are the same, resulting in a precisely predicted MOR (within 0.7 MPa (0.1 ksi)). For a poorly predicted standard deviation, the predicted MOR is usually poor. For example, the worst standard deviation prediction is for billet 15, where the experimental standard deviation is 10.72 and predicted to be 8.75. This caused the experimental MOR of 882.6 MPa (128 ksi) to be predicted as 107.8.

Table D-2 is a summary of the comparison among the prediction methods and the observed MOR values.

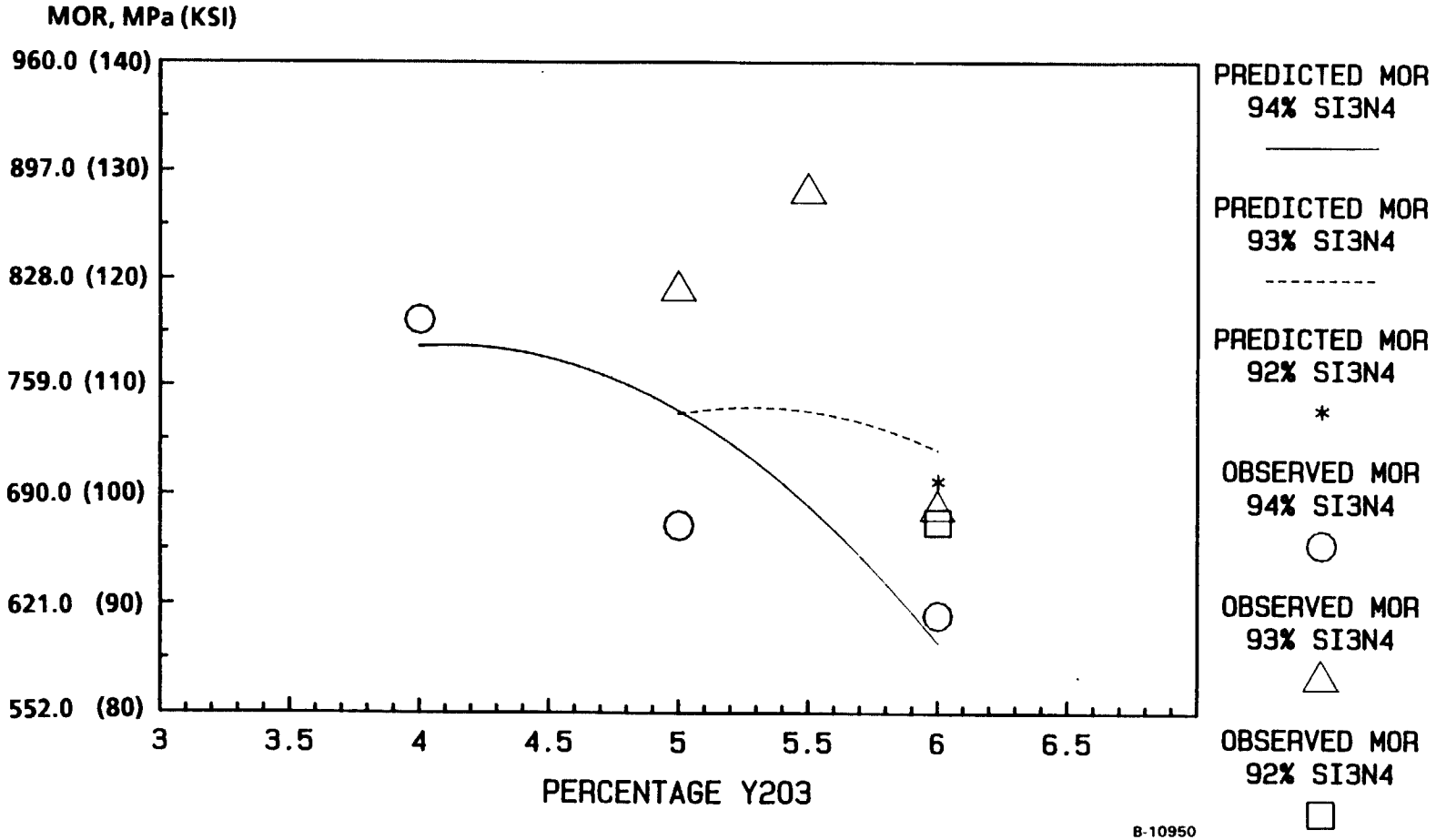

Figure D-1.--MOR Measured at Room Temperature--Least Squares Prediction Method.

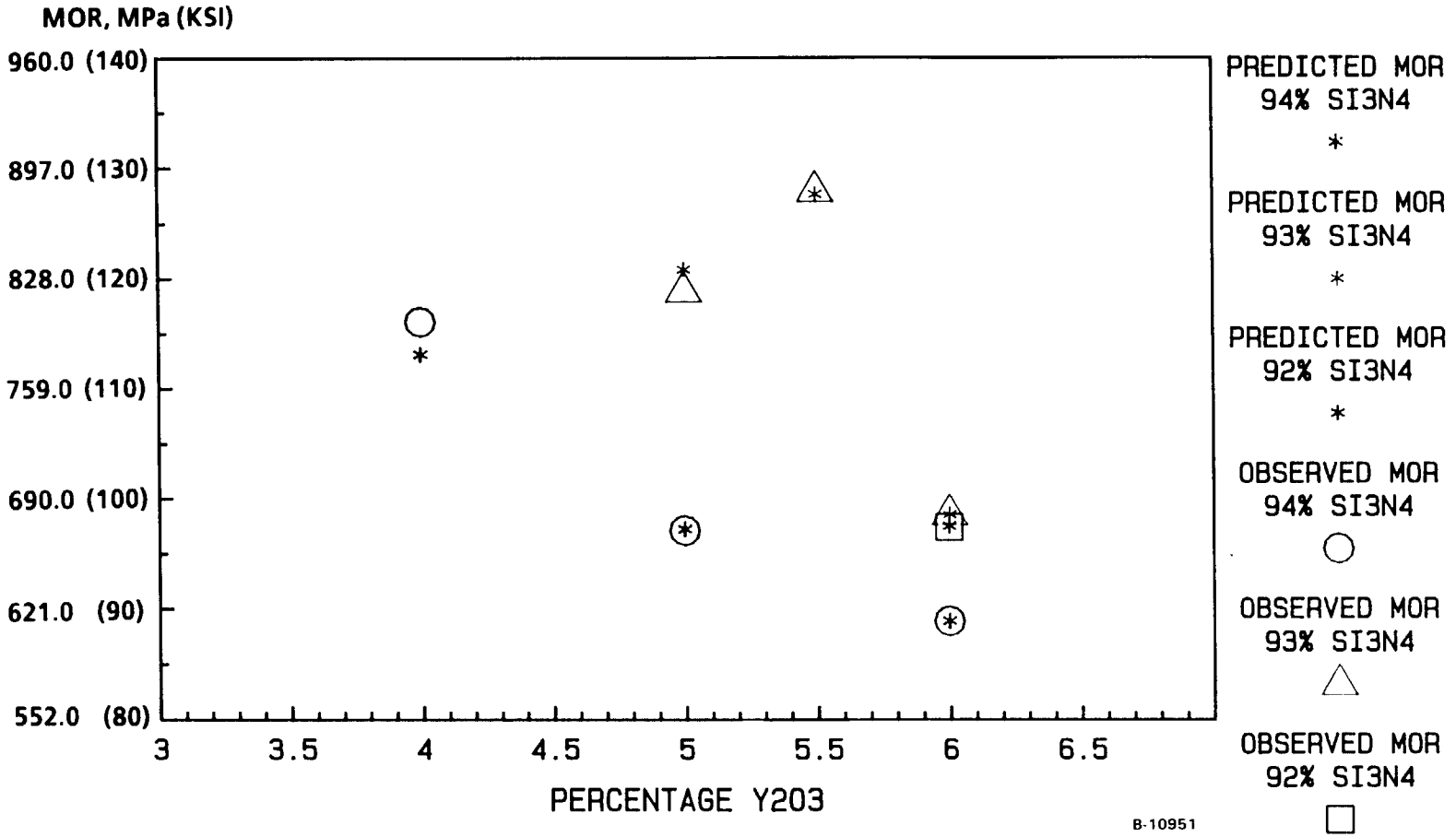

Figure D-2.--MOR Measured at Room Temperature--Weighted Least Squares Prediction Method.

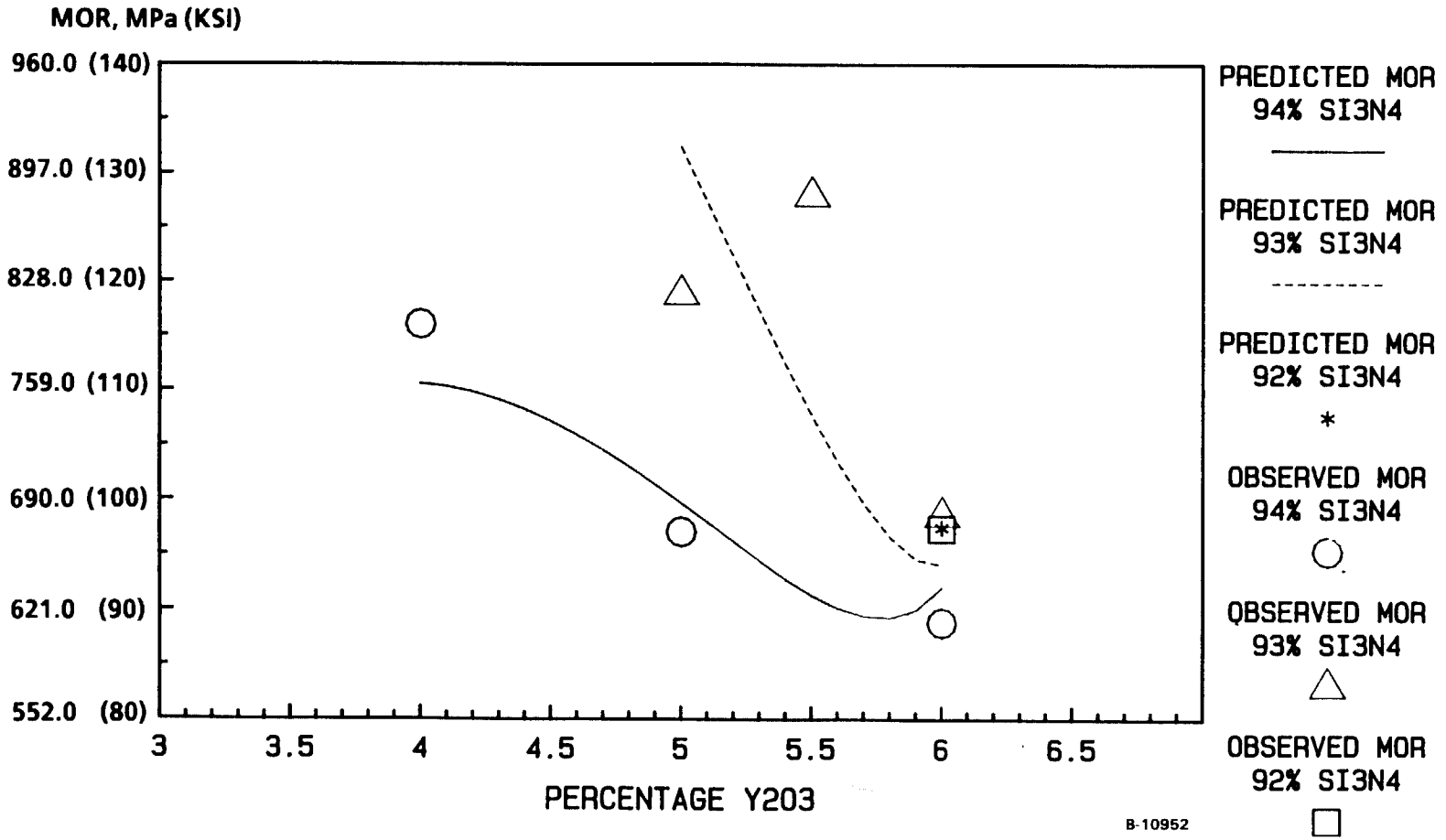

Figure D-3.--MOR Measured at Room Temperature--Two-Step Prediction Method.

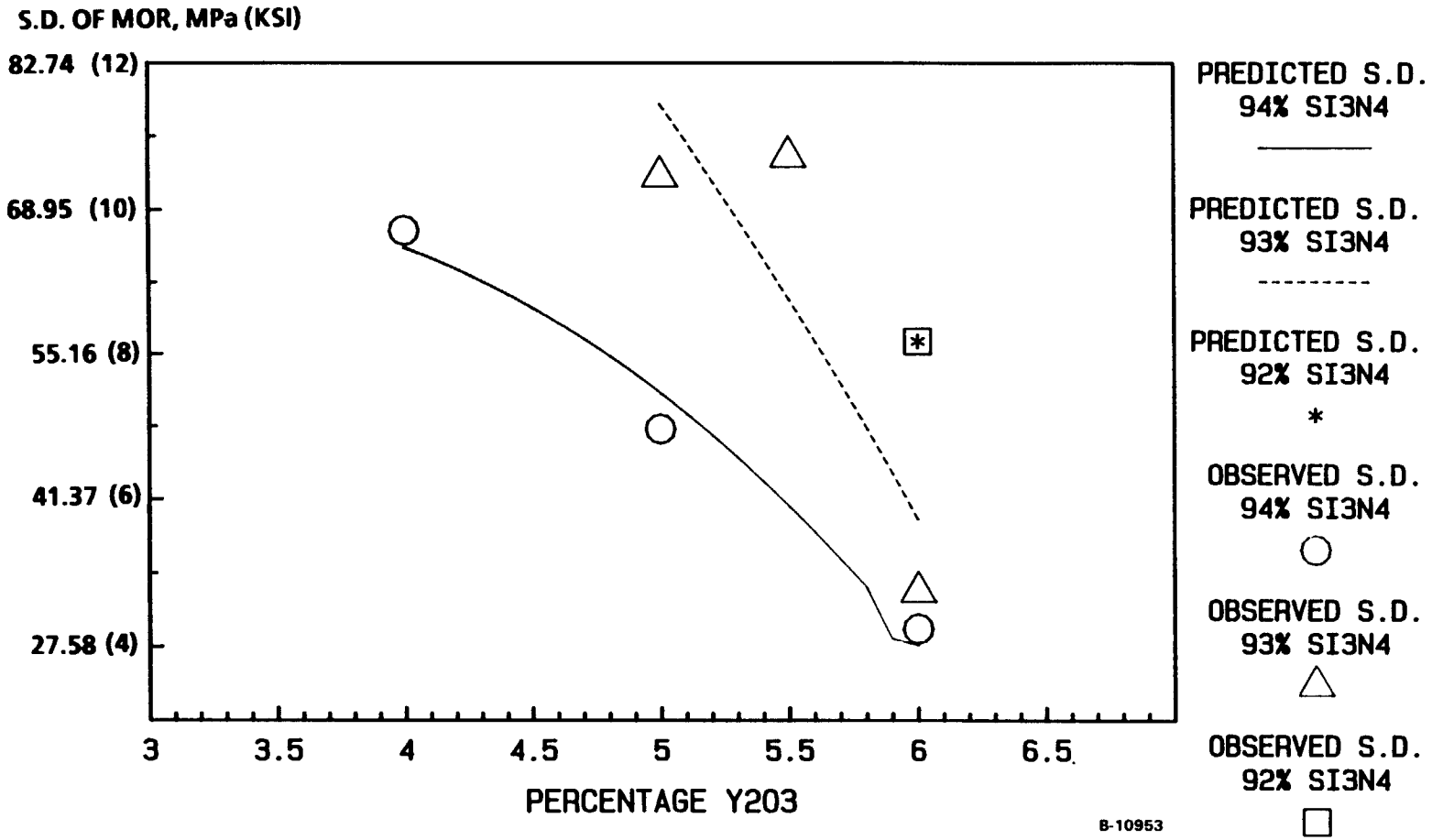

Figure D-4.--MOR Measured at Room Temperature--Standard Deviation (S.D.) Predictions.

TABLE D-2.--COMPARISON OF EXPERIMENTAL AND PREDICTED MOR VALUES AT ROOM TEMPERATURE

Billet No.	Composition (%)			Observed Mean, MPa (ksi)	MOR S.D., MPa (ksi)	LS[2], MPa (ksi)	Predicted WLS[3], MPa (ksi)	MOR[1] Two-Step[4], MPa (ksi)	Predicted S.D., MPa (ksi)
	Si_3N_4	Y_2O_3	Al_2O_3						
11	94	6	0	612.5 (88.9)	29.21 (4.24)	594.6 (86.3)	612.5 (88.9)	634.6 (92.1)	27.56 (4.00)
12	94	5	1	669.0 (97.1)	47.95 (6.96)	741.4 (107.6)	669.7 (97.2)	686.9 (99.7)	51.33 (7.45)
13	94	4	2	799.9 (116.1)	66.90 (9.71)	782.7 (113.6)	779.3 (113.1)	762.0 (110.6)	65.18 (9.46)
14	93	6	1	679.4 (98.6)	32.66 (4.74)	717.2 (104.1)	679.4 (98.6)	648.3 (94.1)	39.41 (5.72)
15	93	5.5	1.5	881.9 (128.0)	73.86 (10.72)	741.4 (107.6)	879.9 (127.7)	742.7 (107.8)	60.29 (8.75)
16	93	5	2	819.2 (118.9)	72.00 (10.45)	739.3 (107.3)	833.0 (120.9)	912.9 (132.5)	78.75 (11.43)
17[5]	92	6	2	671.1 (97.4)	56.36 (8.18)	697.3 (101.2)	671.8 (97.5)	671.8 (97.5)	56.36 (8.18)

[1]Predicted MOR values were obtained by using three methods.

[2]MOR was predicted with the method of least squares (LS).

[3]MOR was predicted with the method of weighted least squares (WLS). The observed standard deviations (S.D.) were used as weights.

[4]MOR was predicted with the two-step prediction method. The predicted standard deviations (S.D.) were used as weights.

[5]No billet was made of the (92, 6, 2) composition. Data used for "billet 17" are Task II Matrix A "ab condition" data.

2.1.3 Selected Model

A model using the two-step prediction method was found to be the best predictor of MOR. To use this method, the standard deviation must be estimated first.

The best model found to estimate the standard deviation is the following quadratic equation:

$$S = -73.0502 + 4751.42\ X_3^{\,2} - 23247.0\ X_2^{\,2} - 11330.9\ X_2X_3 + 2.850.07\ X_1X_2 + 1048.48\ X_1X_3 \qquad (D2)$$

where S = standard deviation of MOR
X_1 = proportion of Si_3N_4
X_2 = proportion of Y_2O_3
X_3 = proportion of Al_2O_3

Using the standard deviations obtained from the above equation, the predicted MOR can be obtained using the equation:

$$Y = 16.0338 - 102.654\ Z_1 + 563.596\ Z_1^{\,2} - 606717\ Z_3^{\,2} + 14294.4\ Z_1Z_3 \qquad (D3)$$

where Y = MOR/S
$Z_1 = X_1/S$
$Z_2 = X_2/S$
$Z_3 = X_3/S$

According to this model, the strength increases as Al_2O_3 increases, and Si_3N_4 and Y_2O_3 approach their center points (93% Si_3N_4 and 5% Y_2O_3) as shown in the contour plot of MOR (figure D-5). The highest MOR is achieved with a mixture of 93% Si_3N_4, 5% Y_2O_3, and 2% Al_2O_3.

2.2 1232 DEGREES CENTIGRADE (2250 DEGREES FAHRENHEIT)

2.2.1 Observed Results

Table D-3 presents a summary of the observed MOR data. Although the standard deviations are not as large as those at room temperature, there are still some variations among the seven experimental compositions.

2.2.2 Comparison of Three Prediction Methods

Figure D-6 is a plot comparing the experimental values of MOR to the predicted values obtained using least squares. As can be seen, at 92% and 94% Si_3N_4, the predictions are fairly close. At 93% Si_3N_4, the predicted line does not appear to follow the shape of the experimental data.

The weighted least square model using the experimental standard deviations as weights is the second model fitted to the MOR data at 1232°C (2250°F). As shown in figure D-7, the predictions are very close, yet no predictions can be made in the region where the standard deviations are unknown.

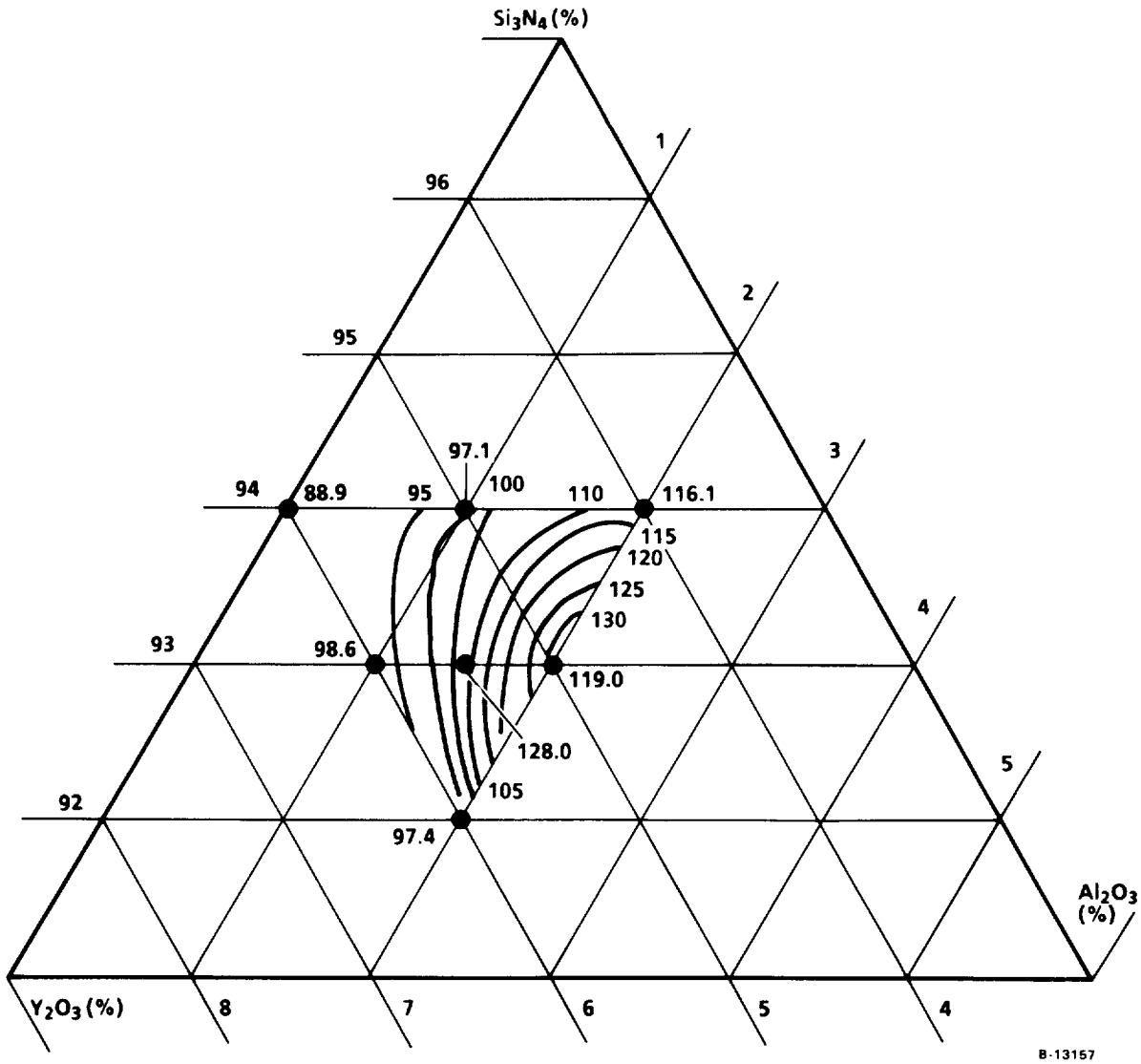

Figure D-5.--Contour Plot of MOR vs Composition at Room Temperature.

TABLE D-3.--SUMMARY STATISTICS OF EXPERIMENTAL MOR AT 1232°C (2250°F)

Billet No.	Composition (%)			No. of Test Bars	Mean, MPa (ksi)	Standard Deviation, MPa (ksi)	Minimum, MPa (ksi)	Maximum, MPa (ksi)
	Si_3N_4	Y_2O_3	Al_2O_3					
11	94	6	0	5	307.57 (44.64)	10.96 (1.59)	297.0 (43.1)	320.4 (46.5)
12	94	5	1	5	337.06 (48.92)	17.29 (2.51)	316.9 (46.0)	356.2 (51.7)
13	94	4	2	5	333.75 (48.44)	30.52 (4.43)	279.7 (40.6)	353.5 (51.3)
14	93	6	1	3	296.27 (43.00)	6.34 (0.92)	289.4 (42.0)	301.8 (43.8)
15	93	5.5	1.5	5	373.58 (54.22)	21.77 (3.16)	351.4 (51.0)	396.9 (57.6)
16	93	5	2	5	373.16 (54.16)	17.64 (2.46)	349.3 (50.7)	396.9 (57.6)
17	92	2	6	4	402.38 (58.40)	18.26 (2.65)	379.6 (55.1)	423.7 (61.5)

The third model fitted to the MOR data at this temperature was the two-step prediction method. Figure D-8 compares the predictions resulting from this method to the experimental values. This model predicts the values at 92% and 94% Si_3N_4 very well, but is not as accurate at 93% Si_3N_4, although the predictions in this range are still good. The reason for the less accurate prediction at 93% Si_3N_4 is illustrated in figure D-9, showing the discrepancies between the experimental and predicted standard deviation values.

Table D-4 is a summary of the comparison among the prediction methods and the observed MOR values.

2.2.3 Selected Model

A model using the two-step prediction method was found to be the best predictor of MOR at 1232°C (2250°F). To use this method, the standard deviation must be estimated first. The best model found to estimate the standard deviation is the following quadratic equation:

$$S = 30.74 + 4257.66\ X_2^{\,2} + 5719.46\ X_3^{\,2} - 790.87\ X_1X_2 - 679.07\ X_1X_3 + 8694.76\ X_2X_3 \quad \text{(D4)}$$

where S = standard deviation of MOR
X_1 = proportion of Si_3N_4
X_2 = proportion of Y_2O_3
X_3 = proportion of Al_2O_3

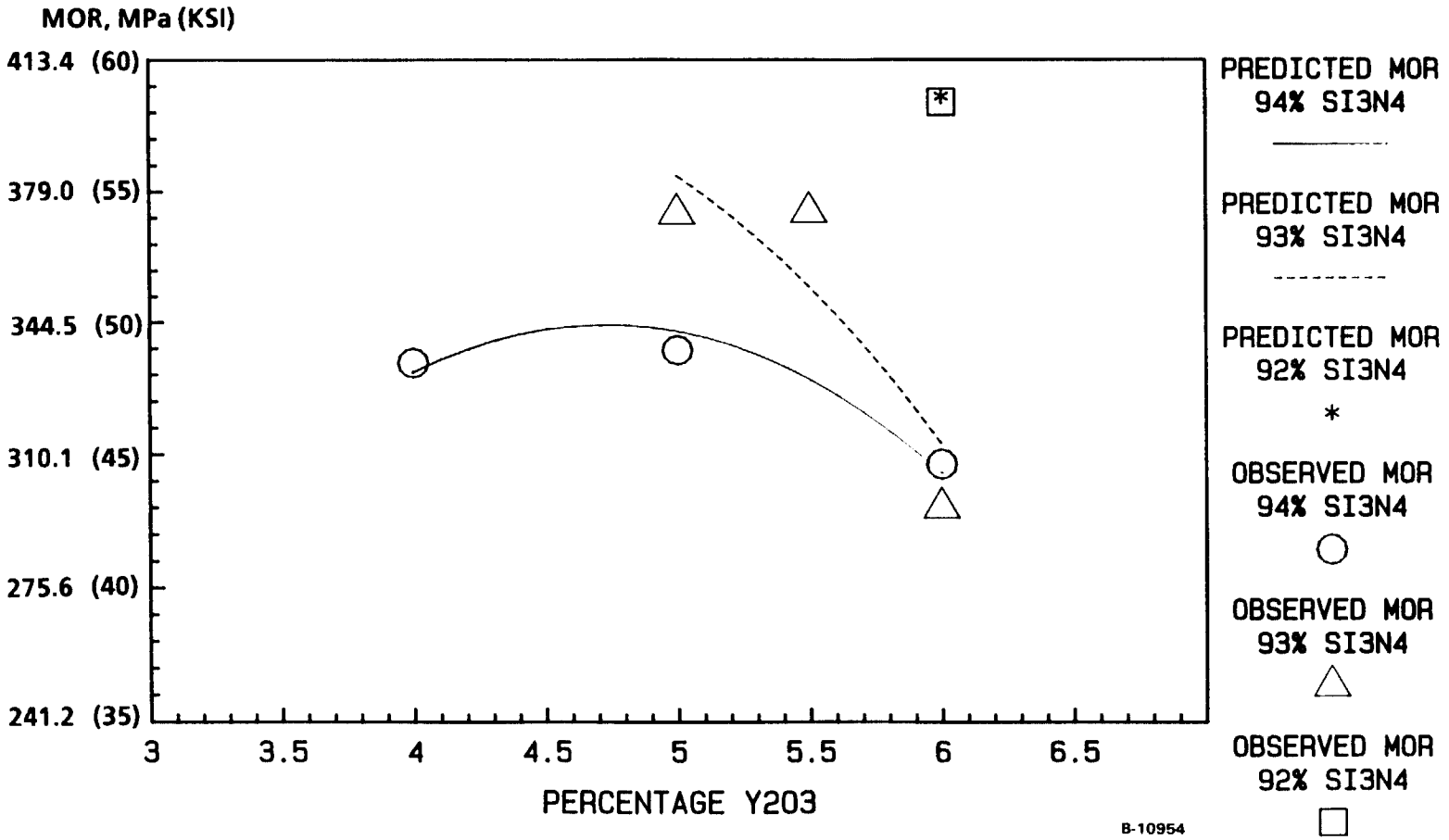

Figure D-6.--MOR Measured at 1232°C (2250°F)--Least Squares Prediction Method.

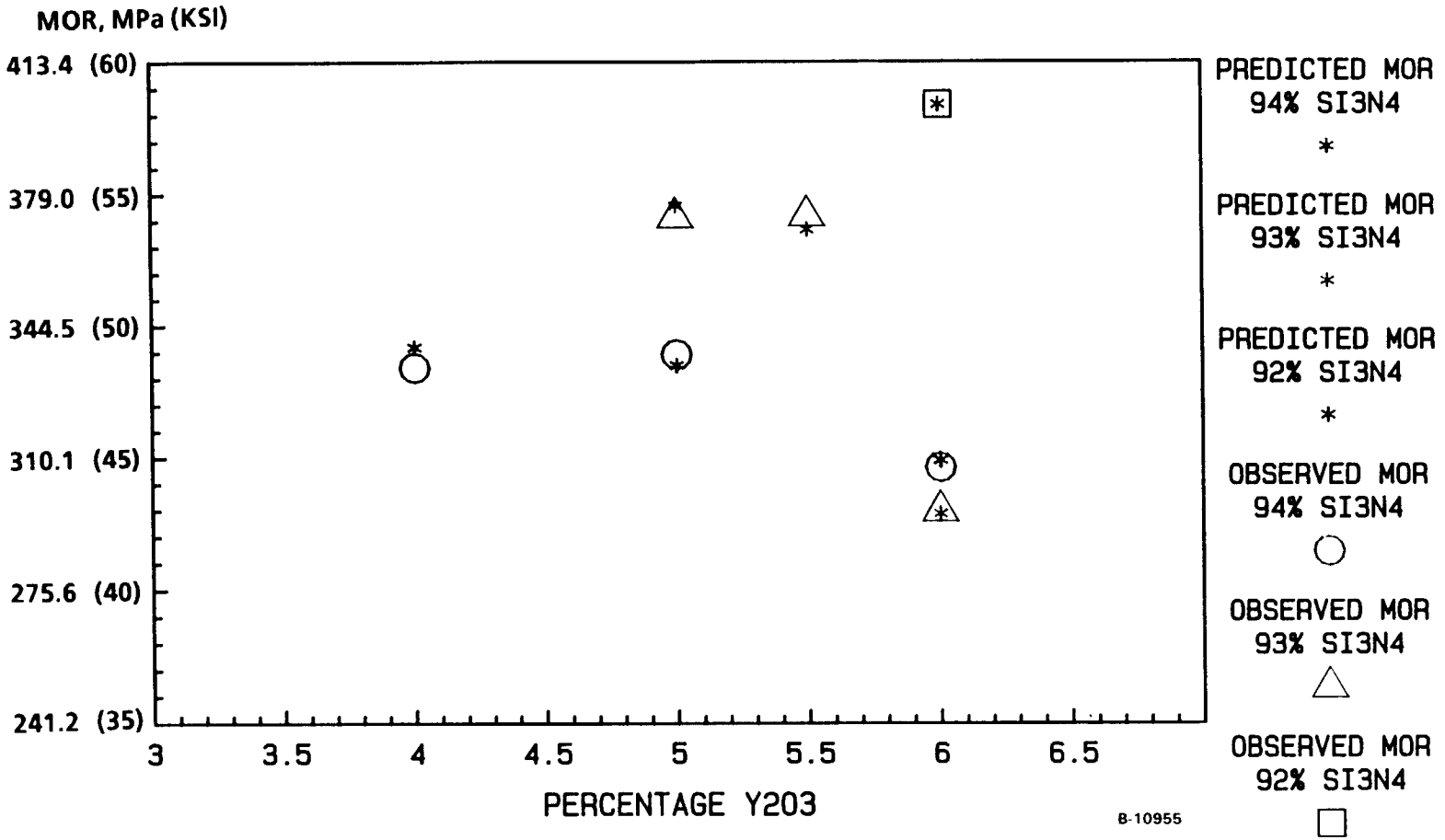

Figure D-7.--MOR Measured at 1232°C (2250°F)--Weighted Least Squares Prediction Method.

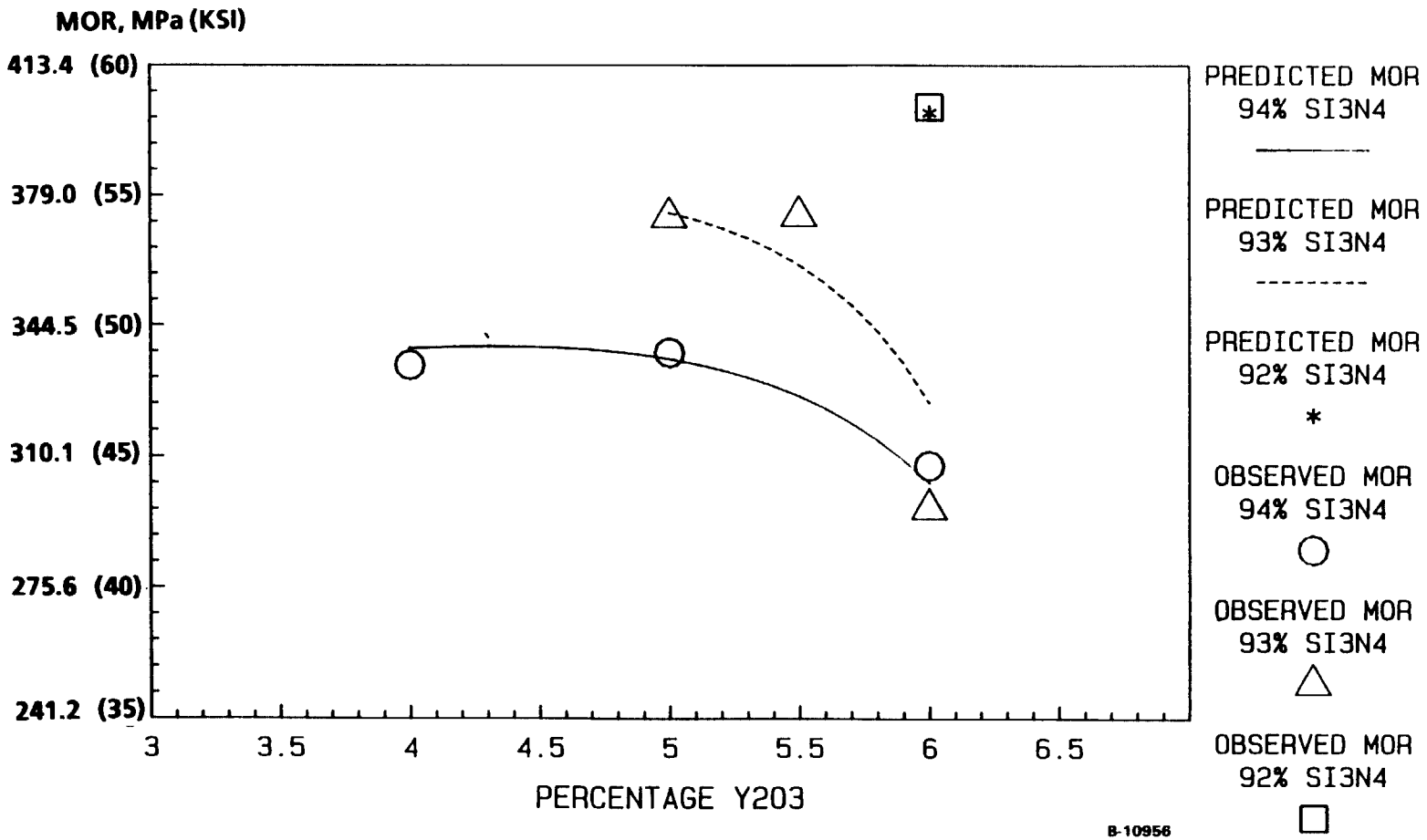

Figure D-8.--MOR Measured at 1232°C (2250°F)--Two-Step Prediction Method.

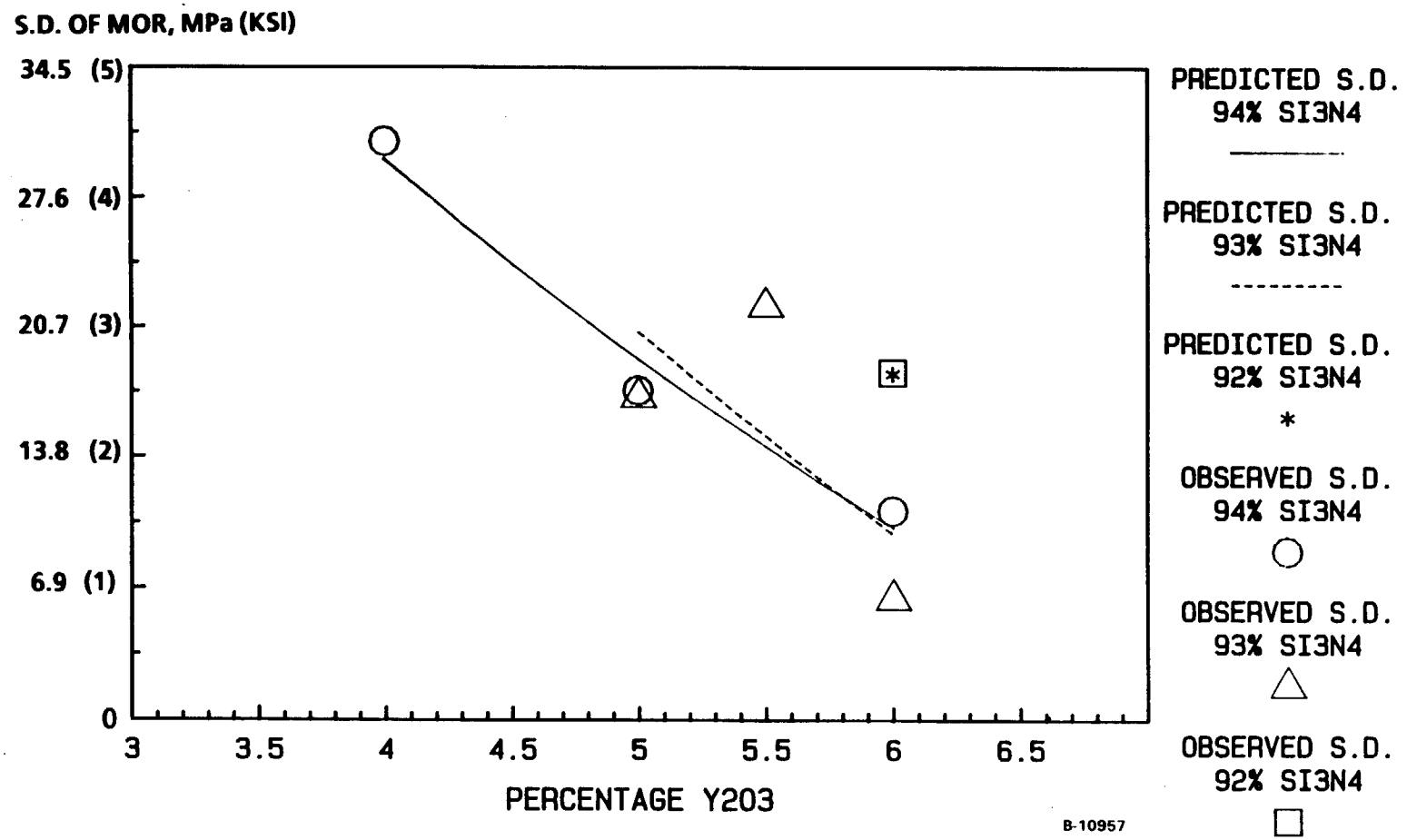

Figure D-9.--MOR Measured at 1232°F (2250°F)--Standard Deviation (S.D.) Predictions.

TABLE D-4.--COMPARISON OF EXPERIMENTAL AND PREDICTED MOR VALUES AT 1232°C (2250°F)

Billet No.	Composition (%)			Observed Mean, MPa (ksi)	MOR S.D., MPa (ksi)	LS[2], MPa (ksi)	Predicted WLS[3], MPa (ksi)	MOR[1] Two-Step[4], MPa (ksi)	Predicted S.D., MPa (ksi)
	Si_3N_4	Y_2O_3	Al_2O_3						
11	94	6	0	307.67 (44.64)	10.96 (1.59)	305.2 (44.3)	309.4 (44.9)	302.75 (43.94)	10.3 (1.5)
12	94	5	1	337.06 (48.92)	17.29 (2.51)	325.2 (47.2)	334.2 (48.5)	335.20 (48.65)	18.6 (2.7)
13	94	4	2	333.75 (48.44)	30.52 (4.43)	340.4 (49.4)	339.0 (49.2)	338.16 (49.08)	29.6 (4.3)
14	93	6	1	296.27 (43.00)	6.34 (0.92)	338.3 (49.1)	295.6 (42.9)	323.76 (46.99)	9.6 (1.4)
15	93	5.5	1.5	373.58 (54.22)	21.77 (3.16)	355.5 (51.6)	370.0 (53.7)	360.42 (52.31)	15.2 (2.2)
16	93	5	2	373.16 (54.16)	16.95 (2.46)	372.1 (54.0)	376.2 (54.6)	374.26 (54.32)	9.6 (1.4)
17[5]	92	2	6	402.38 (58.40)	18.26 (2.65)	403.8 (58.6)	402.4 (58.4)	400.79 (58.17)	17.9 (2.6)

[1]Predicted MOR values were obtained by using three methods.

[2]MOR was predicted with the method of least squares (LS).

[3]MOR was predicted with the method of weighted least squares (WLS). The observed standard deviations (S.D.) were used as weights.

[4]MOR was predicted with the two-step prediction method. The predicted standard deviations (S.D.) were used as weights.

[5]No billet was made of the (92, 6, 2) composition. Data used for "billet 17" are Task II Matrix A "ab condition" data.

Using the standard deviations obtained from the above equation, the predicted MOR can be obtained using the equation:

$$Y = 2.1 + 827.67\ Z_2 + 28.12\ Z_1^{\ 2} + 54313.6\ Z_3^{\ 2} - 10475.7\ Z_2^{\ 2} \qquad (D5)$$

where $Y = MOR/S$
$Z_1 = X_1/S$
$Z_2 = X_2/S$
$Z_3 = X_3/S$

According to this model, the strength increases as Si_3N_4 decreases and Y_2O_3 and Al_2O_3 increase as shown in the contour plot of MOR (figure D-10). It should be noted that the contours were generated from the prediction model and will not necessarily coincide with actual experimental data points. The contour lines are used mainly to show trends between the strength and composition in the predicted area. The highest MOR is achieved with a mixture of 92% Si_3N_4, 6% Y_2O_3, and 2% Al_2O_3.

2.3 1399 DEGREES CENTIGRADE (2550 DEGREES FAHRENHEIT)

2.3.1 Experimental Results

Table D-5 presents a summary of the experimental MOR data. Note that the standard deviations are small and fairly similar. The small variation at this temperature contributed to better predictions.

TABLE D-5.--SUMMARY STATISTICS OF EXPERIMENTAL MOR at 1371°C (2500°F)

Billet No.	Composition (%)			No. of Test Bars	Mean, MPa (ksi)	Standard Deviation, MPa (ksi)	Minimum, MPa (ksi)	Maximum, MPa (ksi)
	Si_3N_4	Y_2O_3	Al_2O_3					
11	94	6	0	5	186.44 (27.06)	4.27 (0.62)	180.5 (26.2)	192.2 (27.9)
12	94	5	1	5	141.25 (20.50)	5.37 (0.78)	134.4 (19.5)	148.1 (21.5)
13	94	4	2	5	148.14 (21.52)	3.31 (0.48)	142.6 (20.7)	150.9 (21.9)
14	93	6	1	3	111.62 (16.20)	3.17 (0.46)	108.9 (15.8)	115.1 (16.7)
15	93	5.5	1.5	5	133.94 (19.44)	4.07 (0.59)	128.8 (18.7)	138.5 (20.1)
16	93	5	2	5	139.73 (20.28)	3.58 (0.52)	135.0 (19.6)	144.7 (21.0)

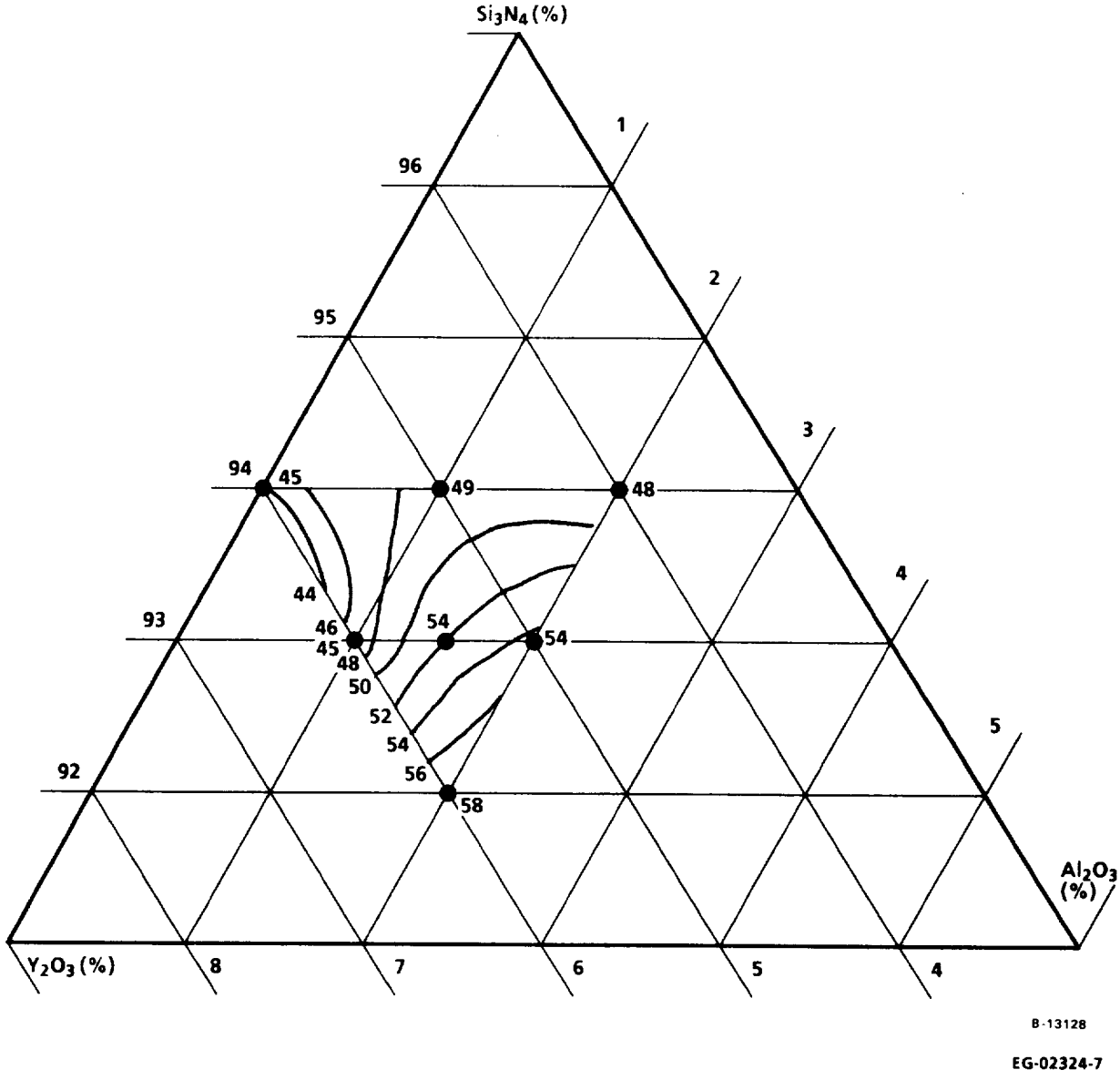

Figure D-10.--Contour Plot of MOR vs Composition at 1232°C (2250°F).

2.3.2 Comparison of Three Prediction Methods

Figure D-11 is a plot comparing the experimental values of MOR to the predicted values obtained using the least squares method. As can be seen, at 94% Si_3N_4, the predictions are very close. At 93% Si_3N_4, the predictions are also close, but the predicted line appears to be curving in the opposite direction of the experimental values.

The second model fitted to the data at 1232°C (2550°F) was the weighted least squares model using the experimental standard deviations as weights. This model fitted the data very well, as shown in figure D-12. However, in regions of unknown standard deviations, no predictions could be made.

The final model used the two-step prediction method with predicted standard deviations as weights, presented in figure D-13. The predictions for the 1399°C (2550°F) data appear to be better than at the other two temperatures because the variations in each of the six compositions were small and similar. Because the variations were similar from composition to composition, they were easier to predict, as can be seen in figure D-14.

Table D-6 summarizes the comparison among the prediction methods and the observed MOR values.

2.3.3 Selected Model

The best model found to predict MOR was the two-step prediction method. The first step in predicting MOR is to estimate the standard deviation. The best model found to estimate the standard deviation is the following quadratic equation:

$$S = -3.34 - 1736.95\ X_2^{\,2} - 617.95\ X_3^{\,2} + 181.00\ X_1X_2 + 45.10\ X_2X_3 \qquad \text{(D6)}$$

where S = standard deviation of MOR
X_1 = proportion of Si_3N_4
X_2 = proportion of Y_2O_3
X_3 = proportion of Al_2O_3

Using the standard deviations obtained from the above equation, the predicted MOR can be obtained using the equation:

$$Y = -40.99 + 81.84\ Z_1 - 20.19\ Z_1^{\,2} + 743.98\ Z_2^{\,2} + 19237.99\ Z_3^{\,2} - 10040.08\ Z_2Z_3 \qquad \text{(D7)}$$

where $Y = MOR/S$
$Z_1 = X_1/S$
$Z_2 = X_2/S$
$Z_3 = X_3/S$

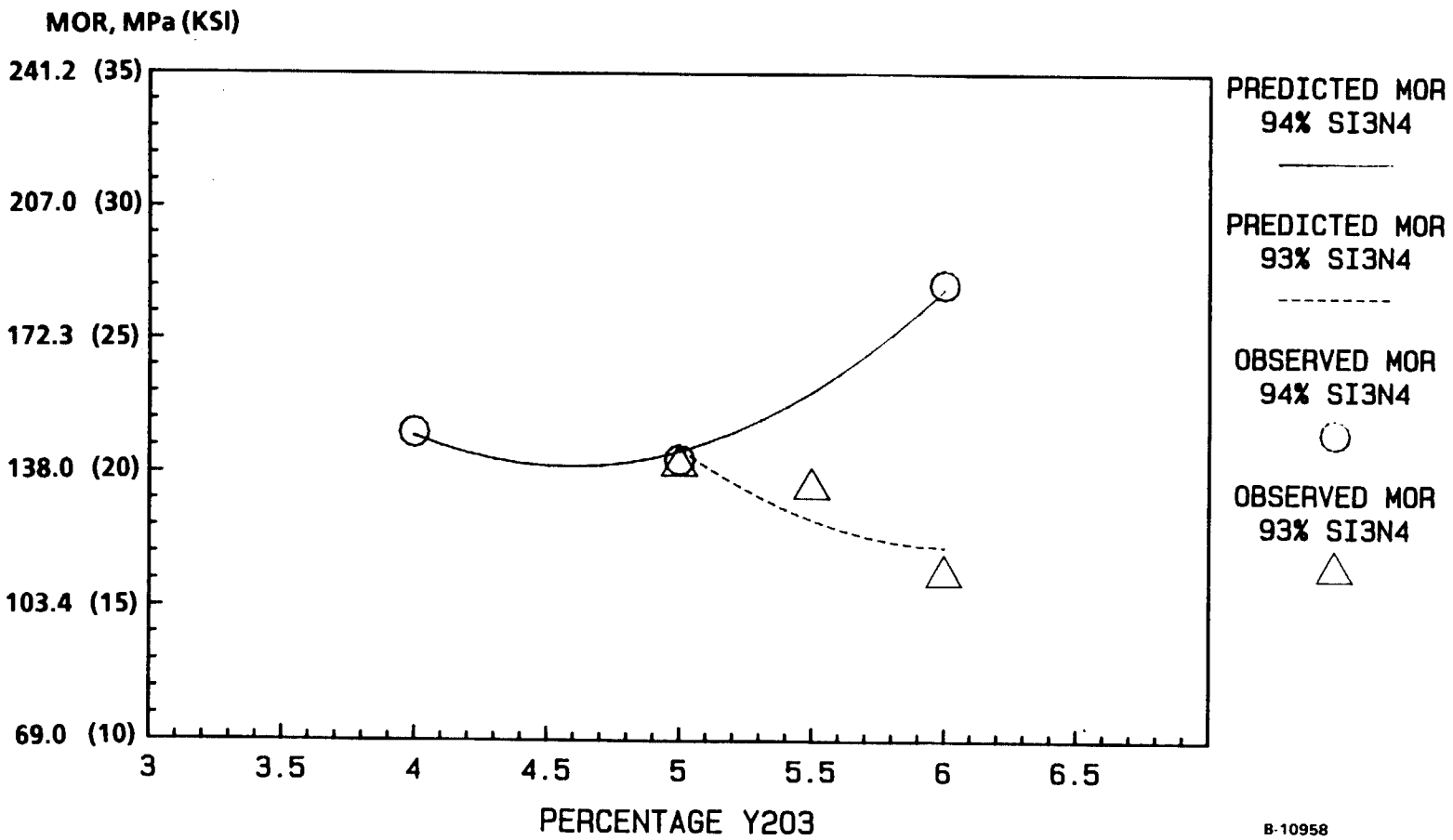

Figure D-11.--MOR Measured at 1399°C (2550°F)--Least Squares Prediction Method.

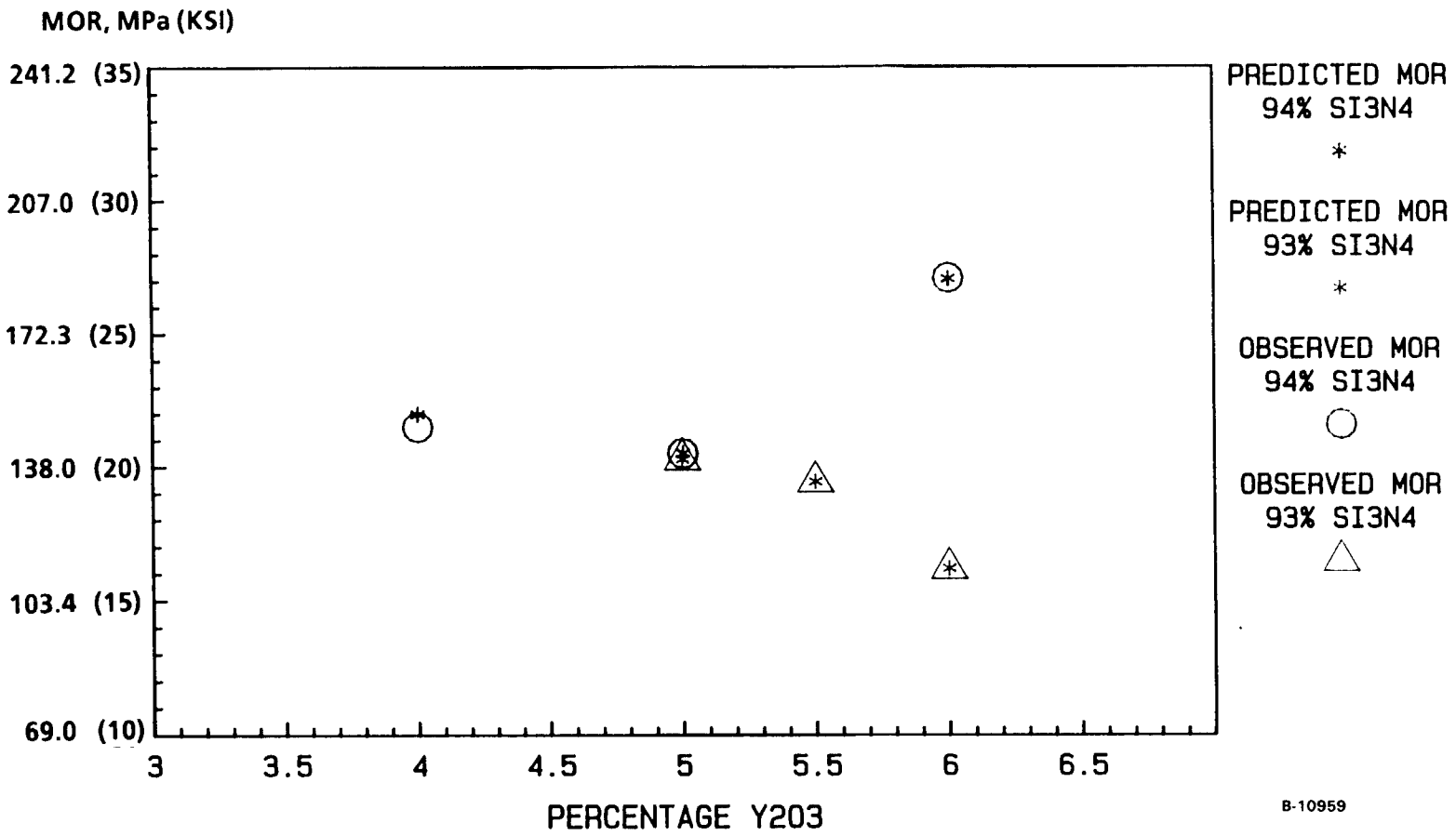

Figure D-12.--MOR Measured at 1399°C (2550°F)--Weighted Least Squares Prediction Method.

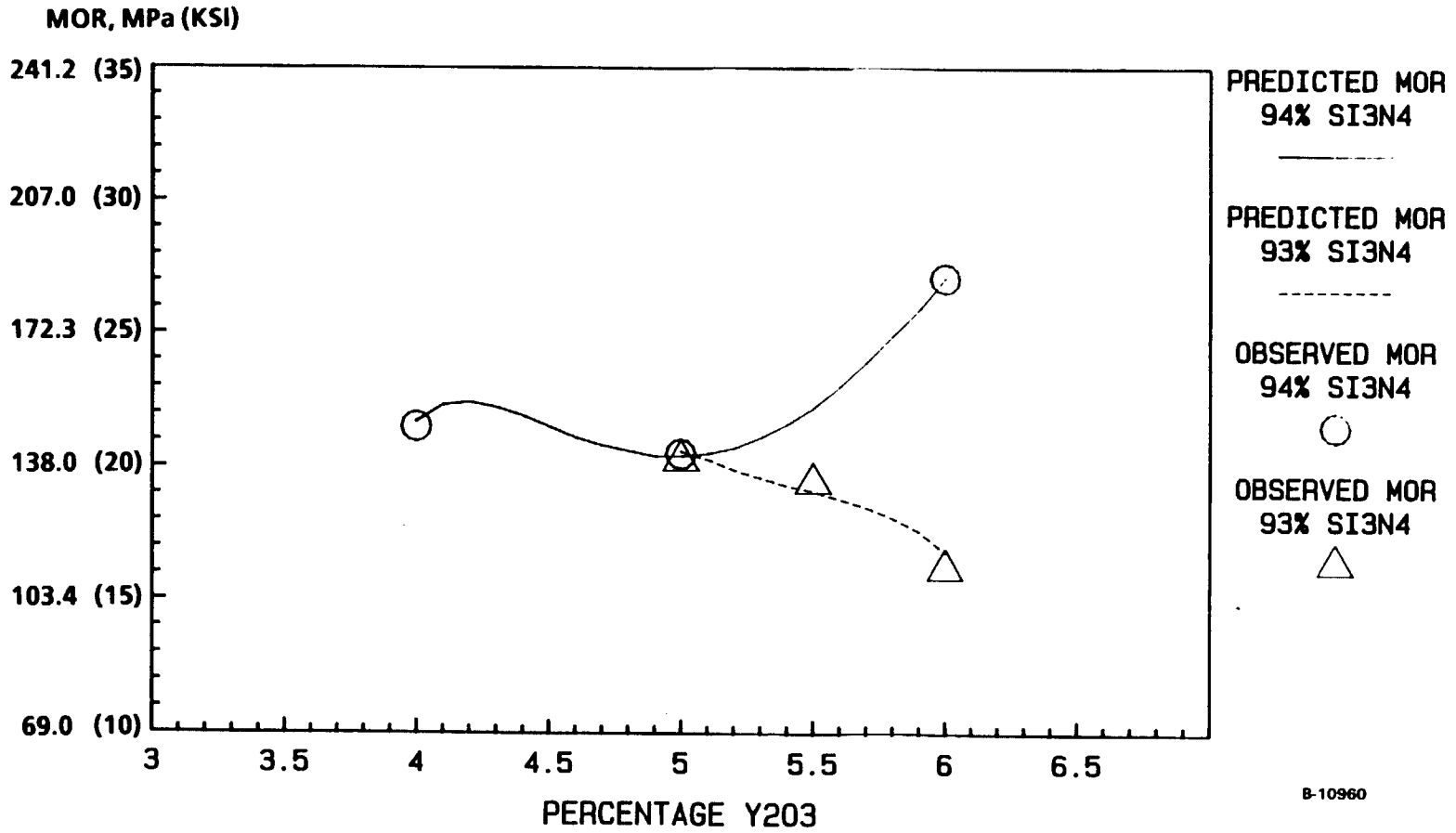

Figure D-13.--MOR Measured at 1399C (2550°F)--Two-Step Prediction Method.

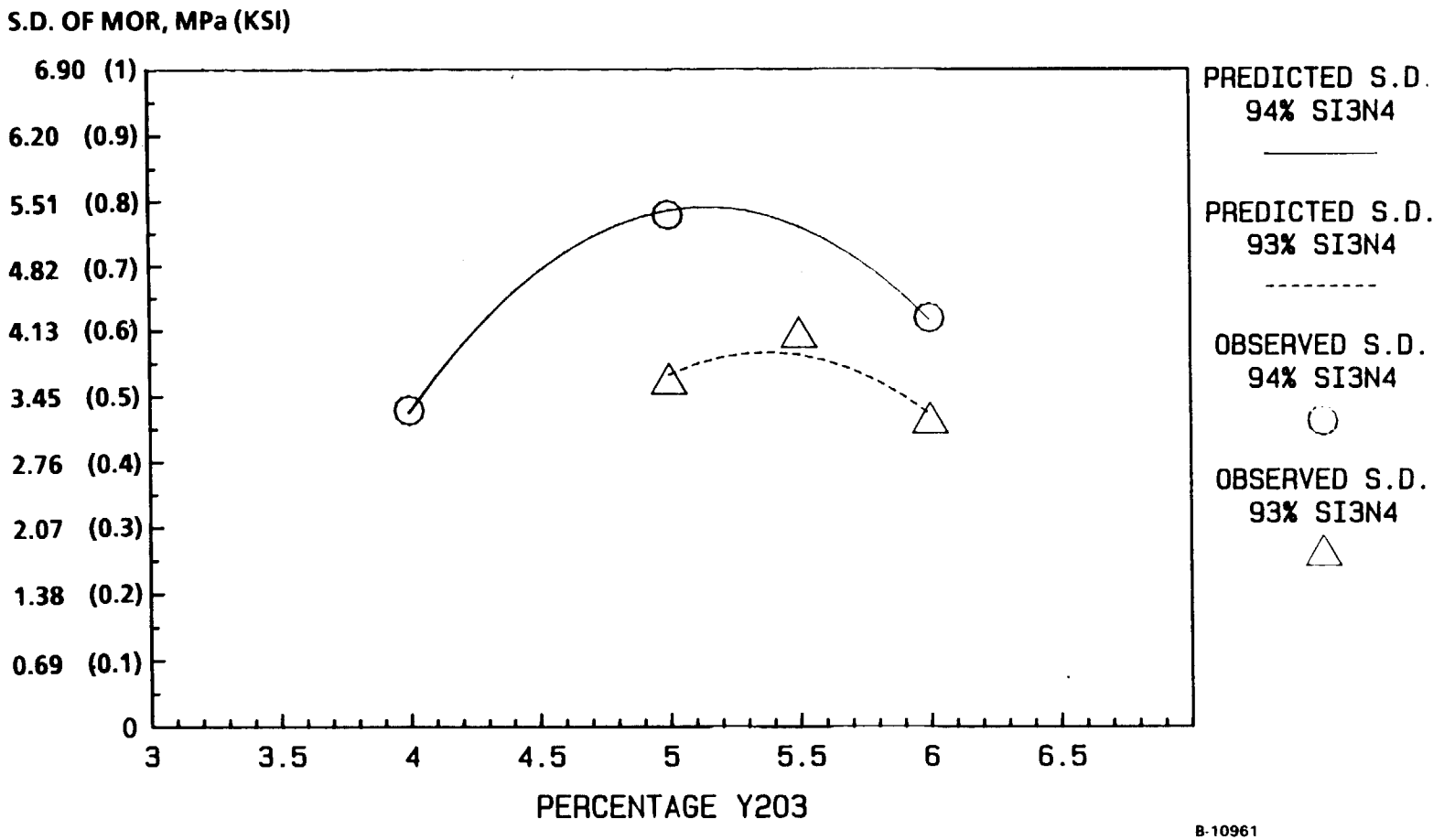

Figure D-14.--MOR Measured at 1399°C (2550°F)--Standard Deviation (S.D.) Predictions.

TABLE D-6.--COMPARISON OF EXPERIMENTAL AND PREDICTED MOR VALUES AT 1399°C (2550F)

Billet No.	Composition (%)			Observed Mean, MPa (ksi)	MOR S.D., MPa (ksi)	LS[2], MPa (ksi)	Predicted WLS[2], MPa (ksi)	MOR[1] Two-Step[3], MPa (ksi)	Predicted S.D., MPa (ksi)
	Si_3N_4	Y_2O_3	Al_2O_3						
11	94	6	0	186.44 (27.06)	4.27 (0.62)	185.68 (26.91)	186.71 (27.06)	186.71 (27.06)	4.27 (0.62)
12	94	5	1	141.25 (20.50)	5.37 (0.78)	143.59 (20.81)	141.45 (20.50)	143.24 (20.76)	5.45 (0.79)
13	94	4	2	148.27 (21.52)	3.31 (0.48)	147.45 (21.37)	151.66 (21.98)	151.66 (21.98)	3.31 (0.48)
14	93	6	1	111.62 (16.20)	3.17 (0.46)	118.82 (17.22)	111.78 (16.20)	114.20 (16.55)	3.24 (0.47)
15	93	5.5	1.5	133.94 (19.44)	4.09 (0.59)	125.72 (18.22)	134.14 (19.44)	127.31 (18.45)	3.86 (0.56)
16	93	5	2	139.73 (20.28)	3.59 (0.52)	144.14 (20.89)	139.93 (20.28)	142.62 (20.67)	3.66 (0.53)

[1]Predicted MOR values were obtained by using three methods.

[2]MOR was predicted with the method of least squares (LS).

[3]MOR was predicted with the method of weighted least squares (WLS). The observed standard deviations (S.D.) were used as weights.

[4]MOR was predicted with the two-step prediction method. The predicted standard deviations (S.D.) were used as weights.

This model predicts that at 1232°C (2550°F), the strength increases as Si_3N_4 and Y_2O_3 increase and Al_2O_3 decreases, as shown in the contour plot of MOR (figure D-15). The mixture yielding the highest MOR consists of 94% Si_3N_4 and 6% Y_2O_3.

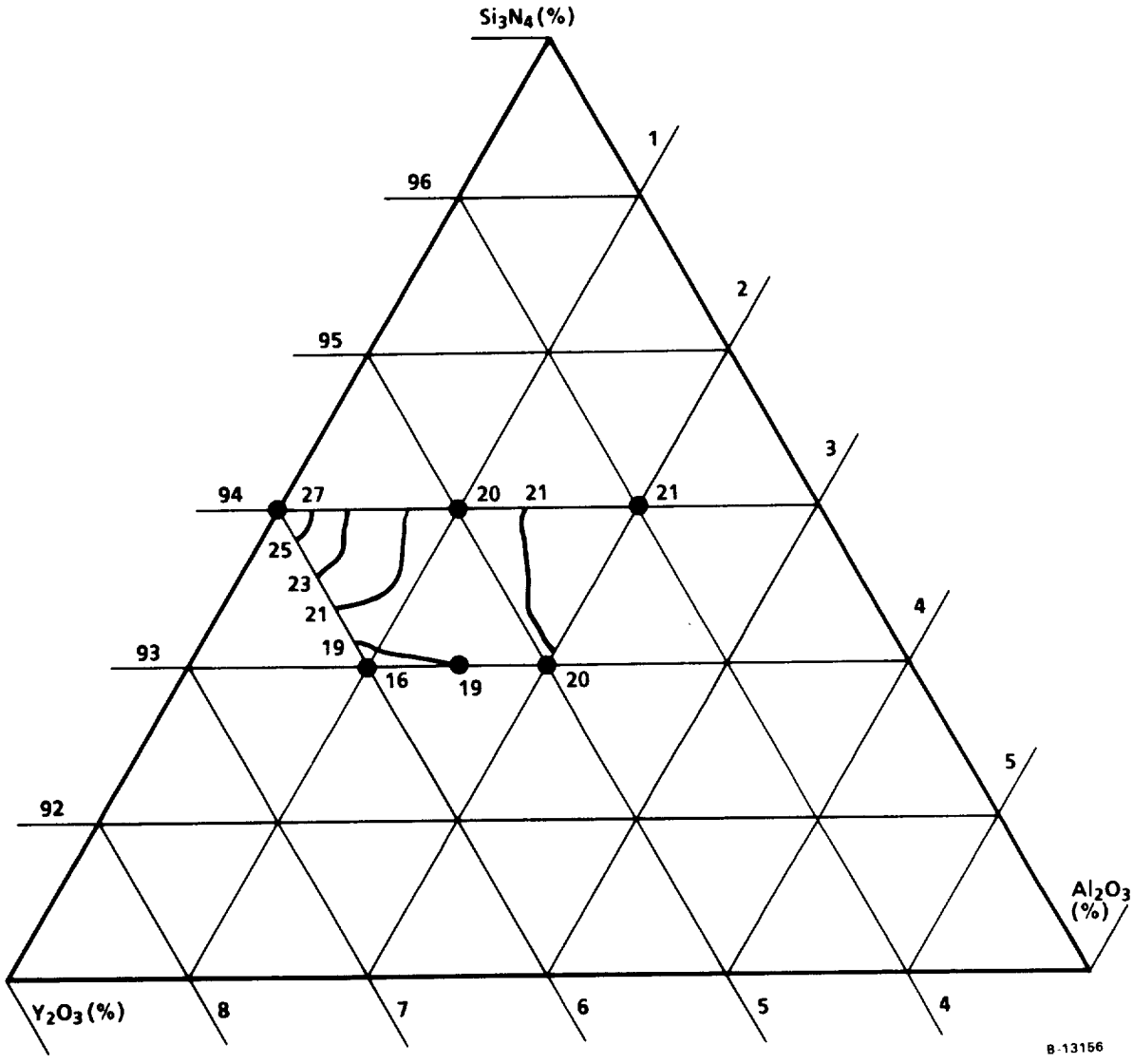

Figure D-15.--Contour Plot of MOR vs Composition at 1399°C (2550°F).

APPENDIX E

MOR AND FRACTOGRAPHY RESULTS OF INJECTION-MOLDED GN-10 TEST BARS

TABLE E-1.--MOR AND FRACTOGRAPHY RESULTS OF INJECTION-MOLDED TEST BARS

		Method	Bar #	MOR	S/I	Type	Loc.	Fracture Observations
Average MOR =	1.03	Standard	6147	1.19	S	Agg.	TF	
Std. Dev. =	0.121	Standard	6153	1.05	S	Agg.	TF	Chamfer
High =	1.23	Standard	6134	0.85	S	Agg.	TF	
Low =	0.82	Standard	6150	0.88	S	Agg.	TF	Material flow
Range =	0.41	Standard	6139	0.82	S	Knit line	TF	Material flow
		Standard	6193	1.02	S	Surface	TF	Agglomorate
		Standard	6205	1.17	S	Surface	TF	Metallic inclusion
		Standard	6169	1.12	S	Surface	TF	
		Standard	6177	1.23	S	Surface	TF	
		Standard	6183	1.10	S	Surface	TF	
		Standard	6173	0.98	S	Surface	TF	
		Standard	6181	1.10	S	Surface	TF	Agglomorate
		Standard	6182	0.92	S	Surface	TF	
		Standard	6197	1.05	S	Surface	TF	Chamfer
		Standard	6189	0.97	S	Surface	TF	
Average MOR =	0.98	Solvent	7053	0.95	S	Agg.	TF	Material flow
Std. Dev. =	0.077	Solvent	7058	0.97	S	Agg.	TF	
High =	1.12	Solvent	7055	0.95	S	Agg.	TF	
Low =	0.86	Solvent	7057	0.93	S	Agg.	TF	Knit line crack
Range =	0.26	Solvent	7051	1.07	S	Agg.	TF	Knit line crack
		Solvent	7045	1.07	S	Agg.	TF	
		Solvent	7080	1.09	S	Agg.	TF	Knit line crack
		Solvent	7052	0.89	S	Agg.	TF	
		Solvent	7046	0.95	S	Agg.	TF	
		Solvent	7049	0.97	S	Agg.	TF	
		Solvent	7056	0.95	S	Corner	Chamfer	Dark Patch
		Solvent	7059	1.12	S	Corner	Chamfer	Dark Patch
		Solvent	7050	0.88	S	Surface	TF	Material flow
		Solvent	7054	0.86	S	Surface	TF	Black shiny inclusion
		Solvent	7047	1.02	S	Surface	TF	Internal crack
Average MOR =	0.96	Henschel	6820	1.03	S	Agg.	TF	Material flow
Std. Dev. =	0.103	Henschel	6817	1.04	S	Agg.	Side	Material flow
High =	1.11	Henschel	6821	1.04	S	Agg.	TF	
Low =	0.76	Henschel	6822	0.85	S	Agg.	TF	
Range =	0.35	Henschel	6818	1.11	S	Corner	Chamfer	Material flow
		Henschel	6819	0.82	S	Corner	Chamfer	
		Henschel	6816	1.07	S	Surface	TF	Material flow
		Henschel	6815	0.89	S	Surface	TF	
		Henschel	6931	1.00	S	Agg.	TF	
		Henschel	6929	1.02	S	Agg.	TF	
		Henschel	6961	0.76	S	Agg.	TF	
		Henschel	6965	0.84	S	Surface	TF	

TABLE E-1.--(Continued)

		Henschel	6930	0.94	S	Surface	TF	
		Henschel	6960	0.99	S	Surface	TF	
		Henschel	6966	1.05	S	Surface	TF	
Average MOR =	1.01	De-air	6485	1.16	S	Agg.	TF	
Std. Dev. =	0.099	De-air	6468	1.01	S	Agg.	C. Corner	
High =	1.16	De-air	6481	0.99	S	Agg.	TF	
Low =	0.82	De-air	6458	1.06	S	Surface	TF	
Range =	0.34	De-air	6422	0.97	S	Surface	TF	
		De-air	6489	0.89	S	Surface	TF	
		De-air	6449	1.04	S	Surface	TF	
		De-air	6459	0.82	S	Surface	TF	
		De-air	6428	1.01	S	Surface	TF	
		De-air	6455	1.07	S	Surface	TF	
		De-air	6494	1.12	S	Surface	TF	
		De-air	6435	0.90	S	Surface	TF	
		De-air	6479	1.02	S	Surface	TF	
		De-air	6442	0.87	S	Surface	TF	Agglomorate
		De-air	6496	1.16	S	Surface	TF	
Average MOR =	1.10	Blend 2	6634	1.15	S	Agg.	TF	
Std. Dev. =	0.108	Blend 2	6711	1.15	S	Agg.	TF	Material swirl
High =	1.30	Blend 2	6666	1.09	S	Agg.	Side	Material swirl
Low =	0.87	Blend 2	6679	1.21	S	Agg.	TF	Material swirl
Range =	0.43	Blend 2	6662	1.02	S	Agg.	TF	Inclusion
		Blend 2	6643	0.87	S	Agg.	TF	
		Blend 2	6688	1.14	S	Agg.	TF	
		Blend 2	6693	1.12	S	Surface	TF	
		Blend 2	6629	1.09	S	Surface	TF	
		Blend 2	6655	1.18	S	Surface	TF	
		Blend 2	6625	1.01	S	Surface	TF	
		Blend 2	6650	1.15	S	Surface	TF	
		Blend 2	6726	0.90	S	Surface	TF	
		Blend 2	6734	1.07	S	Surface	TF	
		Blend 2	6743	1.30	S	Surface	TF	
Average MOR =	1.08	Blend 1	6506	1.16	S	Agg.	TF	
Std. Dev. =	0.115	Blend 1	6613	1.26	S	Agg.	TF	
High =	1.26	Blend 1	6607	1.12	S	Agg.	TF	
Low =	0.88	Blend 1	6546	1.12	S	Surface	TF	
Range =	0.38	Blend 1	6596	1.23	S	Surface	TF	Material flow
		Blend 1	6601	1.19	S	Surface	TF	
		Blend 1	6553	0.88	S	Surface	TF	
		Blend 1	6574	0.92	S	Surface	TF	
		Blend 1	6564	1.12	S	Surface	TF	Material flow
		Blend 1	6500	0.99	S	Surface	TF	
		Blend 1	6569	1.19	S	Surface	TF	
		Blend 1	6537	0.96	S	Surface	TF	Material flow
		Blend 1	6617	1.14	S	Surface	TF	
		Blend 1	6530	0.98	S	Void	C. Corner	Void/Agg. on the side
		Blend 1	6521	1.00	S	Void	C. Corner	Material flow

TABLE E-2.--MOR AND FRACTOGRAPHY RESULTS
OF DEWAXED TEST BARS

		Method	Bar #	MOR	S/I	Type	Loc.	Fracture Observations
Average MOR =	0.307	Standard	6313	0.330	I	Agg.	Internal	
Std. Dev. =	0.050	Standard	6330	0.310	I	Agg.	Internal	
High =	0.370	Standard	6349	0.360	I	Agg/Crack	Sub. Surf.	
Low =	0.170	Standard	6292	0.280	I	Agg/Void	Internal	
Range =	0.200	Standard	6303	0.320	I	Agg/Void	Internal	
		Standard	6314	0.300	I	Agg/Void	Internal	
		Standard	6291	0.330	I	Core	Internal	
		Standard	6293	0.240	S	Agg.	TF	Material flow
		Standard	6347	0.370	S	Agg.	TF	
		Standard	6329	0.170	S	Agg/Void	C. Corner	
		Standard	6315	0.330	S	Surface	TF	
		Standard	6328	0.280	S	Surface	TF	
		Standard	6302	0.360	S	Surface	TF	
		Standard	6301	0.280	S	Surface	TF	
		Standard	6348	0.340	S	Void	Chamfer	Void/Agglomorate
Average MOR =	0.279	Solvent	7042	0.174		DM		
Std. Dev. =	0.055	Solvent	6980	0.278	I	Agg.	Internal	
High =	0.374	Solvent	6975	0.338	I	Agg.	Internal	
Low =	0.174	Solvent	6978	0.277	I	Agg.	Internal	
Range =	0.200	Solvent	7020	0.228	I	Agg.	Internal	Light colored
		Solvent	7037	0.176	I	Agg.	Internal	
		Solvent	7028	0.244	I	Agg.	Sub. Surf.	Flakey crystal
		Solvent	7004	0.290	I	Agg.	Internal	Light colored
		Solvent	6973	0.280	I	Agg.	Internal	
		Solvent	6999	0.348	I	Inclusion	Sub. Surf.	Fiber
		Solvent	6982	0.314	I	Inclusion	Sub. Surf.	Black inclusion
		Solvent	6996	0.315	S	Surface	TF	
		Solvent	6987	0.374	S	Surface	TF	
		Solvent	6993	0.288	S	Surface	TF	
		Solvent	7015	0.265	S	Surface	TF	
Average MOR =	0.320	Henschel	6286	0.220		DM		
Std. Dev. =	0.061	Henschel	6854	0.403	I	Agg.	Sub. Surf.	
High =	0.419	Henschel	6870	0.346	I	Agg.	Sub. Surf.	
Low =	0.220	Henschel	6287	0.220	I	Agg/Void	Internal	Void/Agg. with crack
Range =	0.199	Henschel	6284	0.270	I	Agg/Void	Internal	Void/Agg. with crack
		Henschel	6877	0.335	I	Inclusion	Sub. Surf.	Black inclusion
		Henschel	6829	0.375	S	Agg.	TF	
		Henschel	6837	0.369	S	Inclusion	TF	Rusty wire
		Henschel	6846	0.419	S	Surface	TF	
		Henschel	6450	0.338	S	Surface	TF	
		Henschel	6859	0.364	S	Surface	TF	
		Henschel	6288	0.320	S	Surface	TF	Material flow

TABLE E-2.--(Continued)

		Henschel	6833	0.280	S	Surface	TF	
		Henschel	6866	0.293	S	Surface	TF	
		Henschel	6289	0.250	S	Surface	TF	
Average MOR =	0.288	De-air	6429	0.297	I	Agg.	Sub. Surf.	
Std. Dev. =	0.034	De-air	6436	0.318	I	Agg/Void	Sub. Surf.	
High =	0.346	De-air	6438	0.236	I	Inclusion	Sub. Surf.	Flakey crystal
Low =	0.226	De-air	6441	0.226	I	Inclusion	Sub. Surf.	Fiber
Range =	0.120	De-air	6446	0.303	S	Agg.	TF	
		De-air	6452	0.314	S	Agg.	TF	
		De-air	6432	0.302	S	Agg/Void	TF	
		De-air	6421	0.329	S	Agg/Void	TF	
		De-air	6487	0.263	S	Agg/Void	TF	
		De-air	6482	0.313	S	Surface	TF	
		De-air	6486	0.257	S	Surface	TF	
		De-air	6425	0.346	S	Surface	TF	
		De-air	6417	0.293	S	Surface	TF	
		De-air	6483	0.250	S	Surface	TF	
		De-air	6440	0.272	S	Surface	TF	
Average MOR =	0.312	Blend 2	6686	0.292	I	Agg.	Sub. Surf.	
Std. Dev. =	0.032	Blend 2	6681	0.294	I	Void	Sub. Surf.	
High =	0.379	Blend 2	6663	0.301	I	Void	Internal	
Low =	0.261	Blend 2	6668	0.267	S	Agg.	C. Corner	
Range =	0.118	Blend 2	6657	0.298	S	Agg.	TF	
		Blend 2	6660	0.379	S	Inclusion	TF	Metallic inclusion
		Blend 2	6646	0.307	S	Surface	TF	
		Blend 2	6631	0.318	S	Surface	TF	
		Blend 2	6676	0.318	S	Surface	TF	
		Blend 2	6623	0.285	S	Surface	TF	
		Blend 2	6651	0.359	S	Surface	TF	
		Blend 2	6627	0.318	S	Surface	TF	
		Blend 2	6638	0.358	S	Surface	TF	
		Blend 2	6635	0.261	S	Surface	TF	
		Blend 2	6642	0.325	S	Void	TF	
Average MOR =	0.305	Blend 1	6513	0.328		DM		
Std. Dev. =	0.031	Blend 1	6572	0.332	I	Inclusion	Sub. Surf.	Black shiny inclusion
High =	0.346	Blend 1	6578	0.255	S	Agg.	TF	
Low =	0.252	Blend 1	6588	0.252	S	Agg.	TF	
Range =	0.094	Blend 1	6543	0.262	S	Agg.	TF	
		Blend 1	6507	0.283	S	Agg/Void	TF	Spherical agglomorate
		Blend 1	6501	0.311	S	Inclusion	TF	Flakey crystal
		Blend 1	6520	0.335	S	Surface	TF	
		Blend 1	6533	0.307	S	Surface	TF	
		Blend 1	6540	0.311	S	Surface	TF	
		Blend 1	6558	0.325	S	Surface	TF	
		Blend 1	6565	0.346	S	Surface	TF	
		Blend 1	6550	0.324	S	Surface	TF	

TABLE E-3.--MOR AND FRACTOGRAPHY RESULTS OF SINTER/HIP'ED TEST BARS

Blending Experiment GN-10 test bars
Sinter/HIPped at 1900C
Density average 3.07 g/cc

		Method	Bar #	MOR	S/I	Type	Loc.	Fracture Observations
Average MOR =	72.5	Standard	6312	69.6	S	Agg	TF	
Std. Dev. =	7.52	Standard	6300	55.7	I	Agg	Sub-surf.	Crack around agglomorate
High =	86.3	Standard	6318	65.3	S	Agg	TF	
Low =	55.7	Standard	6350	75.0	S	Agg	TF	
Range =	30.6	Standard	6358	75.5	S	Corner	Chamfer	
		Standard	6326	72.7	S	Corner	Chamfer	
		Standard	6321	78.6	S	Surface	TF	
		Standard	6297	86.3	S	Surface	TF	
		Standard	6339	71.8	S	Surface	TF	
		Standard	6306	78.9	S	Surface	TF	
		Standard	6309	76.2	S	Surface	TF	
		Standard	6343	61.1	S	Surface	TF	Agglomorate
		Standard	6244	76.9	S	Surface	TF	
		Standard	6356	71.5	S	Surface	TF	
Average MOR =	76.1	Solvent	7019	85.1	S	Agg	TF	
Std. Dev. =	8.95	Solvent	7016	82.7	S	Corner	Chamfer	
High =	87.6	Solvent	6976	75.9	S	Corner	Chamfer	
Low =	55.1	Solvent	7026	87.6	S	Corner	Chamfer	
Range =	32.5	Solvent	7038	64.9	S	Crack	TF	Knit line crack
		Solvent	7044	68.4	S	Crack	Chamfer	Knit line crack
		Solvent	7040	55.1	I	Crack	Internal	
		Solvent	7035	78.3	S	Crack	TF	Knit line crack
		Solvent	6998	76.6	S	Surface	TF	
		Solvent	6983	72.7	S	Surface	TF	
		Solvent	7011	79.1	S	Surface	TF	
		Solvent	6989	87.6	S	Surface	TF	
		Solvent	6994	75.8	S	Surface	TF	
Average MOR =	77.2	Henschel	6865	79.4	S	Crack	TF	
Std. Dev. =	3.42	Henschel	6863	82.0	I	Incl.	Sub-surf.	Black shiny inclusion
High =	82.4	Henschel	6862	75.8	S	Surface	TF	
Low =	72.2	Henschel	6868	79.2	S	Surface	TF	
Range =	10.2	Henschel	6860	72.9	S	Surface	TF	
		Henschel	6875	74.6	S	Surface	TF	
		Henschel	6869	81.3	S	Surface	TF	
		Henschel	6852	77.4	S	Surface	TF	
		Henschel	6853	72.2	S	Surface	TF	
		Henschel	6864	74.5	S	Surface	TF	
		Henschel	6861	78.7	S	Surface	TF	
		Henschel	6876	73.4	S	Surface	TF	
		Henschel	6858	82.4	S	Surface	TF	
Average MOR =	73.8	De-Air	6484	69.2	S	Agg	TF	
Std. Dev. =	7.44	De-Air	6420	51.0	I	Agg	Sub-surf.	

TABLE E-3.--(Continued)

High =	84.0	De-Air	6462	77.9	S	Corner	Chamfer	
Low =	51.0	De-Air	6456	73.1	S	Corner	Chamfer	
Range =	33.0	De-Air	6464	69.8	S	Corner	Chamfer	
		De-Air	6476	75.9	S	Surface	TF	
		De-Air	6466	81.1	S	Surface	TF	
		De-Air	6427	72.7	S	Surface	TF	
		De-Air	6483	82.2	S	Surface	TF	
		De-Air	6443	75.9	S	Surface	TF	
		De-Air	6439	84.0	S	Surface	TF	
		De-Air	6471	76.9	S	Surface	TF	
		De-Air	6424	71.2	S	Surface	TF	
		De-Air	6453	72.3	S	Surface	TF	
		De-Air	6458	74.0	S	Surface	TF	
Average MOR =	74.0	Blend 2	6689	79.5	S	Corner	Chamfer	
Std. Dev. =	7.26	Blend 2	6677	60.0	S	Crack	TF	
High =	88.7	Blend 2	6664	73.1	S	Surface	TF	
Low =	51.0	Blend 2	6667	65.9	S	Surface	TF	Agglomorate
Range =	37.7	Blend 2	6687	77.5	S	Surface	TF	
		Blend 2	6659	78.9	S	Surface	TF	
		Blend 2	6647	72.5	S	Surface	TF	
		Blend 2	6652	70.1	S	Surface	TF	
		Blend 2	6658	68.7	S	Surface	TF	
		Blend 2	6653	85.7	S	Surface	TF	Inclusion
		Blend 2	6678	69.1	S	Surface	TF	
		Blend 2	6656	74.3	S	Surface	TF	
		Blend 2	6682	72.8	S	Surface	TF	
		Blend 2	6649	88.2	S	Surface	TF	
Average MOR =	76.2	Blend 1	6590	72.7	S	Agg	Chamfer	
Std. Dev. =	5.11	Blend 1	6528	81.8	S	Corner	Chamfer	
High =	83.1	Blend 1	6570	77.1	S	Corner	Chamfer	
Low =	66.1	Blend 1	6497	72.6	S	Corner	Chamfer	
Range =	17.0	Blend 1	6525	69.2	S	Surface	TF	
		Blend 1	6517	80.8	S	Surface	TF	
		Blend 1	6551	81.1	S	Surface	TF	
		Blend 1	6511	76.2	S	Surface	TF	
		Blend 1	6542	66.1	S	Surface	TF	
		Blend 1	6512	78.6	S	Surface	TF	
		Blend 1	6562	71.8	S	Surface	TF	
		Blend 1	6580	73.8	S	Surface	TF	
		Blend 1	6556	82.0	S	Surface	TF	
		Blend 1	6576	83.1	S	Surface	TF	

APPENDIX F

GN-10 REPRODUCIBILITY TEST BAR RESULTS

MOR and fractography results of sinter/HIP injection molded GN-10 test bars

Bar No.	MOR (ksi)	Fracture Location	Origin Type	Observations/ Comments	Test Temp	Batch	Mold	Density
8150	70.7	Corner	Surface		Room	GN-10	Arb	3.28
8134	78.3	Corner	Surface		Room	GN-10	Arb	3.29
8167	80.9	Corner	Surface		Room	GN-10	Arb	3.19
8149	82.7	Corner	Surface		Room	GN-10	Arb	3.26
8159	84.4	Corner	Surface		Room	GN-10	Arb	3.23
8132	84.5	Corner	Surface		Room	GN-10	Arb	3.27
8157	85.2	Tensile	Surface		Room	GN-10	Arb	3.28
8154	85.8	Tensile	Surface		Room	GN-10	Arb	3.29
8144	86.9	Tensile	Surface		Room	GN-10	Arb	3.23
8143	87.6	Corner	Surface		Room	GN-10	Arb	3.26
8147	101.6	Tensile	Surface		Room	GN-10	Arb	3.28
8140	102.3	Tensile	Surface		Room	GN-10	Arb	3.23
8171	110.0	Tensile	Surface		Room	GN-10	Arb	3.25
8316	69.5	Corner	Surface	Chipped corner	Room	GN-10	Bat	3.21
8268	70.1	Corner	Incl.	Dark inclusion	Room	GN-10	Bat	3.20
8298	72.1	Corner	Surface		Room	GN-10	Bat	3.27
8303	78.4	Corner	Surface		Room	GN-10	Bat	3.29
8286	82.4	Corner	Surface		Room	GN-10	Bat	3.26
8315	83.9	Corner	Surface		Room	GN-10	Bat	3.26
8295	85.7	Corner	Surface		Room	GN-10	Bat	3.22
8283	90.8	Corner	Surface		Room	GN-10	Bat	3.22
8299	92.8	Corner	Surface		Room	GN-10	Bat	3.21
8271	97.7	Corner	Surface		Room	GN-10	Bat	3.19
7734	81.9	Tensile	Surface		Room	PM-4	Arb	3.25
8439	82.2	Corner	Surface		Room	PM-4	Arb	3.30
8431	82.6	Corner	Surface		Room	PM-4	Arb	3.29
8429	83.3	Corner	Surface		Room	PM-4	Arb	3.29
7745	84.5	Tensile	Surface		Room	PM-4	Arb	3.26
7735	87.9	Corner	Surface		Room	PM-4	Arb	3.27
7747	90.7	Corner	Surface		Room	PM-4	Arb	3.26
8442	90.8	Tensile	Surface		Room	PM-4	Arb	3.25
8444	98.8	Tensile	Surface		Room	PM-4	Arb	3.26
7756	100.3	Corner	Surface		Room	PM-4	Arb	3.27
8443	101.0	Tensile	Surface		Room	PM-4	Arb	3.26
8434	106.8	Tensile	Surface		Room	PM-4	Arb	3.29
8438	108.8	Tensile	Surface		Room	PM-4	Arb	3.25
8433	116.0	Corner	Surface		Room	PM-4	Arb	3.28
8573	57.9	Corner	Surface		Room	PM-4	Bat	3.26
8606	68.6	Corner	Surface		Room	PM-4	Bat	3.31
8597	73.0	Tensile	Surface		Room	PM-4	Bat	3.27
8571	83.2	Corner	Surface		Room	PM-4	Bat	3.27
8580	88.2	Corner	Surface		Room	PM-4	Bat	3.27
8583	88.3	Corner	Surface		Room	PM-4	Bat	3.26
8568	88.9	Tensile	Surface		Room	PM-4	Bat	3.27

MOR and fractography results of sinter/HIP injection molded GN-10 test bars

Bar No.	MOR (ksi)	Fracture Location	Origin Type	Observations/ Comments	Test Temp	Batch	Mold	Density
8572	89.7	Corner	Surface		Room	PM-4	Bat	3.26
8603	93.7	Tensile	Surface		Room	PM-4	Bat	3.27
8578	94.9	Corner	Surface		Room	PM-4	Bat	3.28
8608	97.8	Corner	Surface		Room	PM-4	Bat	3.30
8579	108.1	Corner	Surface		Room	PM-4	Bat	3.25
8607	115.4	Tensile	Surface		Room	PM-4	Bat	3.26
8137	47.5	Surface	Void		2250	GN-10	Arb	3.26
8153	64.5	Tensile	Surface		2250	GN-10	Arb	3.28
8180	69.5	Tensile	Surface		2250	GN-10	Arb	3.23
8160	77.6	Tensile	Surface		2250	GN-10	Arb	3.29
8131	79.8	Tensile	Surface		2250	GN-10	Arb	3.25
8278	53.4	Internal	Void		2250	GN-10	Bat	3.17
8296	63.1	Surface	Void		2250	GN-10	Bat	3.23
8317	67.6	Tensile	Surface		2250	GN-10	Bat	3.25
8300	67.8	Tensile	Surface		2250	GN-10	Bat	3.26
8291	71.6	Tensile	Surface		2250	GN-10	Bat	3.27
7757	59.6	Tensile	Surface		2250	PM-4	Arb	3.31
7736	70.3	Tensile	Surface		2250	PM-4	Arb	3.27
8446	74.3	Tensile	Surface		2250	PM-4	Arb	3.30
8440	74.4	Tensile	Surface		2250	PM-4	Arb	3.25
7733	75.1	Tensile	Surface		2250	PM-4	Arb	3.25
8435	76.3	Tensile	Surface		2250	PM-4	Arb	3.26
8582	52.5	Tensile	Surface	SCG & deformed	2250	PM-4	Bat	3.24
8574	65.7	Tensile	Surface		2250	PM-4	Bat	3.25
8569	74.7	Tensile	Surface		2250	PM-4	Bat	3.25
8677	76.8	Tensile	Surface	SCG & deformed	2250	PM-4	Bat	3.27
8600	80.8	Tensile	Surface		2250	PM-4	Bat	3.28
8136	47.7	Tensile	Surface	SCG & deformed	2550	GN-10	Arb	3.25
8166	48.2	Tensile	Surface	SCG & deformed	2550	GN-10	Arb	3.27
8169	50.3	Tensile	Surface	SCG & deformed	2550	GN-10	Arb	3.23
8146	50.7	Tensile	Surface	SCG & deformed	2550	GN-10	Arb	3.29
8156	51.5	Tensile	Surface	SCG & deformed	2550	GN-10	Arb	3.25
8312	42.9	Tensile	Surface	SCG & deformed	2550	GN-10	Bat	3.15
8279	50.6	Tensile	Surface	SCG & deformed	2550	GN-10	Bat	3.18
8314	51.1	Tensile	Surface	SCG & deformed	2550	GN-10	Bat	3.22
8294	53.1	Tensile	Surface	SCG & deformed	2550	GN-10	Bat	3.26
8301	53.1	Tensile	Surface	SCG & deformed	2550	GN-10	Bat	3.26

MOR and fractography results of sinter/HIP injection molded GN-10 test bars

Bar No.	MOR (ksi)	Fracture Location	Origin Type	Observations/ Comments	Test Temp	Batch	Mold	Density
8441	46.8	Tensile	Surface	SCG & deformed	2550	PM-4	Arb	3.31
8427	52.6	Tensile	Surface	SCG & deformed	2550	PM-4	Arb	3.26
8436	53.9	Tensile	Surface	SCG & deformed	2550	PM-4	Arb	3.25
8445	54.5	Corner	Surface	SCG & deformed	2550	PM-4	Arb	3.30
8611	48.5	Tensile	Surface	SCG & deformed	2550	PM-4	Bat	3.27
8567	50.2	Tensile	Surface	SCG & deformed	2550	PM-4	Bat	3.27
8584	50.4	Tensile	Surface	SCG & deformed	2550	PM-4	Bat	3.26
8576	53.3	Tensile	Surface	SCG & deformed	2550	PM-4	Bat	3.25
8599	53.5	Tensile	Surface	SCG & deformed	2550	PM-4	Bat	3.27

★U.S. GOVERNMENT PRINTING OFFICE:1991 -550 -702/

NASA
National Aeronautics and Space Administration

Report Documentation Page

1. Report No.	2. Government Accession No.	3. Recipient's Catalog No.
NASA CR -182193		

4. Title and Subtitle	5. Report Date
Improved Silicon Nitride for Advanced Heat Engines	April 1991
	6. Performing Organization Code

7. Author(s)	8. Performing Organization Report No.
H.C. Yeh and H.T. Fang	88-61608
	10. Work Unit No. 533 -05-01

9. Performing Organization Name and Address	11. Contract or Grant No.
Allied-Signal Aerospace Company Garrett Ceramic Components Torrance, California 90509	NAS3-24385
	13. Type of Report and Period Covered Contractor Report Final

12. Sponsoring Agency Name and Address	14. Sponsoring Agency Code
National Aeronautics and Space Administration Washington, D.C. 20546 - 0001	

15. Supplementary Notes

Project Manager, Marc R. Freedman, Materials Division, NASA Lewis Research Center, (216) 433-3284.

16. Abstract

This report summarizes the results of a four-year program to improve the strength and reliability of injection-molded silicon nitride. Statistically designed processing experiments were performed to identify and optimize critical processing parameters and compositions. Process improvements were monitored by strength testing at room and elevated temperatures, and microstructural characterization by optical, scanning electron microscope, and scanning transmission electron microscope. Processing modifications resulted in a 20-percent strength and 72-percent Weibull slope improvement of the baseline material. Additional sintering aids screening and optimization experiments succeeded in developing a new composition (GN-10) capable of 581.2 MPa (84.3 ksi) at 1399 °C (2550 °F). A SiC whisker-toughened composite using this material as a matrix achieved a room-temperature toughness of 6.9 MPa.$m^{1/2}$ by the Chevron notched bar technique. Exploratory experiments were conducted on injection molding of turbocharger rotors.

17. Key Words (Suggested by Author(s))

Ceramics; Injection molding; Silicon nitride; Statistics; Properties; Sinter/HIP

Date for general release April 1993.
Subject Category 24

19. Security Classif. (of the report)	20. Security Classif. (of this page)	21. No. of pages	22. Price
Unclassified	Unclassified	290	A13

NASA FORM 1626 OCT 86